Communauté
UNIVERSITÉ Grenoble Alpes

THÈSE

Pour obtenir le grade de

DOCTEUR DE LA COMMUNAUTE UNIVERSITE GRENOBLE ALPES

Spécialité :

MATERIAUX, MECANIQUE, GENIE CIVIL, ELECTROCHIMIE

Arrêté ministériel : 7 août 2006

Présentée par

Albert ARGILAGA CLARAMUNT

Thèse dirigée par **Stefano DAL PONT**
Co-dirigée par **Gaël COMBE**
Encadrée par **Denis CAILLERIE**
Encadrée par **Jacques DESRUES**

Préparée au sein du **Laboratoire Sols, Solides, Structures-Risques**
dans **l'École Doctorale IMEP2**

FEMxDEM double scale approach with second gradient regularization applied to granular materials modeling

Thèse soutenue publiquement le **16 décembre 2016**
devant le jury composé de:

M. Frédéric COLLIN
Professeur, Université de Liège, Président du jury
M. Manuel PASTOR
Professeur, Universidad Politécnica de Madrid, Rapporteur
M. Romeo FERNANDES
Docteur, IMSIA, UMR EDF-CNRS-CEA-ENSTA ParisTech 9219, Examinateur
Mme. Varvara KOUZNETSOVA
Professeur, Technische Universiteit Eindhoven, Examinateur
M. Stefano DAL PONT
Professeur, Université Grenoble Alpes, Directeur de thèse
M. Gaël COMBE
Professeur, Université Grenoble Alpes, Co-directeur
M. Denis CAILLERIE
Professeur Émérite, Université Grenoble Alpes, Co-encadrant
M. Jacques DESRUES
Directeur de Recherche, CNRS, Co-encadrant

Abstract

The multi-scale FEMxDEM approach is an innovative numerical method for geotechnical problems involving granular materials. The Finite Element Method (FEM) and the Discrete Element Method (DEM) are simultaneously applied to solve, respectively, the structural problem at the macro-scale and the material microstructure at the micro-scale. The advantage of using such a double scale configuration is that it allows to study an engineering problem without the need of standard constitutive laws, thus capturing the essence of the material properties. The link between scales is obtained via numerical homogenization, so that, the continuum numerical constitutive law and the corresponding tangent matrix are obtained directly from the discrete response of the microstructure.

Typically, the FEMxDEM approach presents some drawbacks; the convergence velocity and robustness of the method are not as efficient as in classical FEM models. Furthermore, the computational cost of the microscale integration and the typical mesh-dependency at the macro-scale, make the multi-scale FEMxDEM approach questionable for practical uses. The aim of this work is to focus on these theoretical and numerical issues with the objective of making the multiscale FEMxDEM approach robust and applicable to real-scale configurations. A variety of operators is proposed in order to improve the convergence and robustness of the method in a quasi-Newton framework. The independence of the Gauss point integrations and the element intensive characteristics of the code are exploited by the use of parallelization using an OpenMP paradigm. At the macro level, a second gradient constitutive relation is implemented in order to enrich the first gradient Cauchy relation bringing mesh-independency to the model.

The aforementioned improvements make the FEMxDEM approach competitive with classical FEM models in terms of computational cost thus allowing to perform robust and mesh-independent multi-scale FEMxDEM simulations, from the laboratory scale (e.g. biaxial test) to the engineering-scale problem, (e.g. gallery excavation).

Keywords: Double scale, numerical homogenization, numerical constitutive law, elasto-plasticity, second gradient, microstructured materials, large strain, finite elements, discrete elements, Newton method, parallelization, uniqueness

Résumé

L'approche multi-échelle FEMxDEM est une méthode numérique innovante pour les problèmes géotechniques impliquant des matériaux granulaires. La méthode des éléments finis (FEM) et la méthode des éléments discrets (DEM) sont simultanément appliquées à résoudre, respectivement, le problème structurel à la macro-échelle et la microstructure du matériau à la micro-échelle. L'avantage d'utiliser une telle configuration à double échelle est de permettre d'étudier un problème d'ingénierie sans la nécessité de lois de comportement standard, capturant ainsi l'essence des propriétés des matériaux. Le lien entre les échelles est obtenu par homogénéisation numérique, de sorte que la loi de comportement continu numérique et la matrice tangente correspondante sont obtenues directement à partir de la réponse discrète de la microstructure.

En règle générale, l'approche FEMxDEM présente quelques inconvénients; la vitesse de convergence et la robustesse de la méthode ne sont pas aussi efficaces que dans les modèles FEM classiques. De plus, le coût de calcul de l'intégration de la micro-échelle et la dépendance du maillage typique de la macro-échelle, rendent l'approche multi-échelle FEMxDEM discutable pour des utilisations pratiques. Le but de ce travail est de se concentrer sur ces questions théoriques et numériques avec l'objectif de rendre l'approche multi-échelle FEMxDEM robuste et applicable à des configurations à l'échelle réelle. Une variété d'opérateurs est proposée afin d'améliorer la convergence et la solidité de la méthode dans un cadre quasi-Newton. L'indépendance de l'intégration des différents points de Gauss et les caractéristiques d'intensivité sur les d'éléments sont exploités par l'utilisation d'une parallélisation Au niveau macro, une relation constitutive second gradient est mise en œuvre afin d'enrichir le modèle apportant indépendance du maillage.

Les améliorations susmentionnées rendent l'approche FEMxDEM compétitive avec les modèles FEM classiques en termes de coût de calcul permettant ainsi d'effectuer des simulations multi-échelle FEMxDEM robustes et indépendantes du maillage, depuis l'échelle du laboratoire (par exemple essaie biaxiale test) jusqu'à celle du problème à l'échelle de l'ingénierie (par exemple, excavation d'une galerie).

Mots clés: Double échelle, homogénéisation numérique, loi constitutive numérique, élasto-plasticité, second gradient, matériaux microstructurés, grande déformation, éléments finis, éléments discrets, méthode de Newton, parallélisation, unicité

Contents

Chapter 1

Introduction

Contents

1.1 Introduction

In the present work a numerical model applied to geomaterials has been developed. Geomaterials are those of granular nature, usually exhibiting a frictional cohesive behavior, mainly soils, rocks and concrete. The problems that can be treated with the model range from a biaxial test at the laboratory scale to a gallery excavation at the engineering scale.

The particularity of the model is that it does not use a phenomenological expression to describe the properties of the material, but rather it uses another numerical model which is assumed to be in a different scale of observation (microscale). The model representative of the microscale is a Discrete Element Model (DEM) which is intended to model granular or particulate materials, while the macroscale Finite Element Model (FEM) is a classical numerical tool to solve continuum problems. This results in a double scale model: FEMxDEM. The advantage of using a double scale configuration is that the essence of the material properties is captured from its heart, without the use of phenomenological descriptions; this may end up with a better description of the modelled materials.

Despite the potential of the approach, in the way it has been built in the present work, it presents some drawbacks: First issue to be considered is the instability of the Newton method. Due to the characteristics of the microscale the classical Newton approach is

not efficient and a study to find better candidates is performed. Secondly, due to the complexity of the microscale, the model needs a very large computational time; this makes it not practical to be used in real applications. A parallelization is proposed in order to take advantage of modern computer architectures to speed up the model. This parallelization allows to very efficiently divide the computational load within several cores and so accelerate the simulations. Finally, the model suffers from a numerical issue called mesh dependency. Due to the kind of constitutive law used to describe the material, the model does not account for size effects: the geometric discretization used in the macroscale FEM conditions the solution. This is a problem since the choice of the geometric discretization does not have a physical signification, it is of numerical nature which should not influence the solution. To fix that, a second gradient regularization is introduced to the model; this one enriches the description of the material by introducing an internal length and avoids the solution to depend on the geometric discretization. The model becomes objective.

The aforementioned improvements allow using the double scale FEMxDEM model for practical purposes, with an objective solution and competitive computational time.

A general introduction in presented in this chapter including a state of the art of multi-scale models, FEMxDEM models and regularization techniques, special emphasis is put into second gradient. Then a brief introduction of the FEMxDEM model is presented with a description of its formulation on a finite element framework, the DEM microscale is described as well and finally the coupling technique between the scales.

1.2 State of the art

Multiscale numerical models allow to have an insight into the microscale origins of complex phenomena such as localization and anisotropy in mechanical problems (Auriault, 1991; Smit et al., 1998; Kouznetsova et al., 2001; Auriault, 2011; Hautefeuille et al., 2012). This allows to avoid the use of phenomenological constitutive laws by obtaining the material properties directly from a microscale simulation. The idea of FEMxDEM is to solve a continuum boundary value problem (BVP) at the macroscale while obtaining the constitutive material behaviour from a DEM microscale in a fully coupled hierarchical multiscale method. Some early works (Kaneko et al., 2003; Miehe et al., 2010a; Nitka et al., 2011), have put in evidence the potential of the method to provide a refined description of complex constitutive behaviors into real-scale computations. Indeed, FEMxDEM methods allow to couple the advantages of Discrete Elements (i.e. a numerical constitutive law for a complex material behavior can be obtained) and the efficiency of Finite Elements. Later works have enhanced and extended this approach to the study of anisotropy (Guo and Zhao, 2013; Nguyen, 2013), granular cohesion (Nguyen et al., 2014), material heterogeneity (Shahin et al., 2016), real scale engineering applications (Nguyen, 2013; Guo and Zhao, 2014, 2015), more realistic constitutive behaviors using 3D DEM (Liu et al., 2015; Wang and Sun, 2016), macroscale hydro-mechanical coupling (Wang and Sun, 2016; Guo and Zhao, 2016b). More recently, (Liu et al., 2015) have embedded non-local regularization at the macro-scale and (Guo and Zhao, 2016a) have

developed a full micro-macro 3D approach.

However, despite these latest developments, some open issues in the development of the method can be identified. The non-linearity of the problem requires an iterative Newton's scheme and therefore the definition of a tangent operator which in the case of a complex constitutive behavior, is usually obtained by numerical derivation, i.e. making use of a perturbation method. For that, the DEM part has to be carried out each time the constitutive relation is required and that computation is time consuming. In addition, the use of Discrete Elements at the micro-scale intrinsically leads to numerical instabilities, i.e. the constitutive law by numerical homogenization of a DEM model gives as a result a function which is not differentiable after the peak. This, together with the softening nature of the law, results in a poor stability and performance of the method (Crisfield and Wills, 1988). The resorting to an auxiliary operator simpler to compute is likely to drastically shorten the computational time. The first objective of the present work is to mitigate this issue by proposing and discussing alternative operators, introducing quasi Newton strategies that prove to be robust, stable and numerically efficient.

Furthermore, once the model is provided with a proper operator, a reduction of the computational time is desired in order to compete with classical analytical law FEM models. Due to the characteristics of the model an element loop parallelization is well suited, this can effectively distribute the computational charge between parallel computations. Different parallelization approaches exist, shared memory, distributed memory and GPU paradigms, an approach based on a shared memory framework using OpenMP directives is used. The aim is to take profit of the multicore architectures usually found in non distributed systems so the use of computation networks is not needed. The combination of these enhancements allow to overcome the FEMxDEM computational limitations, thus making the approach comparable to classical FEM in terms of stability and computational cost.

Using a strain softening material in a Partial Differential Equation (PDE) problem can result in an ill-posed problem (Hill, 1962; Rice, 1976). The consequence of this ill posedness are numerical instabilities and strain mesh dependency (Pietruszczak and Mroz, 1981; Sluys et al., 1993), the mesh dependency implies that, in localization problems, the shear band width is not objective. Regularization techniques have been developed to overcome these problems, the regularization consists in introducing an internal length that eliminates the pathological mesh dependency and so regularizes the problem. Both nonlocal (Eringen, 1972) and local (Mindlin, 1965; Germain, 1973) approaches exist. A nonlocal regularization has already been used with a FEMxDEM model (Liu et al., 2015). Local formulations use a local relationship between stress and strains in the same manner classical constitutive relations are defined, in contrast to nonlocal formulations which depend on the neighborhood of the material point. Second gradient model, as a particular case of the Germain theory (Germain, 1973) has been developed (De Borst and Mühlhaus, 1992; Sluys et al., 1993; Pamin, 1994; De and De Vree, 1996; Chambon et al., 1998; Matsushima et al., 2000; Chambon et al., 2001; Yang and Misra, 2012). It has been extensively applied in geomechanics and engineering

applications with satisfactory results (Collin et al., 2006; Sieffert et al., 2009; Marinelli, 2013; Jouan et al., 2014; Salehnia et al., 2015).

Previous developments of FEMxDEM could not take advantage of Second Gradient regularization due to the poor solution stability and limited available mesh refinement. Recent improvements concerning stability and computational efficiency allow to build a FEMxDEM model including local Second Gradient. This results in an objective model capable of simulating real scale problems with any mesh refinement.

The document is divided in six chapters. Chapter 2 introduces the Newton method, its limitations with the present FEMxDEM model and the proposed alternatives. The main part of the chapter presents development based on the DEM microscale that provides an elastic operator. Chapter 3 is devoted to the introduction of random field methods to the model, the use of DEM is exploited in order to inject spatial variability to the FEM by the use of different DEM assembly generations. Chapter 4 presents the second gradient regularization, the chapter focuses on the results, showing the ability to regularize the FEMxDEM model. Chapter 5 presents the shared memory element loop parallelization, a part of it is devoted to explain how the parallelization can affect the obtained solution. The chapter ends with acceleration benchmarks using different machines. Chapter 6 uses all the aforementioned features to run a series parametric studies of a gallery excavation using the FEMxDEM model, the results show that the model can effectively simulate real scale problems using both micro and macro parameters in order to well characterize the BVP. The document ends with conclusions.

1.3 Brief introduction to the model

In this section, FEM and DEM are described as well as the coupling method. To introduce the model, the BVP is presented in its strong formulation, then the weak formulation needed in the FEM implementation is derived as well as the discretized expression and the equation to be minimized by Newton Raphson. DEM is described including its preparation with a description of all the parameters needed to reproduce the model.

1.3.1 Finite element method

A finite element approach is used for the discretization of the mechanical BVP in the macroscale. The strong formulation of the elasticity equations, without gravity forces, is presented in eqs. (1.1) to (1.3):

$$div\,\sigma = 0\ in\ \Omega \tag{1.1}$$

$$\sigma = c : \epsilon(\vec{u})\ in\ \Omega \tag{1.2}$$

$$\sigma \cdot \vec{n} = \vec{t}\ in\ \partial\Omega_t, \tag{1.3}$$

where Ω is the BVP domain, $\partial\Omega_t$domain boundary, σ the Cauchy stress, c is a fourth order stiffness tensor, $\epsilon(\vec{u})$ the strain field function of the displacement field $\vec{u}$, $\vec{n}$ the normal to the boundary and $\vec{t}$ the applied boundary traction. The problem is made complete with boundary conditions. Additional kinematic restrictions are needed to avoid kinematic indetermination, i.e. displacement restrictions in 3 Degrees Of Freedom (DOF) for a plane strain problem. The first step to obtain the weak formulation is to write the virtual power formulation of the equilibrium. This is done by scalarly multiplying eq. (1.1) by a virtual velocity field $\vec{w}$ and integrating over the domain Ω: eq. (1.1):

$$\int_{\Omega} div\, \sigma \cdot \vec{\omega}\, dA = 0 \tag{1.4}$$

Secondly, integrating by parts and using Ostrogradsky's divergence theorem we obtain eq. (1.5):

$$\int_{\Omega} \sigma : \nabla\vec{\omega}\, dA = \int_{\partial\Omega} (\sigma @ \vec{\omega}) \cdot \vec{n}\, dS, \tag{1.5}$$

where $\partial\Omega$ is the complete boundary of the domain Ω. By considering the symmetry of σ in the left hand side integral and linear manipulating the right hand side we obtain: eq. (1.6):

$$\int_{\Omega} \sigma : \epsilon(\vec{\omega})\, dA = \int_{\partial\Omega} (\sigma @ \vec{n}) \cdot \vec{\omega}\, dS \tag{1.6}$$

The test field acting on the part of the boundary condition without applied traction can be set to zero and substituting the expression in the right hand side integral by eq. (1.3) we obtain the final weak formulation eq. (1.7):

$$\int_{\Omega} \sigma : \epsilon(\vec{\omega})\, dA = \int_{\partial\Omega_t} \vec{t} \cdot \vec{\omega}\, dS \tag{1.7}$$

The weak formulation is finally discretized accordingly to Galerkin's approach, thus having eq. (1.8):

$$Ku = f, \tag{1.8}$$

where u is the nodal displacement vector, f the nodal force vector and K is the global rigidity matrix which is built using the partial derivatives of the constitutive law. Numerical homogenization is used in the present work to obtain the constitutive law; the rigidity matrix K is substituted by K_t assembled using a tangent operator eq. (1.9):

$$K_t = \int_{\Omega} B^T D B\, dA, \tag{1.9}$$

Consistent Tangent Operator is obtained by perturbations, where B is the deformation matrix and D the tangent modulus in the FE discretization. The problem is then about minimizing the residual force R using Newton-Raphson: eq. (1.10):

$$R = \int_{\Omega} B^T \sigma \, dA - f \tag{1.10}$$

The use of a microscale numerical model that, after numerical homogenization, serves as a constitutive law to the macroscale model is the key point of this approach. The use of this numerically homogenized law has not only implications on the obtention of K_t but also on the feasibility and efficiency of eq. (1.10), this means that the stability of the model is compromised due to the discrete behavior of the DEM microscale and the typical quadratic convergence is lost.

A large-scale quasi-static evolution of a continuum media is presented, the medium presents analogies, at least from a numerical point of view, with other geomechanics constitutive laws, e.g. elastoplasticity, hypoplasticity.

1.3.2 Discrete Element Method as a numerical constitutive law

A standard DEM approach (Radjai and Dubois, 2010; Roux and Combe, 2010) has been retained in this work using a 3rd order predictor corrector scheme. This is not intended to be a detailed description of the DEM model but a remainder of the basics. The model uses rigid circular grains that interact via contact point. The normal contact force is given as $f_n = -K_n\delta$, where K_n is the normal contact stiffness and δ is the overlapping magnitude ($\delta < 0$ when the contact occurs). The tangential force increment is given as $\Delta f_t = K_t.\Delta U_t$, where K_t is the tangential stiffness and ΔU_t is an increment of tangential relative displacement computed at the contact point. The total tangential force, f_t, is the sum over the time step Δt. The Coulomb friction coefficient is used to limit f_t such that $|f_t| \leq \mu f_n$, where μ is the contact angle of friction.

Preparation procedures of the DEM assembly are of great importance due to their strong effects on the mechanical properties of the final assembly (Szarf et al., 2009; Radjai and Dubois, 2010; Roux and Combe, 2010; Shahin et al., 2016). The assembly is formed of 400 particles, consistently with the guidelines provided by Nguyen (2013); Nguyen et al. (2014) and Guo and Zhao (2013, 2014). This constitutes a good compromise between the computational cost and the problem stability. Periodic Boundary Conditions are retained in the horizontal and vertical directions Radjai and Dubois (2010); Nitka et al. (2011); Nguyen (2013); Nguyen et al. (2014). In this work, the simulation is focused on a dense frictional granular material. To obtain a dense assembly, the inter-particle friction coefficient has been set to zero during the preparation step as the particles can slide and fill the volume as much as possible. In addition, the grain size range has been taken as R_{max}/R_{min}=2.5, following a uniform grain area distribution.

DEM granular assemblies have been generated following the algorithm proposed in Radjai and Dubois (2010). Starting from a given particle size range and a given number of particles, they are placed in a regular grid and a random generator is used to determine the radius. The particles are then submitted to a random velocity field. The particles move and interact as rigid bodies within a fixed size container. No energy dissipation is introduced during this process. When particles have been shaken enough (i.e. each particle is displaced cumulatively 100 times its diameter), their velocity is set to zero,

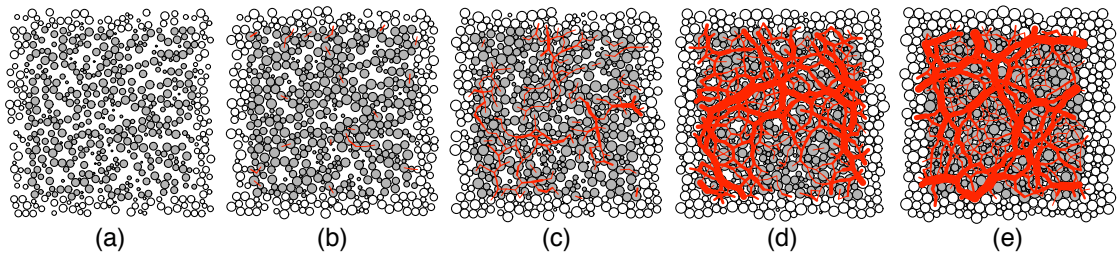

Figure 1.1: Compression stage during the preparation of the REV, from the resultant gas like configuration after shaking (a) to the final dense packing in (e) passing by different compaction stages during the process (b,c,d) in which new force chains are created (red lines).

Table 1.1: The given values of DEM mechanical parameters. κ is the normal stiffness coefficient normalized by confinement pressure σ_0.

Parameter	Value
Stiffness level $\kappa = K_n/\sigma_0$	1000
Tangent/Normal stiffness coefficients K_t/K_n	1
Coulomb friction	0.5

(see Figure 3.23, a). The resultant granular packing, which has a gas-like configuration, is then subjected to a strain-controlled isotropic compression phase (see Figure 3.23, b,c,d) leading to the desired granular assembly, (see Figure 3.23, e).

1.3.3 FEMxDEM coupling

The FEMxDEM multiscale approach is built using a hierarchical procedure in which the DEM is considered as representative of the microscale (Guo and Zhao, 2013; Nguyen et al., 2014). The classical analytical law in each Gauss point in the FEM model is replaced by a Numerically Homogenized Law (NHL) using DEM (Fig. 1.2). The coupling between the two scales is made via numerical homogenization of the DEM microscale at the end of a loading step using the Love (Cauchy-Poisson) average formula (Eq. 1.11) (Love, 2013). The DEM assembly homogenization provides a constitutive law to the macroscale in the same manner as other numerical homogenization approaches could do (Argilaga et al., 2016).

The FEM code solves a Cauchy problem in static conditions, while the DEM code solves a problem based on the 2nd Newton's law, to avoid dynamic effects on the DEM, the loading rate is limited, in addition, a relaxation stage is added after the loading to guarantee quasistatic conditions before the homogenization. Readers interested in models accounting for micro-scale inertia and body force effects as well as models based on the Principle of Multiscale Virtual Power should address Blanco et al. (2014); de Souza Neto et al. (2015).

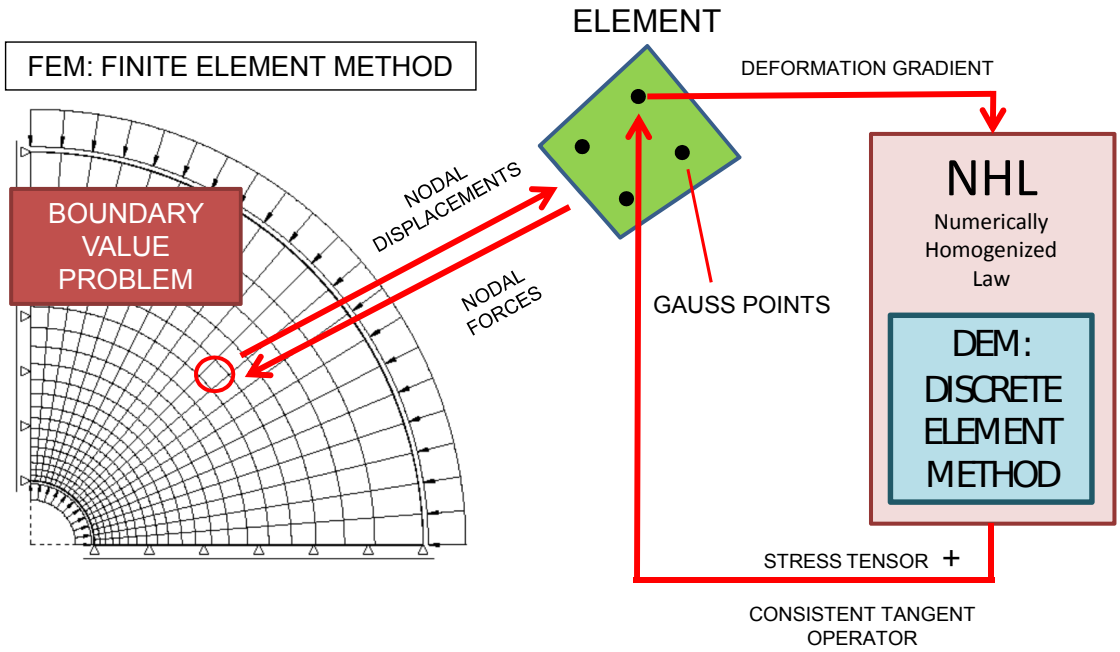

Figure 1.2: Computational homogenization scheme

$$\sigma_{ij} = \frac{1}{S} \sum_{(n,m)\in C} \overrightarrow{f^{m/n}} \otimes \overrightarrow{r^{nm}} \tag{1.11}$$

1.4 Conclusion

A double scale numerical homogenization framework has been presented. It is based in a classical FEM code where the constitutive relation is obtained from a microscale DEM code. The bibliography shows that important works concerning this subject exist, but still, important issues need to be addressed. This sets the bases for the developments presented in this document

Chapter 2

Newton operator

Contents

2.1 Introduction

The essence of the numerical model is introduced in this section pointing out its similarities with classical geomechanics FEM codes. Literature concerning iterative methods and convergence issues concludes the section.

2.1.1 Link with classical geomechanics FEM codes

Except for very small deformations, geomaterials cannot be considered as elastic. Their behaviour is history dependent which means that to be able to determine the stress in a geomaterial at a time t of its evolution it is necessary to know the history of the strain up to that time. The writing of such constitutive equation is not an easy task and most of the constitutive equations of geomaterials are written in a form involving time derivatives of strain, stress or other quantities. Incremental or elastoplasticity constitutive equations are among the most widely used equations to model the behaviour of geomaterials, which does not present viscosity, they read for instance:
incremental equation

$$\dot{\sigma} = C\left(\sigma, \dot{\epsilon}\right) \tag{2.1}$$

where σ is the stress tensor, $\dot{\sigma}$ its material time derivatives and $\dot{\epsilon}$ the strain rate. C is a non linear function. An example of such an incremental constitutive equation is given by the hypoplasticity (see Chambon et al. (1994)) for which C reads $C\left(\sigma, \dot{\epsilon}\right) = A\left(\sigma\right) : \dot{\epsilon} + B\left(\sigma\right) \|\dot{\epsilon}\|$.
perfect elastoplasticity

$$f\left(\sigma\right) \leq c \tag{2.2a}$$
$$\sigma = A : \left(\epsilon - \epsilon_p\right) \tag{2.2b}$$
$$\dot{\epsilon}_p = \lambda \nabla_\sigma g \text{ with } 0 \leq \lambda \tag{2.2c}$$
$$\lambda f = 0 \tag{2.2d}$$

where f is a convex function.

In many cases, the evolution of geomaterials is very slow, slow enough to neglect the acceleration. The evolution is then quasistatic that means that the geomaterial is in equilibrium at each time of its evolution which reads in a virtual power form (assuming large deformations):

$$\forall t, \forall \vec{w}^*\,, -\int_{\Omega_t} \sigma : \nabla \vec{w}^* \mathrm{d}v + \int_{\partial\Omega_t} \vec{F}.\vec{w}^* \mathrm{d}s = 0 \tag{2.3}$$

where Ω_t is the configuration of the medium at time t. $\vec{F}$ is the surfacic density of exterior forces applied on the boundary $\partial\Omega_t$ of Ω_t; the volumic density $\vec{f}$ of forces being disregarded. $\nabla\vec{w}^*$ is the gradient of the virtual velocity field $\vec{w}^*$. It has to be stressed out that in that case t is not the real time but only a loading parameter.

The problem being an evolution problem, its numerical simulation is carried out using a time stepping method. The balance equation is written at each step. In the

following, a quantity with a superscript ^{i} or ^{f}, refers to the value of that quantity at the beginning of the step, resp. at the end of the step. To pass from one step to the next, the constitutive equation have to be integrated over the step: different methods are used to that purpose. For instance for elastoplasticity, the time derivative of the plastic strain is approximated using an Euler forward finite difference and all the equations are written at the end of the step, which yield an algebraic problem the datum of which is the strain ϵ^f at the end of the step, the unknowns being the stress σ^f, the plastic strain ϵ_p^f at the end of the step and the plastic multiplier of the step λ^f. In the case of a 1D problem for which $f(\sigma) = |\sigma|$ and $\nabla_\sigma g = \operatorname{sgn}(\sigma)$ it comes (see Simo and Hughes (2006)):

$$\sigma^{fe} = A\left(\epsilon^f - \epsilon_p^f\right) \tag{2.4a}$$

$$f^{fe} = \left|\sigma^{fe}\right| - c \tag{2.4b}$$

$$\lambda^f = \frac{1}{\Delta t}\frac{f^{fe} + \left|f^{fe}\right|}{2k} \tag{2.4c}$$

$$\sigma^f = \sigma^{fe} - A\lambda^f \Delta t \operatorname{sgn}\left(\sigma^{fe}\right) \tag{2.4d}$$

$$\epsilon_p^f = \epsilon_p^i + \lambda^f \Delta t \operatorname{sgn}\left(\sigma^{fe}\right)$$

where Δt is the step length. It has to be stressed out that the previous equations yield the stress σ^f at the end of the step in terms of the strain ϵ_p^f at the end of the step which can be written:

$$\epsilon^f \mapsto \sigma^f = \mathcal{A}\left(\epsilon^f\right) \tag{2.5}$$

A method often used in FEM codes to deal with an incremental constitutive equation consists in integrating the differential equation along a path $\epsilon(\tau)$ completely determined by the strain ϵ^f for instance $\epsilon(\tau) = \epsilon^i + \tau\left(\epsilon^f - \epsilon^i\right)$, $0 \leq \tau \leq 1$. If large deformations are considered, the strain path $\epsilon(\tau)$ is determined by the deformation gradient F^f at the end of the step; the integration of the incremental consitutive equation, considered as a differential equation in σ, yields therefore an «integrated» constitutive equation that, analogously to (2.5), reads:

$$F^f \mapsto \sigma^f = \mathcal{S}\left(F^f\right) \tag{2.6}$$

In large deformations, the problem to be solved on each time step is a boundary value problem composed of the balance equation (2.3) written at the end of the step:

$$\forall \vec{w}^*, -\int_{\Omega^f} \sigma^f : \nabla \vec{w}^* \mathrm{d}v + \int_{\partial\Omega^f} \vec{F}^f . \vec{w}^* \mathrm{d}s = 0,$$

of the «integrated» constitutive equation (2.6) and of some boundary conditions. Ω^f is the unknown configuration of the medium at the end of the step.

2.1.2 Newton's method

The boundary value problem presented in (Subsec. 2.1.1), non linear in general, is solved using the iterative Newton's method. At each iteration, the equations are expanded up

to the first order with respect to the unknowns, that are mainly the displacement field from Ω^i to Ω^f, the stress σ^f and possibly some parts of $\vec{F^f}$. Then the corresponding linear problem is solved, the unknowns are updated, ready for the following iteration. The strict application of the Newton's method needs to differentiate $\mathcal{S}$ with respect to F^f, the gradient of $\mathcal{S}$ is often called the "consistent operator", it is defined by C:

$$d\sigma^f = \mathcal{S}(F^f + df^f) - \mathcal{S}(F^f) = C : dF^f + \dots$$

With the exception of some simple cases for which closed-form expression of the tensor C can be found, the determining of C is performed numerically using a perturbation method. In the case of a 2D problem, the dimension of the space of F^f's is 4, F^f is therefore perturbed in 4 independent directions, for instance the directions given by the tensors $\Lambda^{nm}, n, m = 1, 2$ defined by:

$$\Lambda^{mn}_{kl} = \delta_{mk}\delta_{nl}$$

where δ is the Kronecker symbol, then the components:

$$(C_{ijmn}) = \frac{\mathcal{S}_{ij}(F^f + \epsilon\Lambda^{mn}) - \mathcal{S}_{ij}(F^f)}{\epsilon} \tag{2.7}$$

are computed. Assuming $\mathcal{S}$ to be differentiable, that determines C. According to the manner it is carried out, the computing of C can be more or less time consuming.

2.1.3 DEM law

In the presently studied case, the determining of σ^f in term of F^f is particular in the sense that it is not provided by the integration of an incremental or partly incremental constitutive equation on a time step as in the case of hypoplasticity or elastoplasticity but by the DEM computing of the displacement field of a spatially periodic assembly of interacting grains. The periodicity condition means that at each step of its evolution the assembly geometry is periodic. That is to say that the positions of the grains are given by those of the grains of a subset, called base cell, translated by vectors $\nu_1\vec{Y}^1 + \nu_2\vec{Y}^2$ (in 2D) with ν_1 and ν_2 being relative integers; $\vec{Y}^1$ and $\vec{Y}^2$, assumed to be linearly independent, are the periodicity vectors. To determine the motion of the grains of the whole assembly, it is enough to determine that of the grains of the base cell taking into account the possible interactions of those grains with those of the adjacent cells, that is the cells for which ν_1, ν_2 are in $\{-1, 0, 1\}$. The rotations of grains are supposed periodic. The motion of the grains of the base cell is determined by numerically integrating the Newton's dynamics equations, the grains interacting by contact forces that are partly elastic and that satisfy the Signorini-Coulomb conditions of friction. Some cohesion can be taken into account, yet interaction torques are disregarded. The kinematic data of that dynamical determining of the motion of grains are the time τ functions $\vec{Y}^1(\tau)$ and $\vec{Y}^1(\tau)$, the unknowns are the displacements and rotations of the grains as well as the interaction forces.

For the DEM computing of relation (2.6), the τ functions $\vec{Y}^1(\tau)$ and $\vec{Y}^2(\tau)$ are taken in the form $\vec{Y}^i(\tau) = F(\tau) \cdot \vec{Y}^i_R$, $i = 1, 2$ where $\vec{Y}^1_R$ and $\vec{Y}^2_R$ are the initial (with respect to the macroscopic evolution) periodicity vectors and where the order 2 tensor function $F(\tau)$ is given by

$$F(\tau) = \begin{cases} F^i + \frac{\tau}{\tau_1}\left(F^f - F^i\right) & 0 \leq \tau \leq \tau_1 \\ F^f & \tau_1 < \tau \end{cases} \tag{2.8}$$

The DEM computing is carried on further than the time τ_1 untill the grains of the base cell are balanced (kinetic energy less than a threshold, no more creation or loss of contact ...) in such a way that the DEM computation should be consistent with the quasi static feature of the macroscopic modeling. To speed up that last part of the computation a damping term can be added to the interacting forces.

At the end of the computation, the DEM provides the positions $\vec{r}^n$ of the grains of the base cell numbered by n, the contact forces $\vec{f}^{m/n}$, $\vec{f}^{m/n}$ being the force applied on the grain n by the grain m. The Cauchy stress tensor is determined according to the Cauchy-Poisson formula:

$$\sigma^f = \frac{1}{S} \sum_{(n,m)\in\mathcal{C}} \vec{f}^{m/n} \otimes \left(\vec{r}^m + \nu_1 \vec{Y}^1 + \nu_2 \vec{Y}^2 - \vec{r}^n\right) \tag{2.9}$$

where $S = \left\|\vec{Y}^1 \wedge \vec{Y}^2\right\|$ is the area of the assembly of grains and $\mathcal{C}$ denotes the set of couples of grains being in contact. Tthe grain n interact with the grain m of the base cell ($(\nu_1, \nu_2) = (0, 0)$) or of a neighbouring cell ($(\nu_1, \nu_2) \neq (0, 0)$). A more precise description of base cell is given in section 2.3.3.

It can be seen that the DEM computation enables to determine σ^f in term of F^f which defines the function $\mathcal{S}$ of (2.6).

2.1.4 Computational expenses

In a DEMxFEM computation, the DEM part has to be carried out each time the function $\mathcal{S}$ of (Eq. 2.6) is required and that computation is time consuming. When the consistent tangent operator (CTO) is used, in a time step of the FEM computation, the DEM computation is performed five times at each iteration of the Newton's method and that for each Gauss point of the FEM discretization. The resorting to an auxiliary operator simpler to compute is likely to drastically shorten the computational time. One more reason to look for another operator than the consistent one is its lack of smoothness. Looking at a strain stress diagram (Fig. 2.1) it can be seen that the curve is rather smooth at a large scale but clearly less at a small scale. That is probably why the consistent tangent operator shows a large variability which can be the origin of the difficult convergence or even the lack of convergence of he Newton's method (Crisfield and Wills, 1988).

The Newton operator is presented with the following notation: (eq. 2.10):

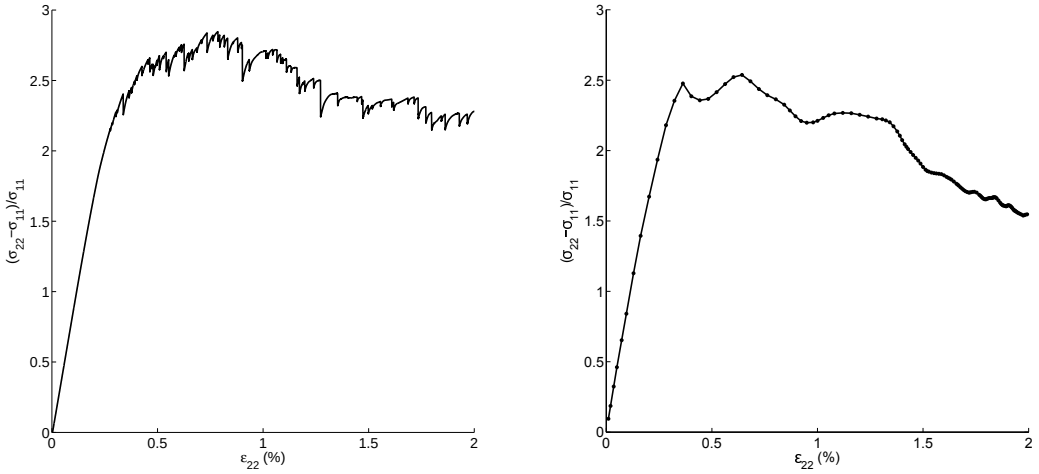

Figure 2.1: Left: stess-strain plot of a compression biaxial test of a pure DEM model, 400 particles with periodic boundary conditions. Right: stess-strain plot of a compression biaxial test of a FEMxDEM model using the previous DEM 400 particles assembly in the micro-scale.

$$\begin{pmatrix} d\sigma^f_{11} \\ d\sigma^f_{12} \\ d\sigma^f_{21} \\ d\sigma^f_{22} \end{pmatrix} = \begin{pmatrix} C_{1111} & C_{1112} & C_{1121} & C_{1122} \\ C_{1211} & C_{1212} & C_{1221} & C_{1222} \\ C_{2111} & C_{2112} & C_{2121} & C_{2122} \\ C_{2211} & C_{2212} & C_{2221} & C_{2222} \end{pmatrix} \begin{pmatrix} dF^f_{11} \\ dF^f_{12} \\ dF^f_{21} \\ dF^f_{22} \end{pmatrix} \tag{2.10}$$

2.1.5 State of the art

Some significant publications concerning non-linear iterative procedures applied to mechanical problems with softening are presented here. The thematics include strain localization, initial state homogeneity, bifurcation and tangent operators among others, those set the bases to develop this chapter.

De Borst (1987) concludes that iterative schemes applied to softening materials are difficult to converge; those present mesh dependency used with FEM discretizations as well as snap-back problems (Fig. 2.2). An arc-length procedure is proposed as a method that could be a good candidate to overcome the Newton method problems at least at the first steps of the iterative process. However, after testing arc-length method in softening materials, De Borst (1987) finds that it is not suited for this kind of problems due to the high localization levels reached. Finally, an attempt to overcome the problems is carried

acting on the eigenvector of the vanishing eigenvalue concluding that it is a good way to trigger the different localization modes.

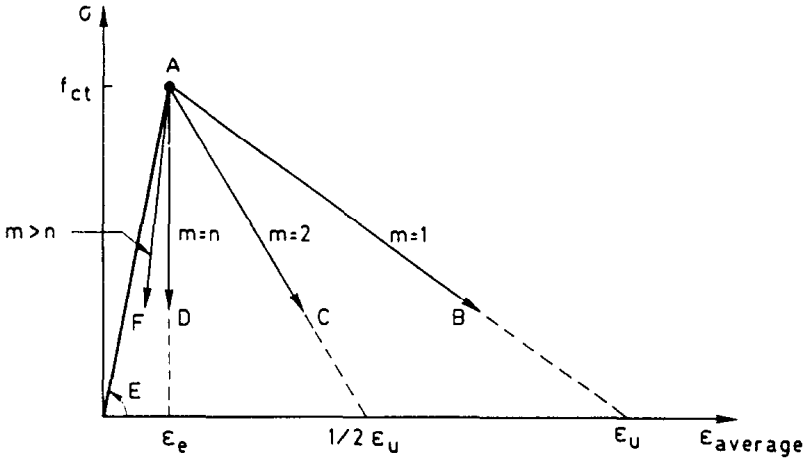

Figure 2.2: Possible post-bifurcation behaviour for a bar loaded in tension. Which equilibrium path is followed depends on the number of elements in which the crack localizes (De Borst, 1987)

.

Bazant and Chang (1987) present an imbricated nonlocal continuum model (Fig. 2.3) applied to model concrete behaviour. The nonlocal enrichment of the model is intended to solve convergence problems due strain-softening. The paper shows that the refinement of the mesh in a local formulation will end up with incorrect convergence. The problem evolves to a physically meaningless state in which the area and energy dissipation due to failure in the localization zone are zero and the strains infinite.

The stability problems due to strain-softening can be avoided by imposing, for the local finite element formulation, the condition that no more than one finite element may enter the strain-softening regime in a single loading step. For the imbricated nonlocal model this condition is not needed. This publication is not only relevant in the present chapter, but later in this document a chapter devoted to Second Gradient will debate about enrichment techniques.

Crisfield and Wills (1988) deal with iterating procedures in softening materials showing that Newton method presents difficulties to converge because it oscillates between localised and non localised states in some integration points during the iterative process. They also treat the problems related to snap-back, snap through and also use different techniques consisting in changing the minimum pivot value in order to trigger the localisation. In some cases, reducing the time step size might not be enough to trigger localization. In a numerical model, the state is likely to be homogeneous unless perturbations are introduced purposely. This homogeneous state may induce the calculation to evolve into an homogeneous non-stable state after the bifurcation while in reality this situation is much less likely to happen due to microscale heterogeneities, manufactur-

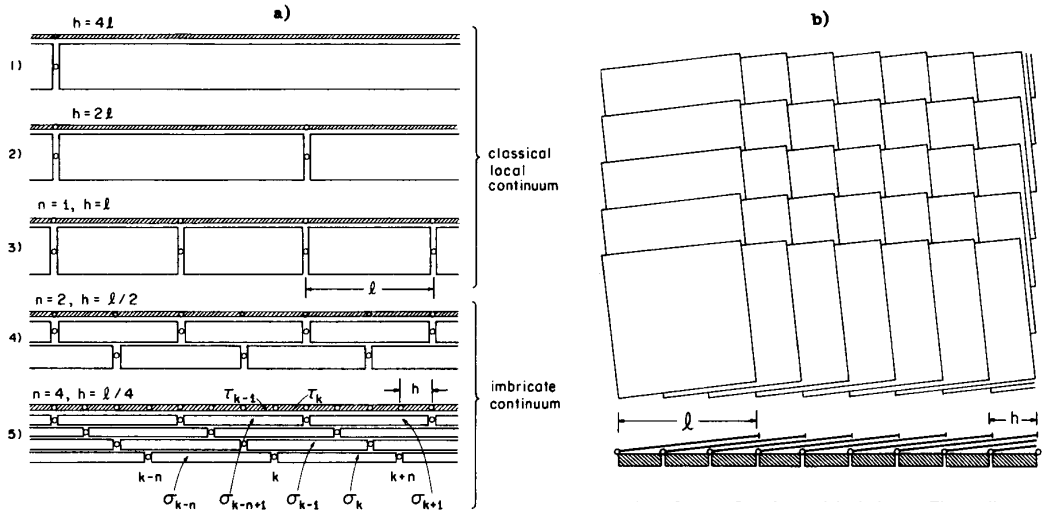

Figure 2.3: (a) Expanded cross section of imbricate finite element meshes at increasing mesh refinements (actual hickness zero); (b) Plan view of imbricate elements slightly rotated out of alignment for purpose of illustration (Bazant and Chang, 1987)

ing imperfections or other kind of geometrical and load perturbations, this will lead to a more localized behaviour than the one predicted in the numerical model leading to potentially catastrophic designs.

Shi and Crisfield (1992) work in the same direction as the previous authors; the aim is to be able to reproduce all the possible bifurcation paths in order to be aware of the ones giving the weaker response (Fig. 2.4). The indicator for possible bifurcations are the minimum pivot and the determinant of the tangent operator. Both indicators give a good clue about the bifurcation triggering in the constitutive law, thus allowing to adopt the proper strategies in order to unfold the different bifurcation modes.

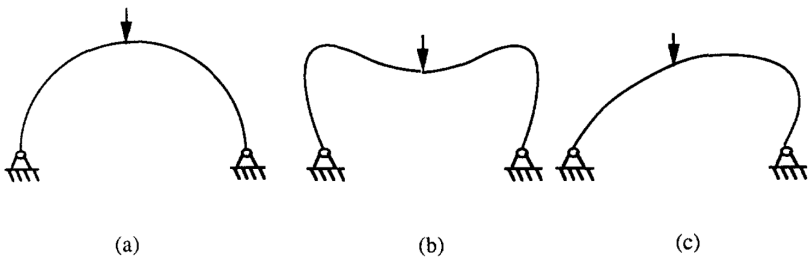

Figure 2.4: (a) The simply supported arch; (b) symetric deformation; (c) asymetric deformation. (Shi and Crisfield, 1992)

Gastebled and May (2000) show that in local bifurcations negative pivots appear and disappear in successive iterations leading to a very slow convergence. This observation agrees with the conclusions of Crisfield and Wills (1988) about oscillation between localized and non localized states. This local bifurcation must be clearly separated from the structural bifurcation and a full bifurcation test concerning local and structural bifurcation may be performed in order to properly unfold them (Fig 2.5).

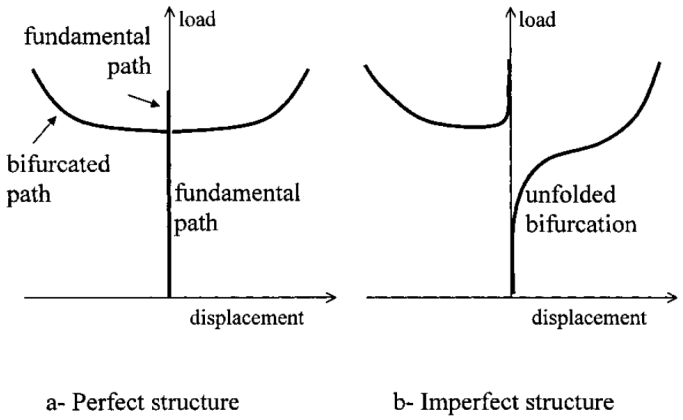

Figure 2.5: Bifurcation unfolding. (Gastebled and May, 2000)

Paulino and Liu (2001) work concerns the tangent operator for Newton method used with Boundary Element Problems (BEP) (Fig. 2.6), suggesting that Continuum Tangent Operator (CON) gives better results than Consistent one. This results show that the use of other operators different from the Consistent Tangent one can improve the convergence rate and stability in numerical models.

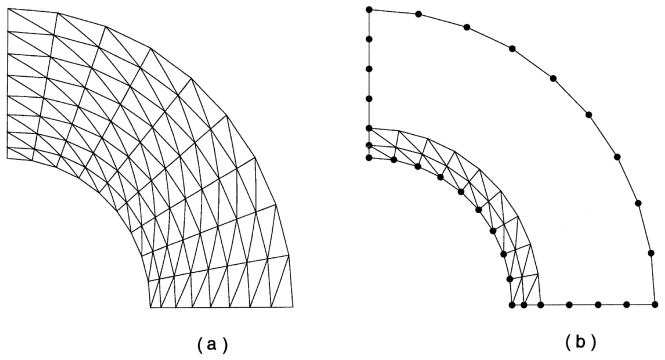

Figure 2.6: Comparison of modeling strategies: (a) FEM mesh 144 linear elements and 90 nodes; (b) BEM mesh boundary discretization consists of 30 elements (2-noded) and 34 nodes on the boundary, and interior discretization consists of 36 linear elements and 30 nodes. (Paulino and Liu, 2001)

Flatscher and Pettermann (2011) use a Consistent Tangent Operator applied to composite materials, this time taking into account in the calculation of the operator the plasticity parameters coming from the constitutive law in order to improve the iterative process.

Despite the opinion of other authors Hautefeuille et al. (2012) successfully use arc-length method in a multiscale model with softening behaviour, however, they use the arc-length method only in the microscale during the first steps meaning that arc-length methods can be useful in softening material problems even if encountering some problems related to the high localization levels.

2.2 Perturbation based operators

In this section two operators obtained by perturbation will be tested, notably the CTO which was introduced in (Eq. 2.7), and a time average which results in an elastic operator:

1. Consistent Tangent Operator (CTO)
2. Auxiliary elastic operator (AEO)

2.2.1 Consistent Tangent Operator (CTO)

The Consistent Tangent Operator is obtained using a perturbation method (Eq. 2.7) integrated over the time step. It consists of applying a small perturbation[1] in all the degrees of freedom of the problem and computing the homogenized stresses for each one of these degrees of freedom, so all the 16 coefficients are obtained. The second and third rows of the operator are identical by definition of the constitutive law (stresses)[2], and the second and third columns are different as they come from different perturbation calculations (strains). As it needs to be recomputed 4 times in each time step for the additional perturbations, this method is 5 times more time consuming than it would be a single computation method.

The CTO is claimed to provide quadratic convergence. In general, the convergence obtained using it in a FEMxDEM model is not quadratic unless the state is nearly elastic. A compression biaxial test simulation is used to exemplify the properties of the operator, the data presented corresponds to the initial stages of test. In (Fig. 2.7) only the simulation with $\epsilon_2 = 1 \cdot 10^{-4}$ presents quadratic convergence at the beginning of the test. The simulation with $\epsilon_2 = 1 \cdot 10^{-5}$ converges with linear velocity, $\epsilon_2 = 1 \cdot 10^{-3}$diverges with respect to the precision threshold at the first step and $\epsilon_2 = 1 \cdot 10^{-6}$ goes to an asymptotic value of UNORM/DNORM because the perturbation is too large compared to the strain increment. The reason why quadratic convergence is lost is the non-continuity of the derivative of the constitutive law. Quadratic convergence can be observed if a very

[1] Small enough to be considered infinitesimal compared to the magnitude of the loading step.

[2] Small strain approximation is taken into account, so $\epsilon = \frac{1}{2}(\nabla \vec{u}^t + \nabla \vec{u})$, this definition makes the strain tensor symmetric $\epsilon = \epsilon^t$

small step is performed, small enough so no grain sliding happens in any REV of the model. In (Fig. 2.8) the profiles of convergence show quadratic velocity except for the second iteration with some oscillations. Usually this quadratic velocity will be lost in a FEMxDEM model for higher deformations. In this particular case, the constitutive law is smooth enough to provide a continuous derivative. Performing such small step makes no sense since the aim of using DEM is to add complexity rather than just elasticity to the constitutive law. Considering time steps big enough to change the grain contact network the Newton method will present linear convergence at its best. This linear convergence is lost as the loading path approaches the softening region. After the stress peak in a biaxial test this convergence rate will remain sublinear.

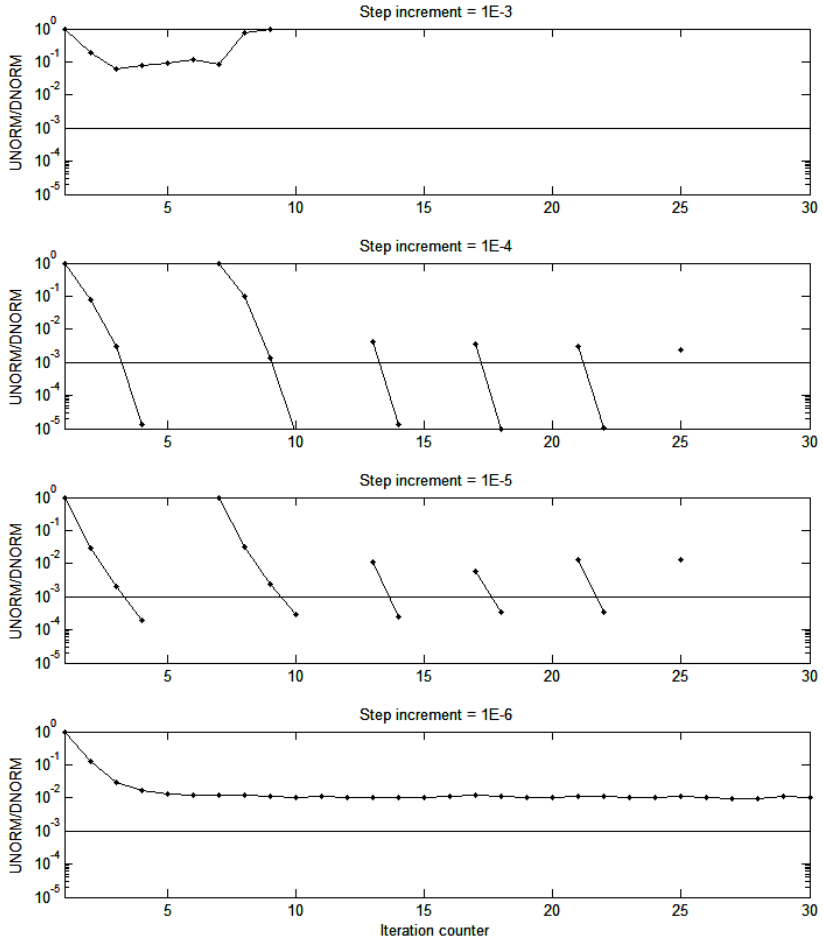

Figure 2.7: Lack of compatibility for the norm of the displacement (UNORM/DNORM) of a biaxial compression test for four different initial step size: $\epsilon_2 = 1 \cdot 10^{-3}$, $\epsilon_2 = 1 \cdot 10^{-4}$, $\epsilon_2 = 1 \cdot 10^{-5}$, $\epsilon_2 = 1 \cdot 10^{-6}$. Consistent tangent operator. The horizontal line indicates the precision threshold PRECU=0.001.

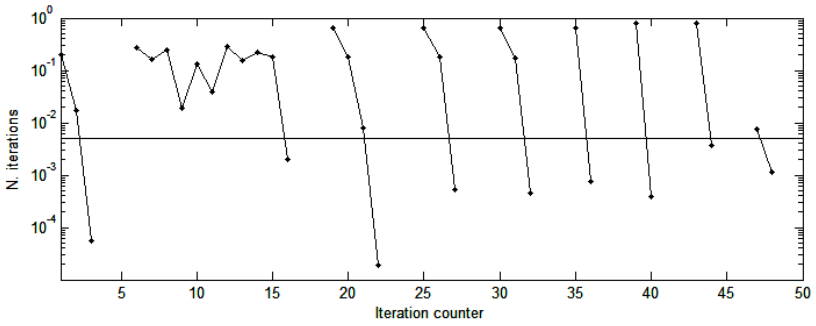

Figure 2.8: Lack of compatibility for the norm of the displacement (UNORM/DNORM) for the 10 first time steps. Consistent tangent operator. The horizontal line indicates the precision threshold PRECU=0.005. This first ten steps correspond to the initial part of a biaxial test for an axial deformation less than 0.2% being far from the plastification zone.

With a softening constitutive law, as it is the case of the homogenized DEM, the positive definition of the operator is lost; this causes the problem to be ill posed and this degradates the Newton method efficiency.

From a theoretical perspective, a negative stiffness coefficient is not possible because of thermodynamic considerations Pasternak et al. (2014). Therefore, materials whose global behaviour exhibits negative stiffness are unstable. However, if only some part of the global structure presents negative stiffness and the surrounding is stiff enough it can absorb the instabilities and the structure can be stable Pasternak et al. (2014). This can be applied to the present case, a multiscale model where the integration of the material points can result in negative stiffness coefficients but the surrounding materials points with positive stiffness are still able to absorb the instability.

However, in a big system using a CTO in the multiscale implementation, no convergence is reached after bifurcation (Nguyen et al., 2014). It is known from FEM applications using phenomenological laws, that the solution can be found after bifurcation. However, the time cost of the FEMxDEM model forces us to stop the simulation before a solution is found, i.e. better numerical approaches are needed. In the following the CTO is shown for a given Gauss point of a 128 element simulation before the stress peak (Eq. 2.11) presenting positiveness and another Gauss point in the same time step (Eq. 2.12) not being positive definite and consequently making the PDE problem ill posed.

The Newton operator is presented with the following notation: (eq. 2.10):

$$(C_{ijmn}) = \begin{pmatrix} 900.3 & -16.4 & -22.1 & 73.8 \\ -14.9 & 384.4 & 418.8 & -6.0 \\ -14.9 & 384.4 & 418.8 & -6.0 \\ 79.3 & -12.8 & -9.9 & 906.1 \end{pmatrix} \tag{2.11}$$

$$(C_{ijmn}) = \begin{pmatrix} -2077.4 & -2789.1 & 493.8 & -991.8 \\ 3799.7 & -165.0 & 391.5 & -9341.1 \\ 3799.7 & -165.0 & 391.5 & -9341.1 \\ -2678.0 & 3008.6 & -4965.9 & -7326.5 \end{pmatrix} \tag{2.12}$$

2.2.2 Auxiliary elastic operator (AEO)

This operator was developed in the work of Nguyen (2013) and it was used as an alternative to the CTO.

The evolution of the stress in a single Gauss point (Fig. 2.1) suggests that the irregularities are restricted only to some iterations, being the operator positive-defined in the others. This can be put down to the DEM behaviour which presents instabilities only when a chain of grains slide occurs, which happens in a systematic way during a monotonic loading path (Fig. 2.1). In order to provide a smoother evolution of the operator, a time average over several well converged steps in the elastic part is performed. This provides a positive defined operator (Eq. 2.13) which can be adopted for the given Gauss point during the rest of the simulation.

However, as the operator remains unchanged, it doesn't take into account the history of the material, so it is not tangent to the law once we leave the pre-peak regime. Consequently, the resulting quasi Newton method will never present quadratic convergence. Nevertheless, no perturbations are needed after obtaining the average so it is 5 times less time-demanding per Newton iteration than the CTO. The AEO allows for stable simulations beyond the stress peak (Fig. 2.9).

$$\left(C^{AEO}_{ijmn}\right) = \begin{pmatrix} 880.3 & -19.0 & -18.27 & 86.9 \\ -13.3 & 379.8 & 415.11 & -15.5 \\ -13.3 & 379.8 & 415.11 & -15.5 \\ 99.3 & -15.1 & -17.05 & 886.9 \end{pmatrix} \tag{2.13}$$

2.3 Elastic operators

In this section the periodic granular media is described and different approaches to extract operators developed. These operators are of elastic nature since no damage or grain sliding is considered in the developments. Compared to the perturbation based operators the elastic operators of this section are not based on perturbations, therefore the relation (Eq. 2.6) doesn't need to be reevaluated, instead, the operator comes from the microscale. Two resulting operators are tested:

1. DEM based Quasi-static Operator (DEMQO)

2. PreStressed Truss-Like Operator (PSTLO)

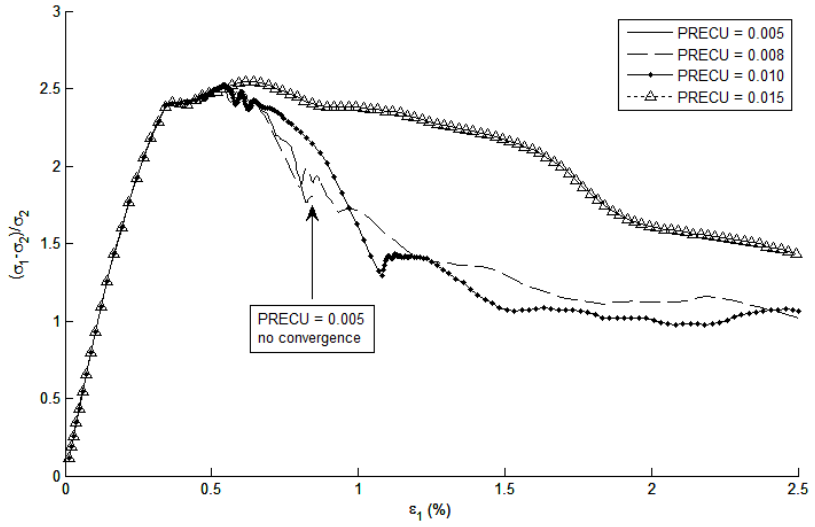

Figure 2.9: Strain stress curves for a multiscale simulation using the auxiliary elastic operator.

2.3.1 DEM based Quasi-static Operator (DEMQO)

A possible auxiliary tangent operator is that of the granular assembly considered as elastic in the present configuration. That consists in assuming that the contacts remain unchanged and that the forces between grains are elastic. The determination of that auxiliary operator can be done numerically by four DEM computations for which the friction coefficient between grains is set to a large value so as to prevent any sliding corresponding to four small increments of the deformation gradient F. The difference with the computation of the consistent tangent operator is that the starting point of those fours computations is the configuration of the grain assembly at the end of the considered time step whereas in the computations of the consistent tangent operator the final deformation gradient F^f of (Eq. 2.6) is modified by four small perturbations leading to perturbations of the integration path and the DEM computations are performed from the beginning of the time step (Eq. 2.7). That numerical computation yields the auxiliary tangent operator DEMQO.

This supposes a major decrease of the time devoted to the DEM computation and the obtaining of a positive definite operator. The technique can still produce a negative definite matrix because buckling is possible within the granular assembly, but this is very unlikely to happen due to the very dense packing.

Strong conditions need to be applied to the DEM computations in order to guarantee a quasi-static state before the numerical homogenization. These conditions include a threshold for the kinetic energy, maximum number of sliding contacts and maximum number of single contact grains. Such conditions force an extended relaxation period after the loading of the DEM assembly. The duration of this relaxation period is strongly

dependent on the velocity of the applied deformation rather than the magnitude of this deformation, this has been observed in the testing of the DEMQO, showing relaxation times of the same order of magnitude both for the main DEM loading path and for the infinitesimal perturbations. In order to accelerate the code, quasi-static conditions have been made less strict for the perturbations resulting in a drastic reduction of the computational time devoted to the perturbations. This does not affect the physics of the model [3] since the main loading path is still subject to strict quasi-static conditions.

The convergence velocity is the best among the tested operators both in the pre and post-peak regimes (Fig. 2.12 and 2.13).

$$\left(C_{ijmn}^{DEMQO}\right) = \begin{pmatrix} 902.3 & 13.4 & -14.2 & 86.2 \\ -13.4 & 384.6 & 421.9 & -12.4 \\ -13.4 & 384.6 & 421.9 & -12.4 \\ 86.2 & -12.4 & -12.4 & 890.3 \end{pmatrix} \tag{2.14}$$

2.3.2 PreStressed Truss-like Operator (PSTLO)

In the DEM computing of the DEMQO operator, the friction coefficient is high and the contacts are persistent without cretation of any new ones, that means that the interactions between brains are elastic. The determination of this operator is the same as that of an elastic assmbly of grains and it can be performed using the homogenization method of a discrete system as a continuous medium.

For that purpose it is necessary to pricesely describe the granular assembly that constitutes the sample.

2.3.3 Description of the periodic granular assembly

Numberings and geometry

The grains are 2D disks, the whole study is limited to 2 dimensions. The grains move in a 2D plane orthogonal to the normed vector $\vec{i}_3$ that orients the plane.

Conditions of periodicity are used which means that the sample of grains is considered as the base cell of a periodic medium, the vectors of periodicity depend on the time and are denoted by $\vec{Y}^1$ and $\vec{Y}^2$. A grain of the base cell can then interact with another grain of that cell of of a neighbouring cell.

The grains of the base cell are numbered $n, m, \ldots$. Let R^n denotes the radius of the grain n. The position of the center of the grain n is given with respect to an origin O by the vector $\vec{x}^n$ ($\vec{x}^n$ depends on the the time).

A contact $c = (n, m, \delta_1, \delta_2)$ is an ordered couple of grains n and m and, as conditions of periodicity are used, two numbers δ_1 and δ_2, taking values in $\{-1, 0; 1\}$ that tell whether the contact is between grains of the base cell or between grains of two neighbouring cells. The set of all contacts is denoted by $\mathcal{C}$.

[3] The perturbation calculations are not considered as part of the physics of the model because they merely provide the operator used in the Newton strategy but they do not take part on the constitutive relation itself.

The couple of grains of the contact c being ordered, one, say n, is called the origin $O(c)$ of the contact and the other m is the end $E(c)$; the two δ's are denoted by δ_1^c and δ_2^c (Fig. 2.10).

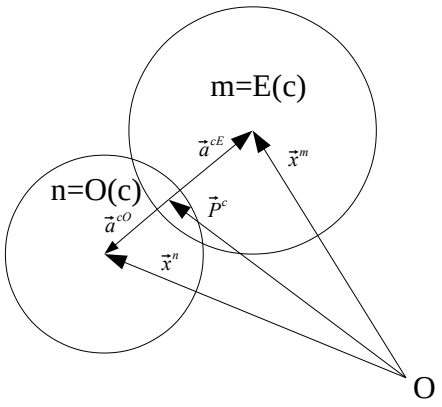

Figure 2.10: 2 circular grains in contact.

The branch vector of the contact c is the vector $\vec{b}^c$ linking the centers of the two grains in contact:

$$\vec{b}^c = \vec{x}^{E(c)} + \delta_1 \vec{Y}^1 + \delta_2 \vec{Y}^2 - \vec{x}^{O(c)} \tag{2.15}$$

In the following, according to the Einstein's summation convention, the sum $\delta_1 \vec{Y}^1 + \delta_2 \vec{Y}^2$ is simplified into $\delta_i \vec{Y}^i$. Let $\vec{e}^c$ and l^c be the unit vector and the length of the branch vector $\vec{b}^c$:

$$\vec{b}^c = l^c \vec{e}^c \,,\; 0 < l^c, \|\vec{e}^c = 1\|$$

$\vec{e}^c$ is the normal vector to the contact, let $\vec{t}^c$ denotes the tangent vector image of $\vec{e}^c$ by the counterclockwise rotation of angle $\pi/2$.

In the considered modelling of the contacts, grains can overlap, let

$$h^c = R^{O(c)} + R^{E(c)} - l^c \tag{2.16}$$

be the overlap of the contact c. As grains in contact can overlap, it is necessary, in order to be able to write balance equations for moments, to define a contact point, the position of which is given by the vector $\vec{p}^c$. Let $\vec{a}^{cO}$ and $\vec{a}^{cE}$ be the vectors:

$$\vec{a}^{cO} = \vec{x}^{O(c)} - \vec{p}^c$$
$$\vec{a}^{cE} = \vec{x}^{E(c)} - \vec{p}^c$$

The contact point is chosen on the segment linking the centers of the two grains. That entails that the lever arms $\vec{a}^{cO}$ and $\vec{a}^{cE}$ are parallel to $\vec{e}^{c}$:

$$\vec{a}^{cO} = l^{cO}\vec{e}^{c} \tag{2.17a}$$

$$\vec{a}^{cE} = -l^{cE}\vec{e}^{c} \tag{2.17b}$$

ith obviously:

$$l^{cO} + l^{cE} = l^{c} \tag{2.18}$$

When two grains in contact overlap ($h^c > 0$), it seems sensible to impose that the contact point should be in the overlap region that reads:

$$l^{cO} = R^{O(c)} - \alpha h^{c} \tag{2.19}$$

where α is a parameter such that $0 \leq \alpha \leq 1$, for instance $\alpha = 1/2$. From(2.18) and (2.16), it comes:

$$l^{cE} = R^{E(c)} + R^{O(c)} - h^{c} - \left(R^{O(c)} - \alpha h^{c}\right)$$

that is to say:

$$l^{cE} = R^{E(c)} - (1-\alpha)\, h^{c} \tag{2.20}$$

Contact forces and equilibrium

Grains in contact interact by sheer forces which means that the rolling torque in disregarded. For a contact c, let $\vec{f}^{c}$ be the force appled by the grain $E(c)$ on $O(c)$, as the rolling couple is disregarded the moment at the center $\vec{x}^{n}$ of the force $\vec{f}^{c}$ is $\vec{a}^{cO} \wedge \vec{f}^{c}$.

The equilibrium of the whole granular assembly reads in a virtual power formulation:

$$\forall \vec{u}^{n*}, \forall \vec{\theta}^{n*}\,, \; -\sum_{c\in\mathcal{C}} \left[\vec{f}^{c}.\left(\vec{u}^{E(c)*} - \vec{u}^{O(c)*}\right) + \left(\vec{a}^{cE} \wedge \vec{f}^{c}\right).\vec{\theta}^{E(c)*} - \left(\vec{a}^{cO} \wedge \vec{f}^{c}\right).\vec{\theta}^{O(c)*}\right] = 0 \tag{2.21}$$

In that formulation, the virtual rotation vectors are $\vec{\theta}^{n*} = \theta^{n*}\vec{i}_3$, in which $\vec{i}_3$ is the normed vector orthogonal to the plane where the 2D grains move.

2.3.4 Determination of PSTLO

The configuration of the base cell being a determined by the two periodicity vectors $\vec{Y}^1$ and $\vec{Y}^2$, the positions of the grains and the contact forces $\vec{f}^{c}$, an increment $\mathrm{d}F$ is added to the macroscopic deformation gradient F, the PSTLO is the operator that yields the increment $\mathrm{d}\sigma$ of the Cauchy stress σin terms of $\mathrm{d}F$. The increment $\mathrm{d}F$ yields increments $\mathrm{d}\vec{Y}^1$ and $\mathrm{d}\vec{Y}^2$ of the vectors $\vec{Y}^1$ and $\vec{Y}^2$ given by:

$$\mathrm{d}\vec{Y}^{i} = \left(\mathrm{d}F \circ F^{-1}\right) @\vec{Y}^{i}\,, \; i = 1, 2 \tag{2.22}$$

where $\mathrm{d}F \circ F^{-1}$ denotes the composition product of $\mathrm{d}F$ and F^{-1} and $(\mathrm{d}F \circ F^{-1}) @\vec{Y}^i$ denotes the image of $\vec{Y}^i$ by the linear application $\mathrm{d}F \circ F^{-1}$. $\vec{Y}^1_R = F^{-1} @\vec{Y}^1$ and $\vec{Y}^2_R = F^{-1} @\vec{Y}^2$ are the periodicity vectors of the initial configuration of the base cell. According to (2.15) the changes of $\vec{Y}^1$ and $\vec{Y}^2$ at least induce changes in the distances between grains and consequently changes $\mathrm{d}\vec{f}^c$ in the contact forces. Consequently the balance of the grains is broken and they have to move and rotate in order that the equilibrium should be recovered.

As the increment $\mathrm{d}F$ is assumed small, the resulting displacements $\vec{u}^n = \mathrm{d}\vec{x}^n$ and rotations $\mathrm{d}\theta^n$ of the grains are small and it is possible to develop the geometric quantities, the forces and the equations of equilibrium up to the first order to define the linear problem to be solved in order to determine $\vec{u}^n$, $\mathrm{d}\theta^n$ in term of $\mathrm{d}F$. Which will yield $\mathrm{d}\vec{f}^c$ in term of $\mathrm{d}F$ and consequently the increment $\mathrm{d}\sigma$ of the Cauchy stress σ in term of $\mathrm{d}F$, so defining the looked for operator.

Incremental balance equation

The differentiation of the virtual power formulation (2.21) of the balance equation reads:

$$\begin{aligned}\forall \vec{u}^{n*}, \forall \vec{\theta}^{n*}, \; & -\sum_{c\in\mathcal{C}} \mathrm{d}\vec{f}^c . \left(\vec{u}^{E(c)*} + \vec{\theta}^{E(c)*} \wedge \vec{a}^{cE} - \vec{u}^{O(c)*} - \vec{\theta}^{O(c)*} \wedge \vec{a}^{cO} \right) \\ & + \sum_{c\in\mathcal{C}} \left(\left(\mathrm{d}\vec{a}^{cO} \wedge \vec{f}^c \right) . \vec{\theta}^{O(c)*} - \left(\mathrm{d}\vec{a}^{cE} \wedge \vec{f}^c \right) . \vec{\theta}^{E(c)*} \right) = 0 \end{aligned} \tag{2.23}$$

where $\mathrm{d}\vec{a}^{cO}$ and $\mathrm{d}\vec{a}^{cE}$ are the small increments of the lever arms $\vec{a}^{cO}$ and $\vec{a}^{cE}$.

Differentiation of the geometry

In the motion of the grains resulting from the change of F into $F + \mathrm{d}F$, the positions of the grains change yielding changes in $\vec{b}^c$, $\vec{e}^c$, $\vec{t}^c$ and of h^c and it is necessary to determine those changes $\mathrm{d}\vec{b}^c$, $\mathrm{d}\vec{e}^c$, $\mathrm{d}\vec{t}^c$ and $\mathrm{d}h^c$, assumed to be small interms of the dsiplacements $\vec{u}^n$ and rotations $\mathrm{d}\theta^n$ of the grains.

Differentiation of $\vec{b}^c$, $\vec{e}^c$, $\vec{t}^c$ and of h^c The differentiation of (2.15) with respect to $\vec{u}^n$ and $\mathrm{d}\theta^n$ yields:

$$\mathrm{d}\vec{b}^c = \vec{u}^{E(c)} + \delta^i_c \mathrm{d}\vec{Y}^i - \vec{u}^{O(c)} \tag{2.24}$$

The differentiation of $\vec{b}^c = l^c \vec{e}^c$ yields:

$$\mathrm{d}\vec{b}^c = \mathrm{d}l^c \vec{e}^c + l^c \mathrm{d}\vec{e}^c$$

Taking into account that $\vec{e}^c$ is a norm vector and consequently that $\vec{e}^c . \mathrm{d}\vec{e}^c = 0$ and that the problem is two dimensionnal, it comes after some algebra:

$$\mathrm{d}\vec{e}^c = \frac{1}{l^c} \left(\vec{t}^c \otimes \vec{t}^c \right) @ \mathrm{d}\vec{b}^c \tag{2.25a}$$

$$\mathrm{d}\vec{t}^c = -\frac{1}{l^c} \left(\vec{e}^c \otimes \vec{t}^c \right) @ \mathrm{d}\vec{b}^c \tag{2.25b}$$

The differentiation of (2.16) yields:

$$\mathrm{d}h^c = -\mathrm{d}l^c = -\vec{e}^c.\mathrm{d}\vec{b}^c \tag{2.26}$$

Differentiation of the lever arms $\vec{a}^{cO}$ and $\vec{a}^{cE}$ The differentiation of (2.17) reads:

$$\begin{aligned}\mathrm{d}\vec{a}^{cO} &= \mathrm{d}l^{cO}\vec{e}^c + l^{cO}\mathrm{d}\vec{e}^c\\ \mathrm{d}\vec{a}^{cE} &= -\mathrm{d}l^{cE}\vec{e}^c - l^{cE}\mathrm{d}\vec{e}^c\end{aligned}$$

Differentiating (2.19) et (2.20), it comes:

$$\begin{aligned}\mathrm{d}l^{cO} &= -\alpha\mathrm{d}h^c\\ \mathrm{d}l^{cE} &= -\left(1-\alpha\right)\mathrm{d}h^c\end{aligned}$$

hence, taking into account (2.26):

$$\mathrm{d}\vec{a}^{cO} = \left(\alpha\vec{e}^c\otimes\vec{e}^c + \frac{l^{cO}}{l^c}\left(\vec{t}^c\otimes\vec{t}^c\right)\right)\circledcirc\mathrm{d}\vec{b}^c \tag{2.27a}$$

$$\mathrm{d}\vec{a}^{cE} = -\left(\left(1-\alpha\right)\vec{e}^c\otimes\vec{e}^c + \frac{l^{cE}}{l^c}\left(\vec{t}^c\otimes\vec{t}^c\right)\right)\circledcirc\mathrm{d}\vec{b}^c \tag{2.27b}$$

Relative sliding of grains at contact points In the motion of the grains $O\left(c\right)$ et $E\left(c\right)$ of the contact c, the displacements of the contact point $\vec{p}^c$ relatively to each of the two grains $O\left(c\right)$ and $E\left(c\right)$ respectively read:

$$\begin{gathered}\vec{u}^{O(c)} + \mathrm{d}\theta^{O(c)}\vec{i}_3\wedge\vec{a}^{cO}\\ \text{and } \vec{u}^{E(c)} + \delta^i_c\mathrm{d}\vec{Y}^i + \mathrm{d}\theta^{E(c)}\vec{i}_3\wedge\vec{a}^{cE}\end{gathered}$$

The relative sliding of grains at their ontact points $\vec{D}^c$ is the difference of these two displacements:

$$\vec{D}^c = \vec{u}^{E(c)} + \mathrm{d}\theta^{E(c)}\vec{i}_3\wedge\vec{a}^{cE} - \vec{u}^{O(c)} - \mathrm{d}\theta^{O(c)}\vec{i}_3\wedge\vec{a}^{cO} + \delta^i_c\mathrm{d}\vec{Y}^i$$

that is to say from (2.17):

$$\vec{D}^c = \vec{u}^{E(c)} - \vec{u}^{O(c)} - \left(l^{cE}\mathrm{d}\theta^{E(c)} + l^{cO}\mathrm{d}\theta^{O(c)}\right)\vec{t}^c + \delta^i_c\mathrm{d}\vec{Y}^i$$

or also, according to (2.24):

$$\vec{D}^c = \mathrm{d}\vec{b}^c - \left(l^{cO}\mathrm{d}\theta^{O(c)} + l^{cE}\mathrm{d}\theta^{E(c)}\right)\vec{t}^c \tag{2.28}$$

the projection D^c_t of which on the tangent vector $\vec{t}^c$ reads:

$$D^c_t = \mathrm{d}\vec{b}^c.\vec{t}^c - \left(l^{cO}\mathrm{d}\theta^{O(c)} + l^{cE}\mathrm{d}\theta^{E(c)}\right) \tag{2.29}$$

Incremental forces and moments

The contact force $\vec{f}^c$ can be decomposed into:

$$\vec{f}^c = f_n^c \vec{e}^{\boldsymbol{c}} + f_t^c \vec{t}^{\boldsymbol{c}} \tag{2.30}$$

the differentiation of which reads:

$$\mathrm{d}\vec{f}^c = \mathrm{d}f_n^c \vec{e}^{\boldsymbol{c}} + f_n^c \mathrm{d}\vec{e}^{\boldsymbol{c}} + \mathrm{d}f_t^c \vec{t}^{\boldsymbol{c}} + f_t^c \mathrm{d}\vec{t}^{\boldsymbol{c}} \tag{2.31}$$

The constitutive equation of the normal component f_n^c being $f_n^c = -k_n \left(h^c - C\right)$, it comes:

$$\mathrm{d}f_n^c = -k_n \mathrm{d}h^c$$

that is to say, according to (2.26):

$$\mathrm{d}f_n^c = k_n \vec{e}^{\boldsymbol{c}}.\mathrm{d}\vec{b}^c \tag{2.32}$$

The constitutive equation of the tangent component $\mathrm{d}f_t^c$ reads:

$$\mathrm{d}f_t^c = k_t D_t^c$$

that is to say according to (2.29):

$$\mathrm{d}f_t^c = k_t \left(\mathrm{d}\vec{b}^c.\vec{t}^{\boldsymbol{c}} - \left(l^{cO}\mathrm{d}\theta^{O(c)} + l^{cE}\mathrm{d}\theta^{E(c)}\right)\right) \tag{2.33}$$

From (2.25a) et (2.25b), on a:

$$f_n^c \mathrm{d}\vec{e}^{\boldsymbol{c}} + f_t^c \mathrm{d}\vec{t}^{\boldsymbol{c}} = \frac{1}{l^c}\left(f_n^c \vec{t}^{\boldsymbol{c}} \otimes \vec{t}^{\boldsymbol{c}} - f_t^c \vec{e}^{\boldsymbol{c}} \otimes \vec{t}^{\boldsymbol{c}}\right) @ \mathrm{d}\vec{b}^c$$

Taking into account the equations (2.31), (2.32), (2.33) and (2.29), the force increment $\mathrm{d}\vec{f}^c$ reads:

$$\mathrm{d}\vec{f}^c = \left(k_n \vec{e}^{\boldsymbol{c}} \otimes \vec{e}^{\boldsymbol{c}} + k_t \vec{t}^{\boldsymbol{c}} \otimes \vec{t}^{\boldsymbol{c}} + \frac{1}{l^c}\left(f_n^c \vec{t}^{\boldsymbol{c}} - f_t^c \vec{e}^{\boldsymbol{c}}\right) \otimes \vec{t}^{\boldsymbol{c}}\right) @ \mathrm{d}\vec{b}^c - k_t \left(l^{cO}\mathrm{d}\theta^{O(c)} + l^{cE}\mathrm{d}\theta^{E(c)}\right) \vec{t}^{\boldsymbol{c}} \tag{2.34}$$

Taking into account the decomposition (2.30) of $\vec{f}^c$ and of $\vec{\theta}^{n*} = \theta^{n*}\vec{i}_3$ the term $\left(\mathrm{d}\vec{a}^{cO} \wedge \vec{f}^c\right).\vec{\theta}^{O(c)*}$ of (2.23) reads:

$$\left(\mathrm{d}\vec{a}^{cO} \wedge \vec{f}^c\right).\vec{\theta}^{O(c)*} = \theta^{O(c)*}\left(-f_n^c \vec{t}^{\boldsymbol{c}} + f_t^c \vec{e}^{\boldsymbol{c}}\right).\mathrm{d}\vec{a}^{cO}$$

that is to say according to (2.27) and to the symetry of the linear applications $\vec{e}^{\boldsymbol{c}} \otimes \vec{e}^{\boldsymbol{c}}$ and $\vec{t}^{\boldsymbol{c}} \otimes \vec{t}^{\boldsymbol{c}}$:

$$\left(\mathrm{d}\vec{a}^{cO} \wedge \vec{f}^c\right).\vec{\theta}^{O(c)*} = \theta^{O(c)*}\left(\alpha f_t^c \vec{e}^{\boldsymbol{c}} - \frac{l^{cO}}{l^c} f_n^c \vec{t}^{\boldsymbol{c}}\right).\mathrm{d}\vec{b}^c$$

in the same way:

$$\left(\mathrm{d}\vec{a}^{cE} \wedge \vec{f}^{c}\right).\vec{\theta}^{E(c)*} = -\theta^{E(c)*}\left((1-\alpha)\, f_t^c \vec{e}^{c} - \frac{l^{cE}}{l^c} f_n^c \vec{t}^{c}\right).\mathrm{d}\vec{b}^{c}$$

so consequently:

$$\begin{aligned}\left(\mathrm{d}\vec{a}^{cO} \wedge \vec{f}^{c}\right).\vec{\theta}^{O(c)*} - \left(\mathrm{d}\vec{a}^{cE} \wedge \vec{f}^{c}\right).\vec{\theta}^{E(c)*} =& \theta^{O(c)*}\left(\alpha f_t^c \vec{e}^{c} - \frac{l^{cO}}{l^c} f_n^c \vec{t}^{c}\right).\mathrm{d}\vec{b}^{c} \\ &+ \theta^{E(c)*}\left((1-\alpha)\, f_t^c \vec{e}^{c} - \frac{l^{cE}}{l^c} f_n^c \vec{t}^{c}\right).\mathrm{d}\vec{b}^{c}\end{aligned} \tag{2.35}$$

Determination of $\mathrm{d}\sigma$ in term of $\mathrm{d}F$

The vectors $\vec{Y}^i$ defining the cell, the positions $\vec{x}^n$ of the grains, the set $\mathcal{C}$ of all the contacts, the contact forces $\vec{f}^c$, the macroscopic deformation gradient F being known and the increment $\mathrm{d}F$ of F being given, the displacements $\vec{u}^n$ and the rotations $\mathrm{d}\theta^n$ of the grains and the incements $\mathrm{d}\vec{f}^c$ of the contact focres are solutions of the problem:

$$\begin{aligned}\forall \vec{u}^{n*}, \forall \vec{\theta}^{n*},\ & -\sum_{c\in\mathcal{C}} \mathrm{d}\vec{f}^{c}.\left(\vec{u}^{E(c)*} - \vec{u}^{O(c)*} - \left(l^{cO}\theta^{O(c)*} + l^{cE}\theta^{E(c)*}\right)\vec{t}^{c}\right) \\ &+ \sum_{c\in\mathcal{C}}\left(\theta^{O(c)*}\left(\alpha f_t^c \vec{e}^{c} - \frac{l^{cO}}{l^c} f_n^c \vec{t}^{c}\right).\mathrm{d}\vec{b}^{c} + \theta^{E(c)*}\left((1-\alpha)\, f_t^c \vec{e}^{c} - \frac{l^{cE}}{l^c} f_n^c \vec{t}^{c}\right).\mathrm{d}\vec{b}^{c}\right) \\ &= 0\end{aligned} \tag{2.36a}$$

$$\begin{aligned}\text{with } \mathrm{d}\vec{f}^{c} =& \left(k_n \vec{e}^{c}\otimes\vec{e}^{c} + k_t \vec{t}^{c}\otimes\vec{t}^{c} + \frac{1}{l^c}\left(f_n^c \vec{t}^{c} - f_t^c \vec{e}^{c}\right)\otimes\vec{t}^{c}\right) @\mathrm{d}\vec{b}^{c} \\ &- k_t\left(l^{cO}\mathrm{d}\theta^{O(c)} + l^{cE}\mathrm{d}\theta^{E(c)}\right)\vec{t}^{c}\end{aligned} \tag{2.36b}$$

$$\text{and } \mathrm{d}\vec{b}^{c} = \vec{u}^{E(c)} - \vec{u}^{O(c)} + \delta_c^i \mathrm{d}\vec{Y}^i \tag{2.36c}$$

The displacements $\vec{u}^n$ of the grains play a part (in $\mathrm{d}\vec{b}^c$) only through the difference $\vec{u}^{E(c)} - \vec{u}^{O(c)}$ which shows that at best the $\vec{u}^n$ can only be defined up to a constant vector.

The displacements $\vec{u}^n$, the rotations $\mathrm{d}\theta^n$ and the increments $\mathrm{d}\vec{f}^c$ of contact forces resulting from the change to $F + \mathrm{d}F$ being determined, it remains to link the increment $\mathrm{d}F$ to the increment $\mathrm{d}\sigma$ of the Cauchy stress σ which, according to the Cauchy-Poisson formula, reads:

$$\sigma = \frac{1}{|Y|}\sum_{c\in\mathcal{C}} \vec{f}^{c}\otimes\delta_c^i\vec{Y}^i$$

where $|Y|$ denotes the surface of the base cell, $|Y| = \left\|\vec{Y}^1 \wedge \vec{Y}^2\right\|$.

After a light amount of algebra, the differentiation of σ reads:

$$\mathrm{d}\sigma = \frac{1}{|Y|}\sum_{c\in\mathcal{C}} \delta_c^i \mathrm{d}\vec{f}^c \otimes \vec{Y}^i + \sigma \circ F^{-T} \circ \mathrm{d}F^T - \left(F^{-T} : \mathrm{d}F\right)\sigma \tag{2.37}$$

where F, σ, the $\vec{Y}^i$'s are known. The increments $\mathrm{d}\vec{f}^c$ are determined by solving the problem (2.36) which is linear, consequently the increments $\mathrm{d}\vec{f}^c$ depend linearly on $\mathrm{d}F$ and does $\mathrm{d}\sigma$.

In that expression $\mathrm{d}F^T$ denotes the transposed of $\mathrm{d}F$ and F^{-T} that of F^{-1} - F^{-T} is also the inverse of F^T.

This approach provides the same results as the DEMQO, the drawback is that the needed resolution of the linear system of equations can be even more time consuming than the integration of the function itself $\mathcal{S}$ of (2.6) depending on the complexity of the microscale.

2.4 Kruyt operators

The other way of obtaining the Newton operator comes within a rougher method of homogenization that consists in considering that the displacements $\vec{u}^n$ and the rotations $\mathrm{d}\theta^n$ of the grains are those of the underlying continuous macroscopic medium. That yields the auxiliary tangent operator denoted Kruyt Auxiliary Operator (KAO).

The section also presents the original Kruyt operator already used in previous works (Guo and Zhao, 2014) and corrections of this operator by the use of calibrated coefficients. The tested operators are:

1. Kruyt Augmented Operator (KAO)
2. Upper bound Kruyt operator (UKO)
3. Upper bound Corrected Kruyt Operator (UCKO)
4. Upper bound Corrected Kruyt Operator 2DOF (UCKO 2DOF)

2.4.1 Small displacements in a prestressed configuration

"Kruyt" type (Kruyt and Rothenburg, 1998) operators are obtained considering that the grain displacements and rotations "follow" the small homogeneous transformation of the macroscopic continuum medium. In particular this means that in general the equilibrium equations are not satisfied so they don't have to be considered.

The homogeneous displacement field of the macroscopic continuum medium is given by:

$$\vec{u}\,(\vec{x}) = \vec{a} + E@\vec{x}$$

Where $\vec{x}$ is the spacial variable of the initial configuration in the base cell. Consequently, we have $E = \nabla_x \vec{u}$, which is in terms of increment $\mathrm{d}F$ of the transformation gradient F:

$$E = \mathrm{d}F \circ F^{-1}$$

To impose that the grains of the periodic medium "follow" the homogeneous transformation of the macroscopic continuum medium means that the displacements of the grain n of the base cell is of the form $\vec{u}^n = \vec{a} + E@\vec{x}^n$ and that the grain n of the adjacent cell defined by (ν^1, ν^2) is $\vec{u}^{\tilde{n}} = \vec{a} + E@\left(\vec{x}^n + \nu^i \vec{Y}_a^i\right)$. For a contact c, the variation $\mathrm{d}\vec{b}^c$ of the branch vector $\vec{b}^c$ is:

$$\mathrm{d}\vec{b}^c = E@\left(\vec{x}^{E(c)} - \vec{x}^{O(c)} + \delta_c^i \vec{Y}_a^i\right)$$

or:

$$\mathrm{d}\vec{b}^c = E@\vec{b}^c = l^c E@\vec{e}^c$$

Remark 1. As $E = \mathrm{d}F \circ F^{-1}$, $\mathrm{d}\vec{b}^c$ is written $\mathrm{d}\vec{b}^c = \vec{u}^{E(c)} - \vec{u}^{O(c)} + \delta_c^i \mathrm{d}F \circ F^{-1}@\vec{Y}_a^i$ and taking into account (2.22) , we find $\mathrm{d}\vec{b}^c = \vec{u}^{E(c)} - \vec{u}^{O(c)} + \delta_c^i \mathrm{d}\vec{Y}_a^i$, that is to say (2.36).

The rotation displacement of the continuum medium is given by the antisymmetric part $E^A = \frac{1}{2}\left(E - E^T\right)$ de E. As the problem is two-dimensional, E^A is:

$$\forall \vec{b}, \vec{b}.\vec{i}_3 = 0\,,\ E^A@\vec{b} = \Omega\vec{i}_3 \wedge \vec{b}$$

which leads to:

$$\forall c\,,\ E^A@\vec{e}^c = \Omega\vec{i}_3 \wedge \vec{e}^c = \Omega\vec{t}^c$$

and consequently:

$$\Omega = \vec{t}^c.\left(E^A@\vec{e}^c\right)$$

To impose that the grain rotations of the base cell "follow" the homogeneous transformation of the macroscopic continuum medium is equivalent to impose:

$$\forall n\,,\ \theta^n = \Omega$$

Taking into account that $l^{cO} + l^{cE} = l^c$, the relation of the kinematic conditions in the expression (2.36) of $\mathrm{d}\vec{f}^c$ gives:

$$\mathrm{d}\vec{f}^c = l^c\left(\left(k_n\vec{e}^c \otimes \vec{e}^c + k_t\vec{t}^c \otimes \vec{t}^c + \frac{1}{l^c}\left(f_n^c\vec{t}^c - f_t^c\vec{e}^c\right) \otimes \vec{t}^c\right)@\left(E@\vec{e}^c\right) - k_t\Omega\vec{t}^c\right)$$

that is to say developing and taking into account expression Ω:

$$\mathrm{d}\vec{f}^c = l^c\left(k_n\vec{e}^c\left(\vec{e}^c.\left(E@\vec{e}^c\right)\right) + \frac{1}{l^c}\left(f_n^c\vec{t}^c - f_t^c\vec{e}^c\right)\left(\vec{t}^c.\left(E@\vec{e}^c\right)\right) + k_t\left(\vec{t}^c.\left(E@\vec{e}^c\right) - \vec{t}^c.\left(E^A@\vec{e}^c\right)\right)\vec{t}^c\right)$$

By decomposing E in symmetric E^S and antisymmetric E^A parts we have:

$$\vec{e}^c.\left(E@\vec{t}^c\right) = \vec{e}^c.\left(E^S@\vec{t}^c\right) + \vec{e}^c.\left(E^A@\vec{t}^c\right)$$

or, taking into account the symmetries:

$$\vec{e}^c.\left(E@\vec{t}^c\right) = \vec{t}^c.\left(E^S@\vec{e}^c\right) - \vec{t}^c.\left(E^A@\vec{e}^c\right)$$

we have also:

$$\vec{t}^{c}.\left(E@\vec{e}^{c}\right)=\vec{t}^{c}.\left(E^{S}@\vec{e}^{c}\right)+\vec{t}^{c}.\left(E^{A}@\vec{e}^{c}\right)$$

and consequently:

$$\vec{t}^{c}.\left(E^{A}@\vec{e}^{c}\right)=\frac{1}{2}\left(\vec{t}^{c}.\left(E@\vec{e}^{c}\right)-\vec{e}^{c}.\left(E@\vec{t}^{c}\right)\right)$$

Taking into account this result, the expression of $\mathrm{d}\vec{f}^{c}$ is written:

$$\mathrm{d}\vec{f}^{c}=l^{c}\left(k_{n}\vec{e}^{c}\left(\vec{e}^{c}.\left(E@\vec{e}^{c}\right)\right)+\frac{1}{l^{c}}\left(f_{n}^{c}\vec{t}^{c}-f_{t}^{c}\vec{e}^{c}\right)\left(\vec{t}^{c}.\left(E@\vec{e}^{c}\right)\right)+\frac{k_{t}}{2}\left(\vec{t}^{c}.\left(E@\vec{e}^{c}\right)+\vec{e}^{c}.\left(E@\vec{t}^{c}\right)\right)\vec{t}^{c}\right)$$

or also:

$$\mathrm{d}\vec{f}^{c}=l^{c}\left(k_{n}\vec{e}^{c}\left(\vec{e}^{c}\otimes\vec{e}^{c}:E\right)+\frac{k_{t}}{2}\vec{t}^{c}\left(\vec{t}^{c}\otimes\vec{e}^{c}+\vec{e}^{c}\otimes\vec{t}^{c}\right):E\right)+\left(f_{n}^{c}\vec{t}^{c}-f_{t}^{c}\vec{e}^{c}\right)\left(\vec{t}^{c}\otimes\vec{e}^{c}:E\right)$$

or also tanking into account this result, the expression $E=\mathrm{d}F\circ F^{-1}$:

$$\begin{aligned}\mathrm{d}\vec{f}^{c}=l^{c}&\left(k_{n}\vec{e}^{c}\left(\vec{e}^{c}\otimes\vec{e}^{c}\circ F^{-T}\right):\mathrm{d}F+\frac{k_{t}}{2}\vec{t}^{c}\left(\vec{t}^{c}\otimes\vec{e}^{c}+\vec{e}^{c}\otimes\vec{t}^{c}\right)\circ F^{-T}\right):\mathrm{d}F\\&+\left(f_{n}^{c}\vec{t}^{c}-f_{t}^{c}\vec{e}^{c}\right)\left(\vec{t}^{c}\otimes\vec{e}^{c}\circ F^{-T}\right):\mathrm{d}F\end{aligned}$$

Direct determination of $\mathrm{d}T$ **and** $\mathrm{d}\sigma$ Because the grains of the base cell are not in equilibrium in this analysis, it's not possible to use the expression

$$\mathrm{d}T=\frac{1}{|Y_{R}|}\sum_{c\in\mathcal{C}}\delta_{c}^{i}\mathrm{d}\vec{f}^{c}\otimes\vec{Y}_{R}^{i}\tag{2.38}$$

and (2.37) of $\mathrm{d}T$ and $\mathrm{d}\sigma$, it's needed to recall the more general expressions

$$T=\frac{1}{|Y_{R}|}\sum_{c\in\mathcal{C}}\vec{f}^{c}\otimes\vec{b}^{c}\circ F^{-T}=\frac{1}{|Y_{R}|}\sum_{c\in\mathcal{C}}\vec{f}^{c}\otimes\left(F^{-1}@\vec{b}^{c}\right)\tag{2.39}$$

and

$$\sigma=\frac{1}{|Y_{a}|}\sum_{c\in\mathcal{C}}\vec{f}^{c}\otimes\vec{b}^{c}\tag{2.40a}$$

$$\tag{2.40b}$$

of T and σ and differentiate them.

Differentiation of T The differentiation of (2.39) gives:

$$\mathrm{d}T = \frac{1}{|Y_R|}\sum_{c\in\mathcal{C}}\left(\left(\mathrm{d}\vec{f}^c\otimes\vec{b}^c + \vec{f}^c\otimes\mathrm{d}\vec{b}^c\right)\circ F^{-T} + \vec{f}^c\otimes\vec{b}^c\circ\mathrm{d}\left(F^{-T}\right)\right)$$

or:

$$\mathrm{d}T = \frac{1}{|Y_R|}\sum_{c\in\mathcal{C}}\left(\left(\mathrm{d}\vec{f}^c\otimes\vec{b}^c + \vec{f}^c\otimes\mathrm{d}\vec{b}^c\right)\circ F^{-T}\right) + T\circ F^T\circ\mathrm{d}\left(F^{-T}\right)$$

now $F^T\circ F^{-T} = \mathbb{I}$ which, differentiating gives: $\mathrm{d}F^T\circ F^{-T} + F^T\circ\mathrm{d}\left(F^{-T}\right) = 0$ hence:

$$\mathrm{d}T = \frac{1}{|Y_R|}\sum_{c\in\mathcal{C}}\left(\mathrm{d}\vec{f}^c\otimes\vec{b}^c + \vec{f}^c\otimes\mathrm{d}\vec{b}^c\right)\circ F^{-T} - T\circ\mathrm{d}F^T\circ F^{-T} \tag{2.41}$$

Differentiation of σ

By differentiating the expression (2.40a) of σ it follows:

$$\mathrm{d}\sigma = -\frac{1}{|Y_a|^2}\mathrm{d}\,|Y_a|\sum_{c\in\mathcal{C}}\vec{f}^c\otimes\vec{b}^c + \frac{1}{|Y_a|}\sum_{c\in\mathcal{C}}\left(\mathrm{d}\vec{f}^c\otimes\vec{b}^c + \vec{f}^c\otimes\mathrm{d}\vec{b}^c\right)$$

Taking into account

$$\mathrm{d}\,|Y_a| = |Y_a|\,F^{-T} : \mathrm{d}F \tag{2.42}$$

(2.42) we have:

$$\begin{aligned}\frac{1}{|Y_a|^2}\mathrm{d}\,|Y_a|\sum_{c\in\mathcal{C}}\vec{f}^c\otimes\vec{b}^c &= \frac{1}{|Y_a|}\left(\sum_{c\in\mathcal{C}}\vec{f}^c\otimes\vec{b}^c\right)F^{-T} : \mathrm{d}F\\ &= \sigma F^{-T} : \mathrm{d}F\end{aligned}$$

now:

$$\frac{1}{|Y_a|^2}\mathrm{d}\,|Y_a|\sum_{c\in\mathcal{C}}\vec{f}^c\otimes\vec{b}^c = \left(\sigma\otimes F^{-T}\right)\circledast\mathrm{d}F$$

So we obtain for $\mathrm{d}\sigma$:

$$\mathrm{d}\sigma = \frac{1}{|Y_a|}\sum_{c\in\mathcal{C}}\left(\mathrm{d}\vec{f}^c\otimes\vec{b}^c + \vec{f}^c\otimes\mathrm{d}\vec{b}^c\right) - \left(\sigma\otimes F^{-T}\right)\circledast\mathrm{d}F \tag{2.43}$$

Remark 2. From (2.41) with $|Y_a| = J\,|Y_R|$, we draw:

$$\mathrm{d}T\circ F^T + T\circ\mathrm{d}F^T = \frac{J}{|Y_a|}\sum_{c\in\mathcal{C}}\left(\mathrm{d}\vec{f}^c\otimes\vec{b}^c + \vec{f}^c\otimes\mathrm{d}\vec{b}^c\right)$$

which taking into account (2.43) and $T\circ F^T = J\sigma$ gives:

$$\mathrm{d}T\circ F^T + T\circ\mathrm{d}F^T = J\mathrm{d}\sigma + T\circ F^T\left(F^{-T} : \mathrm{d}F\right)$$

which is the relationship

$$\mathrm{d}\sigma = \frac{1}{J}\left(\mathrm{d}T\circ F^T + T\circ\mathrm{d}F^T\right) - \left(F^{-T} : \mathrm{d}F\right)\sigma \tag{2.44}$$

As $\mathrm{d}\vec{b}^c = \mathrm{d}F \circ F^{-1} @ \vec{b}^c$, we have:

$$\begin{aligned}\sum_{c\in\mathcal{C}} \vec{f}^c \otimes \mathrm{d}\vec{b}^c &= \sum_{c\in\mathcal{C}} \vec{f}^c \otimes \left(\mathrm{d}F \circ F^{-1} @ \vec{b}^c\right) \\ &= \sum_{c\in\mathcal{C}} \vec{f}^c \otimes \vec{b}^c \circ F^{-T} \circ \mathrm{d}F^T\end{aligned}$$

hence, taking into account the expressions (2.39) and (2.40a) of T and σ:

$$\begin{aligned}\mathrm{d}T &= \frac{1}{|Y_R|} \sum_{c\in\mathcal{C}} \mathrm{d}\vec{f}^c \otimes \vec{b}^c \circ F^{-T} + T \circ \mathrm{d}F^T - T \circ \mathrm{d}F^T \circ F^{-T} \\ \mathrm{d}\sigma &= \frac{1}{|Y_a|} \sum_{c\in\mathcal{C}} \mathrm{d}\vec{f}^c \otimes \vec{b}^c - \left(\sigma \otimes F^{-T}\right) @ \mathrm{d}F + \sigma \circ F^{-T} \circ \mathrm{d}F^T\end{aligned}$$

In the other hand we have:

$$\begin{aligned}\mathrm{d}\vec{f}^c \otimes \vec{b}^c = {} & (l^c)^2 \left(k_n \left(\bar{e}^{\mathbf{c}} \otimes \bar{e}^{\mathbf{c}}\right) \otimes \left(\vec{e}^{\mathbf{c}} \otimes \vec{e}^{\mathbf{c}} \circ F^{-T}\right)\right) @ \mathrm{d}F \\ & + (l^c)^2 \left(\frac{k_t}{2} \left(\vec{t}^{\mathbf{c}} \otimes \vec{e}^{\mathbf{c}}\right) \otimes \left(\left(\vec{t}^{\mathbf{c}} \otimes \vec{e}^{\mathbf{c}} + \vec{e}^{\mathbf{c}} \otimes \vec{t}^{\mathbf{c}}\right) \circ F^{-T}\right)\right) @ \mathrm{d}F \\ & + l^c \left(\left(f_n^c \vec{t}^{\mathbf{c}} - f_t^c \vec{e}^{\mathbf{c}}\right) \otimes \vec{e}^{\mathbf{c}}\right) \otimes \left(\vec{t}^{\mathbf{c}} \otimes \bar{e}^{\mathbf{c}} \circ F^{-T}\right) @ \mathrm{d}F\end{aligned}$$

and:

$$\begin{aligned}\mathrm{d}\vec{f}^c \otimes \vec{b}^c \circ F^{-T} = {} & (l^c)^2 \left(k_n \left(\bar{e}^{\mathbf{c}} \otimes \vec{e}^{\mathbf{c}} \circ F^{-T}\right) \otimes \left(\bar{e}^{\mathbf{c}} \otimes \vec{e}^{\mathbf{c}} \circ F^{-T}\right)\right) @ \mathrm{d}F \\ & + (l^c)^2 \left(\frac{k_t}{2} \left(\vec{t}^{\mathbf{c}} \otimes \vec{e}^{\mathbf{c}} \circ F^{-T}\right) \otimes \left(\left(\vec{t}^{\mathbf{c}} \otimes \vec{e}^{\mathbf{c}} + \vec{e}^{\mathbf{c}} \otimes \vec{t}^{\mathbf{c}}\right) \circ F^{-T}\right)\right) @ \mathrm{d}F \\ & + l^c \left(\left(f_n^c \vec{t}^{\mathbf{c}} - f_t^c \vec{e}^{\mathbf{c}}\right) \otimes \vec{e}^{\mathbf{c}} \circ F^{-T}\right) \otimes \left(\vec{t}^{\mathbf{c}} \otimes \bar{e}^{\mathbf{c}} \circ F^{-T}\right) @ \mathrm{d}F\end{aligned}$$

and we obtain:

$$\begin{aligned}\mathrm{d}T = {} & \frac{1}{|Y_R|} \sum_{c\in\mathcal{C}} (l^c)^2 \left(k_n \left(\bar{e}^{\mathbf{c}} \otimes \vec{e}^{\mathbf{c}} \circ F^{-T}\right) \otimes \left(\bar{e}^{\mathbf{c}} \otimes \vec{e}^{\mathbf{c}} \circ F^{-T}\right)\right) @ \mathrm{d}F \\ & + \frac{1}{|Y_R|} \sum_{c\in\mathcal{C}} (l^c)^2 \left(\frac{k_t}{2} \left(\vec{t}^{\mathbf{c}} \otimes \vec{e}^{\mathbf{c}} \circ F^{-T}\right) \otimes \left(\vec{t}^{\mathbf{c}} \otimes \vec{e}^{\mathbf{c}} + \vec{e}^{\mathbf{c}} \otimes \vec{t}^{\mathbf{c}}\right) \circ F^{-T}\right) @ \mathrm{d}F \\ & + \frac{1}{|Y_R|} \sum_{c\in\mathcal{C}} l^c \left(\left(f_n^c \vec{t}^{\mathbf{c}} - f_t^c \vec{e}^{\mathbf{c}}\right) \otimes \vec{e}^{\mathbf{c}} \circ F^{-T}\right) \otimes \left(\vec{t}^{\mathbf{c}} \otimes \bar{e}^{\mathbf{c}} \circ F^{-T}\right) @ \mathrm{d}F \\ & + T \circ \mathrm{d}F^T - T \circ \mathrm{d}F^T \circ F^{-T} \\ \mathrm{d}\sigma = {} & \frac{1}{|Y_a|} \sum_{c\in\mathcal{C}} (l^c)^2 \left(k_n \left(\bar{e}^{\mathbf{c}} \otimes \bar{e}^{\mathbf{c}}\right) \otimes \left(\vec{e}^{\mathbf{c}} \otimes \vec{e}^{\mathbf{c}} \circ F^{-T}\right) + \frac{k_t}{2}\right) @ \mathrm{d}F \\ & \frac{1}{|Y_a|} \sum_{c\in\mathcal{C}} (l^c)^2 \left(\left(\vec{t}^{\mathbf{c}} \otimes \vec{e}^{\mathbf{c}}\right) \otimes \left(\vec{t}^{\mathbf{c}} \otimes \vec{e}^{\mathbf{c}} + \vec{e}^{\mathbf{c}} \otimes \vec{t}^{\mathbf{c}}\right) \circ F^{-T}\right) @ \mathrm{d}F \\ & + \frac{1}{|Y_a|} \sum_{c\in\mathcal{C}} l^c \left(\left(f_n^c \vec{t}^{\mathbf{c}} - f_t^c \vec{e}^{\mathbf{c}}\right) \otimes \vec{e}^{\mathbf{c}}\right) \otimes \left(\vec{t}^{\mathbf{c}} \otimes \vec{e}^{\mathbf{c}} \circ F^{-T}\right) @ \mathrm{d}F \\ & - \left(\sigma \otimes F^{-T}\right) @ \mathrm{d}F + \sigma \circ F^{-T} \circ \mathrm{d}F^T\end{aligned}$$

The operator "Kruyt" augmented $(C_{ijkl})^{KAO}$ such as $\mathrm{d}\sigma_{ij} = (C_{ijkl})^{KAO}\,\mathrm{d}F_{kl}$ is then:

$$\begin{aligned}(C_{ijkl})^{KAO} &= -\sigma_{ij}\left(F^{-T}\right)_{kl} + \sigma_{ih}\left(F^{-T}\right)_{hl}\delta_{jk} \\ &+ \frac{1}{|Y_a|}\sum_{c\in\mathcal{C}}(l^c)^2\left(k_n e_i^c e_j^c e_k^c e_h^c + \frac{k_t}{2}t_i^c e_j^c\left(t_k^c e_h^c + e_k^c t_h^c\right)\right)\left(F^{-T}\right)_{hl} \\ &+ \frac{1}{|Y_a|}\sum_{c\in\mathcal{C}} l^c\left(f_n^c t_i^c - f_t^c e_i^c\right)e_j^c t_k^c e_h^c\left(F^{-T}\right)_{hl}\end{aligned}$$

or also:

$$\begin{aligned}(C_{ijkl})^{KAO} &= -\sigma_{ij}\left(F^{-1}\right)_{lk} + \sigma_{ih}\left(F^{-1}\right)_{lh}\delta_{jk} \\ &+ \frac{1}{|Y_a|}\sum_{c\in\mathcal{C}}(l^c)^2\left(k_n e_i^c e_j^c e_k^c e_h^c + \frac{k_t}{2}t_i^c e_j^c\left(t_k^c e_h^c + e_k^c t_h^c\right)\right)\left(F^{-1}\right)_{lh} \\ &+ \frac{1}{|Y_a|}\sum_{c\in\mathcal{C}} l^c\left(f_n^c t_i^c - f_t^c e_i^c\right)e_j^c t_k^c e_h^c\left(F^{-1}\right)_{lh}\end{aligned} \tag{2.45}$$

2.4.2 Kruyt Augmented Operator (KAO)

KAO uses the same idea as the Kruyt type operators which consider a homogeneous strain field and null grain rotations, in this case the description is enriched with the prestresses and contact preforces. (Eq. 2.45)

The problem to solve in the elementary cell is the one in: (Eq. 2.45). A numerical example is presented in (Eq. 2.46).

$$\left(C_{ijmn}^{KAO}\right) = \begin{pmatrix} 1117.9 & -10.2 & -10.2 & -0.1 \\ -20.5 & 559.4 & 559.0 & 0.0 \\ 0.0 & 558.8 & 559.2 & -20.4 \\ -0.1 & -10.2 & -10.2 & 1118.3 \end{pmatrix} \tag{2.46}$$

Convergence velocity is better than with UKO but still not as efficient as DEMQO/PSTLO (Fig. 2.12 and 2.13).

Remark 3. From Guo and Zhao (2014) the tensor C in the equation (Eq. 2.1), which we called "Kruyt", is in the notations of the present text:

$$\frac{1}{|Y_a|}\sum_{c\in\mathcal{C}}(l^c)^2\left(k_n\left(\vec{e}^{\,c}\otimes\vec{e}^{\,c}\right)\otimes\left(\vec{e}^{\,c}\otimes\vec{e}^{\,c}\right) + k_t\left(\vec{t}^{\,c}\otimes\vec{e}^{\,c}\right)\otimes\left(\vec{t}^{\,c}\otimes\vec{e}^{\,c}\right)\right) \tag{2.47}$$

which means that neither rotations nor prestresses nor preforces are taken into account.

2.4.3 Upper bound Kruyt operator (UKO)

The elastic operator proposed by Kruyt is tested (Kruyt and Rothenburg, 1998), Kruyt proposes two extremum principles in order to obtain the upper and lower bound of the

elastic moduli of a granular assembly. The extremum principle used in this work is the one corresponding to the upper bound of the elastic moduli. This operator is already used in a multiscale FEMxDEM approach by Guo and Zhao (2014). UKO is obtained assuming homogeneous strain field over the REV and performing a summation over all the contacts taking in consideration the orientation and stiffness of the contact (Eq. 2.47). Cohesion forces are not taken into account. (Fig. 2.11).

As it consists of an elastic definition, the resulting operator is positive defined which provides stability. However, not being a CTO , quadratic convergence cannot be expected (Fig. 2.12). It is recomputed at each iteration accounting for the evolution of the DEM assembly properties. The computational cost of the operator is negligible with respect to the DEM computation and, as for the AEO, no perturbations are needed, meaning that it is 5 times less time-demanding per Newton iteration compared to the CTO.

In the following, different numerical examples of UKO are shown. The coefficients obtained by the Kruyt method are higher in the diagonal than the ones obtained by perturbation method. This is coherent with the fact that the upper bound extremum principle is used: $\left(C_{ijmn}^{AEO}\right)$ (Eq. 2.48 and 2.51 vs. 2.11). In addition, a base of eigenvectors V (Eq. 2.49, 2.52) in which the operator diagonalizes on its eigenvalues D (Eq. 2.50, 2.53) is shown for each case, proving the positiveness of the operator.

UKO (pre-peak):

$$\left(C_{ijmn}^{UKO}\right) = \begin{pmatrix} 1119.12 & -19.48 & 0 & 0 \\ -19.48 & 1119.56 & 0 & 0 \\ 0 & 0 & 1119.12 & -19.48 \\ 0 & 0 & -19.48 & 1119.56 \end{pmatrix} \tag{2.48}$$

Eigenvectors and eigenvalues of the UKO (pre-peak):

$$V = \begin{pmatrix} -0.7031 & 0 & 0 & -0.7111 \\ 0.7111 & 0 & 0 & -0.7031 \\ 0 & -0.7031 & -0.7111 & 0 \\ 0 & 0.7111 & -0.7031 & 10 \end{pmatrix} \tag{2.49}$$

$$D = \begin{pmatrix} 1038.8 & 0 & 0 & 0 \\ 0 & 1038.8 & 0 & 0 \\ 0 & 0 & 1099.9 & 0 \\ 0 & 0 & 0 & 1099.9 \end{pmatrix} \tag{2.50}$$

UKO (post-peak):

$$\left(C_{ijmn}^{UKO}\right) = \begin{pmatrix} 809.40 & 12.50 & 0 & 0 \\ 12.50 & 1033.74 & 0 & 0 \\ 0 & 0 & 809.40 & 12.50 \\ 0 & 0 & 12.50 & 1033.74 \end{pmatrix} \tag{2.51}$$

Eigenvectors and eigenvalues of the UKO (post-peak):

$$V = \begin{pmatrix} 0.0555 & 0 & 0 & -0.9985 \\ 0.9985 & 0 & 0 & 0.0555 \\ 0 & 0.0555 & -0.9985 & 0 \\ 0 & 0.9985 & 0.0555 & 10 \end{pmatrix} \tag{2.52}$$

$$D = \begin{pmatrix} 1034.4 & 0 & 0 & 0 \\ 0 & 1034.4 & 0 & 0 \\ 0 & 0 & 808.7 & 0 \\ 0 & 0 & 0 & 808.7 \end{pmatrix} \tag{2.53}$$

2.4.4 Upper bound Corrected Kruyt Operator (UCKO - UCKO 2DOF)

Using statistical and thermodynamics principles, Kruyt shows that the elastic moduli can be obtained as the average of the upper and lower bounds if certain conditions are fulfilled (Kruyt and Rothenburg, 1998). The upper bound is used in the previous section (Eq. 2.47). Being aware of the linearity between upper, lower bounds and actual elastic moduli shown by Kruyt, the CTO in the pre-peak part is used to obtain a correction coefficient in order to calibrate the UKO (Eq. 2.55) which will be used during the rest of the test in order to obtain a better approximation of the elastic moduli: the UCKO. This operator has the same properties as the UKO with a slight increase of the convergence velocity (Fig. 2.12 and 2.13).

$$\frac{1}{|Y_a|} \sum_{c \in \mathcal{C}} (l^c)^2 \, c_x \left(k_n \left(\vec{e}^c \otimes \vec{e}^c \right) \otimes \left(\vec{e}^c \otimes \vec{e}^c \right) + k_t \left(\vec{t}^c \otimes \vec{e}^c \right) \otimes \left(\vec{t}^c \otimes \vec{e}^c \right) \right) \tag{2.54}$$

Where c_x is the correction coefficient, a numerical example is presented in (Eq. 2.55).

$$\left(C_{ijmn}^{UCKO} \right) = \begin{pmatrix} 902.3 & 13.4 & -14.2 & 86.2 \\ -13.4 & 384.6 & 421.9 & -12.4 \\ -13.4 & 384.6 & 421.9 & -12.4 \\ 86.2 & -12.4 & -12.4 & 890.3 \end{pmatrix} \tag{2.55}$$

A more complex calibration is made by adjusting the coefficients k_n and k_t in the expression (Eq. 2.55) using two coefficients of the operator, i.e. C_{1111} and C_{1122}. This operator is called UCKO 2DOF (2 Degrees Of Freedom Calibration), and it provides still a faster convergence in the pre-peak, close to quadratic velocity (Fig. 2.12). Nevertheless, this does not improve the post-peak convergence velocity because the calibration is done only once at the beginning of the test.

$$\frac{1}{|Y_a|} \sum_{c \in \mathcal{C}} (l^c)^2 \, c_n \left(k_n \left(\vec{e}^c \otimes \vec{e}^c \right) \otimes \left(\vec{e}^c \otimes \vec{e}^c \right) + c_t k_t \left(\vec{t}^c \otimes \vec{e}^c \right) \otimes \left(\vec{t}^c \otimes \vec{e}^c \right) \right) \tag{2.56}$$

Where c_n and c_t are the correction coefficients.

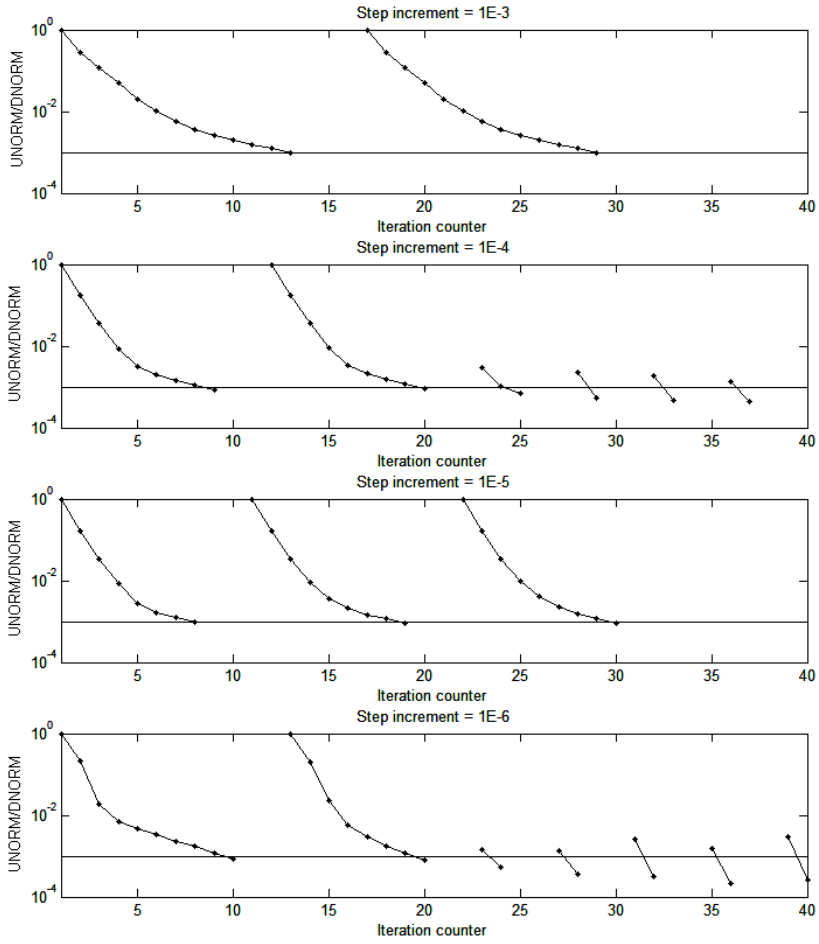

Figure 2.11: Deficit of compatibility for the norm of the displacement (UNORM/DNORM) for four different initial step size: $\epsilon_2 = 1{\cdot}10^{-3}$, $\epsilon_2 = 1{\cdot}10^{-4}$, $\epsilon_2 = 1{\cdot}10^{-5}$, $\epsilon_2 = 1 \cdot 10^{-6}$. Kruyt operator. The horizontal line indicates the precision threshold.

2.5 Results

In this section the results of the operator study are summarized. In the figure (Fig. 2.12) the convergence profiles of a standard compression biaxial test with 128 elements are presented. The two plots represent the evolution of the force vector residual in the initial stage of the compression and well after the stress peak. The case at the beginning of the compression gives the best convergence rates for the OTC, DEMQO/PSTLO and UCKO 2DOF in this order for a threshold $FNORM/RNORM = 1{\cdot}10^{-2}$. It's also interesting to observe the asymptotic value around $FNORM/RNORM = 3{\cdot}10^{-4}$ due to the precision of the constitutive law. The plot for the post-peak regime gives the best convergence for UCKO, DEMQO/PSTLO and OTC in this order for a threshold$FNORM/RNORM = 1 \cdot 10^{-2}$. in this case the asymptotic value for the precision is around $2 \cdot 10^{-4}$ due to the discrete nature of the DEM model and the presence of grain sliding.

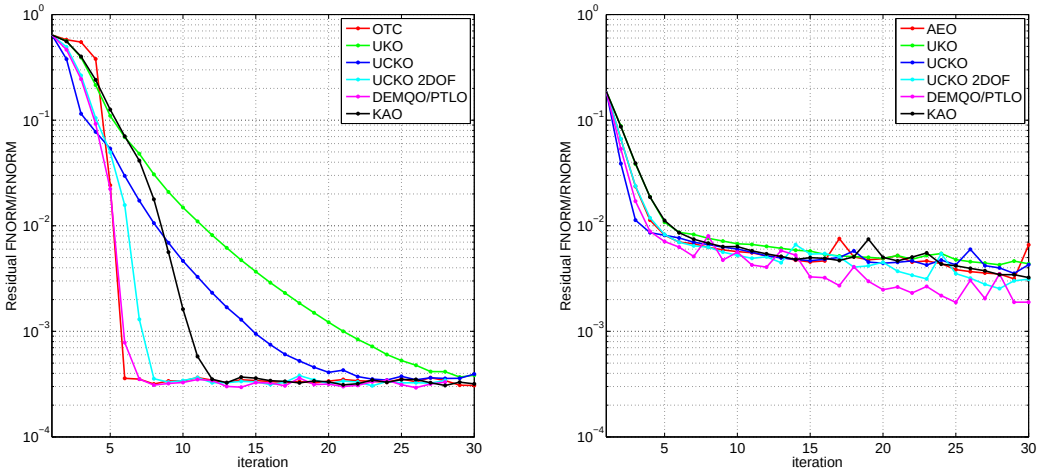

Figure 2.12: Convergence plots for 5 operators used in the quasi-Newton approach; left: at the beginning of a biaxial test, $\epsilon_{22} = 0$ in (Fig. 2.1) , right: post-peak regime, $\epsilon_{22} = 1.5\%$ in (Fig. 2.1), y axis in logarithmic scale.

A second plot (Fig. 2.13) shows the convergence performance of the different operators for the same compression biaxial test focusing on the number of iterations needed to reach convergence with a precision threshold $FNORM/RNORM = 1 \cdot 10^{-2}$. it shows that the best overall performance is due to the DEMQO/PSTLO. In the case of the Kruyt modifications it can be seen that the calibration improves the performance in the initial stage but makes it slower after the stress peak, this is due to the calibration being made with a CTO computed in the initial stage.

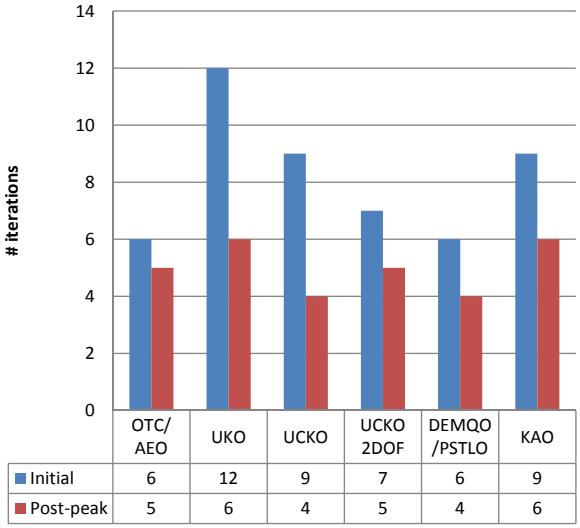

Figure 2.13: Number of iterations needed to reach convergence with the different operators. Convergence threshold: FNORM/RNORM $= 1 \cdot 10^{-2}$

2.6 Conclusion

The FEMxDEM approach is computationally expensive due to the needed integration of the microscale. This is magnified by convergence problems from different origins, mainly because of the softening and noisy behaviour of the DEM model. The method used during the DEM assembly preparation leaves a residual shear stress to the assembly after applying an isotropic compression, this is due to the discrete nature of the DEM and cannot be eliminated by other preparation techniques. The DEM assembly needs to be equilibrated,prior or once injected to the FEM model, in order to avoid convergence problems due to lack of equilibrium between the structure boundary conditions and microscale stress state.

The particularities of the FEMxDEM method makes the use of CTO inappropriate in the Newton method because of a bad conditioning of the system matrix and consequent instability, mainly because the noisy law provided by the DEM and the computational time devoted to integrate the law. The AEO is a solution already presented by other authors that allows the Newton method to work with FEMxDEM, notably in the post-peak region, other approaches like the Kruyt and Kruyt corrections are a pragmatic approach that gives further improvement with respect to AEO, KAO is meant to provide a better description of the DEM medium than the Kruyt like operators, but in terms of performance it has similar properties. Finally, two operators; DEMQO and PSTLO, which in the theoretical plane give the same values, but from the numerical point or view are obtained with different techniques, give the best results in terms of convergence rates both in the pre and post-peak regimes.

Finally, due to the computational time devoted to the resolution of a linear system

with a number of DOF proportional to the number of DEM particles, the PSTLO turns to require more walltime. The DEMQO remains the best operator because of its stability, convergence rate and computational time.

After this section the model is in equilibrium with the boundary conditions in the initial state and it is provided with a fast and stable tangent operator which allows to simulate BVPs.

2.7 Annexe

Definition 4. Being A a linear application of $\mathcal{L}(V)$ and $\underline{A}$ the associated column vector, a base having been chosen from V:

$$\underline{A} = \begin{pmatrix} A_{11} \\ A_{12} \\ A_{21} \\ A_{22} \end{pmatrix}$$

We define the matrices and $\underline{\underline{Amg}}$, $\underline{\underline{Amd}}$ and $\underline{\underline{Amgt}}$ as:

$$\underline{\underline{Amg}} = \begin{pmatrix} A_{11} & 0 & A_{12} & 0 \\ 0 & A_{11} & 0 & A_{12} \\ A_{21} & 0 & A_{22} & 0 \\ 0 & A_{21} & 0 & A_{22} \end{pmatrix}, \ \underline{\underline{Amd}} = \begin{pmatrix} A_{11} & A_{21} & 0 & 0 \\ A_{12} & A_{22} & 0 & 0 \\ 0 & 0 & A_{11} & A_{21} \\ 0 & 0 & A_{12} & A_{22} \end{pmatrix}$$

$$\text{and } \underline{\underline{Amgt}} = \begin{pmatrix} A_{11} & A_{12} & 0 & 0 \\ 0 & 0 & A_{11} & A_{12} \\ A_{21} & A_{22} & 0 & 0 \\ 0 & 0 & A_{21} & A_{22} \end{pmatrix}$$

Lemma 5. *Being A and B two linear applications of $\mathcal{L}(V)$ and $\underline{A}$ and $\underline{B}$ the associated column vectors, a base having been chosen in V, then the column vector $\underline{A \circ B}$ of the linear application $A \circ B$ is written:*

$$\underline{A \circ B} = \underline{\underline{Amg}}\,\underline{B} = \underline{\underline{Bmd}}\,\underline{A}$$

Proof. We have:

$$\begin{pmatrix} A_{11} & 0 & A_{12} & 0 \\ 0 & A_{11} & 0 & A_{12} \\ A_{21} & 0 & A_{22} & 0 \\ 0 & A_{21} & 0 & A_{22} \end{pmatrix} \begin{pmatrix} B_{11} \\ B_{12} \\ B_{21} \\ B_{22} \end{pmatrix} = \begin{pmatrix} A_{11}B_{11} + A_{12}B_{21} \\ A_{11}B_{12} + A_{12}B_{22} \\ A_{21}B_{11} + A_{22}B_{21} \\ A_{21}B_{12} + A_{22}B_{22} \end{pmatrix}$$

and:

$$\begin{pmatrix} B_{11} & B_{21} & 0 & 0 \\ B_{12} & B_{22} & 0 & 0 \\ 0 & 0 & B_{11} & B_{21} \\ 0 & 0 & B_{12} & B_{22} \end{pmatrix} \begin{pmatrix} A_{11} \\ A_{12} \\ A_{21} \\ A_{22} \end{pmatrix} = \begin{pmatrix} A_{11}B_{11} + A_{12}B_{21} \\ A_{11}B_{12} + A_{12}B_{22} \\ A_{21}B_{11} + A_{22}B_{21} \\ A_{21}B_{12} + A_{22}B_{22} \end{pmatrix}$$

□

Corollary 6. *The column vector* $\underline{A \circ B^T}$ *of the linear application* $A \circ B^T$ *is written:*

$$\underline{A \circ B^T} = \underline{\underline{Amgt}}\underline{B} = \underline{\underline{Bmd}}^T \underline{A}$$

Proof. . The column vector $\underline{B^T}$ of the linear application B^T is obtained by interchanging the lines 2 and 3 $\underline{B}$, the matrix $\underline{\underline{C}}$ such as $\underline{A \circ B^T} = \underline{\underline{C}}\,\underline{B}$ is obtained then by exchanging the columns 2 and 3 of $\underline{\underline{Amg}}$ which gives $\underline{\underline{Amgt}}$. Moreover, the matrix $\underline{\underline{D}}$ such as $\underline{A \circ B^T} = \underline{\underline{D}}\,\underline{A}$ is obtained by inverting B_{12} and B_{21} in the matrix $\underline{\underline{Bmd}}$ which gives:

$$\begin{pmatrix} B_{11} & B_{12} & 0 & 0 \\ B_{21} & B_{22} & 0 & 0 \\ 0 & 0 & B_{11} & B_{12} \\ 0 & 0 & B_{21} & B_{22} \end{pmatrix}$$

which is $\underline{\underline{Bmd}}^T$. □

Chapter 3

Introduction of random fields

Contents

3.1 Introduction

One of the challenges for the Newton method is to reach the precision criteria when approaching a bifurcation. Often, when the bifurcation point is left behind, the Newton method increases its efficiency reducing again the number of iterations per step. This can be identified in the previous biaxial tests (Chapter 2) as a higher number of iterations around the stress peak. The initial homogeneity of the sample appears to be in the origin of the convergence slowness. In this chapter different methods to introduce heterogeneity

are tested, of particular interest is the use of the DEM generation itself to create random variability without perturbing the parameters of the model[1].

3.1.1 State of the art

A bibliographic research is made in order to know the state of the art on physical systems symmetry, uncertainties and randomness in numerical modeling, as well as its implications in applications.

The initial homogeneity, resulting from methodological reductionism of numerical models, can lead to radically different results compared to the ones of reality. In the paper (Anderson et al., 1972) the symmetry breaking concept is used to show some of the drawbacks of reductionism. The symmetries in a physical system are the states of this system that are equally seen from different perspectives. The existence of symmetries in a mechanical problem can lead to symmetrical solutions which are very unlikely to happen in reality. In addition the symmetric solution does not usually represent the minimum energy state of the system, meaning that in engineering design, the numerical solution may overestimate the structure strength. Another effect of the existence of symmetries, already introduced in the previous chapter, is the reduced performance of iterative methods such Newton when approaching a symmetry breaking due to the existence of different solutions.

The uncertainties in numerical modeling and the breaking of symmetries are two linked subjects. The spatial variability of a BVP can be considered as an input uncertainty, since it is not possible to have detailed information of the microscale, usually the numerical model is considered initially homogeneous. Not considering this variability leads to a different problem due to the introduction of symmetries.

As suggested by Anderson et al. (1972), the reduction of symmetries is equivalent to the increase of complication. This is what is proposed in this chapter: the reduction of symmetries by the introduction of heterogeneity which supposes an increase of complication of the model. Matthies et al. (1997) gives an extensive literature on the topic of spatial variability and uncertainties in probabilistic analysis, while having different motivations and application range, some of the techniques presented in the paper are equivalent to the ones used in this chapter.

Schuėller et al. (1997) presents a state of the art report about computational stochastic mechanics. In the Chapter 4 of the document, Schuelle discusses about stochastic finite elements (SFEM) using different methods, with uncertainty both from material and geometrical nature.

Sudret and Der Kiureghian (2000) presents a stochastic based random field finite element method, which uses random field theory (Dobruschin, 1968). The study is the first attempt to compare a broad spectrum of stochastic finite element methods on a

[1]The parameters of the model are those that define the material properties at the contact level: contact stiffness, friction angle and cohesion force. Nevertheless, the variables of the model, such ass void ratio and coordination number are slightly modified as a result of the random generation of the granular assembly.

given application. RFEM, adds randomness to the material points of the domain in the same fashion as presented in the present work.

Tailhan et al. (2010) uses a model that takes into account scale effects as well as the heterogeneous nature of concrete via appropriate, experimentally validated, size effect laws and via a statistical distribution of mechanical properties.

Puła et al. (2016) gives an example of RFEM application to an engineering problem of street footing to obtain the characteristic values of soil properties. The paper points out the differences in the results between the use of deterministic approaches and RFEM for this application.

An extension of RFEM by Moradabadi et al. (2015) uses a semi-random field finite element method for masonry computations. Masonry specimens produce highly variable results, SRFEM is an approach in which simulations are performed prior and after the test and uses random field theory in order to determine the variance of the masonry individual components.

The literature shows that very consolidated bases of stochastic methods exists and is ready to be used with FEM models, this encourages to explore its performances with FEMxDEM as well as using the properties of the DEM microscale to generate the random field variability[2].

3.2 Introducing heterogeneity

Classical methods to introduce heterogeneity into continuum models are applied in this section to the FEMxDEM model. These tested methods are the introduction of a punctual geometrical defect in the mesh, punctual material imperfection, in this case some physical parameters in one element are altered, and finally a full field element variability. All the simulations use the same microscale configuration, so the variability is introduced in the macroscale. The section concludes with a biaxial compression test, charge and discharge. This is meant to exemplify the ability of the model to simulate complex loading histories that undergo large strains.

3.2.1 Punctual geometrical defect

A possible technique to avoid the convergence issue is to trigger one of the solutions by different means, for instance introducing a defect in one of the elements that will break the homogeneity of the sample. In the Chapter 2 of this document a biaxial test with two symmetry boundary conditions was used. In the present Chapter, a more general case without symmetry boundary conditions is used (Fig. 3.1), one point has both vertical and horizontal displacements prescribed in order to avoid kinematical indetermination. The reason is that in the precision study a more constricted localization configuration is desired in order to be able to compare different tests. From now on, the more general case will be used with its higher resemblance to real experiments.

[2]Only spatial variability is considered in this chapter, the temporal variability is not considered.

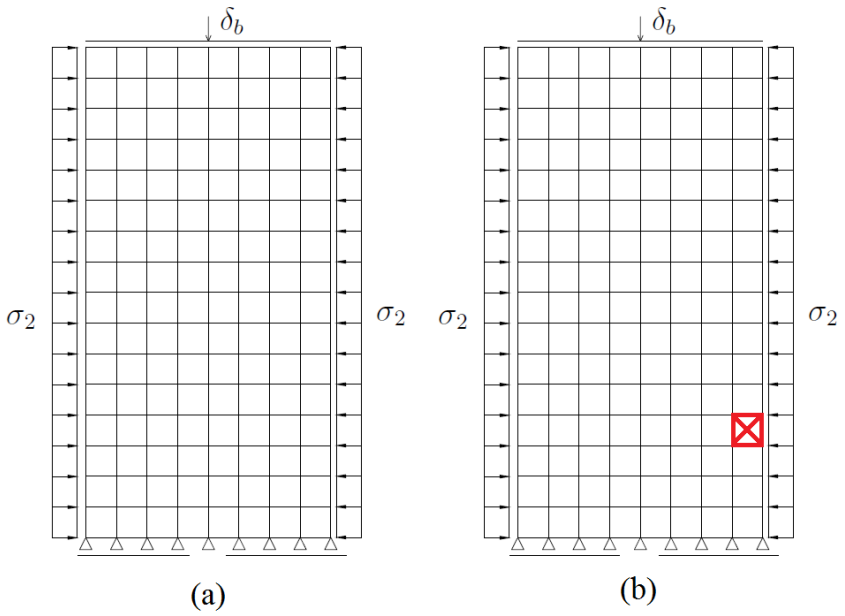

Figure 3.1: Biaxial test geometry and boundary conditions. Full biaxial. 128 Q8 elements. Without (a) and with defect (b).

In the plot (Fig. 3.2) the second invariant of strain is shown at the end of a biaxial compression test with constant lateral pressure (2,5% of axial strain). The figure in the left consists in an initially homogeneous sample presenting a shear band at the end of the test, the figure on the right consists on the same initial configuration with the addition of geometrical defect in one of the elements: the defect consists on a notch in the central node of an element located in the stress boundary condition contour. The notch has a depth of 10% of the element side length. In the results can be observed that the defect will not trigger a different localization mode, the localization will be exactly the same as in the homogeneous case and the stress-strain curve will also be the same (Fig. 3.3). The identical stress-strain curve can be put down to the fact that the perturbation induced by the notch is outside the localization which governs the macroscale behaviour at the end of the test.

The interest of this test is the fact that a finite perturbation of the initial homogeneous state will not make any difference to the homogenized evolution of the test, the reason of this can be explained by the initial shear strain of the DEM assemblies (Eq. 3.1), which during the equilibration stage "empty step" breaks some of the initial symmetries. This phenomena will be detailed in the next section, in which it has more influence to the global behaviour than the introduced geometrical defect in one element. It will determine the orientation of the band making difficult to have a shear band going across the defect unless the defect is located in a sensitive place.

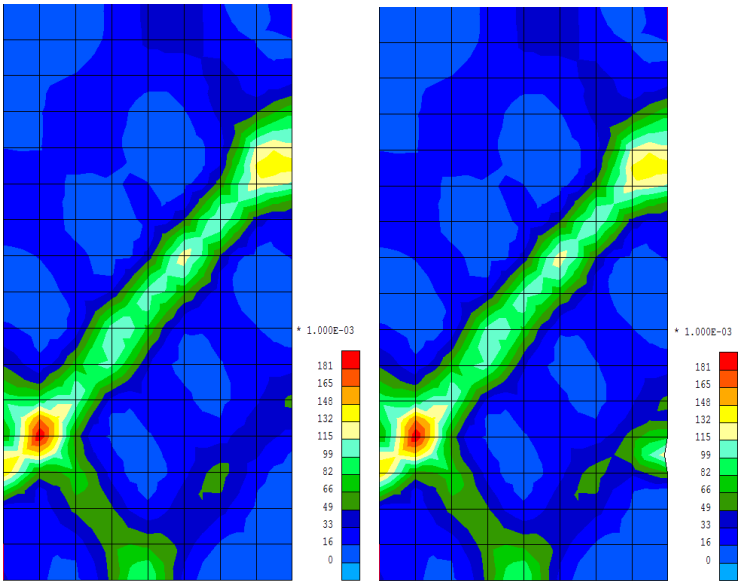

(a) (b)

Figure 3.2: Second invariant of strain for the end of a biaxial test without (a) and with a defect in one element as a localization catalytic (b).

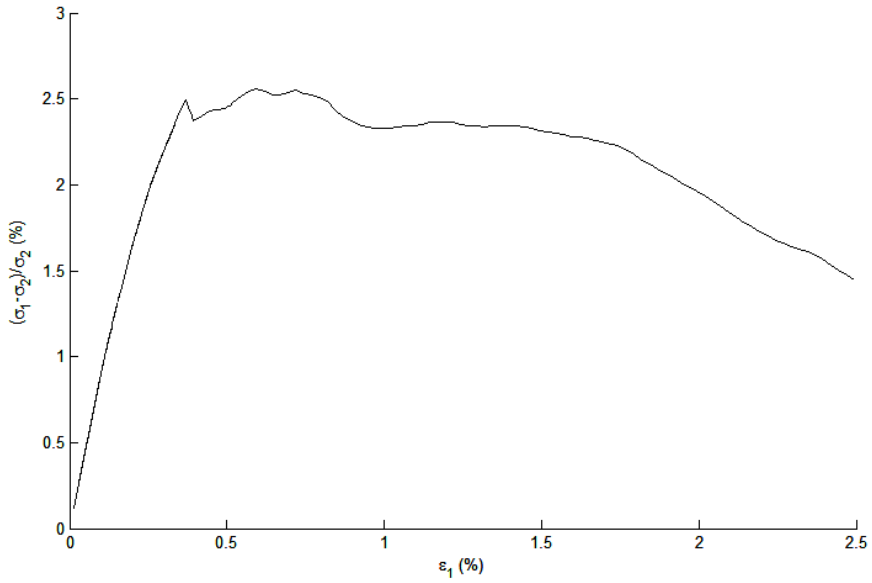

Figure 3.3: Strain stress curves without and with a defect in one element as a localization catalytic. Exactly the same.

$$\epsilon_{kl} = \begin{pmatrix} -0.9999 & 6.2850E-002 \\ 6.2850E-002 & -1.0000 \end{pmatrix} \tag{3.1}$$

Now, the previous biaxial compression test with constant lateral pressure is performed with a higher number of elements (512), with a geometrical defect in the force boundary condition in order to observe the catalysis and evolution of the strain localization due to the defect. The defect has the same characteristics of the previous one in the 128 element test (Fig. 3.1).

A series of plots of the second invariant of strain are presented for different axial strain levels (Fig. 3.4) showing shear patterns starting in the perturbed element with an angle of 50 degrees in both directions[3] (Fig. 3.4). The two high shear areas correspond to two different shear bands triggered at the same time by the notch, it is not a reflection of the same shear band since a stress boundary condition does not produce reflections.

The same test is performed without geometrical imperfection in order to compare the strain localization and evolution of it (Fig. 3.5). Plots of the deficit of compatibility for the norm of the displacement (Fig. 3.6 and 3.7) are also presented in order to compare the convergence of the two The plots show a better convergence for the case with the imperfection. This proves the ability of the imperfection to trigger localization favoring the convergence of the code towards a solution.

[3]This observation agrees with the Mohr-Coulomb failure criterion.

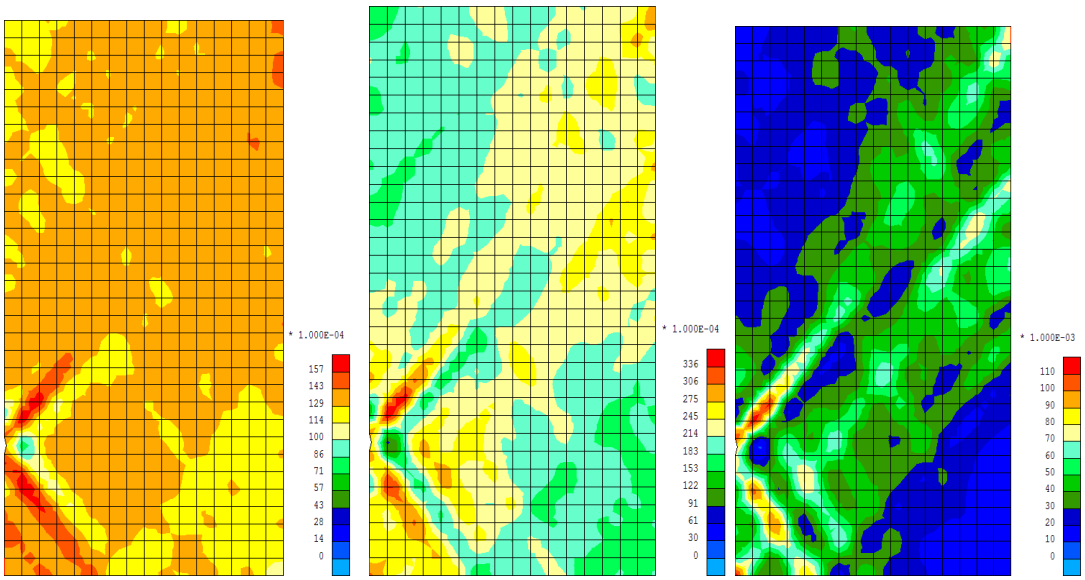

Figure 3.4: Stran localisation catalysis and evolution using a geometrical defect in a 512 element biaxial test. For axial deformation from left to right: 1.10%, 1.45% and 2.50%. Second invariant of strain.

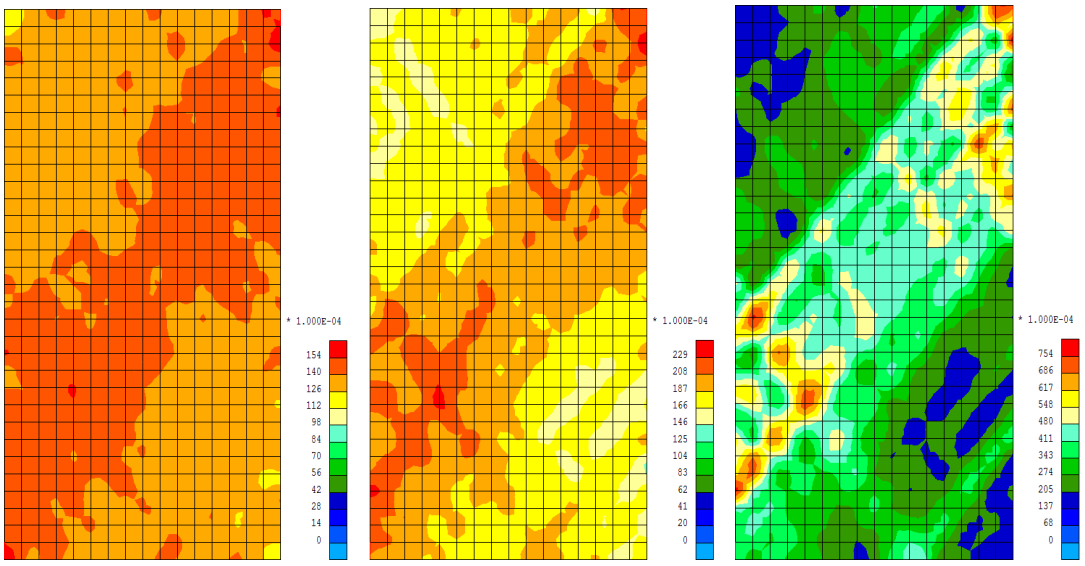

Figure 3.5: Stran localisation catalysis and evolution without geometrical defect in a 512 element biaxial test. For axial deformation from left to right: 1.10%, 1.45% and 2.50%. Second invariant of strain.

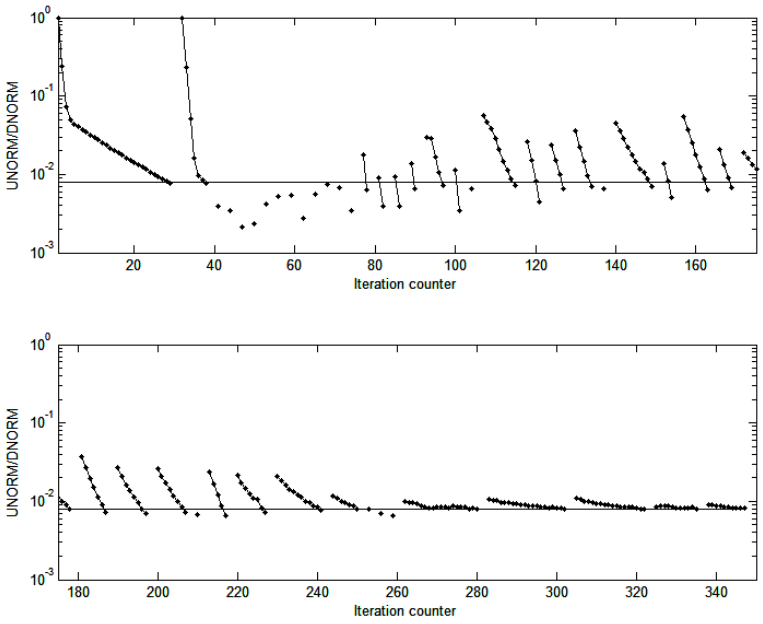

Figure 3.6: Deficit of compatibility for the norm of the displacement (UNORM/DNORM) for a 512 element biaxial test with geometrical defect. Kruyt operator. The horizontal line indicates the precision threshold.

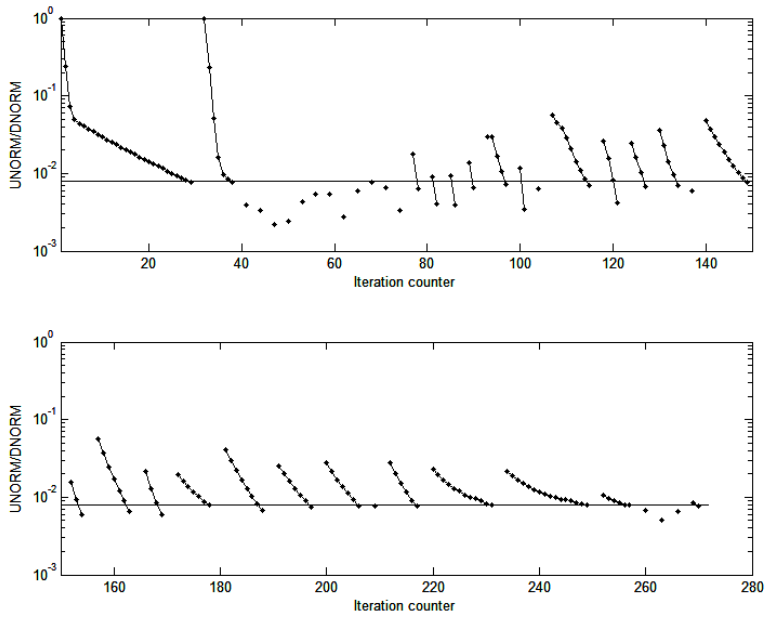

Figure 3.7: Deficit of compatibility for the norm of the displacement (UNORM/DNORM) for a 512 element biaxial test without defect. Kruyt operator. The horizontal line indicates the precision threshold.

3.2.2 Punctual material imperfection

In this subsection the strength of one element will be reduced by action on one DEM microscale.

The catalyzer for the strain localization is a reduction on the interparticle friction coefficient of the DEM assembly in one of the elements, from $\mu = 0.5$ to $\mu = 0.3$ in the element number 4 (Fig. 3.8), differently with respect to the previous case, the weakened element is located in the place where the band is expected to appear because of the sign of the shear stress of the DEM assemblies.

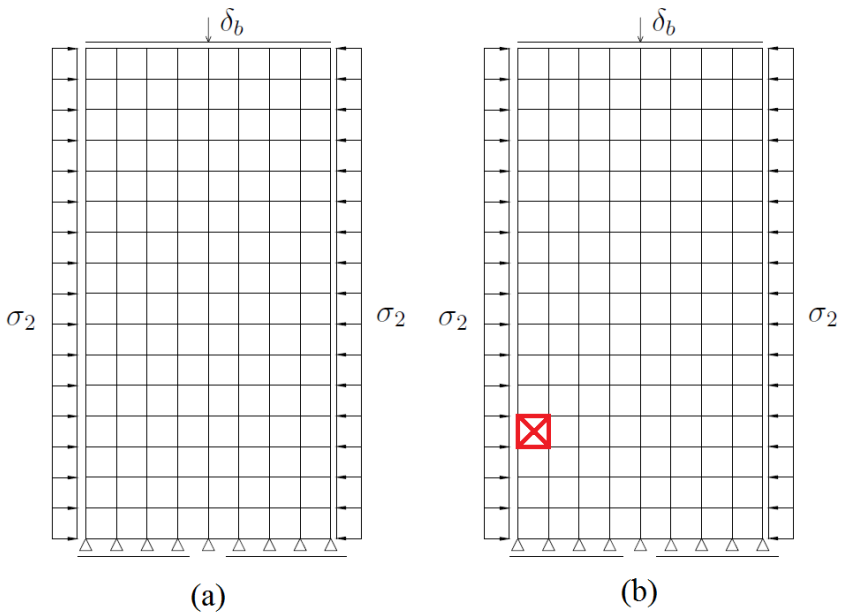

Figure 3.8: Biaxial test geometry and boundary conditions. Full biaxial. 128 Q8 elements. Homogeneous (a) and with material imperfection (b).

A pure DEM biaxial test response is presented for the two different friction coefficients $\mu = 0.5$ and $\mu = 0.3$ (Fig. 3.9)

Comparing the two maps of the second invariant of strain (Fig. 3.10) it can be observed that the weakened element triggers a more advanced state of localization for the same axial strain value (2,5%): 26.4% vs 18.1% for the maximum value of second invariant of strain inside the shear band. This leads to a faster computation and possibly better emulation of real materials with heterogeneous microscale distribution. Later in this chapter, a quantitative study of the simulation acceleration caused by the introduction of heterogeneity is presented.

The strain stress curves (Fig. 3.11) present differences after the bifurcation takes place: the homogeneous sample has a peak stress as the end of the region I elasto-plastic branch, but after several steps the stress increases again, while the sample with a different element presents a more smooth behaviour and reaches softening faster than

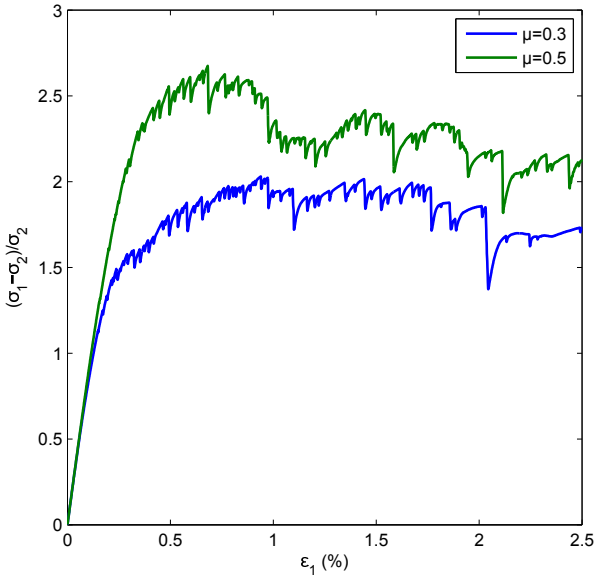

Figure 3.9: Stress-strain response of the same DEM assembly with different friction coefficient $\mu = 0.5$ and $\mu = 0.3$

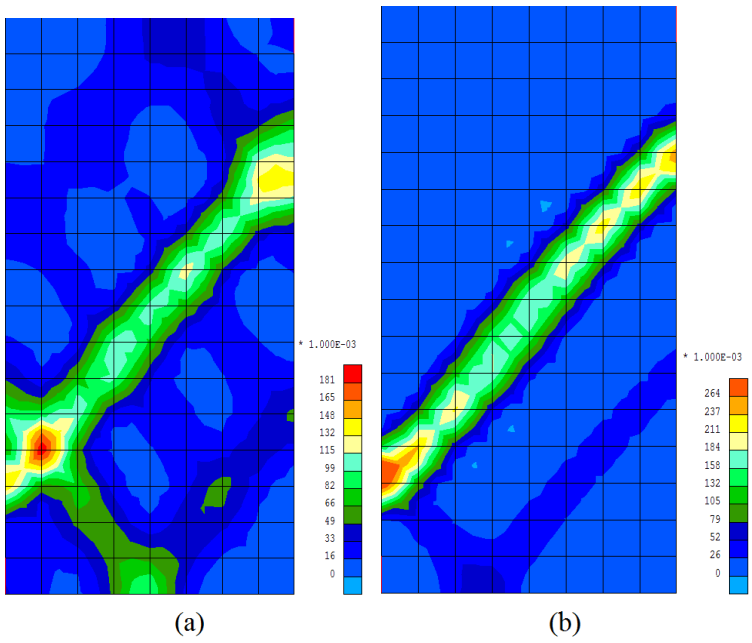

Figure 3.10: Second invariant of strain for the end of a biaxial test. Homogeneous (a) and with a different DEM assembly in one element as a localization catalytic (b).

the homogenous one for strain higher than 1%. At 2,5% of axial strain the homogeneous sample hasn't reached the residual shear stress (Fig. 3.10 (a)), in the other hand, the heterogeneous sample reaches the residual stress value near 1,5% of axial strain due to the faster localization process (Fig. 3.11).

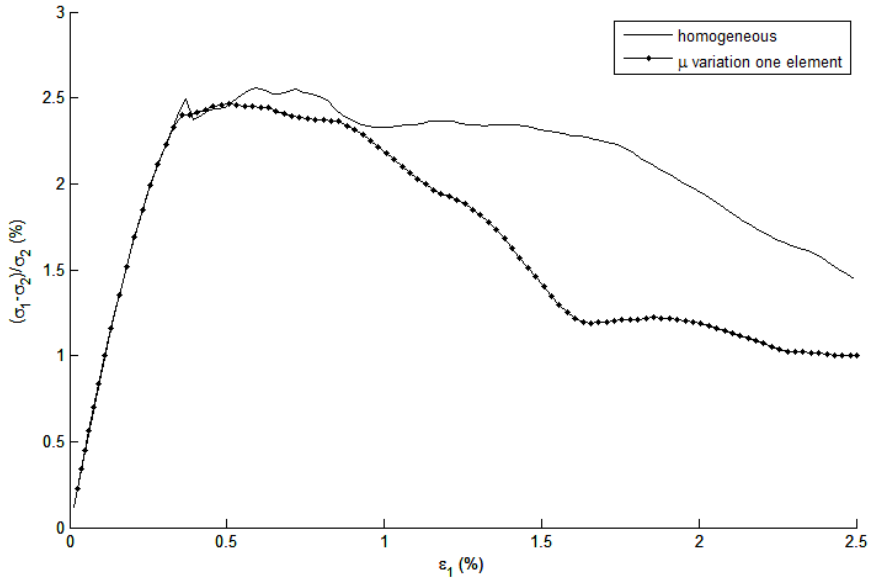

Figure 3.11: Strain stress curves for 1) homogenous and 2) with different DEM assembly in one element as a localization catalytic.

The convergence of the method is improved as well as in the previous tests.

3.2.3 Full field material properties

It has been proved that breaking the homogeneity of the sample will help to trigger strain localization affecting both the physics of the model and the computational cost, i.e. leading to a different stress-strain curve and reducing the wall-time. Following this research direction, a new simulation is prepared, this time introducing a series of different elements (11 elements, 8.5% of the total) along an "arbitrary" orientation (Fig. 3.12).

the DEM assemblies in the elements have the same differential property as in the previous subsection: a reduced contact friction coefficient with respect to the other elements $\mu = 0.3$ vs $\mu = 0.5$.

The result is a faster computation compared to the case with a single different element and a slightly higher value for the maximum strain localization: 27.3% vs 26.4% for one single different element and 18.1% for an homogeneous sample. The localization happens in a faster way than in the homogeneous sample or one different element sample (Fig. 3.14), in the other side, the peak stress is lower than in the previous cases 14% lower with respect to the homogeneous case and 11% lower with respect to the case with one different element, which may be due to the proportion of weakened elements over the

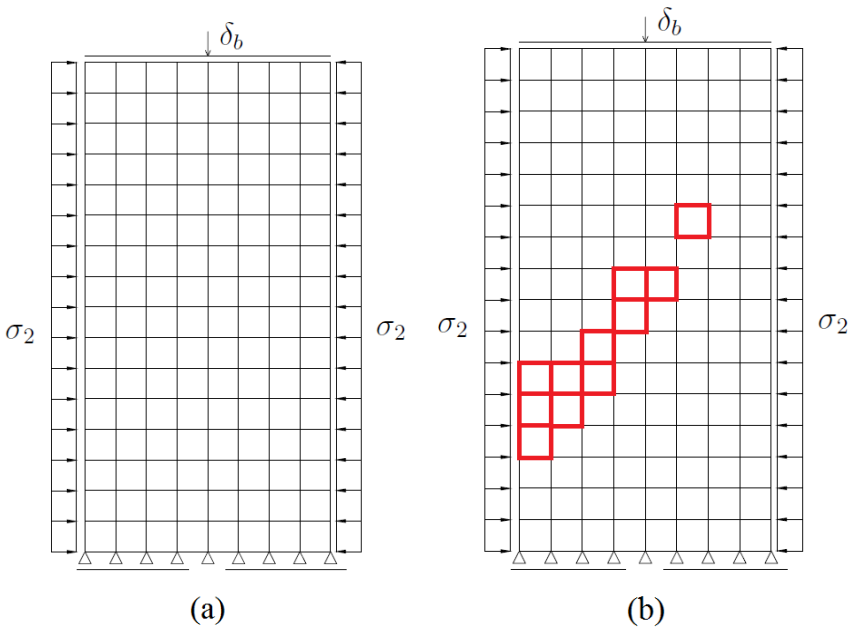

Figure 3.12: Biaxial test geometry and boundary conditions. Full biaxial. Without (a) and with different DEM assemblies in several elements as a localization catalytic (b).

total (8,5%), or weakened elements inside the shear band (62.5%), making an average friction coefficient 25% lower along it.

The previous test (Fig. 3.13) shows that introducing a series of elements with a different property inside the sample can induce strain localization reducing the computational time expenses. But introducing a big number of elements with a different property can also change the average value of the given property. Hence, a comparison with the homogeneous state is not representative anymore. In order to perform a proper study about the effect of heterogeneity introduced by material properties variability, a new series of simulations are prepared: The same sample is filled with 28 different elements, half of them with a decreased contact friction in the DEM assembly and the other half with increased contact friction leading to a non biased average of the friction angle with respect the reference value of contact friction $\mu = 0.5$. This non biased group of elements is "randomly" distributed along a diagonal orientation in order to break the sample spatial homogeneity.

In order to capture the effect of the variability of this zero biased group of heterogeneous elements, a parametric study is carried with the values $\delta = 0.2/0.1/0.05/0.025$ being δ the variability of the contact friction coefficient. The second invariant of strain (Fig. 3.16) shows a more regular and straight shear band for the lower values of δ (nearer to homogeneous state), whit maximum values of shear strain similar for all cases, from less to more homogeneous: 24.3%, 22.3%, 21.7% and 25.2%.

The elements with less contact friction in the DEM assemblies will present sliding

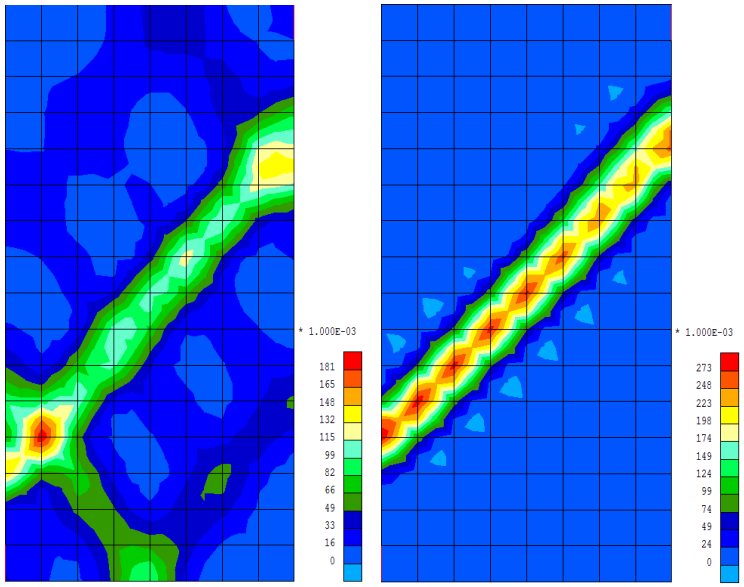

(a) (b)

Figure 3.13: Second invariant of strain for the end of a biaxial test without (a) and with different DEM assemblies in several elements as a localization catalytic (b).

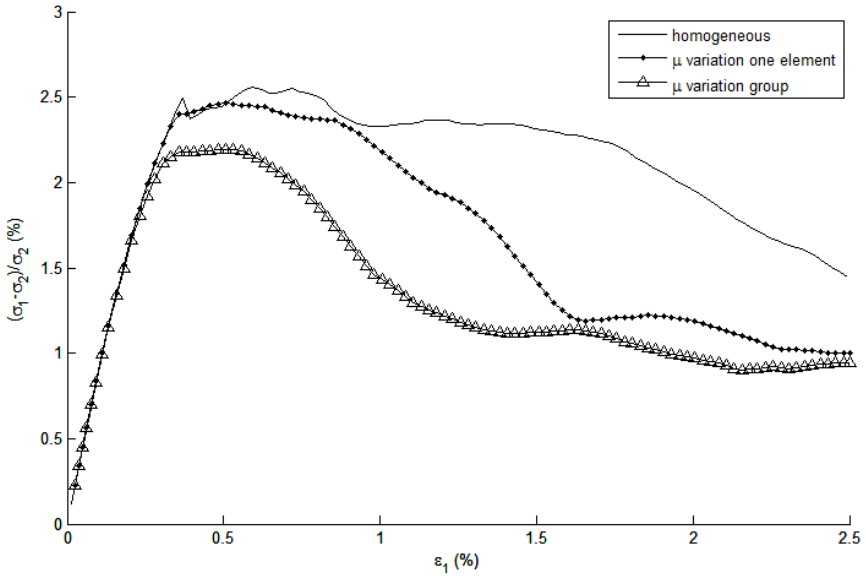

Figure 3.14: Strain stress curves for homogenous and with different DEM assemblies in one element/group of elements as a localization catalytic.

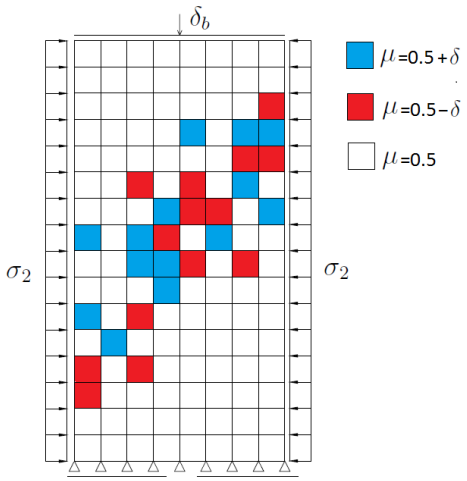

Figure 3.15: Biaxial test geometry, and material point distribution over the elements δ=0.2/0.1/0.05/0.025.

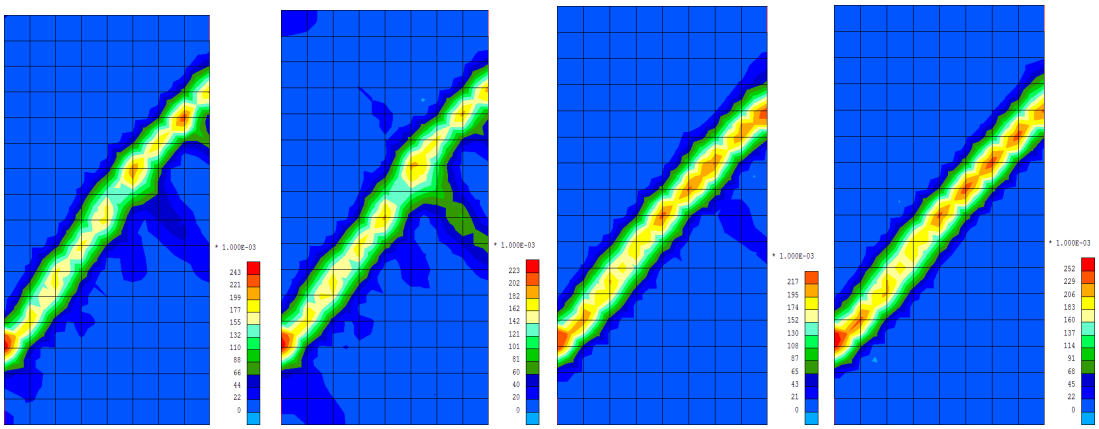

Figure 3.16: Second invariant of strain for the end of a biaxial test for parametric study of material point variability. From left to right: δ =0.2, 0.1, 0.05, 0.025.

contacts earlier, the elements with higher contact friction will be able to withstand more shear without sliding so inducing the strain localization in the already weakened elements. The friction angle differences will also give different contractant-dilatant properties to the concerned DEM assemblies, thus triggering different stress-strain evolution to the macroscale. This autocatalytic process will trigger a strain localization earlier than in the case with a more homogeneous state. Looking at the strain-stress curves (Fig. 3.17) it can be seen that the pre-peak elastoplastic behaviour starts to plastify earlier for the higher values of δ presenting a smoother behaviour at the end of the pre-peak part, more similar to real geomaterials than the simulations with lower values of

δ which present a more brittle behaviour[4]. It's also remarkable that all the simulations present the same residual shear strength, notably due to the non biased average of the friction angle with respect the reference value.

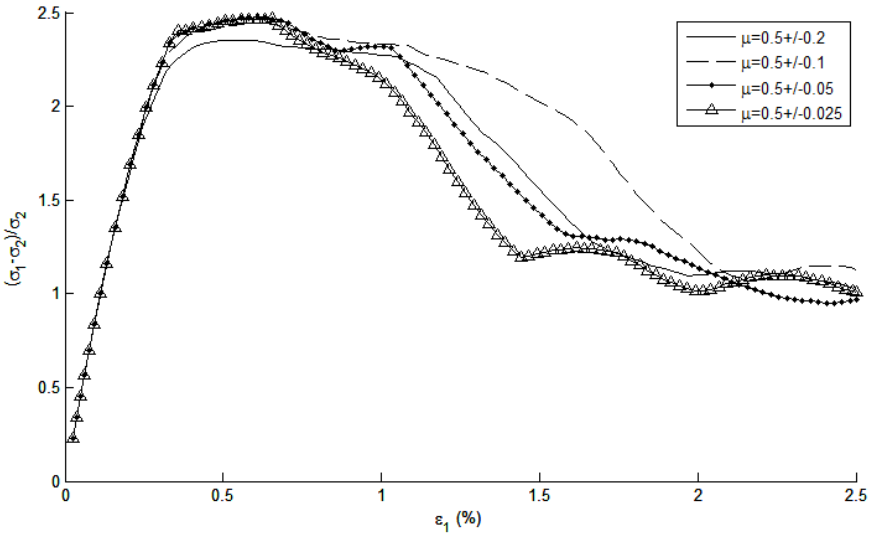

Figure 3.17: Strain stress curves for parametric study of material point variability.

The average peak values for the stress are slightly lower for the cases with higher δ. This can be explained considering that if heterogeneity exists the strain will be concentrated in the weaker elements giving a lower value of the homogenized stiffness although being the average of μ the same across the domain. The early elasto-plastic region I (Roux and Combe, 2002) and the residual shear stress part for large strain are similar or identical in all simulations, the main effect of the element variability is during the localization process. It's worthy remarking that even the case with smallest δ has a typical heterogeneous material behaviour making a difference with the case presented in previous subsections where the value of $\delta = 0$ concluding that any small finite[5] heterogeneity is able to trigger the localization effect earlier than the perturbations introduced by the numerical rounding which is the only responsible of the break of symmetry in homogeneous material cases.

As commented before any help to the localization will help the Newton iterative scheme to go straight to the solution resulting in a faster computation. Quantitative data of computation time is obtained from the present parametric study, the hardware used is a machine with an Intel core i7 2620M processor[6], the results are presented

[4] According to the transition between zones I and II. Roux and Combe (2002), the residual behaviour of region II is not regarded in this comparison

[5] In contraposition to infinitesimal.

[6] Other parameters as the memory are not relevant since this multiscale model is intensive in processor time (integration of the constitutive law), but not in memory usage (the solver deals with a small finite element rigidity matrix, easily factorisable).

together with the previous homogeneous case (δ =0) (Fig. 3.18) showing a decrease of the computation time as the sample increases the inhomogeneity: from 54h for the homogeneous case to 41h for δ =0.1 representing a reduction of 24% of computation time with respect to the homogeneous case.

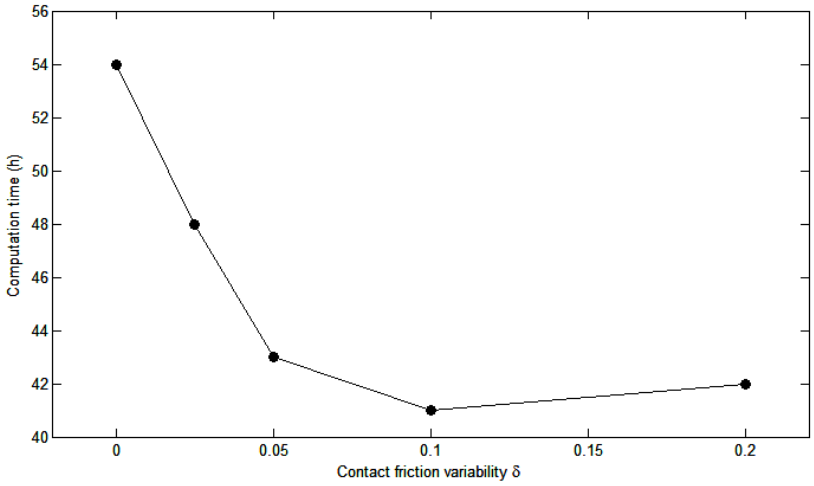

Figure 3.18: Computational time for parametric study of material point variability. The x axis shows the introduced variability parameter δ, zero meaning an homogeneous configuration.

3.2.4 Biaxial test discharge

The previous biaxial test is now discharged till a value of -1% of axial deformation (Fig. 3.19). This test intends to exemplify the ability of the approach to simulate different loading histories and to verify that the residual strength is not influenced by the initial variability. For sake of simplicity only the tests with $\delta = 0.1$ and $\delta = 0.05$ are shown. Both stress-strain curves show a plastic behaviour with a residual value for the deviator of stress near -0.6 (Fig. 3.19).

From the previous results, a Mohr-Coulomb failure envelope can be plotted (Fig. 3.20) this shows a residual friction angle of 18˚and a cohesion of 0.125 stress units.

The second invariant of strain at the end of the test shows the same strain localization as the one created during the compression (Fig. 3.16 and 3.21). A different angle for the shear band would be expected in a extension test starting from an identical initial condition. In this case, the direction is determined by the previous damage created during the compression (rupture of the cohesive bounds)[7].

These tests intend to show the ability of heterogeneous models to simulate complex

[7]Cohesion is considered at the contact level of the discrete assembly, it acts as an attractive force normal to the contact surface. This bounding force can be destroyed according to a contact damage law. Further description of the granular media was presented in (Cha. 2).

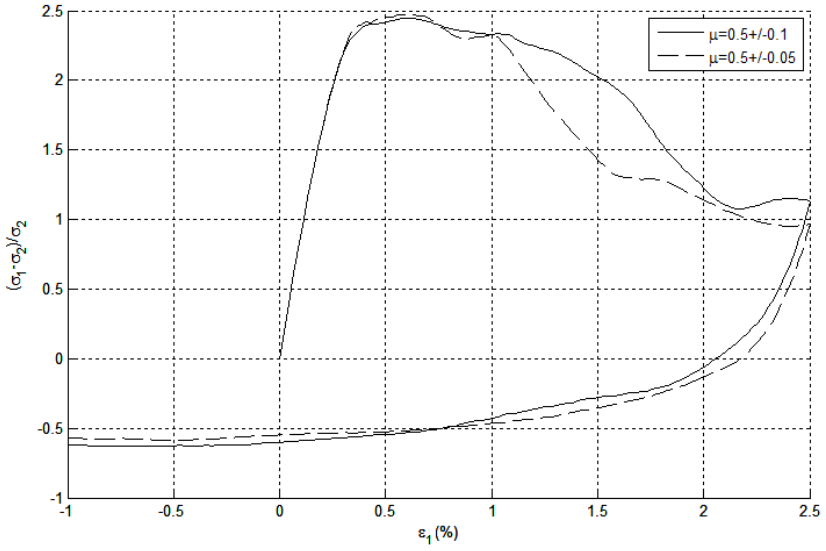

Figure 3.19: Strain stress curves for loading and unloading a biaxial test with constant lateral pressure. Two different contact friction variability in the material point distribution.

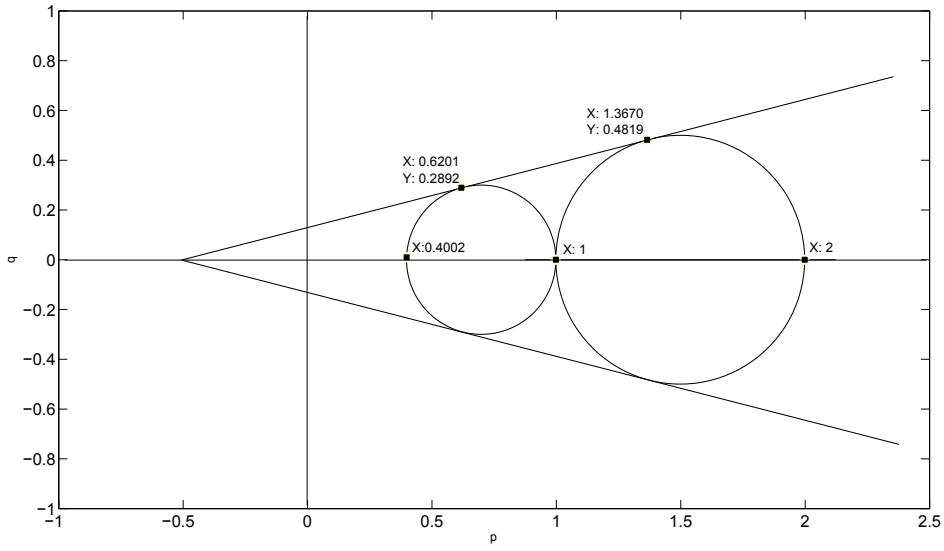

Figure 3.20: Mohr circles and failure envelope in the q-p plane. The failure envelope corresponds to the residual values of compression and extension tests in (Fig. 3.19). Results: residual friction angle 18°and cohesion 0.125 stress units.

loading histories which undergo high strains. The results for this kind of tests show minor differences compared to an initially homogeneous test since the effects of spatial

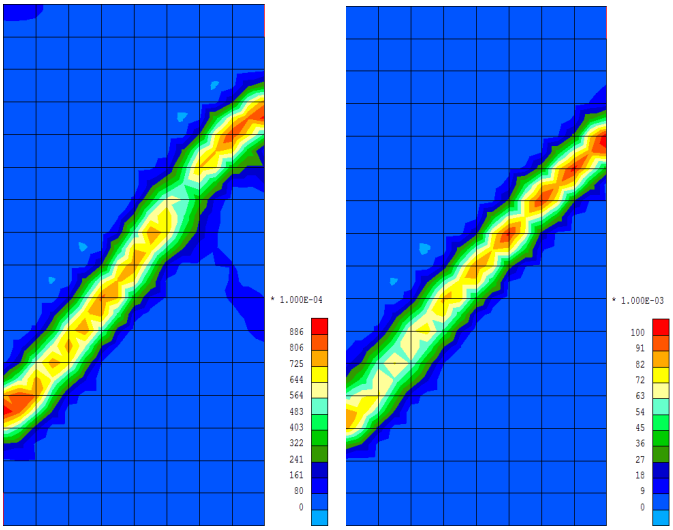

Figure 3.21: Second invariant of strain for the end of an extension biaxial test with constant lateral pressure $\epsilon_1 = -1\%$. Two different contact friction variability in the material point distribution. The plots represent the strain field with respect to the initial configuration with $\epsilon_1 = 0\%$

heterogeneity are more notorious at the beginning of the simulation and during the onset of localization.

3.3 Material properties heterogeneity based on DEM generation

As seen in the previous section, using a continuum mechanics description to solve a boundary value problem will naturally result in a homogeneous description of the domain due to the simplification of the uncertainties. This contradicts the observations of real materials (see e.g. Figure 3.22) which present spatial heterogeneity. This is of importance because the breaking of symmetries will determine the bifurcation unfolding and so the evolution of the problem. The content of this section has been published in (Shahin et al., 2016).

In this sense, the continuum model was enriched with new features to emulate the observed heterogeneity, i.e, give some variability to some parameters across the material points. This was made in the same manner as it could be done in classical analytical FEM model, i.e., modifying some of the phenomenological parameters that describe the constitutive law. The FEMxDEM approach has an advantage with respect to classical FEM when dealing with spatial heterogeneity, the desired heterogeneity can be introduced by generating different DEM assemblies but keeping the same microscale parameters, this results in DEM assemblies that are representative of the same material but present different behaviours due to the different arrangement of the particles in each

cell, in a similar way to real materials.

In this section this feature will be exploited, a series of parametric studies will be carried and the effect of the different arrangement of the heterogeneity studied. The AEO (Auxiliary Elastic Operator)[8] will be retained in this study for the Newton method.

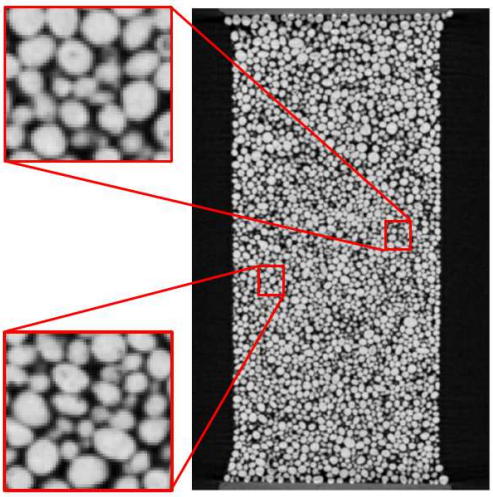

Figure 3.22: A CT scan of dry sand laboratory sample (Andó, 2013). Differently from numerical models, real materials exhibit spatial heterogeneity.

The efficiency of the method has been explored through several study cases, basically consisting of monotonic compression biaxial test (Kaneko et al., 2003; Miehe et al., 2010b; Andrade et al., 2011; Avial and Andrade, 2012; Nguyen et al., 2014; Guo and Zhao, 2014), cyclic simple shear tests (Guo and Zhao, 2014), hollow tube test (Desrues et al., 2015), and slope stability test (Meier et al., 2008). These numerical experiments were run using both cohesive and disperse materials and considering only a single DEM granular assembly to represent the material microstructure constitutive behaviour over the whole specimen.

The scope of the study is to explore the effect of spatial variability by generating different DEM assemblies in the different elements of the FEM discretization.

3.3.1 DEM assembly generation

The assembly is formed of 400 particles, consistently with the guidelines provided by Nguyen et al. (2013, 2014) and Guo and Zhao (2013, 2014). This choice constitutes a good compromise between the computational cost and the problem stability. In order to obtain homogeneous assemblies, the preparation procedures were performed in the absence of gravity, and Periodic Boundary Conditions were retained in the horizontal and vertical directions (Radjai and Dubois, 2010; Roux and Combe, 2010). In this work, the simulation is focused on a dense frictional granular material (without cohesion). To

[8]It has been previously defined in (Cha. 2).

obtain a dense assembly, the inter-particle friction coefficient has been set to zero during the preparation step as the particles can slide and fill the volume as much as possible. The grain size range has been taken as R_{max}/R_{min}=2.5.

The DEM granular assemblies have been generated following the algorithm proposed in (Radjai and Dubois, 2010; Roux and Combe, 2010). Starting from a given particle size range and a given number of particles, the particles are placed in a regular grid and a random radius is given to each of them, (see Figure 3.23, a). The particles are then submitted to a random velocity field. The particles move and interact as rigid bodies within a fixed size container. No energy dissipation is introduced during this process. When particles have been shaken enough (i.e. each particle is displaced cumulatively 100 times its diameter), their velocity is set to zero, (see Figure 3.23, b). The resultant granular packing, which has a gas-like configuration, is then subjected to a strain-controlled isotropic compression phase leading to the desired granular assembly, (see Figure 3.23, c).

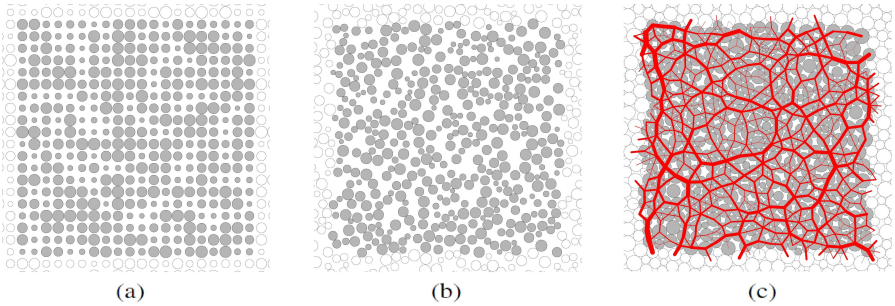

Figure 3.23: The three stages of the granular assembly preparation with Periodic Limit Conditions. (a) The ordered configuration of the assembly, (b) the granular assembly after shaking, and (c) the final configuration after the isotropic compaction of the granular assembly.

Following these procedures, more than 20 granular assemblies have been generated using the material mechanical properties presented in Table (Tab. 3.1). As stated before the different generations are given the same material properties in the contacts but present different grain sizes and arrangement due to a different initial generation. Since the objective of this study is to investigate the consequences of using different DEM assemblies, each of these granular assemblies will be given an identity based on the criteria that are presented in the following subsection.

3.3.2 Granular assembly identity and selection criteria

Radjai and Dubois (2010) introduced a number of criteria to determine the identity of a given granular assembly. They defined a set of "*internal variables*" that distinguishes one granular assembly from another. Among these variables, packing fraction (PF) and coordination number (CN) have been retained hereafter. The packing fraction describes the proportion of solid volume to the overall assembly volume, whereas the coordination

Table 3.1: The given values of DEM mechanical parameters. κ is the normal stiffness coefficient normalized by confinement pressure P. Damping coefficient is a proportion of, η, the critical damping of contact system.

Parameter	Value
Normal stiffness coefficient $\kappa = K_n/P$	1000
Tangent/Normal stiffness coefficients K_t/K_n	1
Coulomb friction	0.5

number represents the average number of inter-particles contacts per particle in the packing. If N_c is the total number of contacts, and n is the number of particles in contact, then $CN = 2N_c/n$.

The generated assemblies present a Gaussian distribution of PF and CN that can be characterized as PF= 0.8157±0.004 and CN=4.153±0.015. Being the first vale the mean and the second value the standard deviation.

As aforementioned, the idea of using different granular assemblies is to represent the configuration variability of the microstructure in a soil sample, separately from any deviation in the mechanical properties. Thus, the selection of the granular assemblies has to be conducted independently from their mechanical properties. Given that the mechanical properties of the assemblies does not show a correlation with PF and CN in the proposed sample, considering PF and CN as selection criteria can offer such sort of independency. The assemblies corresponding to the mean value ± a standard deviation of PF and CN have been selected. The assemblies corresponding to the mean value of PF plus/minus a standard deviation are denoted PF-A/PF-B, respectively. Whereas, the assemblies corresponding to the mean value of CN plus/minus a standard deviation are denoted CN-A/CN-B, respectively.

Another significant variable is considered. In the preparation procedures, the compaction process is conducted as the normal strain components are imposed, but not the shear strain component. Instead, null shear strain is imposed (i.e. orthogonal wall driving). Even though, at the end of the preparation stage, the obtained assemblies always show a deviation from isotropy. Equation 3.2 shows a comparison between the target stress state (left matrix) and the homogenized internal stress state using Equation 3.3 (right matrix) for an arbitrarily chosen packing from the generated assemblies. The deviation from isotropy can be attributed to the discrete nature of DEM. This deviatoric stress component will affect the double-scale computations of FEM×DEM, as it introduces an initial bias to the simulation specimen (Guo and Zhao, 2014).

$$\begin{pmatrix} 1 & 0 \\ 0 & 1 \end{pmatrix} \neq \begin{pmatrix} 1 & +0.07591 \\ +0.07591 & 1 \end{pmatrix} \tag{3.2}$$

$$\sigma_{ij} = \frac{1}{S} \cdot \sum_{(p,q)\in c} f_i^{q/p} \otimes l_j^{p/q} \tag{3.3}$$

Where S is the area of the assembly, $f^{q/p}$ and l^{pq} are, respectively, the interparticle

Table 3.2: The selected DEM assemblies based on the three criteria, packing fraction (PF), coordination number (CN) and remaining shear stress (RS), for microstructure representation in multi-scale simulation.

Notation	Meaning	Target Value	Actual values		
			PF	CN	RS
PF-A	Mean+STD	0.8193	**0.8194**	4.1474	0.0445
PF-B	Mean-STD	0.8122	**0.8129**	4.1575	-0.0206
CN-A	Mean+STD	4.1685	0.8150	**4.1701**	-0.0081
CN-B	Mean-STD	4.1381	0.8147	**4.1376**	0.0015
RS-A	Maximum	0.0759	0.8125	4.1705	**0.0759**
RS-B	Minimum	0.0015	0.8170	4.1399	**0.0079**

forces and the branch links of the p, q grains. c is the set containing all the contacts in the granular assembly.

In the following, this deviatoric stress component will be termed as "*Remaining Shear Stress*" (RS). To investigate the effects of RS on the interplay between the micro and macrostructure, it has been considered as a third selection criterion. The assemblies corresponding to both the maximum positive and the minimum positive remaining shear stress have been selected and denoted RS-A and RS-B, respectively. In fact, the assembly associated to the minimum RS has already been considered for the CN criterion. Replicating the use of the same assembly might render some difficulties at reading the plots. Therefore, another one has been chosen, namely, an assembly with RS magnitude close to zero. Table 3.2 shows the chosen assemblies and their notation, in addition to the associated values of PF, CN, and RS.

3.3.3 FEM×DEM model set-up

Herein, the idea is to use the FEM×DEM approach to develop a biaxial test simulation. A detailed description of the FEM×DEM model and the applied biaxial test procedures are presented hereafter.

The macroscale of the specimen to be modeled, is discretized into 5×10 Finite Elements mesh (aspect ratio 2). The 8-nodes quadrilateral element with four integration Gauss points (Q8) is retained in the study. The finite element mesh and its boundary conditions are illustrated in Figure 3.24. Each Gauss point in this mesh is associated with a specific DEM assembly. The six DEM assemblies already presented in Table 3.2 will be used for this purpose.

The FEM×DEM numerical study is focused on a standard monotonic compressive biaxial test. In its initial state, the specimen is subjected to an isotropic compression. Thereafter, the horizontal confinement pressure is held constant and the deviatoric stress is imposed through strain-controlled vertical compressive loading, for more details see e.g. Desrues and Viggiani (2004).

The numerical procedures of both FEM and DEM methods imply the choice of a set

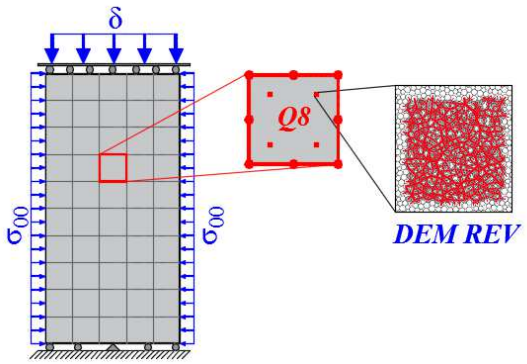

Figure 3.24: The finite element model and its boundary conditions used at the macroscale level of the multi-scale simulation specimens of aspect ratio 2 discretized using (5×10) 50 Q8 finite elements.

of computational parameters which plays a major role on the efficiency of the analysis: the convergence rate at the macro and computation velocity at the micro scale. These parameters are the inertial number (IN) and the level of equilibrium (LE) for the DEM scheme, the perturbation magnitude (PM) and the precision level (E_F and E_D) for the FEM scheme. These parameters were identified via a sensitivity analysis that can be found in (Shahin et al., 2016)and summarized in Table 3.3.

Table 3.3: The adopted computational parameters values based on the performed sensitivity study.

IN	LE	PM	ED|EF
1.0E-4	2	15.0E-6	0.01|NA

3.3.4 Homogeneous configuration

In this part, several FEM×DEM biaxial test simulations are performed using the DEM assemblies introduced in Table 3.2. A unique DEM assembly is used in each simulation, thus obtaining an initially homogeneous specimen having the same mechanical properties over the entire domain. Before conducting the FEM×DEM simulations, the behaviour of the used DEM assemblies is investigated by means of pure DEM simulation of biaxial test. These simulations describe the behaviour of the material itself and they will be used for comparison with the multi-scale FEM×DEM simulations that exhibit, after strain localization, a structural behaviour rather than material behaviour.

The behaviour of the material used in our numerical experiments is first explored through a pure DEM simulation. Each DEM assembly is subjected to a biaxial loading path up to 8% axial strain. Figure 3.25 shows the global response of the six assemblies plotted as a function of the deviatoric stress q normalized by the confinement pressure

σ_{00} versus the applied axial strain. The deviatoric stress is computed as $q = \sigma_1 - \sigma_2$, where σ_1 and σ_2 are the vertical normal stress and the lateral normal stress, respectively. The obtained results show that all cases exhibit, after a pre-peak smooth response, global strength loss which is a characteristic of strain softening behaviour. The strong fluctuations observed in the post-peak part of the curves can be attributed to the relatively small number of particles (400 particles) that leads to a series of sudden contact rearrangements along the deforming process. Despite these differences in the strength peak, all assemblies tend to a similar level of residual strength (plateau around q/σ_{00}=0.9).

The pure DEM simulations show that they have different strength peaks; the resultant normalized deviatoric strength peaks vary from 1.3 to 1.8. This divergence in the granular assemblies behaviour comes only from their geometry differences. Subsequently, these observations show that geometry differences have strong effects on the mechanical properties of the granular assembly.

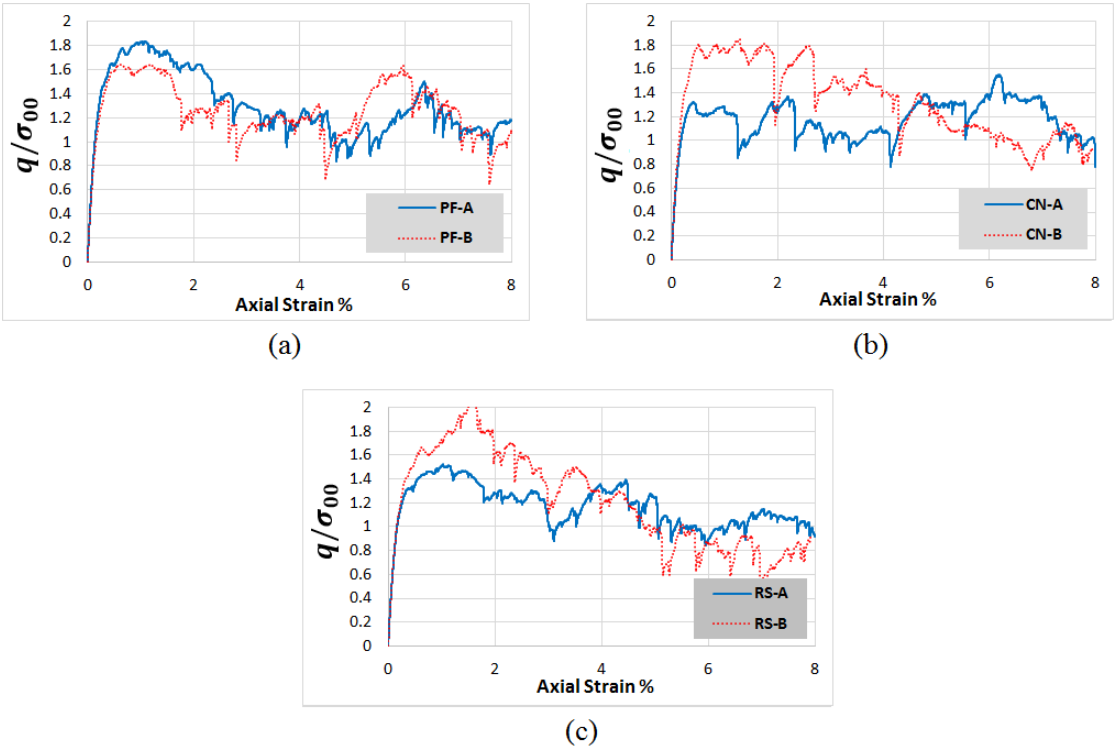

Figure 3.25: Pure DEM simulations of monotonic compression biaxial test up to 8% axial strain performed on six different DEM assemblies of identical material properties but different with respect to geometry (different particles positions and grain size distribution). (a) PF-A and PF-B, (b) CN-A and CN-B, (c) RS-A and RS-B.

FEM×DEM simulations

Each DEM assembly is then used for the initially homogeneous FEM×DEM simulations. The numerical specimen is subjected to a biaxial loading path up to 8% axial strain. Figure 3.26 shows the global response of the six FEM×DEM specimens compared with the pure DEM simulations. In this figure, all the cases show that each FEM×DEM specimen has the same mechanical response as the associated DEM assembly up to the strength peak. In contrast, the post-peak response of FEM×DEM specimens show a clear divergence from the DEM simulation. Indeed, beyond the peak, strain localization starts to develop, which explains the divergence from the material behaviour. Moreover, while the response of the DEM assembly strongly fluctuates, the FEM×DEM specimen exhibits a smoother response. This can be attributed to the averaging effect of the FEM domain over the inherently noisy responses of the different DEM assemblies involved in the structure, especially those associated to the Gauss points that lie in the shear band zone. At the end of the test, the FEM×DEM specimen and the DEM assembly tend to a similar residual strength plateau.

Figure 3.27 compares the six FEM×DEM simulations. It can be observed that even with different strength peaks, all the FEM×DEM simulations tend to a similar residual strength level (around q/σ_0=0.9). This result is consistent with what is classically observed in DEM modeling: for large strain, the mechanical behaviour of granular material is mainly ruled by the particle shapes and the inter-granular angle of friction (Saint-Cyr et al., 2012).

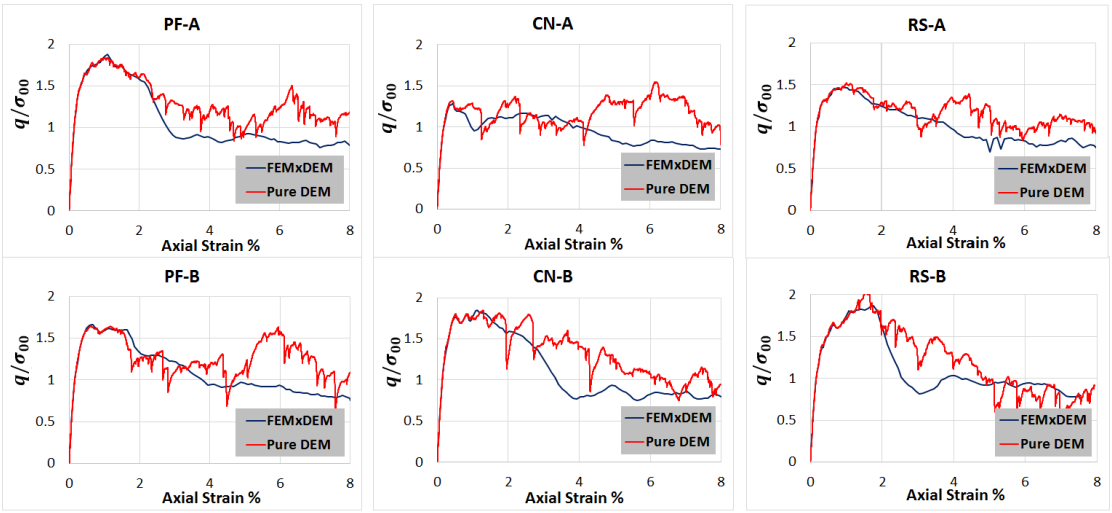

Figure 3.26: A comparison between the global responses of the homogeneous FEM×DEM simulations with the pure DEM simulations of the corresponding DEM assembly in biaxial test simulations up to 8% axial strain.

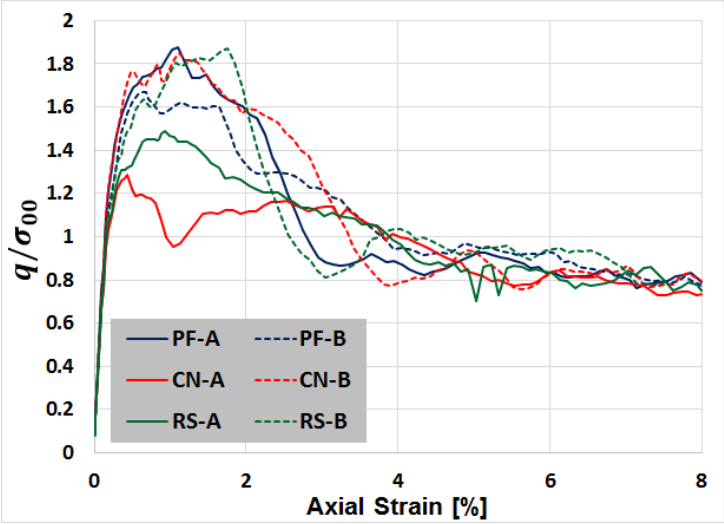

Figure 3.27: Global responses of six homogeneous specimens in a biaxial test up to 8% axial strain simulations. The used DEM assemblies, for microscale, are identical with respect to material properties but different concerning the geometry.

3.3.5 Heterogeneous configuration

So far, a single DEM assembly has been used in each FEM×DEM simulation. The use of a unique DEM assembly over the entire mesh implies a uniform representation of the microstructure and leads to an initially homogeneous specimen. However, the experimental evidence shows that a geomaterial sample presents a variety of microscopic structures, see Figure 3.22. The differences of the microstructure in heterogeneous geomaterials result in a variability of the local mechanical properties which might play a major role in the resulting global behaviour and the formation of the shear band. This part of the work is devoted to this particular issue which is the motivation of the whole study.

Heterogeneous configuration setup

The FEM×DEM approach naturally offers the possibility of taking into account the heterogeneous nature of geomaterials. The variation of the local mechanical properties, originating from the microstructure, is then introduced into an FEM×DEM simulation by using several DEM assemblies, representative of the same material but with geometrical differences, (see Table 3.2). This approach allows to enhance the original model by embedding heterogeneities while the microscale material properties are the same. To simplify this investigation, the heterogeneity has been introduced in the following FEM×DEM simulations by using two different DEM assemblies. The way the two DEM assemblies interplay with the macroscale continuum is investigated hereafter.

Based on the selection criteria introduced in Section 3.3.2, the set of the six DEM assemblies was split into three groups: PF group (PF-A and PF-B), CN group (CN-A

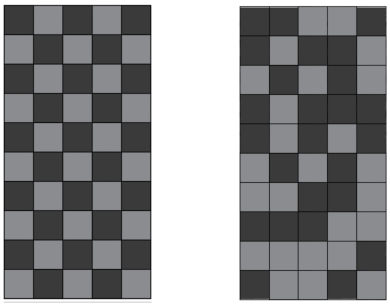

Figure 3.28: The checkerboard pattern and the random distribution pattern of the inhomogeneous specimens. The dark gray refers to the elements that were associated with the "Strong" DEM assembly, whereas the light gray refers to the elements that were associated with the "Weak" DEM assembly.

Table 3.4: The six DEM assemblies split into three different subsets. The dark gray and the light gray refer to the strong and the weak DEM assembly, respectively.

	PFG	CNG	RSG
Strong REV	PF-A	CN-B	RS-B
Weak REV	PF-B	CN-A	RS-A

and CN-B), and RS group (RS-A and RS-B). Each group is referred as PFG, CNG, and RSG, respectively. In Table 3.4, the granular assemblies in each group were distinguished into "Strong" and "Weak" DEM assemblies according to their strength peak, (see Section 3.3.4). The granular assembly with the higher strength peak is referred as "*Strong*" DEM assembly (i.e. PF-A, CN-B, and RS-B), whereas the assembly with the lower strength peak is referred as "*Weak*" DEM assembly (i.e. PF-B, CN-A, and RS-A), see Figure 3.25.

Each pair of these DEM assemblies is then used in different FEM×DEM simulation. The inplane distribution of the two DEM assemblies is performed following two different patterns: a checkerboard pattern and a random distribution pattern, see Figure 3.28. Consequently, the six inhomogeneous specimens have been used to run a set of biaxial test simulations up to 8% axial strain. Each FEM×DEM simulation will be identified by the name of the associated DEM assemblies group, namely, PFG, CNG, and RSG.

3.3.6 Results and discussion

Figure 3.29 shows the results obtained from PFG simulations with the checkerboard pattern (C-PFG) and the random distribution pattern (R-PFG). Figure 3.29 (a) shows the global response of these inhomogeneous specimens. The global response of the corresponding homogeneous specimens, PF-A and PF-B, are presented in the same figure. This comparison shows that the inhomogeneous specimens yield to identical pre-peak responses. In both cases, the strength peak of the inhomogeneous specimen has been determined by the strength capacity of the weak DEM assembly (PF-B). Furthermore,

the inhomogeneous specimens show a clear divergence in the strain softening behaviour; however, they tend to a similar residual strength. Figure 3.29 (b) and (c) display the cumulative deviatoric strain field at 8% axial strain (the end of the simulation) of the specimens with the checkerboard pattern and the random distribution pattern, respectively. In Figure 3.29 (b) it should be noted that the shear band, although it may seem to reach the left boundary of the specimen at the upper-left corner, is in-fact essentially aligned with the line of light gray elements below this corner. As a result, both cases demonstrate that the strain field has localized in the elements that were associated with the weak DEM assembly (PF-B).

The results obtained from the CNG simulations with the checkerboard pattern (C-CNG) and the random distribution pattern (R-CNG) are presented in Figure 3.30. These results confirm the aforementioned observations regarding the identical pre-peak response and the dominant role of the weak DEM assembly (CN-A) at defining the strength peak of the inhomogeneous specimen. The great dispersion of the mechanical behaviour of the DEM assemblies, used in this set of experiments (see Figure 3.25), provide more pronounced evidence of such role. Also, they corroborate the role of the weak DEM assembly at the definition of the shear band pattern.

Figure 3.31 shows the results of the third set of experiments in which the RSG assemblies were retained. The global response of the inhomogeneous specimens compared with the corresponding homogeneous simulations are presented in Figure 3.31 (a). This comparison confirms the observations made above concerning the capability of the weak DEM assembly (RS-A) at defining the strength peak of the inhomogeneous specimen. Also it confirms that, after a divergent strain softening behaviour, the inhomogeneous specimen shows a similar residual strength level. Figure 3.31 (b) and (c) display the cumulative deviatoric strain field at 8% axial strain of the inhomogeneous specimens of checkerboard pattern and random distribution pattern, respectively. Both cases have demonstrated similar observations regarding the shear band pattern that is determined by an alignment of elements attached with the weak DEM assembly.

Moreover, another feature of the shear band pattern has been obtained in the simulation with checkerboard inhomogeneity: the strain field has localized in two different shear bands reflecting the periodicity of inhomogeneity.

The homogeneous simulations of both CNG and RSG have shown clear differences in the strain softening behaviour; while the homogeneous CN-B and RS-B simulations exhibit brittle behaviour, the CN-A and RS-A simulations are rather ductile. However, the results obtained from the CNG and RSG simulations set reveal that the inhomogeneous models tend to exhibit a more ductile behaviour. This matter can be attributed to the role of the weak DEM assembly, which is of more ductile behaviour, at triggering strain localization and then defining the shear band pattern in the inhomogeneous simulation.

As a conclusion, the use of two different DEM assemblies for the microstructure representation helps the specimen to define its shear band pattern that develops at an alignment of elements associated with the weak DEM assembly. Moreover, the weak DEM assembly triggers strain localization and consequently plays a major role in the definition of the specimen strength peak.

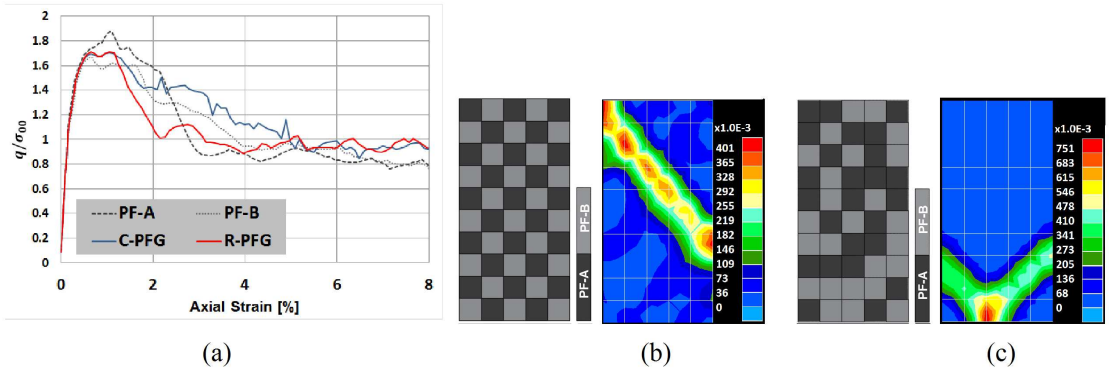

(a) (b) (c)

Figure 3.29: (a) The global response of the inhomogeneous specimen with PF-A and PF-B, DEM response. (b) and (c), cumulative deviatoric strain field.

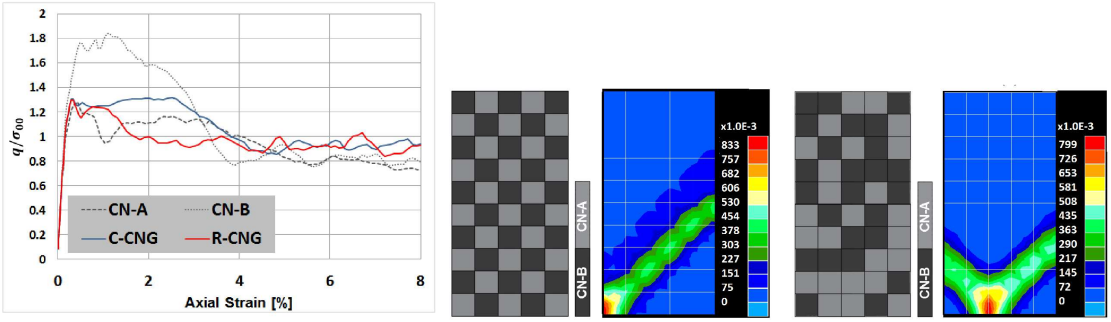

(a) (b) (c)

Figure 3.30: (a) The global response of the inhomogeneous specimen with CN-A and CN-B, DEM response. (b) and (c), cumulative deviatoric strain field.

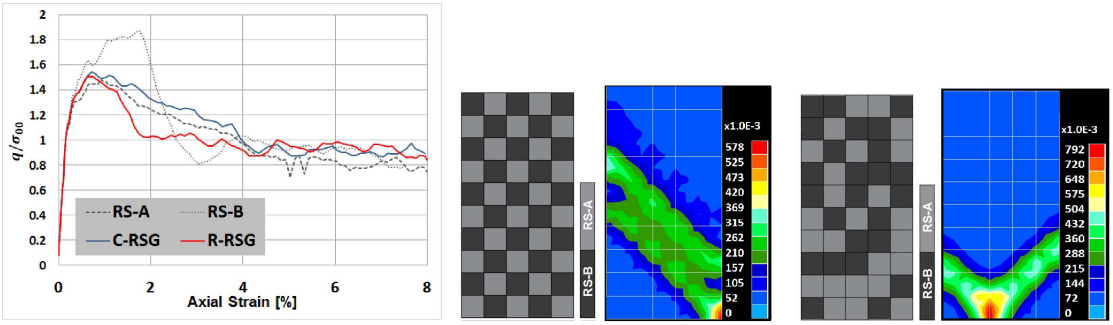

(a) (b) (c)

Figure 3.31: (a) The global response of the inhomogeneous specimen with RS-A and RS-B, DEM response. (b) and (c), cumulative deviatoric strain field..

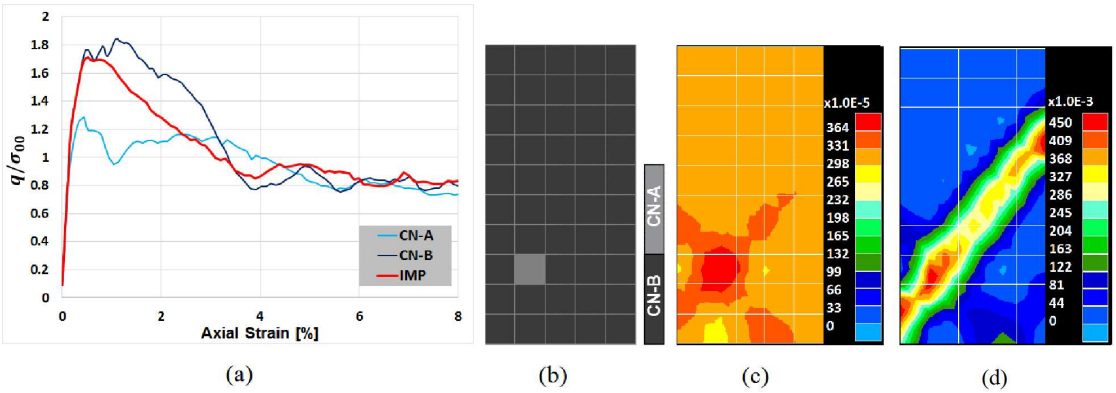

(a) (b) (c) (d)

Figure 3.32: A comparison between homogeneous specimen and a specimen that have been introduced material imperfection by attaching a DEM assembly of weaker strength peak at a single element. (a) Compare the global responses of the imperfect specimen (IMP) and the corresponding homogeneous specimens of the weak and the strong assemblies. (b) show the position of the element which is associated with the weak assembly (light gray). The cumulative deviatoric strain field corresponding to (c) 0.35% and (d) 8.0% axial strain.

3.3.7 Punctual material imperfection

The capability of using several DEM assemblies to capture the intrinsic heterogeneity of geomaterials have been explored in the previous section. In what follows, in the same fashion as done previously (Subsection 3.2.1), a material imperfection, represented by the weak assembly, is introduced into homogeneous simulation.

Experimental evidence show that introducing material imperfection into soil specimen facilitates triggering strain localization and then this imperfection becomes a crucial path of the consequent shear band (Desrues and Viggiani, 2004). The efficiency of simulating this experiment will be investigated using the weak DEM assembly to introduce a material imperfection into homogeneous specimen. The granular assembly set, CNG, has been chosen considering that CN-A and CN-B have shown the greatest dispersion in the microscale mechanical properties (strength peak), (see Figure 3.25, (b)). The imperfection is introduced into the specimen by changing the DEM assembly in a single element. The remaining 49 elements are associated with the CN-B. Figure 3.32 (b) depicts the distribution of the DEM assemblies over the FE mesh. Hereafter, this specimen is referred as (IMP). As in the previous cases, the behaviour of the IMP has been investigated through a biaxial test simulation up to 8% axial strain. Figure 3.32 (a) shows the global response of the IMP specimen; the global responses of the corresponding homogeneous specimens, CN-A and CN-B, have been presented in the same figure as well.

Comparing the IMP response with the homogeneous simulations shows that, after an identical pre-peak behaviour, the IMP yield to a smoother response at and beyond the peak. The weak DEM assembly has not affected the strength capacity of IMP

specimen, as the slight reduction in the strength peak can be neglected comparing to the corresponding inhomogeneous simulations in the previous section.

Figure 3.32 (c) and (d) display the cumulative deviatoric strain field corresponding to 0.35% and 8% axial strain, respectively. As anticipated, it can be observed that the element associated with the weak DEM assembly (CN-A) has triggered strain localization at 0.35% axial strain. Moreover, the consequent shear band passes through the imperfect element as can be seen in Figure 3.32 (d).

It is worthy to mention that the introduction of material imperfection into simulation specimen has a positive effect on the computation time. Table 3.5 displays the time cost associated to both the IMP and the homogeneous CN-B simulations. The introduction of material imperfection has reduced time cost about 35%. This matter can be attributed to the capability of the imperfect element to trigger strain localization and to define the shear band locus along the deformation process. This issue has been extensively studied in (Besuelle et al., 2006). These observations give a first hint to the capability of using different DEM assemblies with the aforementioned specifications to improve the stability of the FEM×DEM simulations.

Table 3.5: The relative time cost of the homogeneous CN-B simulation and IMP simulation.

Specimen	Time cost [%]
Homogeneous CN-B specimen	100
IMP specimen	68

3.4 Conclusion

The consequences of introducing heterogeneity in a FEM model, and more particularly, the macroscale alternating of several DEM assemblies for the microscale simulation in the framework of multiscale FEM×DEM modeling approach have been treated in this chapter.

In a first part, heterogeneity is introduced by spatial variability of macroscale parameters. In a second part, the heterogeneity comes from the generation of different DEM assemblies in the microscale. The DEM assemblies were generated having the same material properties, meaning that the only difference are the grain diameters and contact network arrangement. Despite being the assemblies representatives of the same material, these differences can have a strong effect on the mechanical behaviour of the granular assembly as shown by the pure DEM simulations. The performed homogeneous FEM×DEM simulations have shown a similar behaviour to the respective microscale used, but with a much smoother response.

According with the bibliography, the breaking of symmetries and consequent increase of complication of the model allows FEM×DEM model to better predict the mechanical behaviour of real materials and supposes an increase of computational performance.

In future work, it is worth to consider the following: A FE mesh of 50 elements has been used for second part at the macroscale level and it is of significant importance to reevaluate the findings of this work with a finer FE mesh, as the approach is applied in an element basis, the spacial heterogeneities introduced are mesh dependent, an approach in which the variability is given not according to an element basis, but according to a macroscale space parameter is desired. Another approach to avoid mesh dependency can be the use a regularization technique such as the second-gradient theory; this issue was out of the scope of this study, it will be treated later in this document.

Chapter 4

Second Gradient

Contents

4.1 Introduction

Continuum media from classical mechanics cannot properly reproduce the evolution of materials exhibiting strong heterogeneities in the strain field, e.g. strain localization. Models without a microscale representation cannot properly reproduce the microscale mechanisms that trigger the strain localization, in addition, first gradient relations don't present any length parameter in the formulation, thus resulting in a model without a characteristic length. In problems presenting shear banding, the band will not have an objective width, i.e. it will depend on the size of the mesh. In this chapter, different techniques to introduce an internal length will be presented; microstuctured materials will be retained and in particular Second Gradient models will be illustrated and used along with the FEMxDEM approach. Numerical results showing the abilities of the enriched model will conclude the chapter.

4.1.1 State of the art

It is known that for a strain softening material the initiation of strain localization can lead to an ill-posed Partial Differential Equation (PDE) problem (Hill, 1962; Rice, 1976). The consequence of this ill posedness are numerical instabilities and strain mesh dependency (Pietruszczak and Mroz, 1981; Sluys et al., 1993). Regularization techniques have been developed to overcome these problems, the regularization consists in introducing an internal length that eliminates the pathological mesh dependency; in addition, the introduction of an internal length at the macro-scale allows the model to fulfill the separation of scales (Geers et al., 2010). Both nonlocal (Eringen, 1972) and local (Mindlin, 1965; Germain, 1973) approaches exist. An example of nonlocal regularization in a FEMxDEM model is presented in (Liu et al., 2015). Local formulations use a local relationship between stress and strains in the same manner as classical constitutive relations are defined, in contrast to nonlocal formulations which depend on the neighborhood of the material point.

Second gradient model, as a particular case of the Germain theory (Germain, 1973) has been developed by (De Borst and Mühlhaus, 1992; Sluys et al., 1993; Pamin, 1994; De and De Vree, 1996; Chambon et al., 1998; Matsushima et al., 2000; Chambon et al., 2001; Yang and Misra, 2012). It has been extensively applied in geomechanics and engineering applications with satisfactory results (Collin et al., 2006; Sieffert et al., 2009; Marinelli, 2013; Jouan et al., 2014; Salehnia et al., 2015), these examples use a macroscale phenomenological calibration of the second gradient parameters, another approach is to obtain the second gradient parameters from the microscale in a double scale framework; Kouznetsova et al. (2004) presents a second-order computational homogenization procedure suitable for a multi-scale modelling of macroscopic localization and size effects. The second-order scheme is based on a proper incorporation of the gradient of the macroscopic deformation gradient tensor into the kinematical macro–micro scale transition. The second order terms are obtained from the microscale in the same manner as the first order ones. The first approach, where the second gradient parameters are obtained phenomenologically, is retained in this work. Previous developments of FEMxDEM could not take advantage of Second Gradient regularization due to the poor solution stability and limited available mesh refinement. Recent improvements concerning stability and computational efficiency allow to build a FEMxDEM model including local Second Gradient. This results in an objective model capable of simulating real scale problems with any mesh refinement.

4.1.2 First order model and separation of scales

A first order model uses a constitutive relation of first order between stresses and strains. In the FEMxDEM approach a computational homogenization of the microscale DEM provides this relation (Fig. 4.1).

The principle of separation of scales states: "The microscopic length scale is assumed to be much smaller than the macroscopic characteristic length" (Geers et al., 2010), in a double scale model it can be formulated as eq. (4.1):

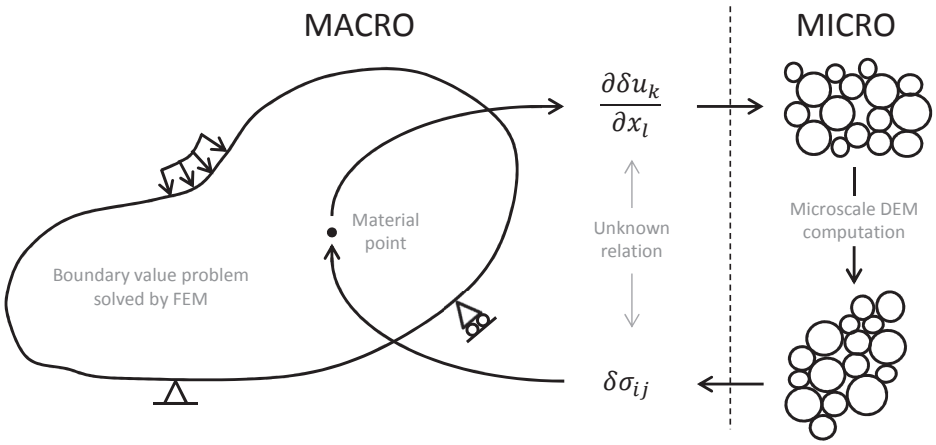

Figure 4.1: First order Computational homogenization scheme

$$l_{discrete} \lll l_{micro} \lll l_{macro} \tag{4.1}$$

Where $l_{discrete}$ can be a length associated to the size of the heterogeneities in the DEM model, assuming that no localization occurs in the microscale this length is the size of the particles, l_{micro} the size of the DEM REV and l_{macro} a characteristic length associated to the strain gradient in the macro-scale.

The left part of eq. (4.1) is fulfilled if the size of the granular assembly is big enough to properly take into account the heterogeneity of the medium, this has not been treated in the present work, the guidelines provided by Nguyen (2013); Nguyen et al. (2014) and Guo and Zhao (2013, 2014) are used instead. Consequently the separation of scales between $l_{discrete}$ and l_{micro} is considered true. Next the limitations are presented:

- The method obeys the principle of local action which automatically fulfills the right part of eq. (4.1) if the strain gradient in the macro-scale is smooth enough. Due to mesh dependency in post-localization this condition is not fulfilled, therefore the approach is not appropriate to model post-localization.

- Due to the lack of scale relation between l_{micro} and l_{macro} the size-effects of the micro-scale have no impact on the macro-scale.

Geers et al. (2010) states that first-order models must be restricted to their field of applicability, second-order models are needed in post-localization regimes.

4.2 Introduction of an internal length

As shown in the previous section, models using a first-order constitutive relation of classical mechanical continuum cannot properly predict the behaviour of a medium with

high strain gradients. Those approaches suffer from non-objectivity due to mesh dependency in localization problems, this also violates the local action principle and so the separation of scales.

Possible causes: the first-order constitutive relation does not give any information about the internal length of the model; due to that, the localization band thickness will tend to shrink to a size proportional to the mesh size. In this way, if the mesh is refined making the size of elements tend to zero in order to get an exact solution, the strain will concentrate in a null size band posing obvious problems.

It's needed to set a relationship between the micro-scale heterogeneity and the macro-scale characteristic length in order to establish a proper micro-scale size effect on the macro-scale. Several approaches exist in the literature, here three methods based on a continuum approach are cited:

- Viscoelastic models: introduce rate dependency which is easy to demonstrate that in transitory problems introduces an internal length, nevertheless, in quasi-static problems the viscous terms do not provide any spatial regularization (Needleman, 1988; Loret and Prevost, 1990).
- Non-local models: use a space averaging around the material points in order to enrich the constitutive relation with second-order terms, nevertheless non-local models do not obey local action principle and can present conflicts in the boundary of the domain.
- Microstructured local models: based on (Germain, 1973) consider a micro-scale continuum enriched with higher order terms, this is further developed in the following.

In order to overcome the problems linked to the loss of ellipticity, mesh dependency and separation of scales, an enriched model with microstructure is proposed, i.e. a local second gradient model (De Borst and Mühlhaus, 1992; Sluys et al., 1993; Pamin, 1994; De and De Vree, 1996; Chambon et al., 1998; Matsushima et al., 2000; Chambon et al., 2001; Matsushima et al., 2002; Yang and Misra, 2012). In the previous section a first-order multiscale FEMxDEM model has been presented in order to set the bases for the second-order approach.

4.3 Large strain Finite element analysis of a local second gradient model

Microstructured material descriptions consider a continuum enriched by higher order terms (Germain, 1973). In this way, the kinematics of the media is enriched by its micro-scale introducing a local dependence on an internal length parameter. This characteristic length (Chambon et al., 1998) regularizes the solution making strain localization mesh independent. A local formulation complies with the principle of local action so it states a stress-strain relationship in the same manner a classical constitutive laws does, this

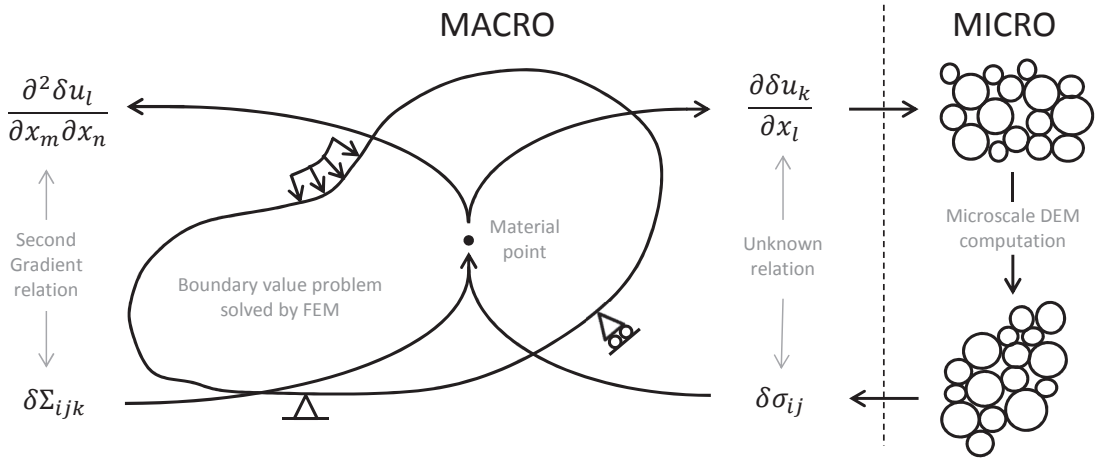

Figure 4.2: Computational homogenization scheme with Second Gradient

Variational principle We start with the weak form of the balance equations written for the strain gradient theory viewed as a particular case of the microstructured continuum theory (Mindlin, 1964; Germain, 1973; Chambon et al., 2001):

$$\int_{\Omega^t} \left(\sigma_{ij}^t \frac{\partial u_i^\star}{\partial x_j^t} + \Sigma_{ijk}^t \frac{\partial^2 u_i^\star}{\partial x_j^t \partial x_k^t} \right) d\Omega^t - \bar{P}_e^\star = 0 \tag{4.2}$$

where, superscripts t and $\star$ denote, quantities at a given time t and virtual quantities, σ_{ij}^t is the Cauchy stress tensor, Σ_{ijk}^t is the corresponding double stress tensor, $u_i^\star$ is a kinematically admissible virtual displacement feld, x_i^t are the current coordinates of the points of the studied body and $P_e^\star$ is the external virtual work generated by the corresponding external forces (Matsushima et al., 2002).

Assuming for simplicity that there is no body double force and that the boundary of Ω^t is regular which means that it is possible to define an external normal in every point of this boundary, external virtual work reads as:

$$\bar{P}_e^\star = \int_{\Omega^t} \rho^t f_i^t u_i^\star d\Omega^t + \int_{\Gamma_\sigma^t} (p_i^t u_i^\star + P_i^t D u_i^\star) d\Gamma^t \tag{4.3}$$

were, f_i^t is the body force per unit mass, ρ^t is the mass density, p_i^t is the external force per unit area, and P_i^t an additional external (double) force per unit area, all applied on a part Γ_σ^t of the boundary Γ^t. D denotes the normal derivative of any quantity q, $(Dq = (\partial q / \partial x_k) n_k)$

The constitutive equations are assumed here to give the values of σ^t and Σ^t as functions of the local kinematic history up to the time t generalizing the classical definition of constitutive equations. This is a very big difference compared to non-local models.

Strong form of the balance equations As usual, starting by (Eq. 4.2), using the divergence theorem and integrations by part allow us to get the strong form of the balance equation the whole continua:

$$\frac{\partial \sigma_{ij}^t}{\partial x_j^t} + \frac{\partial^2 \Sigma_{ijk}^t}{\partial x_j^t \partial x_k^t} + \rho^t f_i^t = 0 \tag{4.4}$$

Similarly the links between p_i^t, P_i^t and the local values (on the boundaries) of the stress and the double stress can be deduced (Mindlin, 1964; Germain, 1973; Mindlin, 1965)

$$\sigma_{ij}^t n_j^t - n_k^t n_j^t D\Sigma_{ijk}^t - \frac{D\Sigma_{ijk}^t}{Dx_k^t} n_j^t - \frac{D\Sigma_{ijk}^t}{Dx_j^t} n_k^t + \frac{Dn_l^t}{Dx_l^t} \Sigma_{ijk}^t n_j^t n_k^t - \frac{Dn_j^t}{Dx_k^t} \Sigma_{ijk}^t = p_i^t \tag{4.5}$$

and

$$\Sigma_{ijk}^t n_j^t n_k^t = P_i^t \tag{4.6}$$

where Dq/Dx_j denotes the tangential derivatives of any quantity q. In the present implementation the double stresses in the boundary are taken as zero:

$$P_i^t = 0 \tag{4.7}$$

$$\frac{Dq}{Dx_j} = \frac{\partial q}{\partial x_j} - \frac{\partial q}{\partial x_k} n_k n_j \tag{4.8}$$

4.3.1 Lagrange multipliers

Unlike classical modelling, the previous way of dealing with second gradient models implies the use of C^1 functions for the displacement field as the second derivatives of the displacement are involved in the variational principle written in (Eq. 4.2). This generates some difficulties when Finite Elements are used to solve boundary value problems. In order to avoid such complexities it is usual to weaken the constraint between a function and its derivatives and to introduce a corresponding field of Lagrange multipliers related to a weak form of the constraint.

So let us introduce, as new independent variables, the derivatives of the displacement field u_i^t with respect to the current configuration, denoted as v_{ij}^t in the following. As usual, the corresponding virtual quantity is denoted as $v_{ij}^\star$.

According to this (Eq. 4.2) is transformed as follows:

$$\int_{\Omega^t} \left(\sigma_{ij}^t \frac{\partial u_i^\star}{\partial x_j^t} + \Sigma_{ijk}^t \frac{\partial v_{ij}^\star}{\partial x_k^t} \right) d\Omega^t - \int_{\Omega^t} \lambda_{ij}^t \left(\frac{\partial u_i^\star}{\partial x_j^t} - v_{ij}^\star \right) d\Omega^t - \bar{P}_e^\star = 0 \tag{4.9}$$

where λ_{ij}^t denotes the field of Lagrange multipliers. The Lagrange multipliers can be interpreted as the so-called microstress in the framework of the microstructured materials (Chambon et al., 2001; Matsushima et al., 2000). Moreover, the fields u_i and v_{ij} have to meet the following weak form constraint:

$$\int_{\Omega^t} \lambda_{ij}^\star \left(\frac{\partial u_i^t}{\partial x_j^t} - v_{ij}^t \right) d\Omega^t = 0 \tag{4.10}$$

It is now natural to write the external virtual power as

$$\bar{P}_e^\star = \int_{\Omega^t} \rho^t f_i^t u_i^\star d\Omega^t + \int_{\Gamma_\sigma^t} (p_i^t u_i^\star + P_i^t v_{ik}^\star n_k^t) d\Gamma^t \tag{4.11}$$

Similarly it is now natural to assume that the constitutive equations give σ^t and Σ^t as functions of the history of u_i^t and v_{ij}^t.

Time discretization: the time step problem The problem of the evolution of a body assumed to obey a local second gradient constitutive equation can now be formulated, with the purpose of building a C^0 finite element model. Considering a body submitted to a given loading path driven by the boundary conditions history, solving the problem is finding the unknown fields u_i, v_{ij}, λ_{ij} in (Eq. 4.9-4.11) for any time t. As well as in (Chapter 2), the loading process is discretized into finite time steps Δt in order to solve the time-dependent problem.

4.4 Numerical simulations

A classical biaxial test with aspect ratio 1:2, constant confining pressure and one node with restricted movement in the center of the base is used to exemplify the second gradient model (Fig. 4.3).

4.4.1 Analytical law FEM model with second gradient

A first series of tests is executed using a FEM discretization of 512 elements and a classical analytical constitutive law: *Plasol*. Plasol was implemented in Lagamine (finite element code ULg) by Barnichon (2007). It is characterized by a linear elastic behaviour and a plastic criteria of Drucker-Prager type (Drucker and Prager, 2013). The Plasol law is chosen because, from the numerical point of view, the similarities between the FEMxDEM model and hypoplastic or elastoplastic finite element codes, and from the material constitutive behabiour point of view, the plastic criteria of Drucker-Prager (frictional-cohesive) of Plasol is of the same nature as the one provided by the DEM microscale.

8 simulations are executed, one without second gradient regularization, and the other 7 with different values of the second gradient parameter D, D=31,63,125,250,500,1000 and 2000, (Fig . 4.4). The objective of these simulations is to calibrate the value of D; since the relation between D and the internal length depends on the unloading stiffness

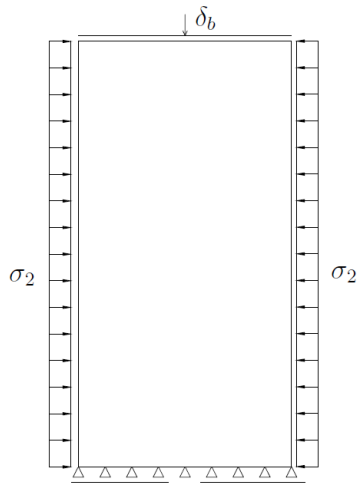

Figure 4.3: Biaxial test geometry and boundary conditions

of the material, which a priori is not known, a series of simulations is needed in order to set this relationship. Doing so with a FEMxDEM model can be very time consuming due to the computational expenses of the model. The biaxial tests with Plasol allow to obtain a first approximation of D with a reasonable time.

The results (Fig. 4.4) show a first simulation without regularization where the width of the shear band is constricted by the size of the elements, which makes the model non-objective and violates the local action principle. The following simulations with an increasing value of the second gradient parameter D present an accordingly increasing shear band width, as expected, proportionally to the root square of the parameter D. Note that small values of D may introduce an internal length that is not bigger than the internal length defined by the mesh size, in those cases the regularization will not have the expected effect on the model since the governing factor is still the mesh size.

In the following the regularization is introduced into a FEMxDEM model.

4.4.2 FEMxDEM model with second gradient

The figure (Fig. 4.5) presents a compression biaxial test with the above geometry and boundary conditions (Fig. 4.3), the model is a first-order approach without any regularization.

The 3 cases correspond to different mesh refinements: 128, 512 and 2048 elements, this gives a characteristic element size of 0.125m, 0.063m and 0.031m respectively. The strain localization has a clear mesh size dependency giving different solutions in each case. Not only the macro-scale strain field will present a different solution but also the fact of concentrating more strain in thiner bands will give as a result some microscales with high strains and those will eventually lose the ability to provide smooth constitutive laws. needless to say that the principle of local action and separation of scales is violated in the 3 cases because the high strain gradients.

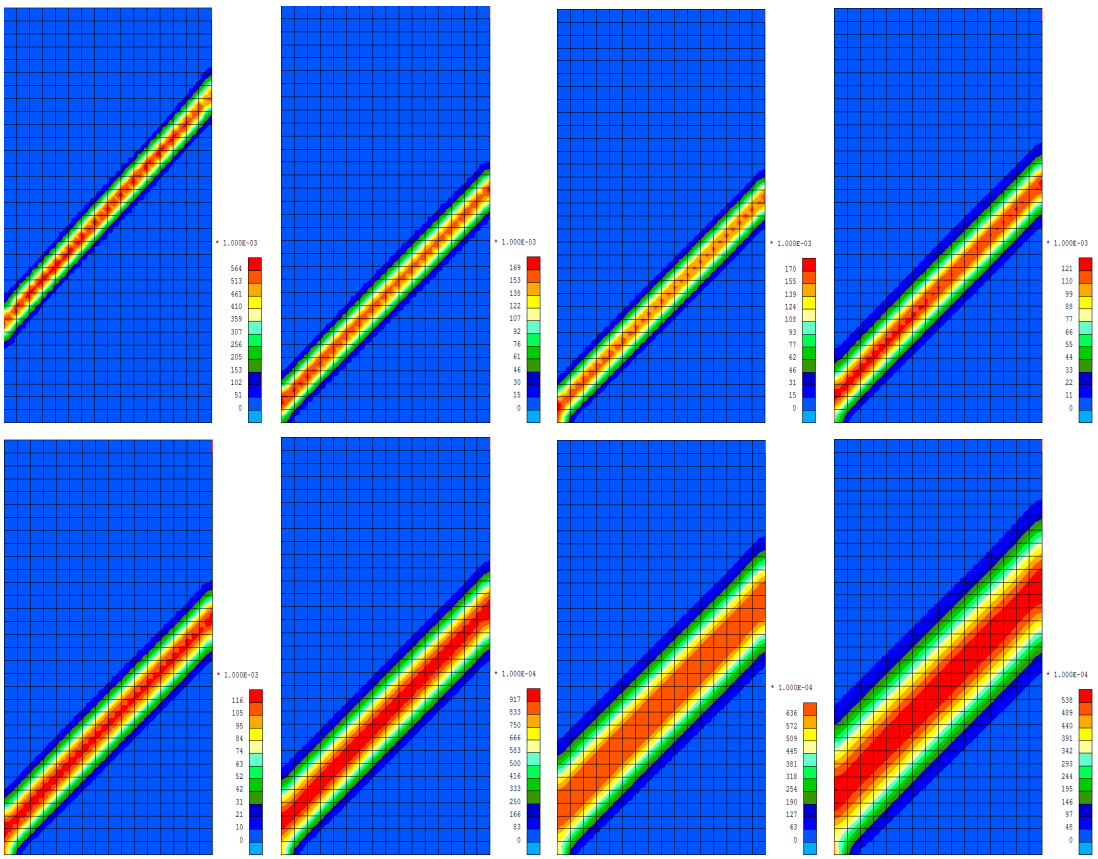

Figure 4.4: Second invariant of strain at 2,5% axial strain (constant pressure biaxial test with 512 elements). Parametric study of the second gradient value D. Respectively: D= no second gradient,31,63,125,250,500,1000 and 2000.

The figure (Fig. 4.6) presents the same biaxial test as in figure (Fig. 4.5) but this time modeled with a second-order model enriched with a local Second Gradient approach. Despite the different localization mode in the case with 128 elements, the 3 cases show a virtually equal characteristic localization length. This gives the freedom to refine the mesh as needed in order to get closer to the exact solution of the BVP. The different localization mode of the test with 128 elements may be triggered by a characteristic length introduced by the Second Gradient terms not far enough from the mesh characteristic size. Nevertheless the provided solution is one of the possible ones. In this case the strain gradient is controlled by the Second-order terms rather than by the mesh size, allowing this to properly limit this gradient and account for local action principle and separation of scales.

A compression biaxial test with second gradient enrichment shows how the regularization turns the shear band patterns independent from the mesh size (Fig. 4.6). This regularization not only enriches the physics of the model but also accelerates the simu-

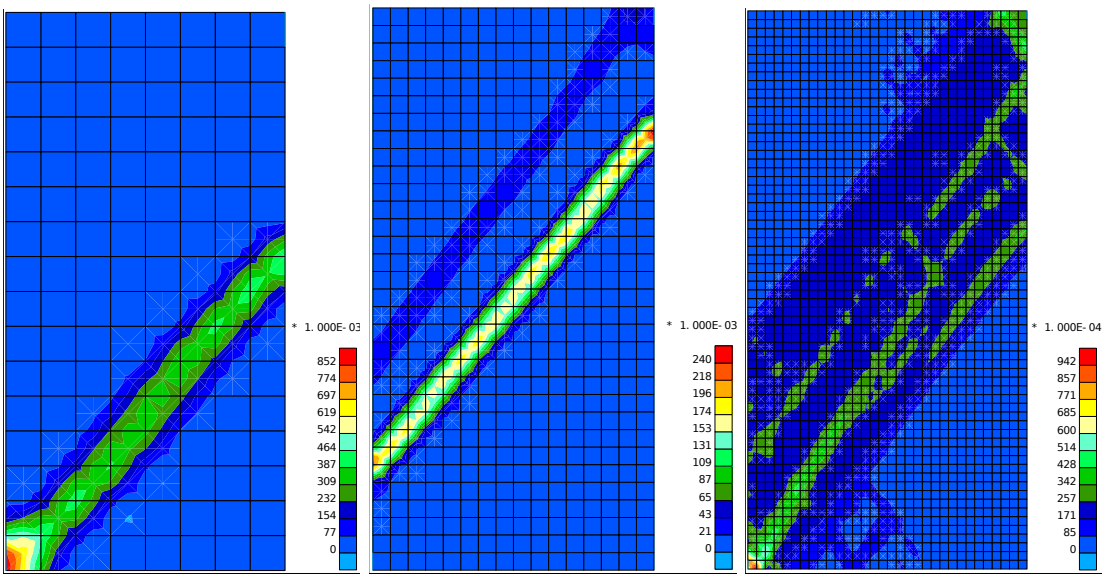

Figure 4.5: Biaxial compression test with different mesh size: 128, 512 and 2048 elements. Mesh dependency and a strong influence on the solution can be observed. Second invariant of strain.

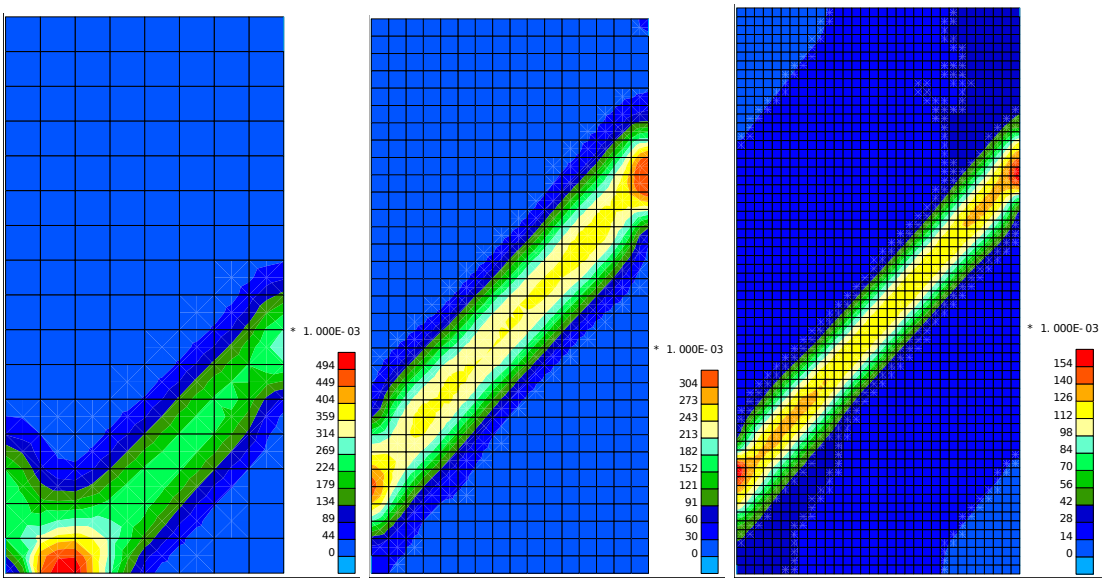

Figure 4.6: Biaxial compression test with different mesh size: 128, 512 and 2048 elements. Band width independent of mesh size. Second invariant of strain.

lation because of an improvement of the iterative efficiency, i.e. a regularized problem has less possible solutions meaning that the Newton scheme will converge faster.

4.4.3 Onset of localization

The same test with 512 elements is simulated twice with a different value of the second gradient D parameter. The purpose is to use small values of D which have shown not to introduce an internal length bigger than the one defined by the mesh and determine if this has or not any effect on the simulations. Two values of D are used: $D = 2.04 \cdot 10^{-2}$ and $D = 5.12 \cdot 10^{-3}$.

Plot (Fig. 4.7) shows the onset and evolution of a shear band for the test with $D = 2.04 \cdot 10^{-2}$, at the very beginning other bands seem to form in the opposite orientation but very soon the strain localizes in one unique band. The convergence profiles for the forces (Fig. 4.8) and displacements (Fig. 4.9) show that the governing criteria for the convergence are the forces, with a value of 1200 accumulated iterations to reach a deformation of 1.88%.

Plot (Fig. 4.10) shows the onset and evolution of a shear band for the test with $D = 5.12 \cdot 10^{-3}$, compared to the previous this has a different initiation of the localization, conjugated bands in 2 orientations will develop at the same time at least till a deformation of 1.88%. The convergence profiles for the forces (Fig. 4.11) and displacements (Fig. 4.12) show, as well as in the previous case, that the governing criteria for the convergence are the forces, with a value of 690 accumulated iterations to reach a deformation of 1.88%.

The parameter D with an associated internal length smaller than the one introduced by the mesh appear to have an influence on the onset and evolution of localization (Fig. 4.8 and 4.8). This influence can also be observed in the convergence velocity; the test with $D = 2.04 \cdot 10^{-2}$ needs only 58% of the iterations the test with $D = 5.12 \cdot 10^{-3}$ needs (Fig. 4.8, 4.9, 4.11 and 4.12).

The observations evidence that the introduction of the second gradient term regularizes the solution having an effect even if the introduced internal length is smaller than the one introduced by the mesh size. Furthermore, the regularization supposes an important decrease of the computational expenses due to the increase of convergence velocity.

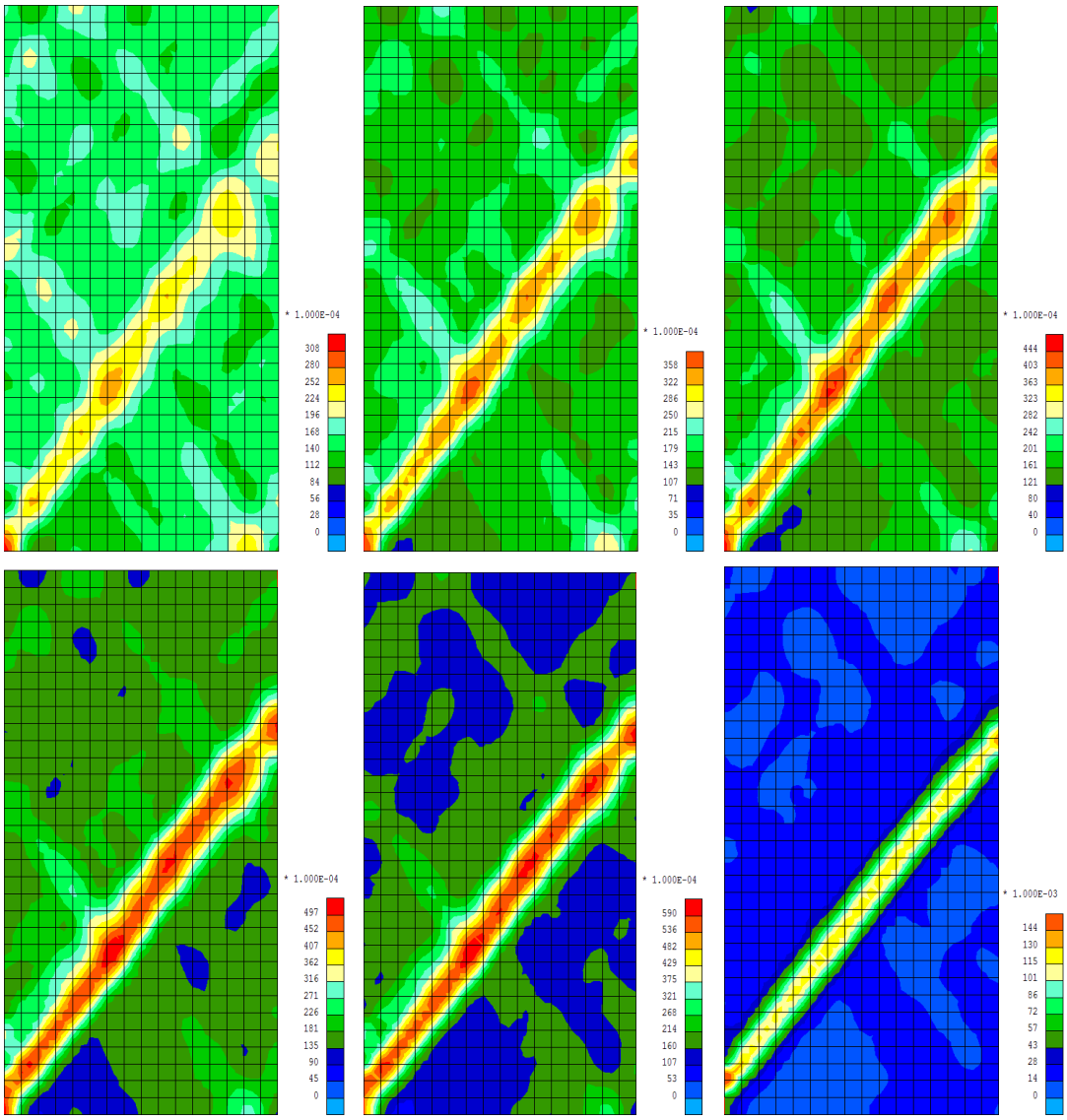

Figure 4.7: Second invariant of strain (constant pressure biaxial with 512 elements). Second gradient parameter $D = 5.12 \cdot 10^{-3}$ For axial deformation from left to right: 1.31%, 1.39%, 1.47% 1,51%, 1,56% and 1,88%

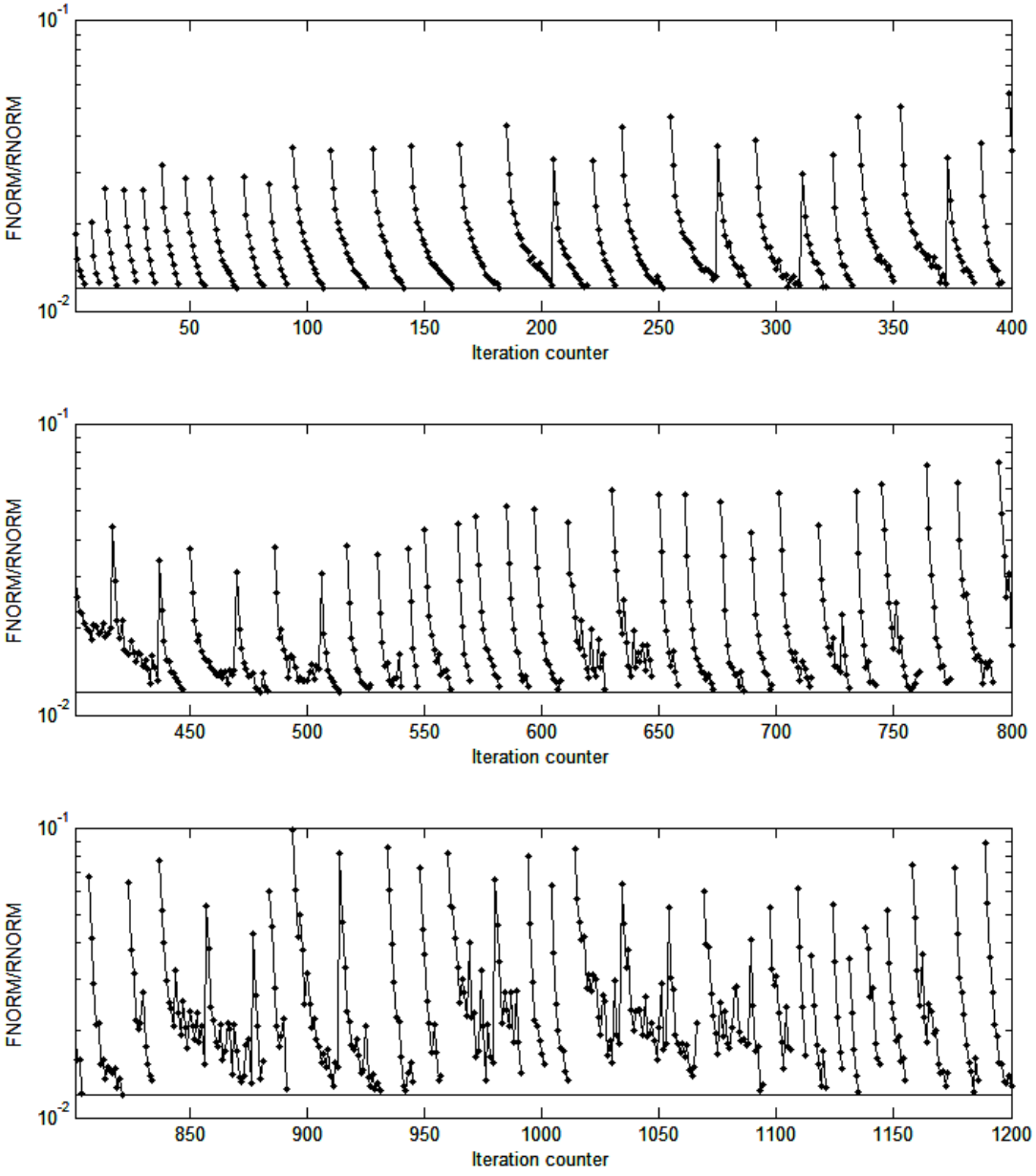

Figure 4.8: Deficit of equilibrium for the norm of the forces (FNORM/RNORM) in a constant pressure biaxial test till with second gradient law, parameter $D = 5.12 \cdot 10^{-3}$, till 1,85% of axial strain. Kruyt operator. The horizontal line indicates in each of the plots the precision threshold.

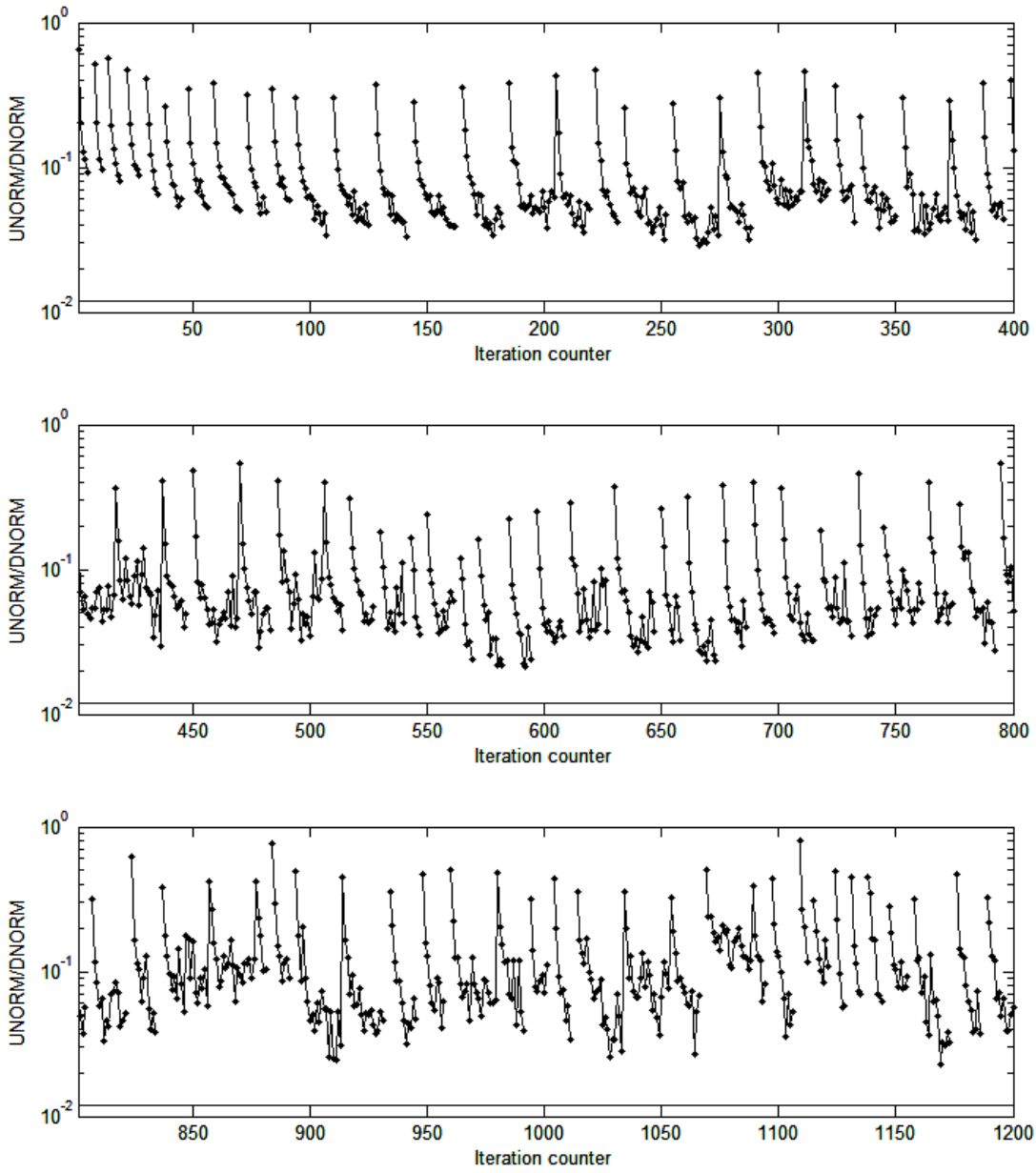

Figure 4.9: Deficit of compatibility for the norm of the displacements (UNORM/DNORM) in a constant pressure biaxial test till with second gradient law, parameter $D = 5.12 \cdot 10^{-3}$, from 1% till 1,85% of axial strain. Kruyt operator. The horizontal line indicates in each of the plots the precision threshold (forces).

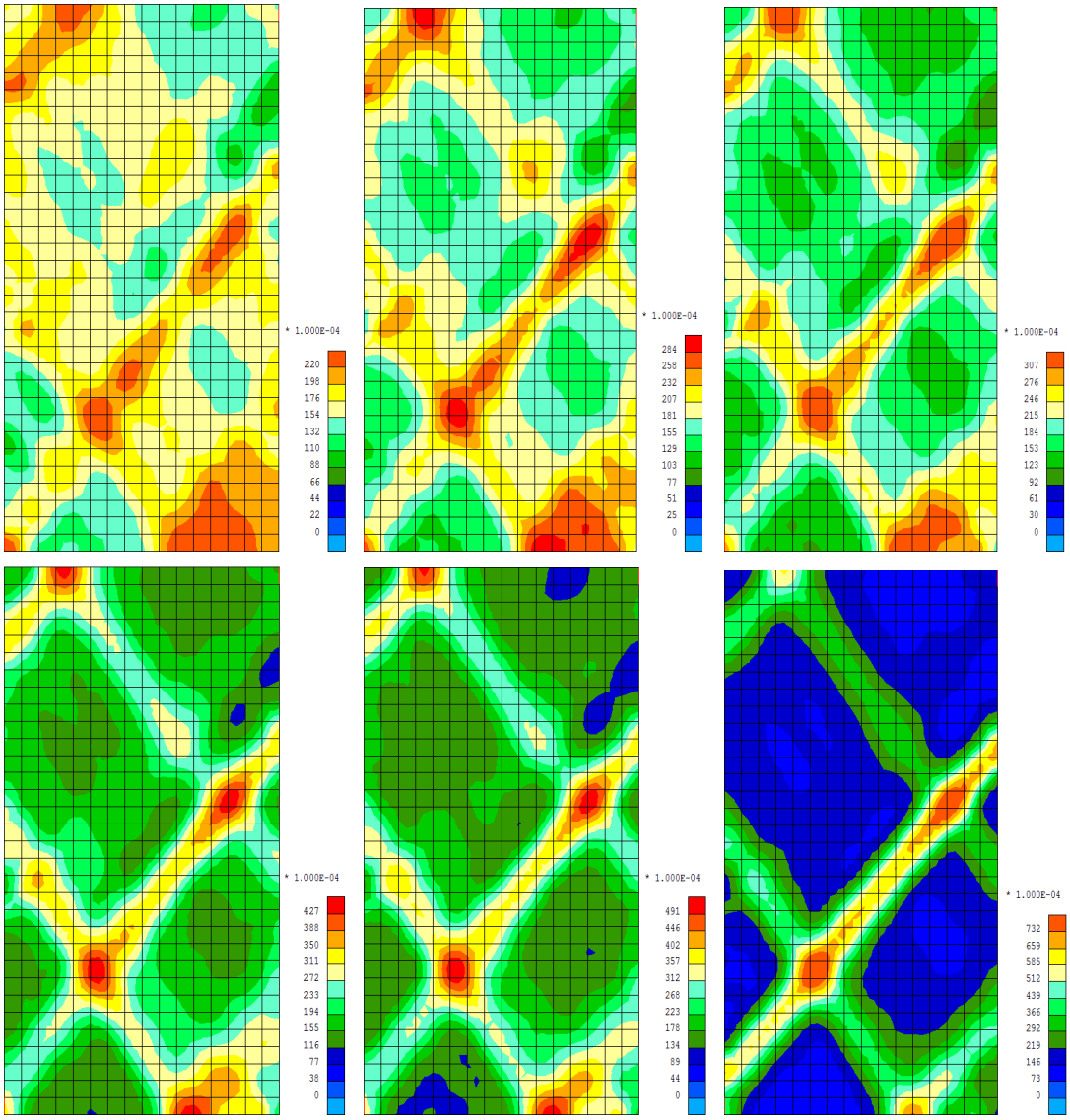

Figure 4.10: Second invariant of strain (constant pressure biaxial with 512 elements). Second gradient parameter $D = 2.04 \cdot 10^{-2}$ For axial deformation from left to right: 1.31%, 1.40% and 1.50%, 1.60%, 1.67% and 1.88%

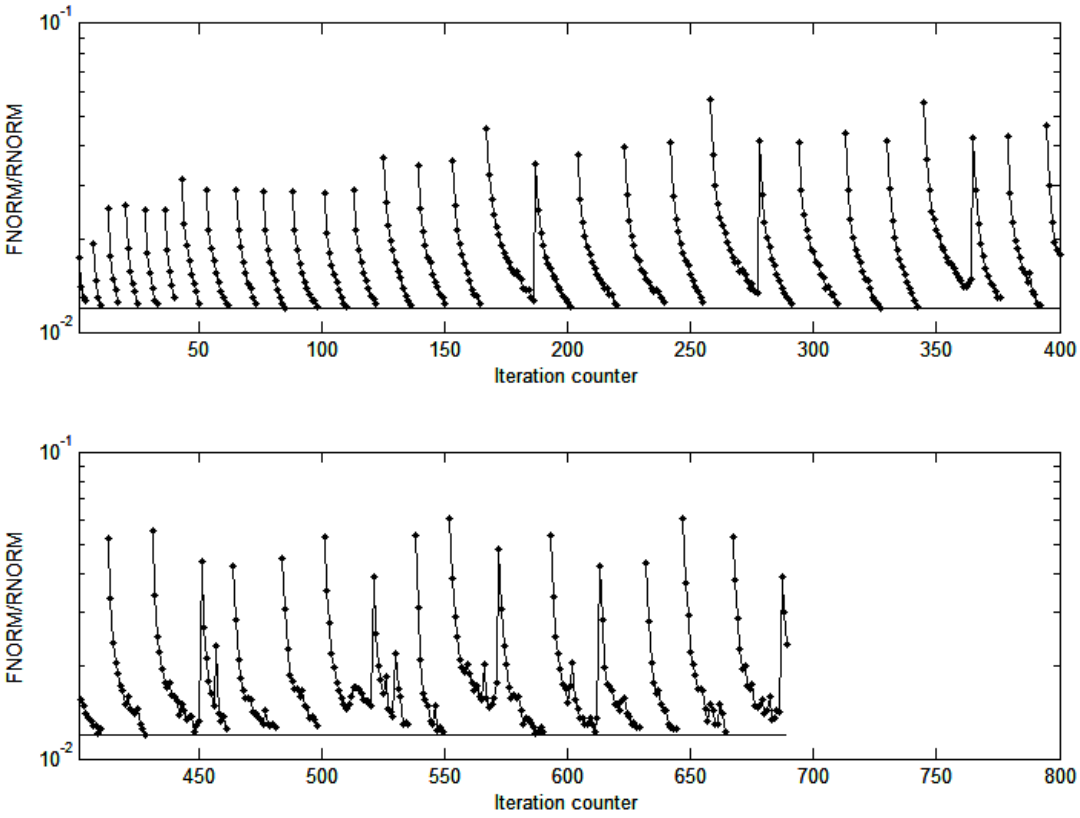

Figure 4.11: Deficit of equilibrium for the norm of the forces (FNORM/RNORM) in a constant pressure biaxial test till with second gradient law, parameter $D = 2.04 \cdot 10^{-2}$, till 1,85% of axial strain. Kruyt operator. The horizontal line indicates in each of the plots the precision threshold.

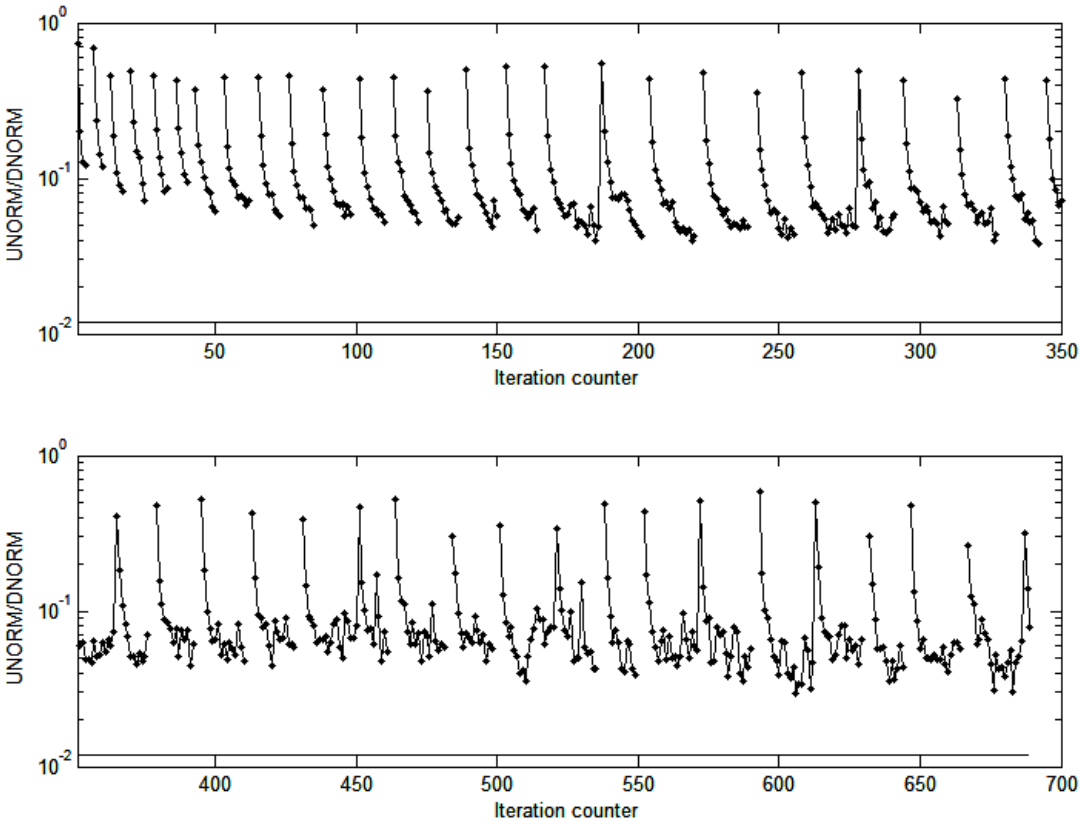

Figure 4.12: Deficit of compatibility for the norm of the displacements (UNORM/DNORM) in a constant pressure biaxial test till with second gradient law, parameter $D = 2.04 \cdot 10^{-2}$, from 1% till 1,88% of axial strain. Kruyt operator. The horizontal line indicates in each of the plots the precision threshold.

4.5 Conclusion

A second gradient regularization has been presented in this chapter. First gradient mechanical models do not present any internal length, this poses some issues as the problem undergoes softening and strain localization, i.e. mesh dependency. Second gradient is used to provide the model with an internal length and regularize the problem. By restoring the objectivity of the model, the approach also allows to fulfill the local action principle and so the scale separation in the material points.

Second gradient is a microstructured local model, this means that the relation can be applied in a material point in the same fashion as a classical constitutive law is. This has advantages with respect to non-local models which rely on the neighborhood of the material points to build the constitutive relation, this needs additional considerations in the boundaries of the domain.

The internal length introduced by the second gradient relationship is obtained phenomenologically, then the second gradient parameters are calibrated in order to obtain the desired internal length. In the present case the second gradient constitutive equation depends on only one parameter. The internal length depends on the unloading moduli of the material, which is a priori unknown, because of that, in order to find the appropriate second gradient parameter a parametric study is needed. An analytical law model is used in order to calibrate the second gradient parameter, this is done to avoid the computational cost of a series of parametric studies using FEMxDEM.

The regularization is of special interest in the FEMxDEM model; because of the noisy behaviour of the DEM constitutive law the problem is very likely to lose its ellipticity leading to an ill posed problem. The second gradient allows to soften the loss of ellipticity not only regularizing the problem but also allowing for a faster convergence.

Results are presented, simulations without a second gradient regularization are shown in order to exemplify the mesh dependency issues. The same simulations with a second gradient enrichment show that the regularization sets an internal length which makes the model mesh independent as far as the mesh size is fine enough.

Introducing an internal length by the second gradient smaller than the one introduced by the mesh does not change the shear band width but it does have effects on the convergence by accelerating it.

Chapter 5

Parallelization

Contents

5.1 Introduction

The FEMxDEM approach substitutes the analytical expression of the constitutive law by a DEM numerical model embedded in the material points. The computational overhead created by the extra needed computations can increase the wall-time in a way that the method becomes not practical to be used. In this chapter, the available computational techniques, in particular parallelization, are studied in order to mitigate the computational cost issue. Finally, the new results are validated and discussed.

5.1.1 State of the art

Moore's theories (Moore, 2006) about the future of transistor technology first appeared in Electronics magazine in April 1965. Termed a "law" years later by Caltech professor Carver Mead, Moore's Law (Fig. 5.1) predicted that the number of components in an integrated circuit would double every year at least during the next decade. In 1975 he actualized his prediction: the number of components would double every two years Moore et al. (1975).

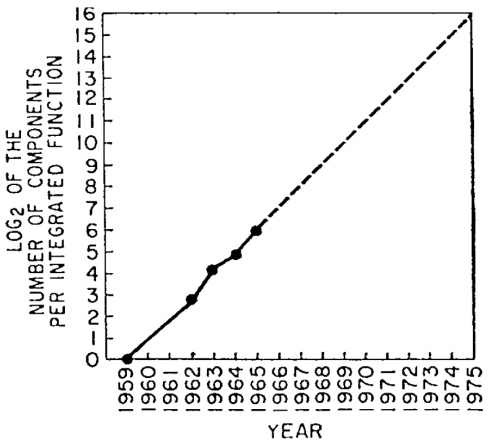

Figure 5.1: Approximate component count for complex integrated circuits vs. year of Introduction. de Montleau et al. (2002)

Moore's laws were applicable far beyond one decade, the prediction was still valid till around 2012. The increase of computational power of computers was closely related to the number of components, so Moore's law could be used to predict the increase of computational power. However, because of power consumption and temperature dissipation issues, in 2004 the size and clock speed of processors could not be further increased.

The increase of components in an integrated circuit predicted by Moore was then used to provide the processor with several cores. These multicore architectures are able to perform parallel computations in the different cores of a processor.

This scenario had been predicted long before, in the notorious publication Amdahl (1967) the author shows that the advances in computational power cannot rely in a single computer anymore, advances can be done only by interconnecting a multiplicity of computers working in a cooperative way.

To take advantage of these new architectures the old computing paradigms must be adapted to be able to split the computation load in parallel regions (Asanovic et al., 2006).

To be able to run a parallelized version of the FEM code Lagamine, a research on FEM parallelization is done, including evaluation of the FEM computational cost, single and double scale models, and evaluating the implications of using shared memory

parallelization model versus distributed memory.

Shmigelskyi et al. (2011) evaluate the computational complexity of finite element analysis in order to make a prediction of the needed computational time to execute the simulation. In the cases considered by Shmigelskyi et al. (2011) the predominant factor is the solving of the global system and in those cases the complexity of the whole problem is that of the solver, this is called a"solver intensive" code. Number of nodes and bandwidth of the global matrix appear as the two main variables increasing the solver time. The situation can be different when using constitutive laws of higher complexity: in such cases, the predominance of the solver in the global complexity can be questioned.

Numerous examples of FEM parallelization exist in the literature: early works by Farhat and Crivelli (1989) already focus on nonlinear FEM problems with shared memory architectures achieving improvements by reducing the overhead required by the element-by-element concurrent computations, Pantalé (2005) presents a study of the effect of different strategies on the speed up in an object oriented FEM code, Nakajima (2005) uses an hybrid MPI/OpenMP implementation applied to a 3D FEM linear elastic problem being able to solve a configuration with $2.2 \cdot 10^9$ DOF using the Earth Simulator [1] (Habata et al., 2003) and achieving peak performance of 3.80 TFLOPS. Guo et al. (2014) use an hybrid MPI/OpenMP implementation in order to parallelize an unstructured finite element model applied to fluid mechanics, pointing out the fact that for the parallelization of the element loop the global matrix assembly must be "thread safe", this refers to the fact that when the contributions of different Gauss points are injected into the global stiffens matrix, from the computational point of view there is the risk of different threads trying to access and write into the matrix file at the same time, some strategy must be adopted to circumvent this situation.

Moto Mpong et al. (2002) and de Montleau et al. (2002) present an OpenMP shared memory parallelization of the finite element code Lagamine (Fig. 5.2) used in this work. The paper benchmarks the performance of the parallelization in a 3D FEM simulation of a steel plate forming. The simulations are part of the PhD thesis Duchêne (2003). The mesh of the model has 4020 finite elements nodes and 1504 volume elements, for a total of 7000 degrees of freedom. In a SGI Origin3800 machine, 8 processors are used giving a speedup greater than 4. Only the element loop was parallelized in this work, so the solver load was computed sequentially.

5.2 Parallelization strategies

In this section the FEMxDEM model is analyzed in order to characterize the computational expenses of the different parts of the code, the interest is mainly on discerning between the solver and the integration of the numerical constitutive law. The computational expenses balance of these two will determine the optimal parallelization strategy. In this chapter, the ratio solver-elements will be treated again, but in that occasion it

[1] Was a highly parallel vector supercomputer system in Japan for running global climate models and problems in solid earth geophysics, it was the fastest in the world between 2002 and 2004 with a capacity of 35,85 TFLOPS.

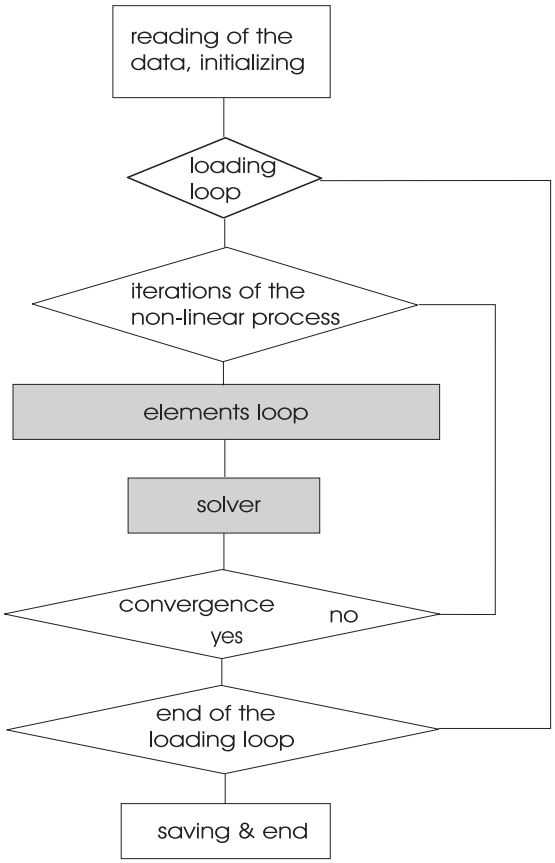

Figure 5.2: Structure of the code LAGAMINE. de Montleau et al. (2002)

will serve to find the threshold after which, once the code is parallelized in the elements, the code switches to solver intensive. The performance of the parallelization, together with the total expense of the solver will give the guidelines to set the upper size limit of a feasible problem.

The parallelization paradigm used in this work is a shared memory paradigm (OpenMP). This choice was made because of the availability in the lab of several muticore machines with shared memory architecture. Moreover, the addition of extra cores becomes less and less efficient as it will be shown later in this section. The alternative to shared memory is a more complicated paradigm; message passing interface (MPI), which allows the implementation of a Massive Parallelization, and so take profit of High Performance Computing (HPC). A MPI parallelization of Lagamine has also been performed (Desrues J. unpublished, in preparation), this second technique is not treated in this document.

5.2.1 Element loop vs solver, speedup

The critical path of a FEM model can be divided between the integration of the constitutive law at the Gauss point level and the solving of the global stiffness matrix (solver). The computational time of any of this two parts will contribute to increase the total computational time. Parallelization can be used to effectively decrease the total computational time both in the Gauss Points and the solver.

The integration of a Gauss Point in a FEM domain is independent from one Gauss Point to another. This renders the Gauss Point parallelization a straight forward procedure. The potential speedup is proportional to the number of available processors/cores.

On the other hand, the solver needs to solve a linear system of equations conformed by the global stiffness matrix, the forces vector and the displacements vector. e.g. using LU factorization. This task cannot be split into different threads as it consists of a backward dependent procedure. One possible technique to parallelize the solver (Chow et al., 2006) is to split the domain into several subdomains, each of them will have its own stiffness matrix which can be solved individually and the result used to assemble a global stiffness matrix with a much lower dimension. This has a big impact on the time complexity of the solver algorithm because the number of floating point operations needed to solve a linear system using a LU decomposition has cubic dependence on the size of the system (Golub and Van Loan, 2012, pp. 94-103) (Eq: 5.1):

$$T(n) = O(n^3), \tag{5.1}$$

where T is the running time and n the dimension of the linear system.

Depending on the problem, the ratio between the time spent on the elements and the solver can vary. Typically, problems with analytical laws and fine meshes are solver intensive meaning that most of the computational time is spent on the solver. On the other hand, double scale problems with coarse macroscale mesh are element intensive meaning that most of the computation time is spent on the integration of the gauss points in the element loop. The present case is clearly element intensive, therefore, a parallelization of the Gauss Point integration is used.

The speedup potential, according to Amdahl (1967) is (Eq: 5.2):

$$S(n) = \frac{T(1)}{T(n)} = \frac{1}{B + \frac{1}{n}(1 - B)}, \tag{5.2}$$

where S is the speedup, n the number of parallel regions, T the total time and B the non parallelizable part. The Gauss point parallelization has less impact on the total time as we increase the number of elements, because of the time complexity of the solver algorithm (Eq: 5.1). For a big number of cores the speedup factor tends to an asymptotic value linked to the time devoted to the non parallelizable part (Fig. 5.3). For less than 512 elements the speedup presents an almost linear relation with the number of cores if this number is less than approx. 50 (Fig. 5.4).

In the previous lines we showed that the element loop parallelization speedup becomes asymptotic with respect to the number of cores (Fig. 5.3) meaning that the problem

switches from element intensive to solver intensive. In this case, the parallel architectures will be less efficient because as we increase the number of cores the time devoted to the element loop decreases. It is worth noting that this situation is equivalent to the classical FEM using analytical laws thus becoming FEMxDEM an appropriate approach to model real scale problems in equality with pure FEM schemes.

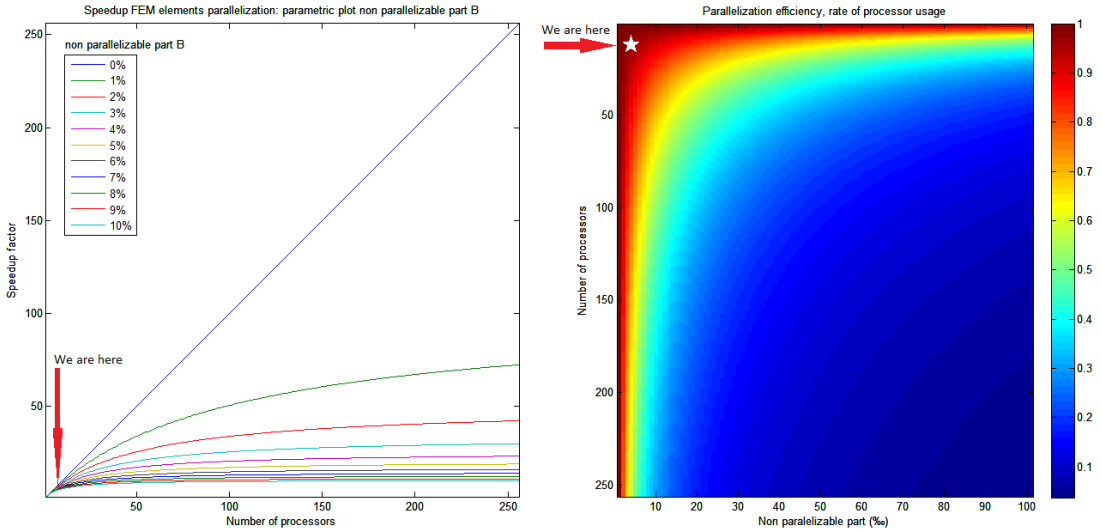

Figure 5.3: Plot of theoretical speedup factor using Amdahl (1967) formula. Parametric study for different values of B (non parallelizable part) from 0% to 10%. And Parallelization efficiency depending on B (non parallelizable part) and n (number of cores or processors available.

In the present work, consisting on a multiscale FEMxDEM model, the situation is clearly element intensive (Tab. 5.1, 5.2), therefore an element parallelization is implemented. It consists of an OpenMP (shared memory paradigm) which allows the element loop subroutine to be executed simultaneously by several cores using the same memory. One concern is to avoid concurrency in the global stiffness matrix assembly, this is done using the "atomic" construct in the OpenMP implementation: !$OMP ATOMIC, this ensures that a specific storage location is updated automatically, rather than exposing it to the possibility of multiple, simultaneous writing threads (OpenMP, 2011).

As the previous theoretical framework suggests (Fig. 5.4) the speedup obtained is almost linear with the number of cores.

5.2.2 Transition to solver intensive code

The previous section shows how, by means of element loop parallelization, an initially element intensive model can be turned into solver intensive, this means that the initially too computationally expensive code is now not more computationally expensive than classical analytical law FEM models.

Time spent 128e:	Time (s)	%
Elements	145063	99.93
Solver	32	0.02
Other	66	0.05
Total	145161	100

Table 5.1: Time spent on the different parts of the computation for a biaxial test FEMxDEM with 128 elements in the FEM and 400 particles in the DEM. Total: 40h.19m.21s.

Time spent 512e:	Time (s)	%
Elements	517348	99.67
Solver	1615	0.31
Other	125	0.02
Total	519088	100

Table 5.2: Time spent on the different parts of the computation for a biaxial test FEMxDEM with 512 elements in the FEM and 400 particles in the DEM. Total: 144h.11m.28s.

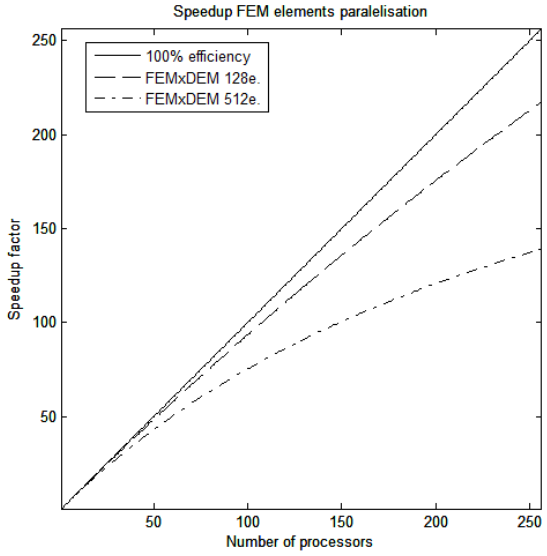

Figure 5.4: Plot of theoretical speedup factor using Amdah formula (Amdahl (1967)) for the cases FEMxDEM 128 elements and 512 elements.

The natural step now is to study the impact of the increasingly heavy solver as the size of the mesh is increased. This will provide an estimation of the upper limit of problem size that can be computed efficiently using an element/Gauss point loop parallelization.

A test consisting in a hollow cylinder geometry and increase of the inner pressure

2880 el. test	Time (h)	Ratio (%)
Elements	80.7	97.1
Solver	2.4	2.9
Total	83.1	100.0

Table 5.3: Solver vs element loop computation time summary.

is prepared. The mesh is formed by 2880 elements and 10980 nodes. In the present FEMxDEM model, the time devoted to element loop is strongly dependent on the strain magnitude sent to the elements. As a result of this, the element/solver time ratio will increase drastically when the model undergoes strain localization, due to the large strain magnitude in the elements located inside the shear band. A loading history reaching high levels of localization is used. The machine used for this test is a 2 x 4 core processor which handles up to 8 threads in parallel (2 x Intel Xeon CPU E5410 @2.33GHz). The summary of the computational time results are presented in table 5.3. This time the ratio solver/total time is increased to 2,9%, not negligible like in the previous tests, but yet not too prohibitive according to Amdahl (1967).

A bigger test is prepared; 4950 elements and 18900 nodes which gives a total computational time of 1852 hours, and a solver/total time ratio of 11%. The purpose is to study the relation number of nodes - degrees of freedom of the problem and the time devoted to the solver. The solver strategy used is a skyline storage of the global stiffness matrix and a direct solver by LU decomposition.

According to (Eq. 5.1), the computational time for the solver using direct LU decomposition is cubic with respect tho the number nodes/degrees of freedom, using this relation and extrapolating the expected solver time a ratio solver/total is obtained (Fig. 5.5).

The plot (Fig. 5.5) shows that for a non parallelized problem, at least 100000 nodes are required to talk about a solver intensive problem. On the contrary, if the problem is parallelized in the element loop, a 20000 node problem can easily become solver intensive limiting the performance of the parallelization. Indeed, the figure (Fig. 5.6) shows how the potential speedup tends to become asymptotic when the number of cores increases.

The plot (Fig. 5.6) shows that for 18900 nodes the speedup approaches an asymptotic value of 10 when the number of cores surpasses few tenths. The case with 10980 nodes (less solver intensive) can be accelerated up to 22 times with 64 cores not approaching yet an asymptotic value. The relation illustrated in (Fig. 5.7) shows the maximum theoretical speedup for an infinite number of cores related to the size of the problem (number of nodes). This curve shows how the speedup potential decreases as the size of the problem increases, e.g. a model with more than 5000 nodes can not be accelerated more than 100 times and a problem with more than 15000 nodes not more than 10 times.

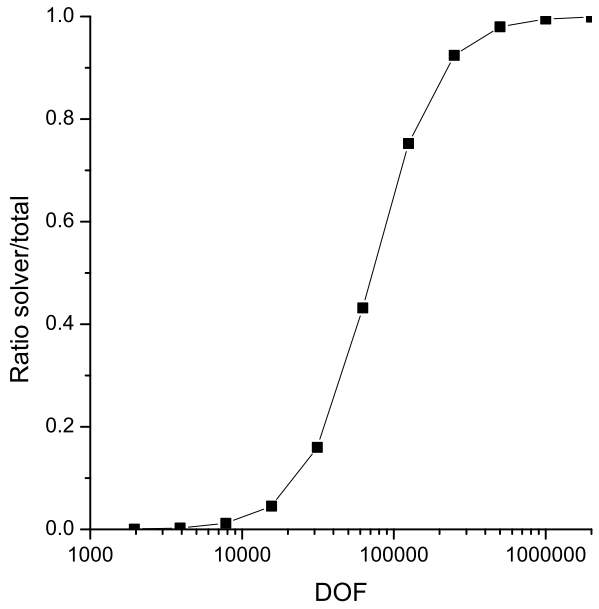

Figure 5.5: Ratio solver time/total time for a non parallelized problem.

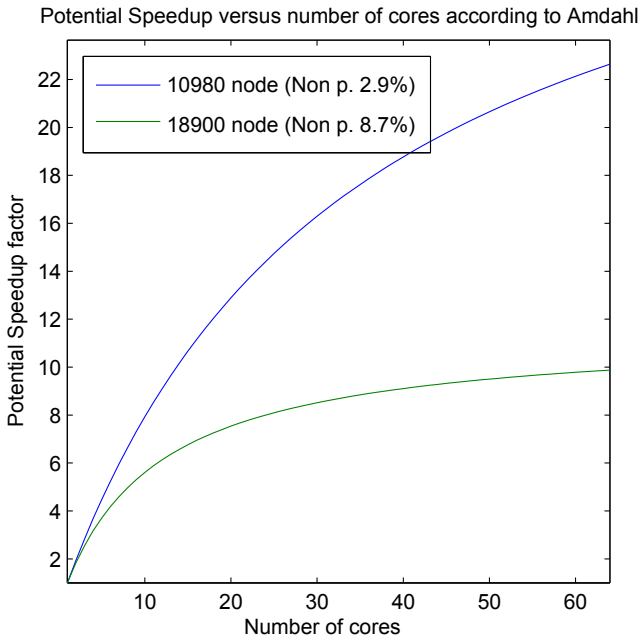

Figure 5.6: Potential speedup according to the solver weight (non parallelizable part).

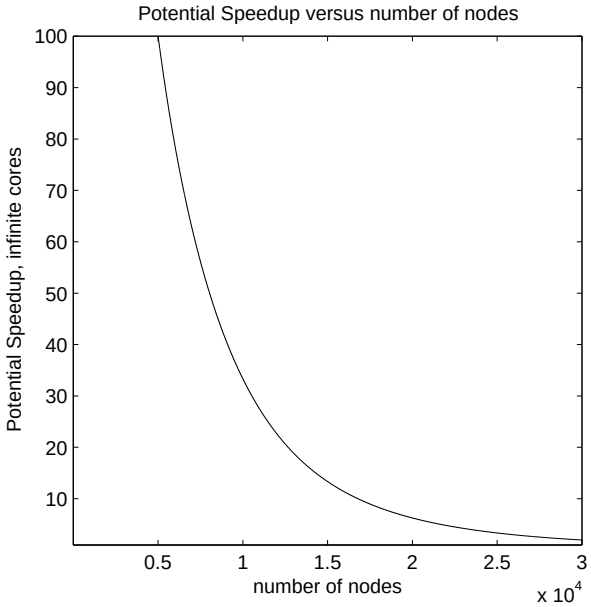

Figure 5.7: Maximum of speedup depending on the non parallelizable part

5.3 Validation

The next step after the parallelization of the code is the validation of the results with the sequential case (in which only one thread can be used simultaneously so the Gauss points are sequentially integrated).

5.3.1 Comparison with the sequential code

As it can be seen (Fig. 5.8), two calculations give non-identical results , questionning the objectivity of the results when parallelization is used. The order of magnitude of the difference and the fact that the localization mode is the same, suggests that the perturbation introduced by the parallelization may be of numerical origin.

To study these effects, the code is compiled and executed in the same hardware with three different options:

1. OpenMP parallelization is taken into account both in compilation and execution.
2. OpenMP is taken into account in the compilation but the code is executed in one single thread.
3. Intrinsically sequential case : No OpenMP clauses are taken into account (OpenMP, 2011).

From the comparison of these three cases, it can be affirmed from careful comparison of the results (not shown here) that no difference exists between 2 and 3, showing

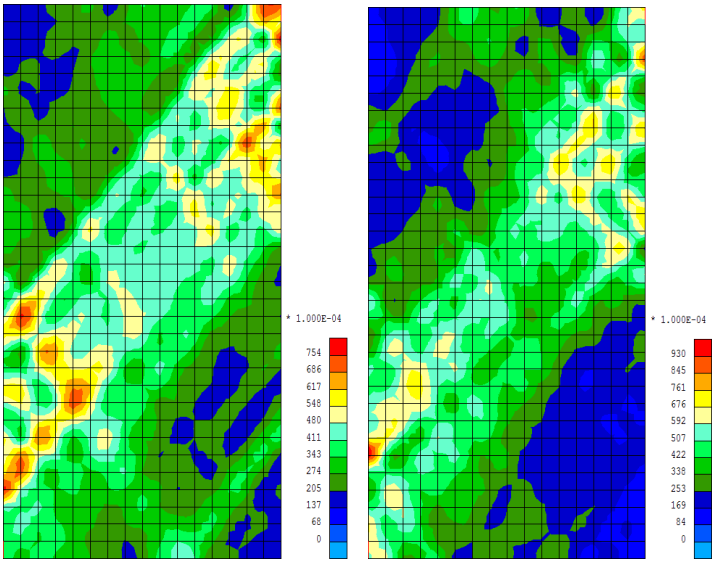

Figure 5.8: Comparison between the same simulation computed using a non-parallelized code and parallelized one. Second invariant of strain at the end of the test.

that the differences observed in (Fig. 5.8) between the parallelized case and the non parallelized one does not come from the OpenMP parallelization clauses by itself (Fig. 5.8). Furthermore, running several times the same simulation in the case 1 with the same number of cores will give different results. A closer look focuses now in these differences. In the plots (Fig. 5.8) a finite difference can be observed between the tests.

Looking at the convergence values for the iterative scheme (Tab. 5.4) a slight difference can be observed starting at the third iteration: $1.29 \cdot 10^{-1}$ vs $1.28 \cdot 10^{-1}$. The precision of this global output does not give us enough information, so in a second step the values of stress tensor computed at each Gauss point are compared between the two computations. This comparison shows identical values for the first iteration, but already differences in the second. This observation confirms that no difference exists after the integration of the gauss points in the first iteration suggesting that the perturbation is introduced after the integration subroutine.

ITER	Sequential	Parallel
1	$6.56 \cdot 10^{-1}$	$6.56 \cdot 10^{-1}$
2	$2.05 \cdot 10^{-1}$	$2.05 \cdot 10^{-1}$
3	$1.29 \cdot 10^{-1}$	$1.28 \cdot 10^{-1}$
4	$1.13 \cdot 10^{-1}$	$1.17 \cdot 10^{-1}$
5	$9.20 \cdot 10^{-2}$	$9.14 \cdot 10^{-2}$

Table 5.4: Comparison between the same simulation computed using a non parallelized code and parallelized one starting from an identical configuration. Norm of the deficit of compatibility UNORM/DNORM.

5.4 Numerical randomness

The previous section arose the need to find out the origin of the differences between the parallelized and non parallelized codes. In this section the origin of the differences is identified and quantified, possible alternatives are discussed as well as the necessity and convenience of those. The node renumbering of a FEM mesh is presented as another factor that can trigger non objectivity in the solution. Finally, the same case is exemplified with a classical hypoplastic law.

5.4.1 Origin and quantification of the randomness

The possibility of the discrepancy coming from the microscale subroutine has been discarded in the previous section. This was based on the observation of the local stress tensors after the first integration loop. The following findings emerge. In the OpenMP clauses the parallelization of the element loop is implemented using the command: !$OMP DO SCHEDULE(dynamic,1) meaning "dynamic" that the order of the elements in the loop can be changed dynamically according to the job queue and core availability. This can be done since we know we are parallelizing independent computations; however, this is responsible of inducing small differences. Indeed, the differences lie in the assembling of the global stiffness matrix. Remark that the commutativity property of the sum doesn't apply in numerical applications: a simple example written with Matlab is provided by emulating the values and dimensions of a fictitious global stiffness matrix and force vector (Alg. 1), where the rand(1,n) returns an array of random numbers uniformly distributed between 0 and 1, the array is a vector with n components, in Arand(i) i denoted the vector position :

As a result of the Matlab experiment an apparent random distribution in the range $(-9.0949 \cdot 10^{-13}$ $+9.0949 \cdot 10^{-13})$ is obtained (Fig. 5.9): this illustrates the origin of the differences between the parallelized and non parallelized versions of the FEM code.

To explain why differences are also encountered in the same parallelized code executed in the same number of cores it's needed to consider that the computer dynamically assigns different Gauss point integrations to different cores, but the computer can manage the cores in a different way and use them for other tasks than the simulation itself, this makes the assembly order of the global stiffness matrix different even with identically parallelized simulations.

The magnitude $+9.0949 \cdot 10^{-13}$ is much lower than the precision of the model, but still, this phenomena appears to be of crucial importance since it is able to trigger solutions with finite discrepancies after bifurcation.

In order to characterize the mentioned numerical perturbation, its distribution is presented in a bar histogram. This time without the stiffness multiplier used in the previous plot (Fig. 5.9) (900), so the calculations refer to the error introduced in the addition of 3 realizations[2] of a uniform distribution[0,1]. First of all a simulation with m=1000 global matrix values and vector length n=3 is performed (Fig. 5.10). The

[2]The observed value from the random variable, what actually happened.

Algorithm 1 Matlab code simulating the numerical perturbation generated by changing the order of the assembling into the global stiffness matrix in a FEM model with 2145nodes (512elements).

```
m=2145 !number DOF for the given geometry
for j=1:m !loop over the nodes
sumup=0; !initialisation
sumdown=0;
n=4; !number of writings in each node (shape functions from different elements)
Arand=900*rand(1,n); !900 is a typical value for the diagonal coefficients of the stiffness
tensor
for i=1:n !loop writings global stiffness matrix
sumup=sumup+Arand(i);
end
for i=1:n !loop inverse order writings global stiffness matrix
sumdown=sumdown+Arand(n-i+1);
end
error=sumup-sumdown; !theoretically it should be zero
err(1,j)=error;
end
plot(err)
```

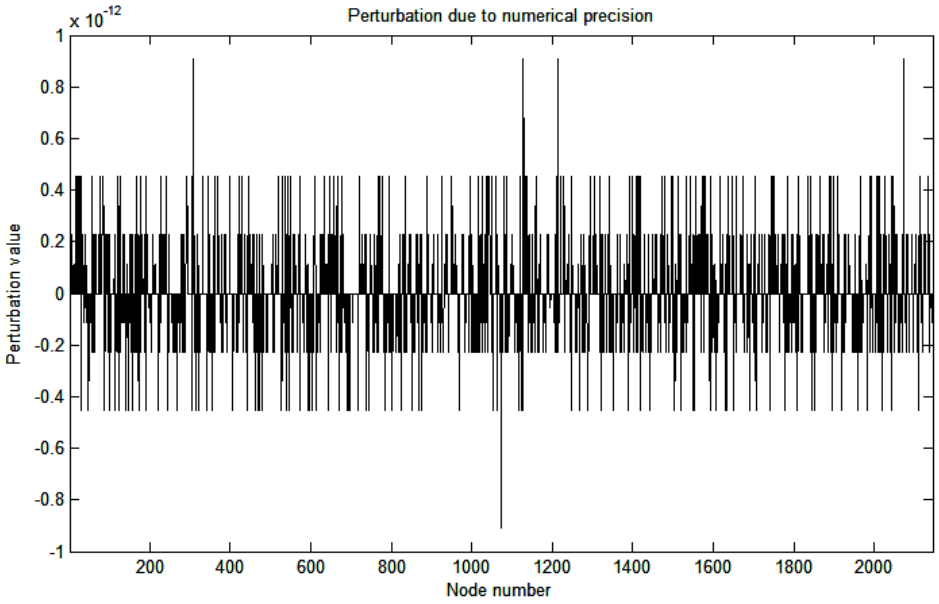

Figure 5.9: Numerical perturbation resulting from changing the order of addition in numerical application. Double precision, 4 number addition, 2145 tests, magnitude multiplier: 900.

results show that 83% of the realizations of the global matrix values have 0 error, 14% $+/-2.22\cdot10^{-16}$ and 3% $+/-4.44\cdot10^{-16}$, the vector length n=3 is the minimum that can give error in the renumbered addition. The distribution of the error is not a continuous over the domain but only discrete values multiple of the basic error $2.22\cdot10^{-16}$ can take place.

Next, a simulation with m=1000 and n=4 is performed (Fig. 5.11), this is of interest because n=4 is the case that emulates a possible position of the global stiffness matrix of our FEMxDEM problem. In this case the upper bound for the error is $+/-8.88\cdot10^{-16}$.

Finally, a simulation with $m = 1\cdot10^6$ and n=2500 is performed in order to plot a pseudo-continuous distribution of the error (Fig. 5.12). The distribution is not continuous because only realizations of the global matrix values in the support composed by multiples of $2.22\cdot10^{-16}$ are possible but for practical purposes it will be treated as a continuum distribution which is likely to fit a normal distribution zero biased ($mean = -2.5614\cdot10^{-15}$) and standard deviation $2.3993\cdot10^{-12}$.

We conclude that randomness is introduced to the model and this can trigger different solutions. All of them are valid solutions of the BVP but since there is no control over the assembly order in the parallelized scheme they are not reproducible.

5.4.2 Alternatives to obtain an objective model

In order to obtain an identical objective simulation using a parallel computation the !$OMP DO SCHEDULE(dynamic,1) clause is changed into !$OMP DO SCHEDULE(static,1), meaning "static" that the order of the computations will be respected. The result is still a different solution from the one of the sequential code. The reason of this is that even if the different calculations are sent to the cores in the "static" order, this doesn't assure that the results will be written into the global stiffness matrix in this same order. In the DEM subroutine the computation time depends on the strain input given to each Gauss point meaning that the writing order into the global stiffness matrix will be different again giving a new result non equal to the sequential one. Writing the different contributions to the global stiffness matrix in a pre-established order would dramatically reduce the efficiency of the code, so this possibility is not explored.

5.4.3 Analogy with node renumbering

Following the trend of the previous lines, the renumbering of the nodes is now studied as it can also change the, a priori, deterministic results. In FEM applications the performance of the solver depends on the efficiency of the factorization: a lower bandwidth of the global stiffness matrix will result in a more efficient factorization meaning a faster computation. The default numbering, no matter if it comes from structured or unstructured mesh, in general doesn't give the optimal organization of the stiffness matrix so a renumbering procedure is usually applied in order to increase solver performance Burgess and Giles (1997).

This manipulation doesn't change the theoretical framework but the same statement is not true for the numerical solution. Applying a renumbering in order to get a banded

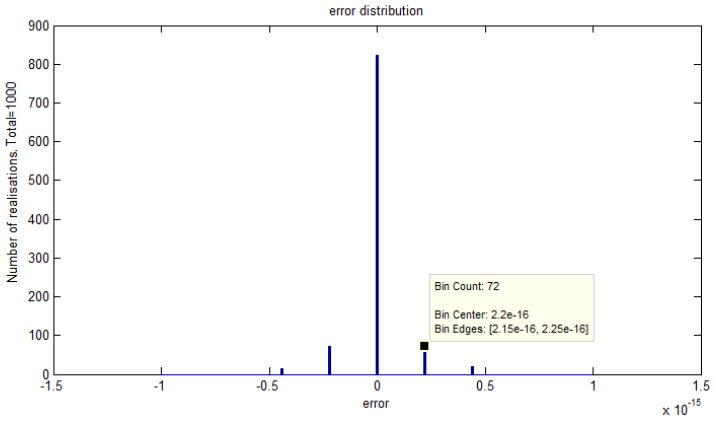

Figure 5.10: Error distribution n=3 m=1000

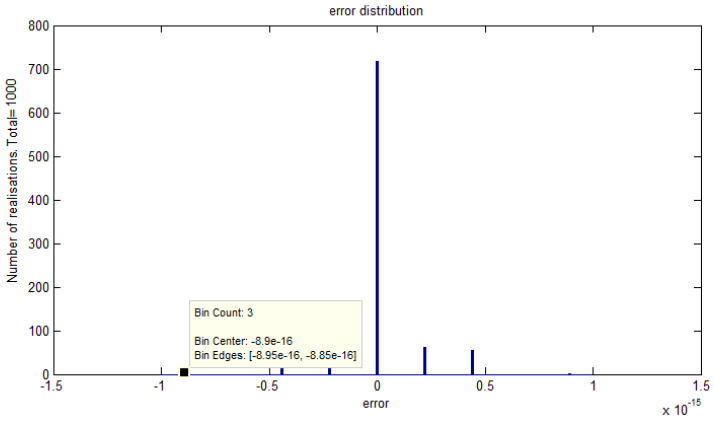

Figure 5.11: Error distribution n=4 m=1000

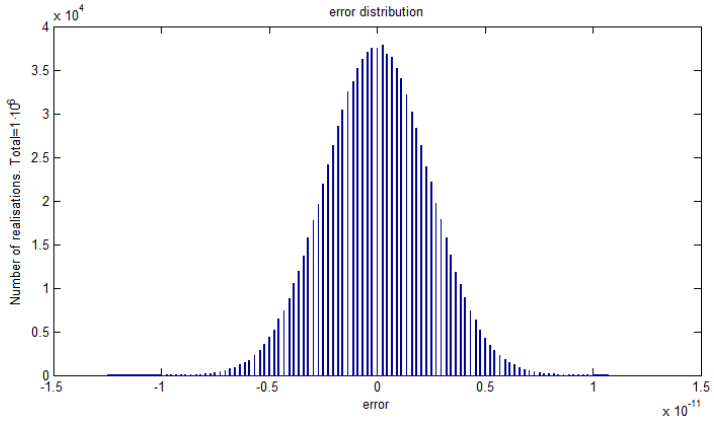

Figure 5.12: Error distribution n=2500 m=1E6

Iteration 7	Non renumbered	Renumbering 1	Difference
FNORM/RNORM	$0.1991640 \cdot 10^{-2}$	$0.1991643 \cdot 10^{-2}$	$-3 \cdot 10^{-9}$
UNORM/DNORM	$0.3578087 \cdot 10^{-1}$	$0.3578087 \cdot 10^{-1}$	0

Table 5.5: First difference in the output file of a loading step for a reference configuration and renumbering 1 (smaller bandwidth)

Iteration 6	Non renumbered	Renumbering 2	Difference
FNORM/RNORM	$0.2234314 \cdot 10^{-2}$	$0.2234314 \cdot 10^{-2}$	0
UNORM/DNORM	$0.4260298 \cdot 10^{-1}$	$0.4260299 \cdot 10^{-1}$	$-1 \cdot 10^{-9}$

Table 5.6: First difference in the output file of a loading step for a reference configuration and renumbering 2 (larger bandwidth)

stiffness matrix will affect the numerical computation in two ways. The first is that the condition number of the matrix will be reduced compared to the non renumbered case, also referred as preconditioning in previous chapters (Saad and Van Der Vorst, 2000); this results in a more precise computation. The second one is that any renumbering will introduce numerical randomness regardless of the bandwidth, resulting in a different result especially in nonlinear problems presenting bifurcation. Consequently the determinism of the solution with respect to the parameters of the model is lost.

In the following, 3 test are performed in order to quantify the effect of the node renumbering on the results. The reference test is a biaxial compression test with constant lateral pressure, 128 FEM elements and 400 particles in the DEM. This test is subjected to two different renumbering strategies: one renumbers it in order to decrease the bandwidth according to the longest dimension of the sample (renumbering 1), and the other the contrary (renumbering 2). In a loading step starting from an identical initial state, the first differences in the norm of forces or displacements are found respectively after the 7th (Tab. 5.5) and 6th (Tab. 5.6) iteration. However this difference detection threshold is constrained by the precision of the output format; indeed, like in the previous results, differences in the stress tensor are already found in the second iteration.

The result for a biaxial test with constant lateral pressure, subjected to a compressive strain in the vertical direction up to 1% shows the same localization as can be seen by comparing the non renumbered case with the renumbering 2 and only slightly different strain distributions (Fig. 5.13).

The result for the renumbering 1 is not presented because it gave rise to a different localization mode and eventually didn't converge (Tab. 5.7). The strain stress plot (Fig. 5.14) shows almost identical values for the deviatoric stresses in the elastoplastic part (differences of the order of the relative accuracy of the model) and more divergent results in the post-peak part, reaching the larger difference ($q/\sigma_2 = 0.019$) near 0,7% of longitudinal strain.

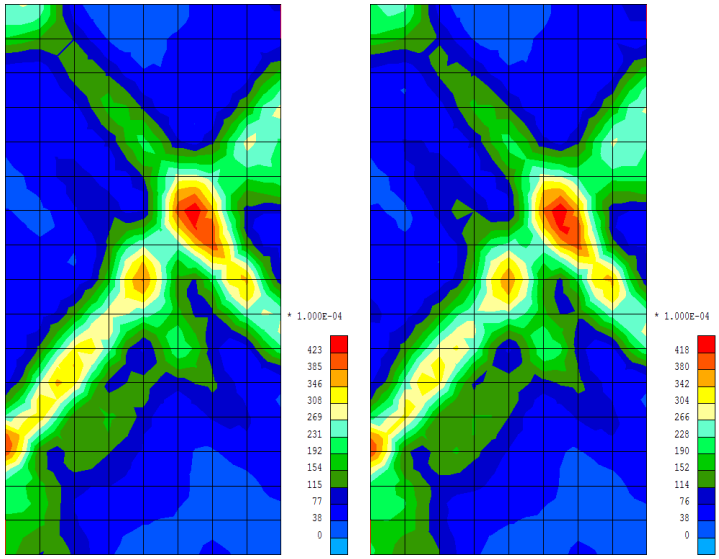

Figure 5.13: Comparison between the same simulation without renumbering and with renumbering 2. Second invariant of strain at the end of the test.

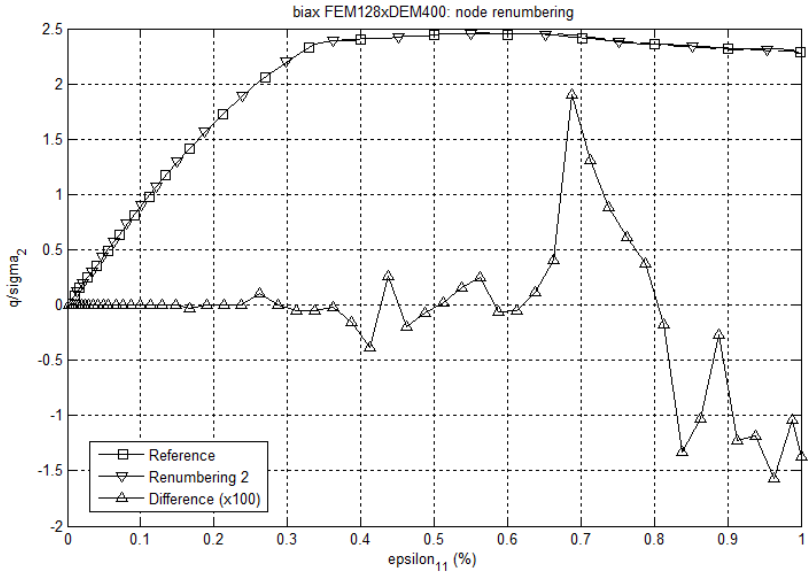

Figure 5.14: Comparison between the same simulation without renumbering and with renumbering 2. FEMxDEM model. Strain-stress plot with difference between the two.

Simulation	q/σ_2	Difference (%)
Non renumbered	2.270	0
Renumbering 1	Non converged	-
Renumbering 2	2.257	-0.57%

Table 5.7: Comparison between 3 cases: non renumbered, renumbering 1 and renumbering 2. Stress for the end of a biaxial test (1% longitudinal strain)

5.4.4 Node renumbering and parallelization with a non DEM law

Till this point, the effect of the element parallelization and an analogy with node renumbering has been discussed for a FEMxDEM scheme. In order to conclude this study extending it to a more general situation, the same parallelization and node renumbering is applied to a non DEM constitutive law, the chosen law is PLASOL due to the similarities with the DEM law. From the numerical point of view, the main difference between the DEM law and PLASOL is the high sensitivity of the DEM law with respect to the strain input, the PLASOL law is much less sensitive to small variations of the input strains which makes it more easily differentiable and less prone to trigger a bifurcation due to local softening.

The PLASOL constitutive law was implemented in Lagamine by Jean Dominique Barnichon (Barnichon, 2007), it is characterized by a linear elastic isotropic behaviour and a Drucker-Prager plasticity criteria (Barnichon, 2007). Drucker-Prager (Drucker and Prager, 2013) yield surface is characterized by a cone in the space of principal stresses, its shear strength depends on the first invariant of stress accounting for the confining pressure effect in geomaterials.

The comparison of the results of a biaxial test with constant lateral pressure between sequential and parallelized computations give identical results for the strain-stress curve with the output format precision (Fig. 5.15). Conversely, if looking at the individual gauss point integration results, little differences can be found related to the floating-point relative accuracy, but those will not trigger any change on the macroscale bifurcations.

The same comparison between renumbered and non renumbered nodes gives the same results: no difference in the strain-stress curve (Fig. 5.16) and only floating-point relative accuracy differences between the Gauss points integration.

From this observation we conclude that: for a DEMxFEM model, the high sensitivity of the microscale gives as a result finite differences in the constitutive law, these finite differences can trigger a bifurcation in the macroscale ending up with sensibly different solutions. For an analytical law as PLASOL, after the integration of the gauss points the differences are still as small as the floating-point relative accuracy, not being able to trigger, in the present example, any major macroscale bifurcation.

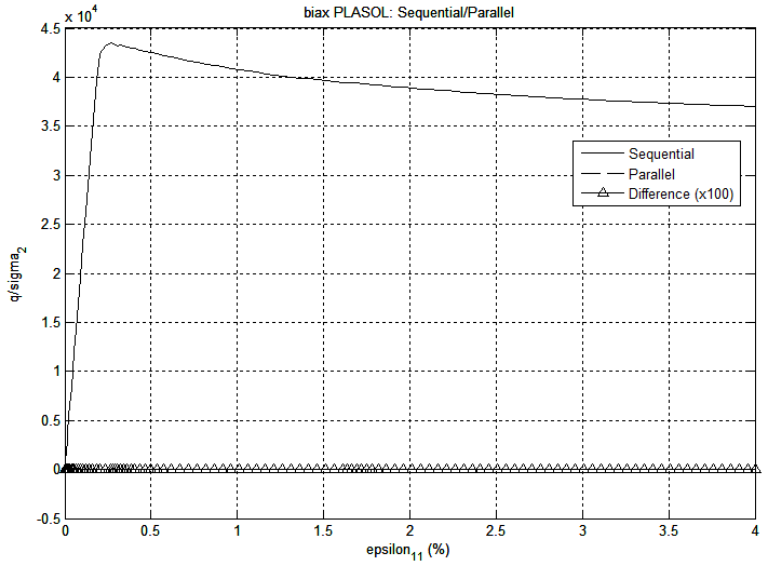

Figure 5.15: Comparison between the same simulation without and with parallelization. PLASOL law. Strain-stress plot with difference between the two.

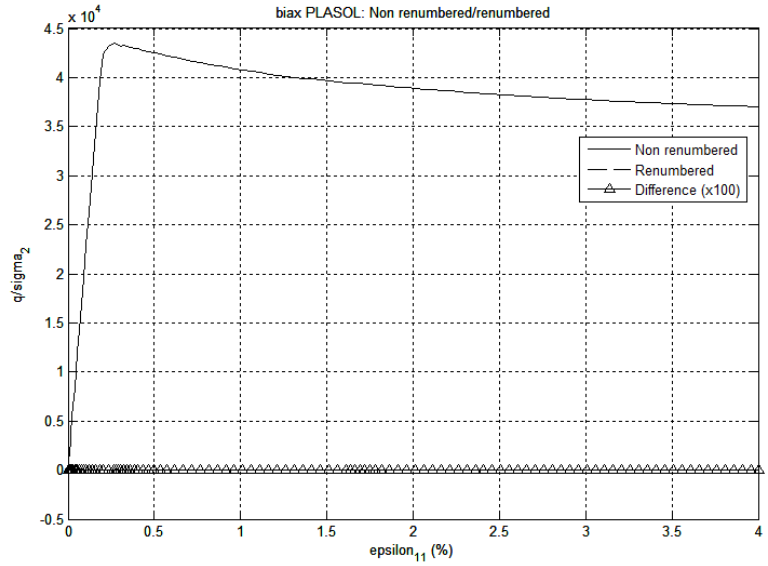

Figure 5.16: Comparison between the same simulation without and with renumbering. PLASOL law. Strain-stress plot with difference between the two.

5.5 Performance

Here the parallelized code is executed in different machines in order to benchmark its performances. The machines are two servers, one with two Intel Xeon CPU E5410 @2.33GHz 4 core processors (8 core total) and the second with two Intel Xeon CPU E5650 @2.67GHz 6 core processors (12 core total). A standard 512 element simulation consisting in a compression biaxial test till 2% of longitudinal strain is executed both sequentially and parallelized in the two machines. The results show a speedup of $7,15$ for the machine with 8 cores and 9.06 for the machine with 12 cores. (Fig. 5.17). The good efficiency of the parallelization proves the aforementioned features of the model.

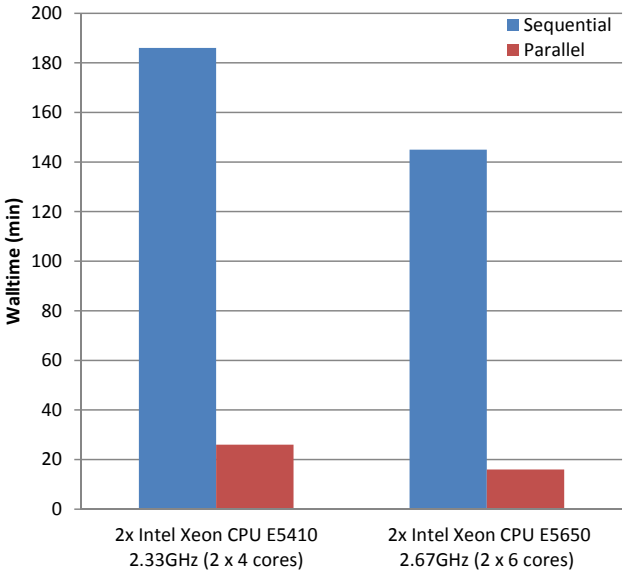

Figure 5.17: Parallelization performance: comparison of sequential and parallel walltime of a FEMxDEM simulation in different machines.

5.6 Conclusion

For the present project the parallelization of the element loop can provide a major improvement of the performance, up to 99% of time saving based on the elements-solver ratio of a 512 element test. For the moment there is no interest on the parallelization of the solver, this scenario can change if in the future, taking advantage of the parallel architectures, the size of the problem (number of DOF) is sensibly increased.

The non deterministic results with respect to the input parameters of the parallel code does not invalidate the implementation because the differences are explained as being different possible solutions of the problem. The triggering of the different solutions is caused by numerical perturbations introduced by random changes of the order of treatment of the different elements, since the assembly order has to be let free in order to optimise the parallelization efficiency.

The same non objectiveness phenomena is observed if node renumbering is used in the FEM implementation.

Depending on the nature of the problem this can result in a very different solution: different localization mode, no convergence, or only numerical difference without practical relevance. In a FEMxDEM model the first one is more likely to happen due to the high sensitivity of the DEM.

The computational time acceleration provided by the implemented parallelization allows the FEMxDEM code to compete with classical FEM models in terms of walltime. Together with the second gradient regularization presented in a previous chapter, this allows to consider real scale problems with complicated meshes. This is treated in the next chapter.

Chapter 6

Real scale Boundary Value Problems

Contents

6.1 Introduction

In this document several developments of the multiscale FEMxDEM approach have been presented. In this chapter, the model is applied to a real scale case, consisting on a hollow cylinder which can correspond to a gallery excavation or a pressuremeter test. We recall

that the developments that made possible to perform these real scale simulations are mainly:

- Allowing convergence with the use of alternative operators
- Improving convergence via the introduction of heterogeneity
- Speedup via parallelization
- Second Gradient regularization

The importance of the scale of the macroscopic problem is related to the complexity of the microscale Anderson et al. (1972) and the separation of scales Geers et al. (2010); to fulfill the separation of scales the mesh needs to be fine enough to well represent the variations of the strain field, this means that bigger macroscopic problems will contain more Gauss points, each of this Gauss points will require a computational time proportional to the complexity of the microscale.

DEM models can efficiently model BVPs with few hundreds or thousands of particles. With modern GPU acceleration, DEM codes can even treat problems involving millions of particles (Govender et al., 2015). This orders of magnitude may seem sufficient to model problems in a rather big domain, but the fact is that depending on the grain size this may not be enough, e.g. to treat a railway track problem, where the particles constituting the ballast are rocks with a size of several centimeters, a problem including several longitudinal meters of the railway will only contain some thousands of particles which can be easily treated with nowadays computers. In the other hand, if the material treated is a typical sand, one cubic centimeter of the domain will contain around 15.000 particles, this makes not possible to treat engineering scale problems with this particle size using a pure DEM approach, even using GPU acceleration in the big supercomputers. It is in this condition when the FEMxDEM approach can provide a tool to model engineering scale problems involving granular materials.

In previous chapters, the different features of the FEMxDEM approach have been exemplified with biaxial simulations that emulate a lab biaxial test, this is a test of rather academical interest with small dimensions. The separation of scales principle (the strain and loading fields must vary smoothly around the Gauss points) will be more restrictive in a real scale discretization, this is because of the needed mesh refinement: in order to well represent the localization phenomena a finer mesh is needed and this results in a bigger problem.

6.1.1 State of the art

Hereafter, some of the existing works related to the content of this chapter are mentioned, these are used to introduce the following simulations and justify the interest of the chosen BVP. The literature selection includes non-uniqueness studies in a hollow cylinder hydromechanical problem using Lagamine FEM, experimental study of anisotropy effect in a hollow cylinder triaxial test, several studies concerning underground gallery excavation stability. The later uses both mechanical and hydromechanical models and focuses

on the material anisotropy. Most of those have the application of building radioactive waste disposal facilities, involving contact problems which consider the effect of a concrete lining in the gallery and models using a combined continuum-discrete approach among others. In addition to all the gallery excavation problems, one publication about the pressuremeter test is also commented.

Marinelli et al. (2015) presents a non-uniqueness study of a hydromechanical boundary value problem using the finite element code Lagamine. A Biot material is considered, using two constitutive equations for the skeleton based on the Druker-Prager yield criterion with a hyperbolic hardening rule for the cohesion and friction angle as a function of an equivalent plastic strain. The two constitutive equations (Plasol and Aniso-Plasol) present isotropic elasticity and cross anisotropic elasticity respectively. The parameters are calibrated in order to model a Boom Clay experiment consisting in a hydromechanical unloading (Fig. 6.1). Non-uniqueness studies are carried using both constitutive equations, the results show that the use of different time step discretizations has an effect on the initialization of the Newton-Raphson algorithm on a given time step. This leads the emergence of different solutions for the same BVP. Marinelli concludes that, as soon as degradation is incorporated in a constitutive equation, uniqueness of the solution of initial boundary value problems is questionable even in coupled problems. The author concludes that the results produced using the isotropic rock model consistently underestimate the borehole collapse pressure for all failure criteria when compared to the anisotropic case.

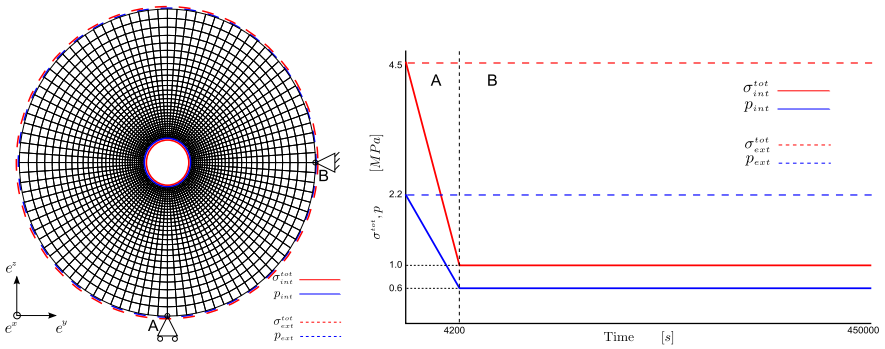

(a) (b)

Figure 6.1: (a) Spatial discretization of the hollow cylinder: 2790 elements. (b) The initial boundary conditions on the inner and external side of the hollow cylinder: phase A and phase B. (Marinelli et al., 2015)

This time using experimental means, You et al. (2015) perform a series of triaxial laboratory experiments on thick-walled hollow cylindrical samples of boom clay aimed to understand the anisotropic deformation during excavation. The testing conditions are those to be experienced by host rocks in disposal galleries for radioactive waste. The 3D results of the image processing show that an unsymmetrical damaged zone is induced around the hole, with a reverse deformation trend being found at the boundary

after unloading, which indicates that the significant anisotropic deformation of boom clay can be induced by mechanical unloading. In the conclusions the authors remark a significant mechanical anisotropy of the boom clay, which is related to its bedding planes. There are three key observations: (i) The convergence of the clay close to the hole wall parallel to the bedding planes is higher than the perpendicular one; (ii) A unsymmetrical damaged zone is induced around the hole after mechanical unloading. (iii) A reverse trend is observed at the boundary, and also verified inside of the sample, i.e. convergence perpendicular to the bedding is higher than the parallel one. (Fig. 6.2)

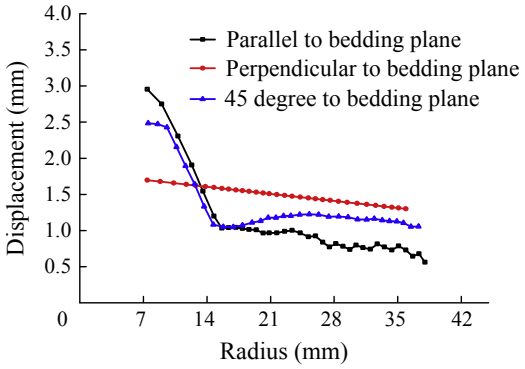

Figure 6.2: Profile of displacement in directions parallel (black), perpendicular (red), and at 45 degree (blue) to the bedding planes. (You et al., 2015)

In a similar problem than Marinelli, Kanfar et al. (2015) study the wellbore stability using a FEM model. The model considers a Biot material in order to perform a time-dependent analysis. The use of pseudo-3D FEM based on the theory of generalized plane strain, allows the freedom to analyze complex geometries such as inclined boreholes in anisotropic formation under three dimensional stress field. The study focuses on the effect of anisotropy to the failure prediction. Analytical solutions available in the literature assume transversely isotropic material with the plane of isotropy always perpendicular to the borehole axis. kanfar numerical model eliminates these assumptions accounting for a general case.

Tokiwa et al. (2013) studies the formation mechanism of fractures induced by excavation of a gallery in soft sedimentary rocks in Horonobe area, Japan. The mapping of the gallery shows that the fractures consist of both pre-existing shear fractures and excavation damaged zone (EDZ) fractures. EDZ fractures correspond to the bedding planes associated to the geological genesis of the sedimentary rock. The EDZ fractures end when intersect the pre-existing shear fractures. Therefore, formation of the EDZ fractures are controlled by pre-existing fractures and earlier weak planes (Fig. 6.3).

Underground research laboratories (URLs) for the development of high-level radioactive waste geological disposal exist in a series of countries. Wang (2014) proposes a concept of “area specific URL”. It is referred to as the facility that is built at a site within an area that is considered a potential area for HLW repository or near the future repository

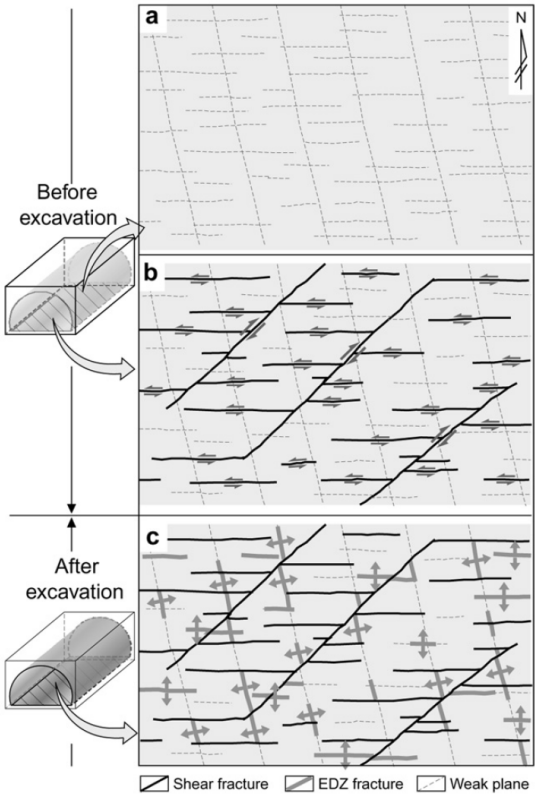

Figure 6.3: Conceptual models showing the fracture formation process before excavation (a and b) and after excavation (c) on the floor of the gallery. Weak planes (a) were formed in the first stage. Shear fractures (b) were formed in the second stage. EDZ fractures (c) were formed along weak planes at the last stage. (Tokiwa et al., 2013)

site. The paper focuses on the construction of the URL in a designated candidate area in China with a deadline in 2020.

Using experiments, Dao et al. (2015) studies the Thermo-Hydro-Mechanical (THM) behaviour of Boom Clay as a possible candidate to serve as a host-rock for the geological radioactive waste disposal in Belgium. The Connecting gallery (excavated in 2002) in the Mol underground Research Laboratory HADES (Fig. 6.4) (High-Activity Disposal Experimental Site) was investigated. The results show a cross anisotropy of natural Boom Clay and an impact of the excavation damage on the thermal property of samples near the gallery. The mechanical tests confirm the anisotropic behaviour of Boom Clay. Finally, from these experimental data, an EDZ of 4 m from the connecting gallery axis was determined.

Also using Boom Clay, Salehnia et al. (2015) present a coupled numerical model using the Lagamine finite element code. The study aims at predicting the extent of the EDZ at the large scale's excavation, around the Connecting gallery (HADES URL, Mol,

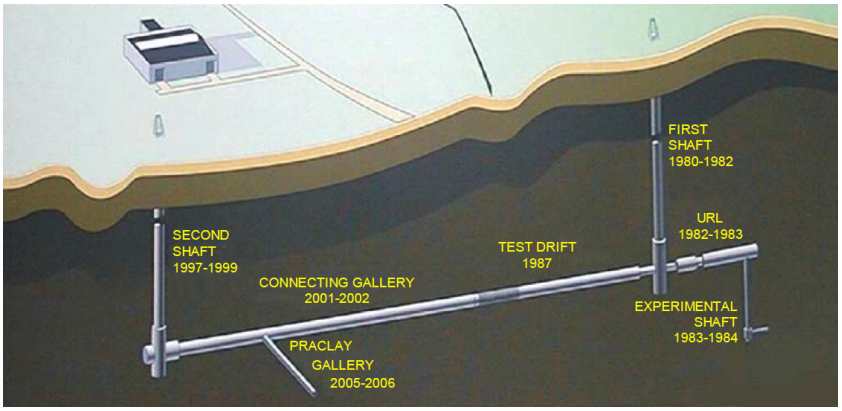

Figure 6.4: Sketch of different galleries in HADES for studying the high-level nuclear waste disposal in Boom clay. (Bastiaens et al., 2003)

Belgium) through analyzing the evolution of strain localization in shear bands mode. The mechanical constitutive law is a Drucker-Prager elasto-plastic model. The model is regularized by means of second gradient, the regularization provides the model with mesh independent results. A quarter of the gallery is used instead of the full gallery this will restrict the number of possible solutions due to the two introduced symmetries, but it is an effective way to reduce the computational cost (Fig. 6.5). A concrete lining is introduced into the model in order to determine the gallery wall impact on the evolution of the EDZ around the gallery. The paper focuses on the coupled hydro-mechanical behaviour of Boom Clay host rock during and after the gallery excavation with respect to the evolution of shear bands. The study also considers the contact problem between the lining and the rock massive. The results provide a comprehensive insight of the evolution of the EDZ, water pressure and lining contact force along time.

van den Eijnden et al. (2016) use a double scale, i.e. finite element squared (Fig. 6.6), for modelling hydromechanical coupling in the simulation of gallery excavation in the context of radioactive waste repositories. The micromechanics of Callovo-Oxfordian claystone is modelled at the microscale including pore fluid. For assessing material softening and localization phenomena in a finite element method without losing the objectivity of solutions due to the well-known mesh-dependency effects, a local second gradient paradigm is used. The local second gradient is implemented in the macroscale as a phenomenological constitutive relation. This configuration allows to keep the scale separation. The paper studies the intrinsic REV anisotropy and uses it to explain the localization orientation at the macroscale. Finally the model is calibrated with experimental measurements of Callovo-Oxfordian claystone and simulations concerning several cases of the "Transverse action" benchmark by ANDRA are carried out.

The paper concludes that the model is capable of capturing the global characteristic of strain localization in the excavation fractured zone. The difference in microstructure is demonstrated to have an important effect on the anisotropy of the macroscale material behaviour and thereby on the onset of strain localization around the gallery wall. This

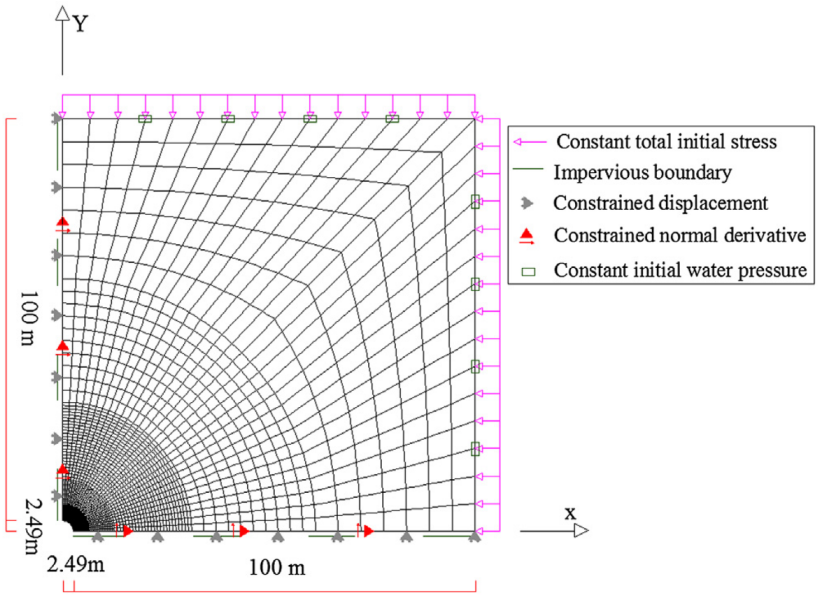

Figure 6.5: Quarter of the gallery geometry used by (Salehnia et al., 2015).

material anisotropy seems to have a decisive effect on the evolution of the localization compared to the effect of the in situ stress state anisotropy.

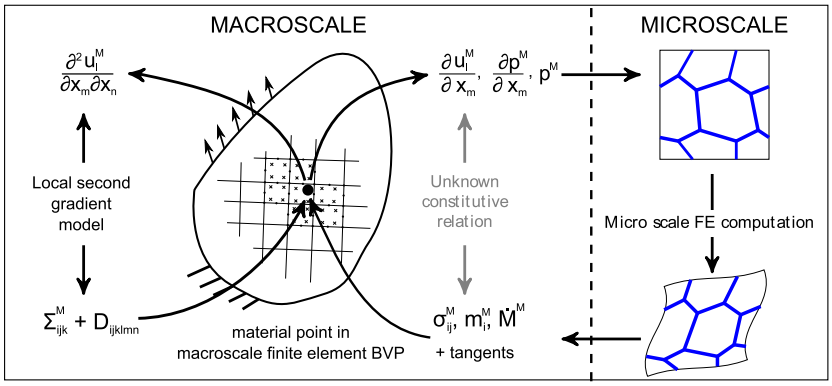

Figure 6.6: Schematic representation of the FE2 method for hydromechanical coupling with a local second gradient paradigm (van den Eijnden et al., 2016).

Lisjak et al. (2014) uses a Continuum-discontinuum model to analyze the failure mechanisms around circular excavations in anisotropic clay shales. Experimental evidence shows that the EDZ is strongly influenced by the mechanical anisotropy induced by the layered structure of the material. The model is developed in order to capture anisotropic strength. The effectiveness of the model is demonstrated by performing mechanics tests on an indurated claystone, namely Opalinus Clay. The results show good

agreement with experimental observations. The model is then applied to simulate the EDZ of a horizontally excavated tunnel (Fig. 6.7) concluding that the bedding planes have strong influence in controlling the EDZ formation process.

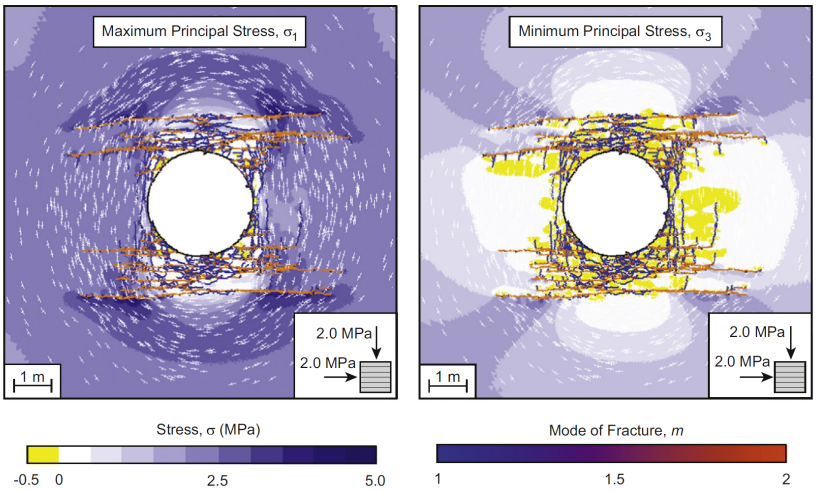

Figure 6.7: FDEM simulation results of the failure around the excavation. Colour contours on the left and right hand side represent maximum and minimum principal stresses, σ_1 and σ_3 respectively. Principal stress trajectories are indicated as cross icons with the long and short axes oriented σ_1 and σ_3 respectively. (Lisjak et al., 2014)

In a second publication, Lisjak et al. (2015) presents the results of the rock mass monitoring during the excavation of a 3 m diameter, 50 m long tunnel in the Mont Terry underground rock laboratory (URL) with special emphasis on the short-term deformation response. Later, the observations are analyzed using the hybrid finite-discrete element (FDEM) model to study the formation of the EDZ. The results show that failure is initiated in bedding planes with a critical orientation with respect to the compressive circumferential stress induced around the tunnel. The simulated fracture patterns are consistent with those observed in Mont Terri URL.

Chen et al. (2014) study the interaction between adjacent galleries in the framework of the feasibility study of high-level radioactive waste (HLW) geological disposal. The research is based on some experimental investigation by ANDRA and is devoted to provide a preliminary evaluation on the interaction between adjacent galleries using numerical simulations. The repository concept in France consists of a multi-barriers geological and engineering system. The study of the different unities involves hydromechanical behaviour of host rock (claystone) and concrete, characterized by a coupled elastoplastic damage model. A nonlinear elastic model of the Cam-clay type is applied to the bentonite plug. The numerical simulations involving all the barriers are performed with different spacing distances. The results are used to give a minimum gallery interdistance.

Different than a gallery excavation, but with a similar geometry, the pressuremeter

test will be also considered in this chapter. Menard (1965) establishes the standard rules in order to use pressuremeter test to obtain the bearing capacity of foundations. This test uses the pressure readings into an insitu borehole rather than the cohesion and angle of friction usually obtained in lab tests. The test has applications to bearing capacity of piles, foundation settlement, passive earth pressure and slope stability.

6.1.2 Controllability

The notion of controllability in a stress-strain path is introduced here in order to later understand the results of the simulations. Here controllability applies to the notion of constitutive law applied in a material point. In the later results, its meaning will be extrapolated to a macroscale BVP with mixed strain-stress boundary conditions.

In order to be able to reproduce any arbitrary time-history in the macroscale BVP, a controllability approach is needed (Nova, 1994). Controllability refers to the possibility of arbitrarily controlling stresses or strains or a combination of both in the mechanical problem, it applies to a constitutive relation in a material point. The stress and strain vectors in each iteration σ^n and ϵ^n are decomposed into two vectors in their supplementary spaces of the second order tensor space.

In each time step (n):

$$\sigma^n = \sigma_1^n + \sigma_2^n \tag{6.1}$$

$$\epsilon^n = \epsilon_1^n + \epsilon_2^n \tag{6.2}$$

We impose σ_1^n and ϵ_2^n and look for σ_2^n and ϵ_1^n:

$$\sigma_1^n + \sigma_2^n - \mathcal{T}^n(\epsilon_1^n + \epsilon_2^n) = 0 \tag{6.3}$$

Where $\mathcal{T}^n$ is a function, in our case the numerical homogenization coming from the REV. A priori $\mathcal{T}^n$ is nonlinear, Newton method will be used in order to find the solution of (Equation 6.3). The linearized form of (Equation 6.3) reads:

$$\delta\sigma_2^n - C^n : \delta\epsilon_1^n + \sigma_1^n + \sigma_2^n - \mathcal{T}^n(\epsilon_1^n + \epsilon_2^n) = 0 \tag{6.4}$$

Where C^n is the operator computed in $(\epsilon_1^n + \epsilon_2^n, \sigma_1^n + \sigma_2^n)$ in the previous iteration of the Newton method. Newton method presents quadratic convergence near the roots if a consistent tangent operator is used:$C^n = \frac{d\mathcal{T}^n}{\delta\epsilon^n}$, and the derivative of the function $\mathcal{T}^n(\epsilon^n)$ exists and it is continuous.Already seen in a previous chapter, other operators rather than the consistent tangent one have been tested in this work due to the particular properties of the function and the need to reduce the computation time.

$$C^n = \frac{d\mathcal{T}^n}{\delta\epsilon^n} \tag{6.5}$$

Depending on the combination of known stress and strain, the controllability of the loading path can be lost. In a practical sense this uses to happen with force controlled

conditions and softening material. The physical meaning of a loss of controllability can be a mechanical failure due to infinite propagation of deformation, this feature is observed in several of the simulations presented in this chapter.

6.2 Numerical model

In this section the BVP to be solved is described, as well as the numerical strategy, FEM discretization, and the result of the microscale initial state equilibration. The relation with real experiments is briefly mentioned.

6.2.1 Implementation

The problem consists on a hollow cylinder (Fig. 6.8), e.g. gallery excavation or pressuremeter test (Arcamone and Tritsch, 1985). Being in the case of a gallery excavation or a pressuremeter test will depend on the loading path. Two loading paths will be used (Fig. 6.9), one: starting from an initial stress state, equal in the outer and inner boundaries, decrease the inner pressure (gallery excavation), second: same but increase the inner pressure (pressuremeter test). In contrast with the biaxial test simulations, in the hollow cylinder, the loading is force controlled, force boundary conditions apply both in the inner and outer radius.

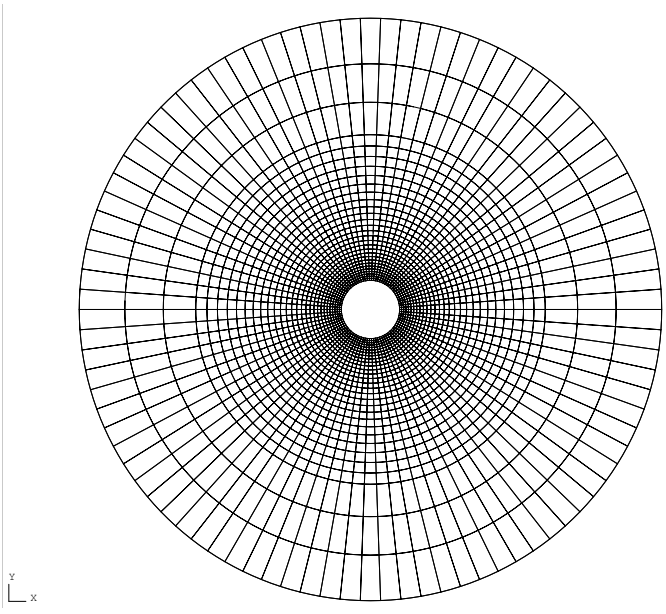

Figure 6.8: Standard hollow cylinder geometry used in all the test except in the Boundary radius study and the DEM assembly size study, inner radius=10m, outer radius=100m, 2700 Q8 elements, 160 boundary elements.

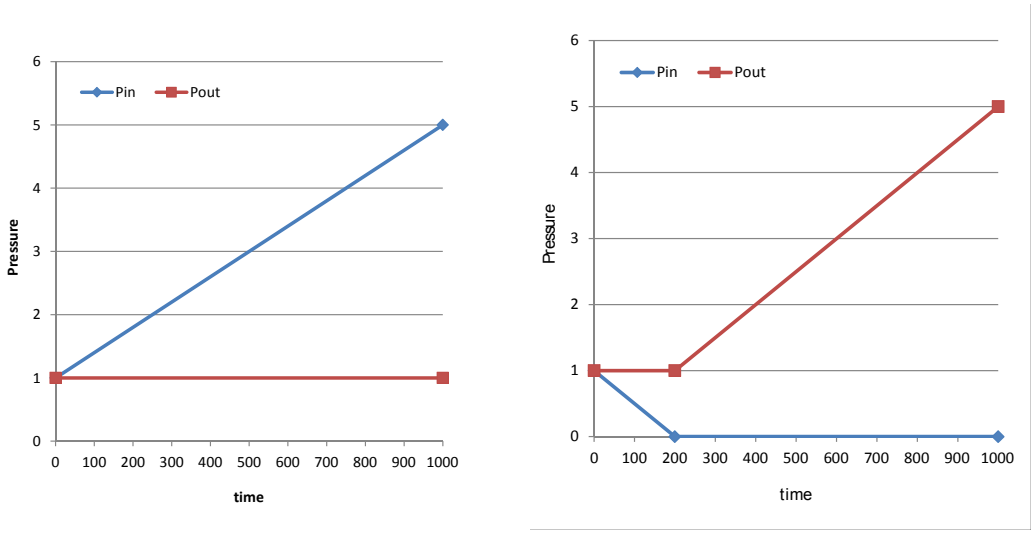

Figure 6.9: Two different loading histories used.

A radial structured mesh is used in the FEM scheme, 9 node and 4 Gauss point elements are used, the 9th node is placed in the center of the element and is needed by the Second Gradient regularization. The stress boundary condition is applied normal to the boundary surface. Additionally, 3 degrees of freedom are restricted in order to avoid kinematic indetermination. In contrast to the biaxial test, the hollow cylinder DEM assemblies can experience an homogeneous macrostructure deformation in order to accommodate the bias shear stress and be in equilibrium with the boundary conditions [1]. Because of this kinematically admissible mechanism no procedure such as a white step is needed before starting the simulation.

In a biaxial test the inclination of the shear band will be determined by the stress state in the q-p plane (Coulomb). In a hollow cylinder the situation is more complex since the state is not homogeneous before the localization as it was in the biaxial. In addition, the principal axes of stresses will likely follow the cylindrical coordinates (Fig. 6.10), in equilibrium with the the boundary conditions.

Therefore, in the cylinder there is an additional degree of freedom, the direction ψ, a priori this is not determined and any direction of a shear band would be a feasible solution for an initially isotropic case, nevertheless, any initial deviation from isotropic state can create a preferential direction in which the shear bands develop.

One possible perturbation of the initial state is the orientation of the axes of principal stresses in the DEM assemblies, when those are isotropically compressed, the σ_{xx} and σ_{yy} are imposed in the two directions of the Cartesian coordinate axes, while the σ_{xy} is

[1] Remember that this non equilibrium state was caused by a bias stress coming from the DEM assembly after the isotropic compression during the initial assembly preparation stage. The bias stress is related to the discrete nature of the microscale (Chapter 3)

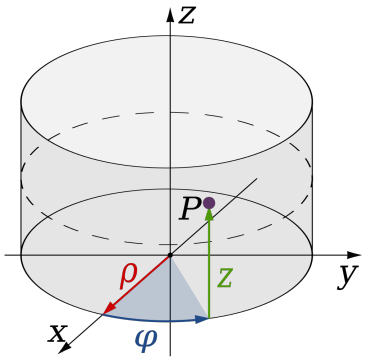

Figure 6.10: Cylindrical coordinates.

part of the solution and in general is not perfectly zero [2].

Because of the existence of the bias shear stress σ_{xy} the radius of the Mohr circle is different than zero thus it exists an orientation of the principal axes with respect the Cartesian coordinate system of 45 degrees. After the accommodation of the DEM assemblies to the cylinder boundary conditions the shear component is reduced to smaller values, as small as desired according to the precision threshold of the Newton method. Due to that, the structure presents an initial strain field (Fig. 6.11), this initial deviation from isotropic state can break the initial symmetries and determine the orientation of the localization.

6.2.2 Numerical resolution

A first test is simulated consisting in a decrease of the inner pressure. The material properties of the microscale were calibrated with results from laboratory biaxial tests (Richefeu et al., 2012).

The result is that after reaching zero pressure in the inner radius an homogeneous deformation along the circumferential direction is obtained, so no localization occurs (Fig. 6.12).

In order to push forward the deviatoric stress state and explore the possible failure, the outer radius stress is increased after removing the inner one (Fig. 6.9). This will trigger strain localization in the inner radius. The use of second gradient with a parameter $D = 5 \cdot 10^{-2}$ allows to regularize the problem having a shear band width equal to 0.21m thus restoring the mesh size independence. Due to the force controlled loading path, it is possible to reach a state of controllability loss. According to the crack growth resistance curve or R-curve (Erdogan, 2000) (fracture mechanics) and extrapolating this to the study of shear band propagation, depending on the total energy dissipation rate as a function of the band size, shear band can have an slow stable growth or become unstable so propagate indefinitely, the last case is equivalent to a loss of controllability.

[2] already mentioned bias shear stress.

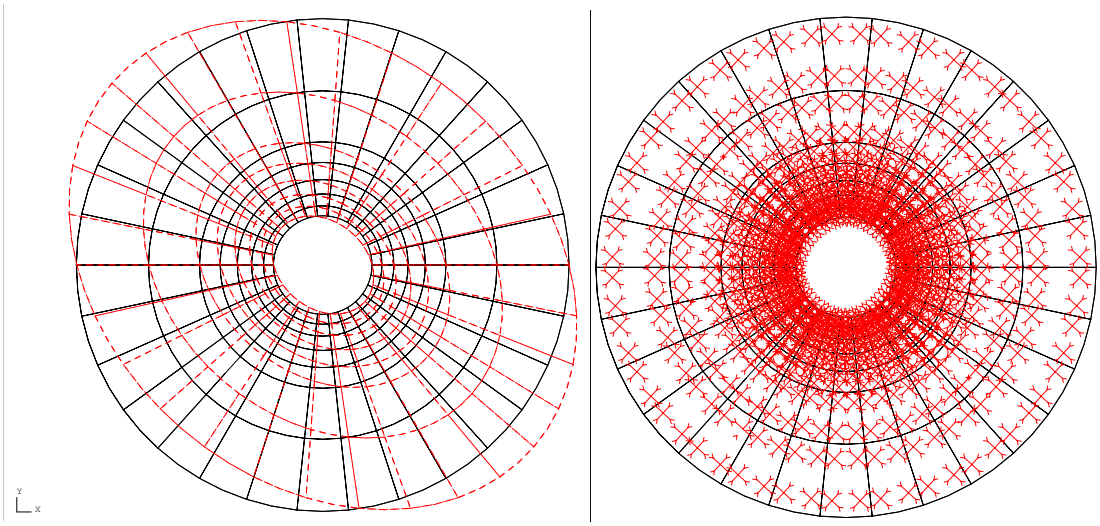

Figure 6.11: Left: Deformation of the structure after the relaxation of the bias shear stress of the DEM assemblies magnified 500 times. Right: the crosses of stresses show that after the accommodation of the DEM assemblies to the new boundary conditions without shear stress the principal axes of stresses are still 45 degrees rotated with respect to the Cartesian axes.

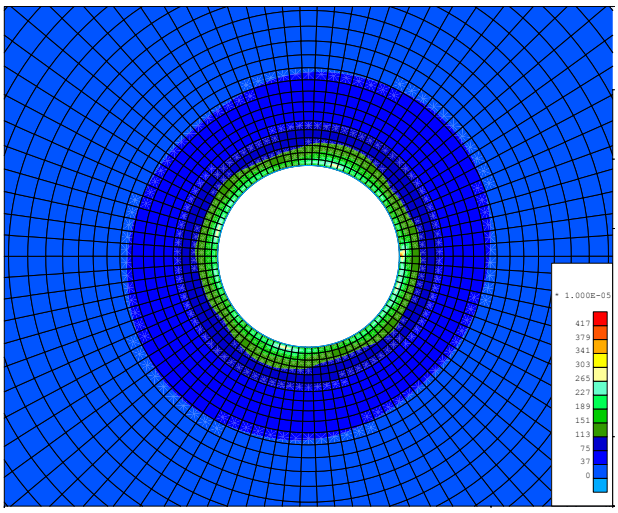

Figure 6.12: Gallery excavation test, no localization after the removal of inner pressure.

The equivalent situation in reality is the failure of the structure. During a tunnel excavation the soil will deform till it reaches a new stress state in equilibrium with the new boundary conditions. If, due to the material properties, this state cannot be reached, the deformations will grow indefinitely till the failure.

The numerical sample consists of a finite domain with an outer boundary condition,

the proximity of the outer boundary condition to the localization phenomena will affect this localization, presumably accelerating the propagation. In order to study the effect of the ratio between the outer and inner radius a parametric study is performed, in this study the inner radius is kept constant (10m) while the outer radius is varied (50m, 100m, 200m).

The results show that the distance affected by the shear bands in the 50m case is strongly affected by the outer radius with respect to the 100 and 200m cases (Fig. 6.13).

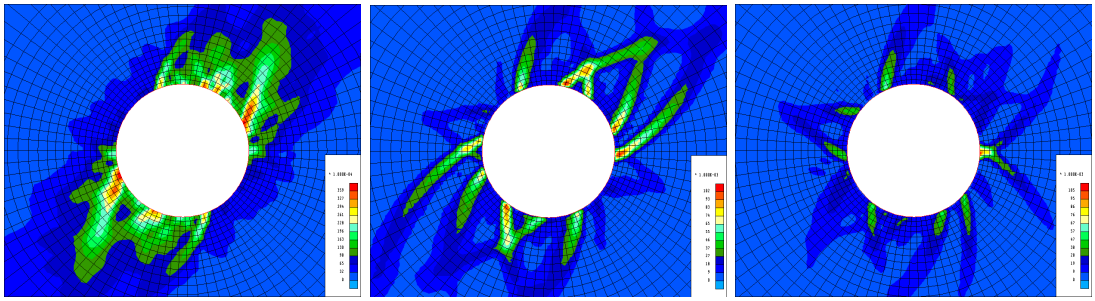

Figure 6.13: Results for the three configurations: outer radius=50, 100 and 200 m. Total value of the second invariant of strain at the end of the test.

The charging history finishes due to loss of controllability when these shear bands approach the boundary giving a sensibly different result compared to the other cases (100m and 200m). In the two other cases the charging path reached much higher final value (inner pressure 4.8 and 5 times the outer respectively). Given the similar localization mode it is concluded that the shear band development is not strongly influenced by the outer radius in the 100 and 200m cases. These result are presented before the parametric study section because their outcome will determine the geometry used for the rest of the tests. The 100m choice obeys a compromise; the biggest possible value for the outer radius is desirable to assure minimal influence to the calculations, but this would increase the computational expenses, 100m is the lower value that gives a reasonably independent behaviour with respect the outer boundary.

Comparing these simulations to FEM^2 results it's obvious that the DEM assembly is much more elastic than the micro-FEM VER, due to the high packing fraction and coordination number, so the case of decreasing the inner pressure doesn't produce any failure. In order to generate a higher variety of constitutive responses of the DEM assembly new samples are generated. The classical sample used is a 400 grains cohesive frictional assembly with cohesion force between grains equivalent to the confining pressure p*=1, coordination number 2*843/400, being 843 the number of contacts. This coordination number is abnormally high, this means that our sample is near the compacity limit, an isotropic compression cannot cause any reorientation of the grains, this is the cause of the highly elastic properties of the assembly. In order to obtain a less coordinated sample, during the isotropic compression performed to the particles, the friction is not kept zero but rather increased to some small value like $\mu = 0.1$, this gives as a result a sample with a number of contacts of 720, $\mu = 0.5$ gives a number of con-

tacts even smaller of 570. The use of these DEM assemblies is expected to provide a less elastic result, reaching localization for a lower deviatoric stress state and presenting less peak behaviour.

Another means to reduce the elasticity of the DEM assembly is to reduce or switch off the cohesion, note that gravity is not considered in the model, so the tunnel, or hollow cylinder, could be stable even without cohesion. The tests show the expected results, with a failure mode fulfilling the Mohr Coulomb criteria this time for lower values of the stress due to the lack of cohesion. The values of the driven pressure are set to be always positive non-zero (compression), having the smallest pressure equal to 1% of the initial confinement. This is done because of the unpredictable behaviour of the DEM model for zero pressure[3].

6.3 Parametric studies

In this section a series of parametric studies are presented (Table 6.1). They are intended to serve as base for the understanding of the FEMxDEM approach applied to real/engineering scale problems, in particular the hollow cylinder configuration.

Study case	No. assembly	Particles	p*	μ prep.	μ test	σ_{0H}/σ_{0V}
Outer boundary radius	1	400	1	0	0.5	1/1
Loading Path	2					
Second Gradient	2					
Far field anisotropy	2					1/1
	11					1/1.3
	10					1/2
DEM assembly size	5	400				1/1
	6	1600				
DEM coordination	9	400		0		
	8			0.625		
	7			0.25		
DEM cohesion	2		1	0		
	4		0.5			
	3		0			

Table 6.1: Input parameters for the DEM assemblies preparation

In the table 6.1 the input parameters used for the DEM assembly generation are presented, the different DEM assemblies are given an identifier from 1 to 11. The number of particles of the DEM assemblies is 400 with the exception of the DEM assembly size study in which 1600 particles are used. The cohesion is represented by the p* parameter which represents a ratio between the confining pressure and cohesion at the contact level. μ is usually 0 as described is the DEM chapter during the preparation of the sample,

[3]The particle assembly may become a gas

only in the particular of the DEM coordination study the value of the friction parameter μ is different from zero, after the preparation of the DEM assemblies μ is switched on with the desired value, $\mu = 0.5$ in all the cases. σ_{0H}/σ_{0V} refer to the initial stress state of the assemblies, 1/1 for the isotropic state and 1/x for the far field anisotropy study.

Parameters not presented in this table are the normal and tangential contact stiffnesses k_n/k_t equal to 1000/1000 for all the assemblies and the minimum and maximum particle radius R_{min}/R_{max} equal to 0.2/0.5 for all the assemblies.

The table 6.2 summarizes some output parameters resulting from the generation of the DEM assemblies. $e0$ is the void ratio of the sample after the isotropic compression stage. The lower values represent denser samples. $fn/; max/min$ is the maximum and minimum contact normal force, the negative values are possible thanks to the cohesion, in the assembly No. 3 the minimum normal contact force takes a positive value due to the lack of cohesion. The number of contacts is correlated to the coordination of the sample, being a 400 particle/843contact sample a highly coordinated one. Finally, the Wallclock time tells us how computationally heavy the computation was, being the anisotropic cases the higher ones with values up to 4 times higher than the isotropic standards, this can be put down to the plastic mechanisms being mobilized during the preparation of the anisotropic samples.

Study case	No. assembly	e_0	$f_n$max/min	Contacts	Wallclock (min)
Boundary radius	1	0.189	3.85/-0.83	843	5
Loading path	2	0.189	3.85/-0.83	843	5
Second Gradient	2				
Far field anisotropy	2				
	11	0.134	2.62/-0.10	800	15
	10	0.100	3.10/-0.34	826	20
DEM assembly size	5	0.186	3.85/-0.83	801	5
	6	0.198	2.78/-0.72	3365	12
DEM coordination	9	0.211	3.14/-0.71	820	5
	8	0.235	3.48/-0.62	733	4
	7	0.311	4.16/-0.64	628	3
DEM cohesion	2	0.189	3.85/-0.83	843	5
	4	0.187	2.53/-0.02	820	6
	3	0.179	2.55/0.07	800	7

Table 6.2: Output parameters from the assemblies preparation

The table (Table 6.3) summarizes the input parameters into the macroscale (Lagamine). The column "particles" is the total number of particles if we consider the particles contained in each of the DEM assemblies attached to a Gauss point in all the domain, this gives an indication of the computational complexity of the problem rather than a physical characteristic.

Study case	No. assembly	Outer radius	Number elements		Particles	D
			Boundary	Q8		
Boundary radius	1	50	180	1,800	2,880,000	$5 \cdot 10^{-2}$
		100		2,700	4,320,000	
		200		3,600	5,760,000	
Loading path	2	100		2,700	4,320,000	$5 \cdot 10^{-2}$
Second Gradient	2					$5 \cdot 10^{-1}$
Far field anisotropy	2-11-10					$5 \cdot 10^{-2}$
DEM assembly size	5	50	60	210	336,000	
	6				1,344,000	
DEM coordination	9-8-7	100	180	2,700	4,320,000	
DEM cohesion	2-4-3					

Table 6.3: Macroscale input parameters (Lagamine)

6.3.1 Outer boundary radius

The problem consists on a hollow cylinder in plane strain 2D, the inner radius being 10m the outer radius is yet to be determined in order to avoid any influence of the outer boundary to the results, note that in reality there is not such thing as the outer cylinder boundary. For this purpose a parametric study using 3 different outer boundary radius are carried, the 3 chosen radius are 50m, 100m and 200m. The resulting number of elements in the FEM discretization is respectively: 1980, 2880 and 3600, this values include the boundary elements named "LICHA" in the code Lagamine (Fig. 6.14).

The result of this parametric study is a clear influence of the outer limit in the case with outer radius of 50m and no qualitative influence for the cases with radius 100m and 200m (Fig. 6.13).

This can be quantitatively observed in the stopping time during the loading history (Tab. 6.4) because of loss of controllability in the 50m case. The lower the outer radius the bigger the influence on the simulation and so the earlier the loss of controllability. The third case is the only one which does not meet the end of controllability. As expected bigger meshes are translated into heavier computations (Tab. 6.5)

Outer radius (m)	Ratio Re/Ri	Force multiplier	Max. VM strain[4] (%)
50	10	3.41	3.59
100	20	4.81	10.2
200	40	5.00	10.5

Table 6.4: Outer boundary study: output data

[4]VM refers to the second invariant of strain (Von Mises strain), "Max. VM strain" is the maximum value of the Von Mises strain in the domain, so it is a punctual value. Usually it is located in the area

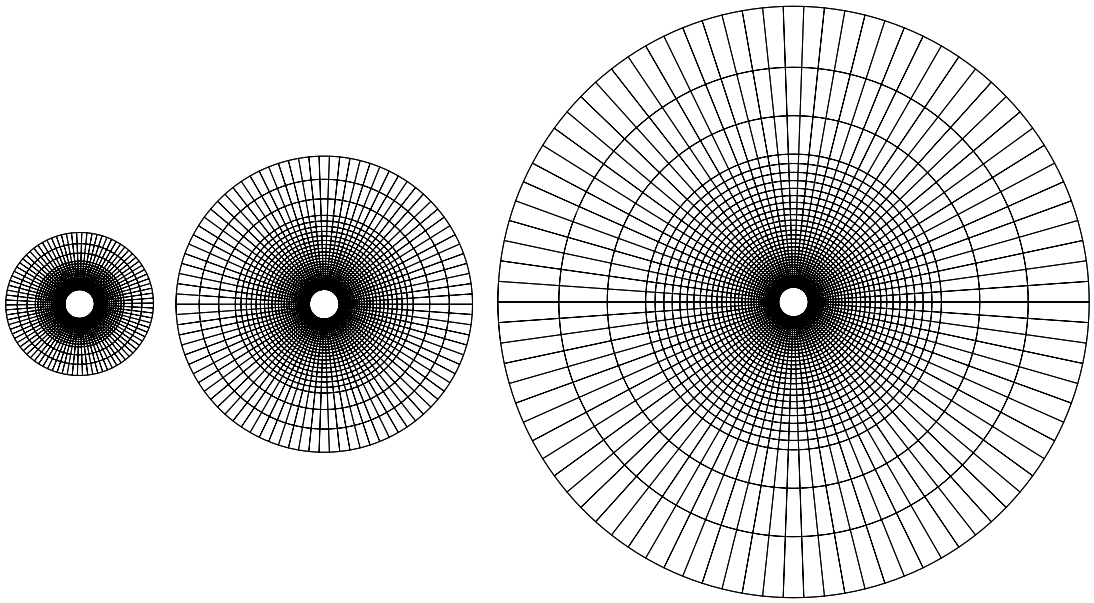

Figure 6.14: Meshes used for the outer boundary radius study: outer radius=50, 100 and 200 m.

Outer radius (m)	Number of itrations	Number of steps	Non conv. steps[5]	Wallclock time (days)	Stopping criteria[6]
50	256	129	30	1.17	10 steps not converging
100	691	200	32	1.88	10 steps not converging
200	443	205	0	2.85	end of loading

Table 6.5: Outer boundary study: output numerical

These results will determine the geometry for the rest of parametric studies to inner radius 10m, outer radius 100m being this the smallest radius that provides acceptable results.

6.3.2 Loading path

In this subsection the two possible loading paths are presented (Fig. 6.9), the first one, consisting on an increase of the inner pressure, and keeping constant the outer one, is intended to emulate a pressuremeter test. This is a classical test used in geotechnical

where the band meets the inner boundary.

[5] In total, including the last 10 consecutive non converged steps.

[6] "10 steps not converging": Lagamine loading strategy is set to allow 10 consecutive steps without convergence before stopping, then the simulation is halted. "manual" means that several non converged loading steps are already observed and the simulation is very likely to follow this trend till the threshold of 10, given this situation the simulation is manually stopped to save computational time.

applications. It consists in applying pressure in a balloon introduced in a drilling, the evolution of the pressure vs the volume changes of the balloon gives very rich information about the mechanical properties of the soil. In addition it is a very vastly documented test allowing us to use the existing data to validate the numerical results.

The second loading path consists on a decrease of the internal pressure, it emulates the release of tensions occurring around the gallery during the excavation of it. A particular loading path is applied in order to reach the failure of the model in some cases: if the plastification is not reached when the inner pressure becomes zero, then, the outer pressure is increased till it induces a plastification around the gallery excavation.

The loading path corresponding to the increase of inner pressure leads to a more localized result. Several sets of shear bands appear around the gallery while in the case of the decrease of inner pressure the plastification zone is more diffuse without clear definition of shear bands (Fig. 6.15).

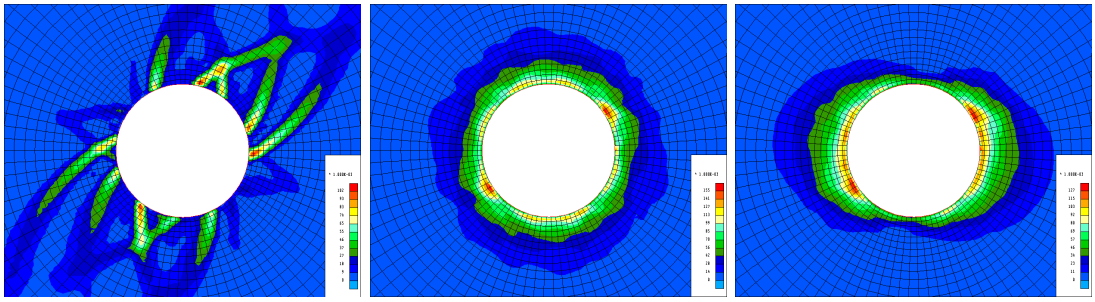

Figure 6.15: Results for the two configurations: increase of inner pressure and decrease of inner pressure. And decrease of inner pressure with an anisotropic far field stress state. Total value of the second invariant of strain at the end of the test.

The simulation of the first case reaches the end of the loading history while the second and third cases do not (Tab 6.6), the loading scenario of the first case will be retained for the rest of simulations, specially because of the developing of shear bands which renders it interesting for the second gradient analysis. The stopping of the second and third simulations seem to be due to a loss of controllability of the force controlled loading, the computational time and stopping point in the loading history corroborate that (Tab 6.7).

Loading path (internal pressure)	σ_{V0}/σ_{H0}	Force multiplier	Max. VM strain (%)
Increase	isotropic 1/1	5.00	8.58
Decrease	isotropic 1/1	3.12	15.5
Decrease	anisotropic 1.3/1	2.56	12.7

Table 6.6: Loading path study: output data

Loading path	Number of itrations	Number of steps	Non conv. steps	Wallclock time (days)	Stopping criteria
Increase inner p.	383	205	0	0.96	end of loading
Decrease inner p.	188	158	2	2.75	manual (not conv.)
Decrease inner p.	312	144	5	3.25	manual (not conv.)

Table 6.7: Loading path study: output numerical

6.3.3 Second Gradient

A Second Gradient macroscale regularization has been proved to be effective to bring mesh independence and improve the Newton method iterative scheme near the bifurcation. This has been shown in a biaxial test. This subsection is intended to test the performance of this approach in a real scale problem. To do so, two simulations are executed, one of them with the same second gradient parameter as all the other simulations in this chapter, and a second one with a ten times bigger second gradient parameter. This parametric study tries to confirm the Second Gradient parameter correlation with the shear band width. The results show the expected behaviour (Fig. 6.16) according to the relation:

$$l_{SG} = \alpha\sqrt{D} \tag{6.6}$$

Being:
α a coefficient
l_{SG} the characteristic length
D the second gradient parameter

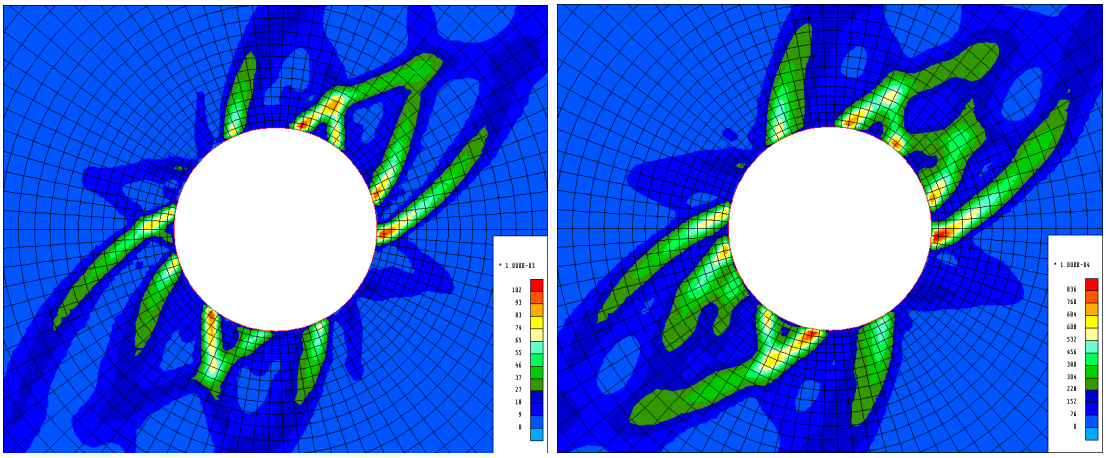

Figure 6.16: Results for the two configurations: Second gradient parameter $5 \cdot 10^{-2}$ and $5 \cdot 10^{-1}$. Total value of the second invariant of strain at the end of the test.

The first case reaches the end of the loading history, (i.e. force multiplier=5), while the second is manually stopped when the force multiplier is 4.91 (Tab. 6.8). This end

of the simulation is due to convenience because of the computational cost (Tab. 6.9) rather than the end of controllability. The maximum shear strain is lower for the second simulation at the stopping stage, this observation is rather puzzling since the second gradient regularization is expected to improve the convergence rates. The explanation why the second sample is taking more time is because, the two cases being regularized, the second one having a larger internal length, the strain localization of the second one involves a larger number of elements which causes the DEM integrations to consume a bigger proportion of computational time.

Second gradient parameter (D)	Force multiplier	Max. VM strain (%)
$5 \cdot 10^{-2}$	5.00	8.58
$5 \cdot 10^{-1}$	4.91	8.36

Table 6.8: Second Gradient study: output data

Second gradient parameter (D)	Number of iterations	Number of steps	Non conv. steps	Wallclock time (days)	Stopping criteria
$5 \cdot 10^{-2}$	383	205	0	0.96	end of loading
$5 \cdot 10^{-1}$	411	205	43	4.85	manual (not conv.)

Table 6.9: Second Gradient study: output numerical

The conclusion is that the second gradient regularization can effectively control the characteristic length of the problem and so determine the with of the shear bands preventing from mesh dependency and preserving the separation of scales.

6.3.4 Far field stress state anisotropy

The previous simulations are performed considering an isotropic state, both in the far field stress state and in the material properties. It is known that this ideal state is hardly found in reality (Armand et al., 2013, 2014; Guayacán-Carrillo et al., 2016), depending on the geological history of the soil this will present different combinations of anisotropic stress states and also material anisotropy. The combination of this two features will determine the mechanical behaviour of the soil. In this subsection the subject of study is the far field anisotropy keeping the material properties isotropic.

In order to be in equilibrium with the imposed far field anisotropic stress state at the beginning of the test the microscale assembly must be driven to the desired stress state. This is done via DEM techniques, in particular, a biaxial loading is applied to the assembly in order to reach the desired stress in both axes. This biaxial compression remains in the very beginning of the pre-peak elasto-plastic branch, so it can be assured that the contact network is essentially unaltered keeping the material properties constant.

Three different assemblies are prepared for the 3 parametric cases, with a ratio between the vertical and horizontal pressure respectively V:H=1:1, 1.3:1, and 2:1. being 1:1 the isotropic case, 1.3:1 a typical value coming from in situ observations (Armand et al., 2013, 2014; Guayacán-Carrillo et al., 2016) and 2:1 a hypothetical case with strong stress state anisotropy.

From the results it can be observed that the cases with anisotropy present a very different failure mode (Fig. 6.17).

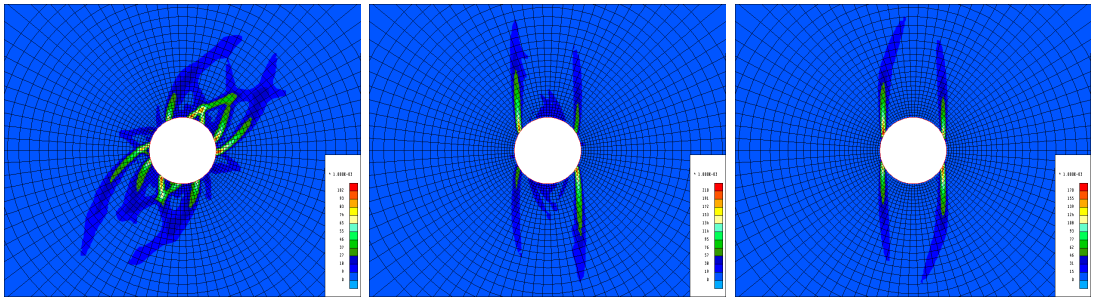

Figure 6.17: Results for the three configurations: isotropic, $\sigma_{0H}/\sigma_{0V} = 1/1.3$ and $\sigma_{0H}/\sigma_{0V} = 1/2$. Total value of the second invariant of strain at the end of the test.

Only the isotropic stress state case reaches the end of the loading history within the controllable conditions, the other two simulations lose controllability, earlier for the case with the biggest anisotropy (Tab. 6.10). The computational cost is in accordance with the previous observations (Tab. 6.11), the computational cost comparison between the two anisotropic cases is not representative since the simulation was stopped manually.

Initial stress state (σ_{V0}/σ_{H0})	Force multiplier	Max. VM strain (%)
1/1	5.00	8.58
1/1.3	4.40	21.0
1/2	3.00	17.0

Table 6.10: Far field anisotropy study: output data

Initial stress state (σ_{V0}/σ_{H0})	Number of itrations	Number of steps	Non conv. steps	Wallclock time (days)	Stopping criteria
1/1	383	205	0	0.96	end of loading
1/1.3	194	847	144	5.92	manual (not conv.)
1/2	290	126	92	3.13	manual (not conv.)

Table 6.11: Far field anisotropy study: output numerical

6.3.5 DEM assembly size

Making a decision on the size of the DEM assembly is not an easy task. The chosen DEM model must be big enough to fulfill the assembly conditions but still provide us light enough computations in order to run multiscale simulations with reasonable time. In the other side, the DEM model must not present localization, if it does it can not be considered an REV anymore. In order to avoid the microscale localization the assembly is kept below some size limits. It is not clear if keeping the assembly below some size limits avoids the localization, or the localization still happens but we are not able to visualize it due to the resolution provided by the resulting discrete assembly. In previous works by Nguyen et al. (2013, 2014) and Guo and Zhao (2013, 2014), studies have been carried in order to determine the optimal DEM assembly size, ending up in a value of 400 particles. The study conducting to this results was done with one FEM element, 4 integration points, 8 nodes. The criteria to choose this size was to use the smallest possible assembly that can still converge using the Newton method without the improvements done in the present project.

Both the macroscale size of that test and the performance of the iterative schemed are outdated, without mentioning the speedup due to the parallelization of the code. A study of the size of the DEM assembly and its effects on a real scale problem is needed. In this study two cases are presented, one with the classical 400 grains DEM assembly and a second one with 1600 grains. For this study the macroscale geometry used is coarser in order to avoid non reasonably high computational values for the 1600 grains case. The geometry is the same as in previous cases but with a discretization of 270 elements, the loading history consists in an increase of the inner pressure.

The results obtained from this test are not representative enough to extract a conclusion concerning the optimal DEM assembly size, nevertheless, the results show a qualitative resemblance that validates the two sizes (Fig. 6.18).

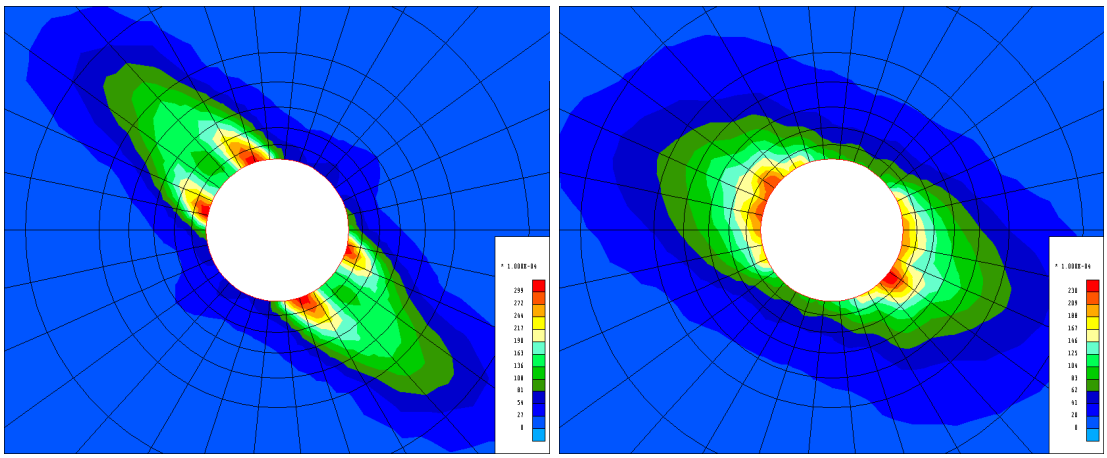

Figure 6.18: Results for the three configurations: assembly size = 400 and 1600 particles. Total value of the second invariant of strain at the end of the test.

Both simulations stop before the end of the loading history because of loss of controllability. Both of them stop in a similar stage of applied load (Tab. 6.12), this enforces the fact that both microscales are representative of the same material.

Number of grains	Force multiplier	Max. VM strain (%)
400	3.49	2.99
1600	3.42	2.30

Table 6.12: DEM REV size study: output data

The computational time of the 400 particle microscale is higher than the one with 1600 particles (Tab. 6.13), this is interesting since in the previous experiences by Nguyen et al. (2013, 2014), the computational time was invariantly increasing with the size of the microscale. The lower computational time of the simulation with 1600 particle microscale can be put down to a more efficient convergence of Newton method. This faster convergence could be explained by the better quality constitutive law provided by a bigger microscale, nevertheless, since the stopping method was manual, this can not be confirmed. Also remark that the simulations in (Nguyen et al., 2013, 2014) where not taking profit of an element loop parallelization, element loop parallelization may improve its efficiency with a coarser granularity [7] specially if the number of parallel processes is large, i.e. massive parallelization.

Number of grains	Number of itrations	Number of steps	Non conv. steps	Wallclock time (days)	Stopping criteria
400	582	143	117	3.63	manual (not conv.)
1600	339	133	58	2.00	manual (not conv.)

Table 6.13: DEM assembly size study: output numerical

Another key point to take into account is the precision obtained in the numerical simulations, this is the precision used to stop the Newton iterative scheme, a typical value used in FEMxDEM is 5E-3 for the norm of the forces or 1E-2 for the norm of displacements. Due to the noisy behaviour of the constitutive law coming from the integration of the DEM assemblies, these seem to be the more precise values we are able to get with this FEMxDEM approach. Using a bigger DEM assembly seems to provide a smoother response, so it could be a way to improve the precision of the method.

Future developments of the method, mainly a MPI Gauss point parallelization could be a promising way to increase the DEM assembly size without ending up with too high wallclock times.

[7] In a parallelization paradigm, the granularity is the ratio between the time devoted to compute the parallel jobs and the time devoted to communicate data between the parallel jobs and the main process.

6.3.6 DEM coordination number

In a DEM assembly the coordination number is the average number of contacts per grain, e.g. a coordination number of 4 represents a highly coordinated sample, while a coordination number of 2-3 would be a poorly coordinated sample, values over 4 are extremely high and difficult to reach in reality unless there is a lot of overlapping between particles.

In the previous tests the coordination number of the DEM assemblies is around 4.2, this represents a highly coordinated sample, near the upper limit of what can be considered realistic. This choice was made because in the DEMxFEM model a high density of the sample is required in order to avoid buckling phenomena which results in a hardly derivable constitutive law.

Buckling happens in a granular assembly when, under compressive loads, the grains rearrange in a new, more compact configuration, this leads to a sudden decrease of the stresses (in a strain controlled path), the stresses will not recover the previous values till the applied strain catches up with the new granular configuration. In a force controlled path this may cause an eventual loss of controllability. This phenomena is one of the reasons that can trigger negative eigenvalues of the Newton operator, and so end up with an ill posed boundary value problem at the macroscale.

In a normal DEM assembly preparation procedure, i.e. isotropic compression, the coordination number is strongly correlate to the density or packing fraction, so if we want a high density sample, we will obtain also a highly coordinated sample.

In order to study the influence of the coordination number on the results, a specific technique is used in order to create a high density sample with a low coordination number. It is known from DEM experiments that such specimen will yield a mechanical behaviour with a less stiff pre-peak loading branch, and a less brittle behaviour after peak. This results are more close to 3D DEM simulations.

The procedure followed to obtain the low coordinated samples is the following: first a sample with high coordination number and high density is used. An isotropic expansion is applied to this sample in a way that no overlapping exists between any contact, after that the isotropic compression is applied again in order to reach the desired confining pressure but this time a friction coefficient is used in the contacts[8], the variation of this coefficient allows us to obtain differently coordinated samples with almost the same density.

Three simulations are performed, assemblies with 628, 730 and 820 contacts respectively, the 820 contacts is in the same order of magnitude as the one used in the previous tests. The results show that with a less coordinated sample results in a less localized specimen and higher values of the maximum deviatoric strain (Fig. 6.19).

Only the sample with 820 contacts reaches the end of the loading history, the other two reach the end of controllability, the lower the coordination number the earlier. (Table 6.14), the computational times are in accordance with this, when the loading path

[8] in contrast to the classical preparation method in which during the compression stage the friction is set to zero in order to obtain dense samples.

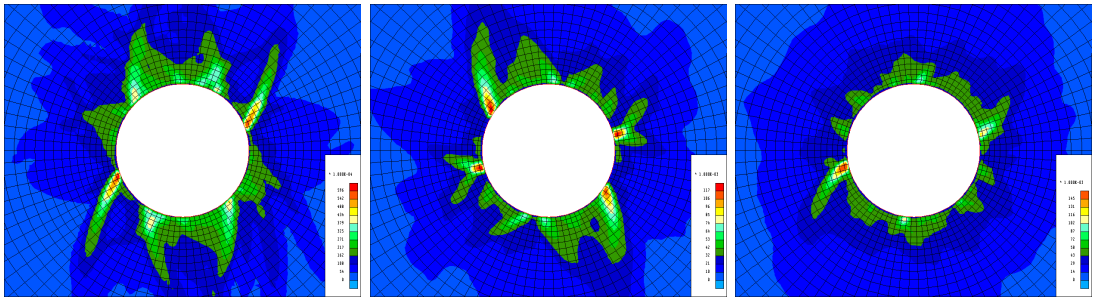

Figure 6.19: Results for the three configurations: assembly's number of contacts = 820, 733 and 628. Total value of the second invariant of strain at the end of the test.

approaches the end of controllability the iterative method becomes slow (Table 6.15).

Number of contacts	Coordination number (Z)	Force multiplier	Max. VM strain (%)
820	4.10	5.00	5.96
733	3.67	4.65	10.0
628	3.14	3.69	15.6

Table 6.14: DEM coordination study: output data

Number of contacts	Number of itrations	Number of steps	Non converged steps	Wallclock time (days)	Stopping criteria
820	383	205	0	2.00	end of loading
733	793	197	50	5.77	manual (not conv.)
628	1427	172	185	5.77	manual (not conv.)

Table 6.15: DEm coordination study: output numerical

The conclusion is that the control of the coordination number independently from the density at the DEM level is an effective technique to govern the constitutive behaviour of the material. This can be of interest when using a 2D DEM model in order to simulate 3D granular materials.

6.3.7 DEM cohesion

Following the same pattern as the previous two subsections another microscale feature is modified, this time consisting on the DEM cohesion. p* is defined as the ratio between confining force and cohesion force. In the previous simulations the value was p*=1, in this study two additional simulations are executed with values p*=0.5 and p*=0.

The manner how cohesion is introduced into the DEM model is the following: after the isotropic compression of the granular assembly, and when the grain contacts have not yet friction, the cohesion force is added according to the definition of p*, then

another isotropic compression stage with imposed boundary force is performed in order to equilibrate the new cohesive conditions. Once the sample reaches equilibrium the friction coefficient is added at the contact level, which does not alter the equilibrium state. The DEM assembly is ready to be injected into the Gauss points of the FEMxDEM model.

The results show, in a similar way than for the parametric study on the coordination number, that a lower cohesion yields a less brittle response so a less localized deformation field (Fig. 6.20).

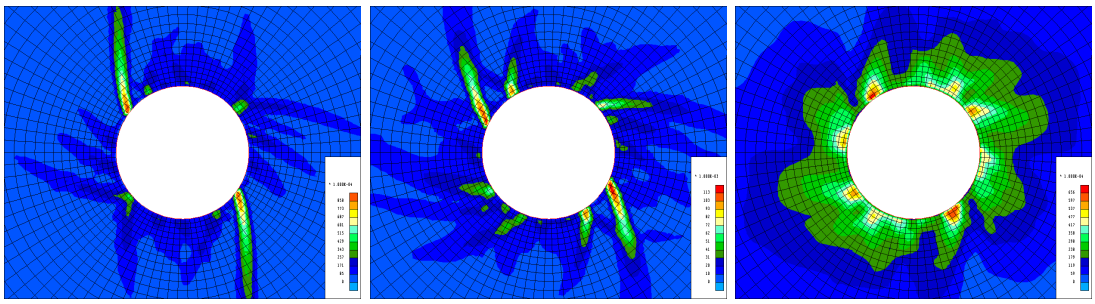

Figure 6.20: Results for the three configurations:cohesion p* = 1, 0.5 and 0. Total value of the second invariant of strain at the end of the test.

Same as for the parametric study on the coordination number, only the standard p*=1 reaches the end of the loading history (Table 6.16), the other two simulations will reach the end of controllability the lower the cohesion the earlier.

Cohesion (p*)	Force multiplier	Max. VM strain (%)
1	5.00	8.58
0.5	4.62	11.3
0	3.76	6.56

Table 6.16: DEM cohesion study: output data

Cohesion (p*)	Number of itrations	Number of steps	Non converged steps	Wallclock time (days)	Stopping criteria
1	383	205	0	0.96	end of loading
0.5	806	202	107	10.94	manual (not conv.)
0	203	145	46	5.94	manual (not conv.)

Table 6.17: DEM cohesion study: output numerical

The conclusion is that cohesion forces can effectively be introduced in the microscale, this renders the FEMxDEM approach capable of modelling a wide range of Mohr-Coulomb materials.

6.4 Intrinsic material anisotropy

Previously to this section a parametric study on the far field stress state anisotropy has been presented. In that case the anisotropy of the problem was due to the boundary conditions, i.e. extrinsic anisotropy, while the material properties being isotropic. In this subsection the material anisotropy is studied, i.e. intrinsic anisotropy (Wang et al., 2013). To do so a special preparation of the DEM is needed.

6.4.1 DEM generation

The DEM assembly has been submitted to a time-history of deformation reaching its yield surface so inflicting non reversible deformations. This deformations will reorganize the contact network in a way that the material will become intrinsically anisotropic.

The used procedure is to perform a biaxial test after the isotropic compression stage at the end of the preparation of the assembly (Figure. 6.21). Two points of this strain-stress story are chosen, one around 0.3% of axial deformation represents an elastoplastic stage in which no massive grain sliding occurred yet, the second one around 0.63% is representative of a much more deformed state in which massive grain sliding occurred resulting in an important contact network reorganization (Figure. 6.22).

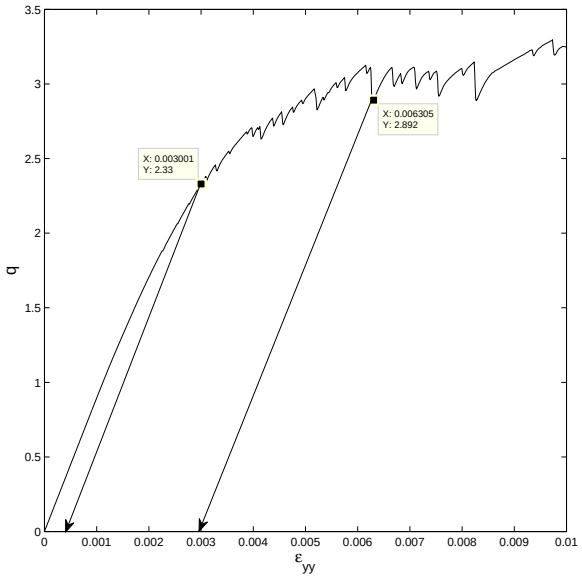

Figure 6.21: Preparation of the DEM assembly, biaxial stress-strain plot, two yield states reached.

The initial assembly status is used now to run a biaxial test with an end in each of the previous defined points, at this stage each of the tests is discharged as shown in

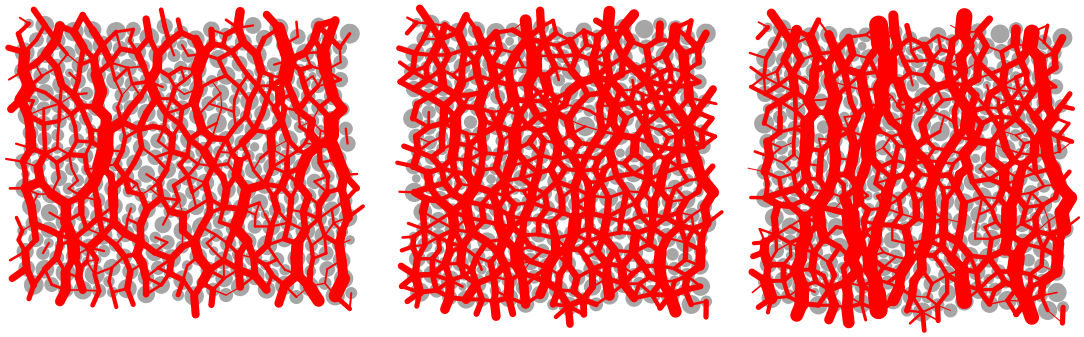

Figure 6.22: DEM granular assembly preparation. Form left to right: only isotropic compression, anisotropic precharge 0.3%, anisotropic precharge 0.6%.

figure 6.21. The discharged assemblies have an isotropic stress state and they are ready to be used in a FEMxDEM simulation (Figure. 6.23).

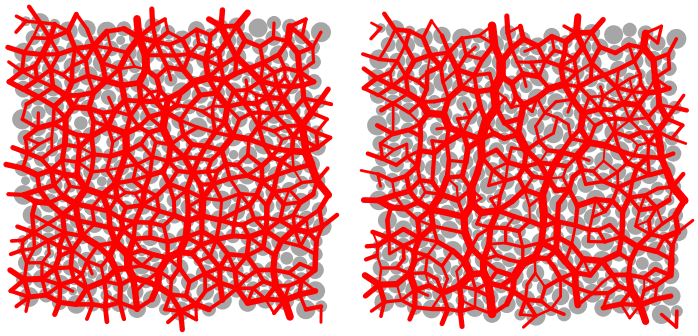

Figure 6.23: DEM granular assembly preparation, discharged states. Form left to right, maximum anisotropic precharge 0.3%, maximum anisotropic precharge 0.6%.

In order to quantify the material anisotropy of these assemblies the elastic tangent moduli is computed via perturbation and consistent homogenization. In order to simplify the analysis of the tangent matrix, the coefficients C_{1111} and C_{2222} are the only ones presented representing the horizontal and vertical stiffnesses respectively (Table. 6.18). The assembly with a precharge equal to 0.3% presents the same values as in the initial state showing that at this precharge level the deformation is mostly elastic. The assembly with a precharge equal to 0.63% shows an important degradation of the elastic moduli, this is more accentuated in the horizontal direction resulting in a material anisotropy of 12.3% in contrast to the initial 1.3%

The anisotropy generated is said to be intrinsic to the material since after the computational homogenization each microscale is representative of a material point at the macroscale. Another mean to introduce anisotropy to the model could be to build a layered structure at the macroscale with different materials being intrinsically isotropic, this

would be an extrinsic anisotropy model. Combinations of both intrinsic and extrinsic anisotropies are also possible.

Deviatoric precharge (%)	Moduli C_{1111}	Moduli rate C_{1111}/C^0_{1111}	Moduli C_{2222}	Moduli rate C_{2222}/C^0_{2222}	assembly anisotropy C_{2222}/C_{1111}
0	1125	1	1110	1	0.987
0.3	1125	1	1110	1	0.987
0.63	880.7	0.782	988.9	0.891	1.123

Table 6.18: DEM precharge stress material anisotropy: assemblies properties

6.4.2 Results

Three simulations are prepared using the reference gallery geometry from previous study cases, one is fed with the DEM assembly after isotropic compression as a reference, and the other two with the anisotropic assemblies. The test consists on an increase of the internal pressure from 1 to 5 keeping the outer pressure constant equal to 1. The middle state is shown (inner pressure=2.5) (Figure. 6.24), as well as the end of the tests (Figure. 6.25).

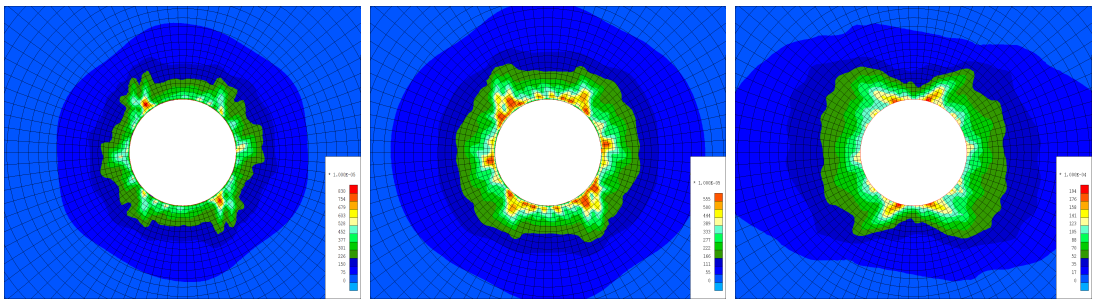

Figure 6.24: Results for the three configurations at the time 500: isotropic, anisotropic precharge 0.3%, anisotropic precharge 0.6%. Inner pressure=2.5. Total value of the second invariant of strain at the end of the test.

The deformation state at the middle of the loading story (Figure. 6.24) already shows a loss of radial symmetry for the second and third configurations due to the material anisotropy, this shows the ability of the material anisotropy to effectively influence the onset and evolution of localization in this problem.

Concerning the stability of the structure, the first and second simulations reached the end of the imposed loading history while the third one, which corresponds to the highest anisotropy, does not reach the end of the loading due to a loss of controllability (Figure. 6.25) (Table 6.19). This makes evident the effect of the intrinsic material anisotropy on the simulation. The more advanced state of deformation and failure can be reflected on the higher computational cost of the third case (Table 6.20)

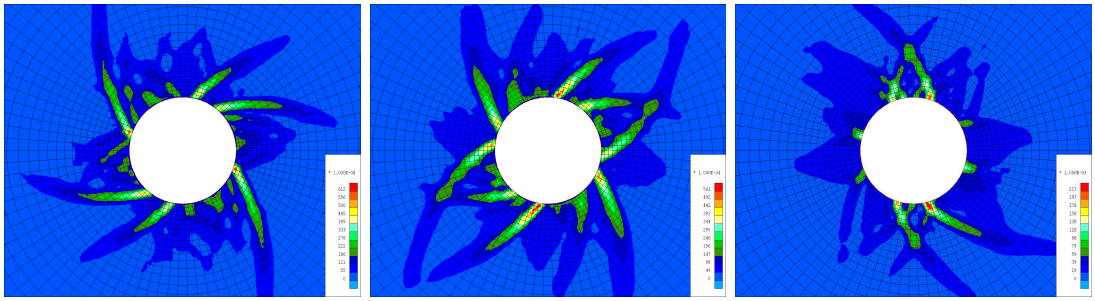

Figure 6.25: Results for the three configurations at the end of the test: isotropic, anisotropic precharge 0.3%, anisotropic precharge 0.6%. Inner pressure=5.0. Total value of the second invariant of strain at the end of the test.

Deviatoric precharge (%)	Force multiplier	Max. VM strain (%)
0	5.00	5.41
0.3	5.00	6.12
0.63	4.46	21.70

Table 6.19: DEM precharge stress material anisotropy: output data

Deviatoric precharge (%)	Number of itrations	Number of steps	Non converged steps	Wallclock time (days)	Stopping criteria
0	363	203	0	0.12	end of loading
0.3	376	204	0	0.25	end of loading
0.63	1131	199	12	8.12	10 steps not conv.

Table 6.20: DEM precharge stress material anisotropy: output numerical

The technique shows the ability to embed a DEM microscale with intrinsic anisotropy, this can be used in geotechnical problems to account for the material anisotropy result of the geological genesis. The intrinsic material anisotropy can be used together with the extrinsic as the one result of geological layering or the stress state anisotropy.

6.5 Conclusion

A series of parametric studies have been presented in this chapter, those include macroscale variations: BVP geometry, loading scenario, second gradient regularization and stress field anisotropy, and microscale variations: DEM assembly size, DEM coordination number and DEM cohesion. In addition, the use of DEM in the microscale is exploited in order to provide the model with intrinsic material anisotropy which can be used together with extrinsic material anisotropy and stress field anisotropy.

The macroscale variations show the ability of the multiscale FEMxDEM model to treat continuum BVP as if it was a classical FEM approach, furthermore, the second

gradient regularization allows to control the constitutive behaviour till the second order of the displacements which regularizes the problem.

The microscale parametric studies show the advantages of the FEMxDEM model in terms of microscale richness, allowing to control the macroscale behaviour with the manipulation of the microscale parameters. The ambition of the model is to be able to extract the microscale characteristics of the material from experiments and calibrate the microscale without the need of a macroscale calibration. The multiscale nature of the model, and in particular the characteristics of the DEM, is exploited to introduce intrinsic material anisotropy which does not come from a phenomenological relation but rather from the microscale genesis. This microscale genesis can emulate the geologic genesis of real geomaterials in order to obtain a representative material without macroscale calibrations.

One of the main differences when comparing the numerical results with the observations in tunnel drilling on granular materials is that in the numerical model few big shear bands govern the evolution of the failure while in the observations many little shear bands will develop near the excavation surface. In a previous chapter, a study on the material variability based on the DEM assembly generation was done in order to understand what are the mechanisms involved during the onset of localization. In this case the comparison between the numerical results and real observations suggest that similar approaches might be of interest to build a more accurate model. All the parametric studies presented during the present chapter can be used along with spatial material variability, and the appropriate mesh refinement and second gradient parameters in order to characterize different materials.

Chapter 7

Conclusion

A multi-scale FEMxDEM model has been presented; this approach overcomes the need of macroscale phenomenological assumptions and calibrations needed in a classical analytic law FEM model. The model shows the ability to use a microscale numerical homogenization of a DEM model to provide a constitutive relation.

The particularities of the FEMxDEM model in the way it has been implemented makes inappropriate the use of a Consistent Tangent Operator (CTO) in the Newton method, mainly because the computational time and noisy law provided by the DEM. Alternatives to the CTO existed prior to this work, namely the Auxiliar Elastic Operator (AEO) and the Upper bound Kruyt Operator (UKO), although being good alternatives to the CTO they still present some drawbacks. Other operators are developed in order to improve the performances of the model. The DEM Quasi-static Operator (DEMQO) uses the same numerical approach as the consistent (CTO) but considering an elastic DEM assembly; the Pre-Stressed Truss-Like Operator (PSTLO) uses an analytical description of the granular assembly to obtain the elastic moduli directly from the vectorial expression of its contact network. Finally, the same analytical description is used to provide an improved version of the UKO: the Kruyt Augmented Operator (KAO), this time including in the equations the pre-stresses and particle rotations. The benchmarking shows that the PSTLO gives the best results in terms of convergence, and the DEMQO in terms of computational time.

A chapter has been devoted to the introduction of random field to the Boundary Value Problem (BVP), and more particularly to the random generation of different DEM assemblies to introduce macroscale heterogeneity. The random generation of different DEM assemblies with the same properties at the contact level is exploited in order to simulate the variability of real granular materials. The breaking of symmetries and consequent increase of complication of the model allows FEM×DEM model to better predict the mechanical behaviour of real materials and supposes an increase of computational performance.

First order models do not present any internal length, this poses some issues as the problem undergoes softening and strain localization, i.e. mesh dependency. A second gradient regularization is used to provide the model with an internal length. The second gradient regularization is of special interest in the FEMxDEM model; because of the noisy behaviour of the DEM constitutive law the problem is very likely to lose its ellipticity leading to an ill posed problem. The second gradient regularization allows to avoid the loss of ellipticity not only regularizing the problem but also allowing for a faster convergence.

The computational time acceleration provided by the OpenMP parallelization allows the FEMxDEM code to compete with classical FEM models in terms of walltime. Together with the second gradient regularization presented in a previous chapter, this allows to consider real scale problems with complicated meshes. Eventually, the non-unicity of the model showed up due to the parallelization implementation, it has been shown that the results are still valid solutions of the boundary value problem (BVP).

The parametric studies applied to gallery excavations show the ability of the model to cope both with microscale and macroscale inputs in order to reproduce the characteristics of a BVP.

The aforementioned improvements make the FEMxDEM approach competitive with classical FEM models in terms of computational cost thus allowing to perform robust and mesh-independent multi-scale FEMxDEM simulations, from the laboratory scale (e.g. biaxial test) to the engineering-scale problem, (e.g. gallery excavation).

Bibliography

Amdahl, G. M., 1967. Validity of the single processor approach to achieving large scale computing capabilities. In: Proceedings of the April 18-20, 1967, spring joint computer conference. ACM, pp. 483–485.

Anderson, P. W., et al., 1972. More is different. Science 177 (4047), 393–396.

Andó, E., 2013. étude experimentale de l'évolution de la microstructure d'un milieu granulaire sous chargement mécanique a l'aide de la tomographie rayons x. Ph.D. thesis, Docteur de L'Université de Grenoble.

Andrade, J., Avial, C., Hall, S., Lenoir, N., Viggiani, G., 2011. Multiscale modelling and characterization of granular matter: from grain kinematics to continuum mechanics. Journal of the Mechanics and Physics of Solids 59 (2), 237–250.

Arcamone, J., Tritsch, J., 1985. The cerchar method of pressiometric testing. Mining Science and Technology 2 (3), 229–233.

Argilaga, A., Papachristos, E., Caillerie, D., Dal Pont, S., 2016. Homogenization of a cracked saturated porous medium: Theoretical aspects and numerical implementation. International Journal of Solids and Structures 94, 222–237.

Armand, G., Leveau, F., Nussbaum, C., de La Vaissiere, R., Noiret, A., Jaeggi, D., Landrein, P., Righini, C., 2014. Geometry and properties of the excavation-induced fractures at the meuse/haute-marne url drifts. Rock Mechanics and Rock Engineering 47 (1), 21–41.

Armand, G., Noiret, A., Zghondi, J., Seyedi, D., 2013. Short-and long-term behaviors of drifts in the callovo-oxfordian claystone at the meuse/haute-marne underground research laboratory. Journal of Rock Mechanics and Geotechnical Engineering 5 (3), 221–230.

Asanovic, K., Bodik, R., Catanzaro, B. C., Gebis, J. J., Husbands, P., Keutzer, K., Patterson, D. A., Plishker, W. L., Shalf, J., Williams, S. W., et al., 2006. The landscape of parallel computing research: A view from berkeley. Tech. rep., Technical Report UCB/EECS-2006-183, EECS Department, University of California, Berkeley.

Auriault, J., 1991. Heterogeneous medium. is an equivalent macroscopic description possible? International journal of engineering science 29 (7), 785–795.

Auriault, J.-L., 2011. Heterogeneous periodic and random media. are the equivalent macroscopic descriptions similar? International Journal of Engineering Science 49 (8), 806–808.

Avial, C., Andrade, J., 2012. Advances in multiscale modelling and characterization of granular matter. Procedia IUTAM 3 (0), 157–171.

Barnichon, J.-D., 2007. Finite element modelling in structural and petroleum geology. Ph.D. thesis.

Bastiaens, W., Bernier, F., Buyens, M., Demarche, M., Li, X., Linotte, J., Verstricht, J., 2003. The connecting gallery-the extension of the hades underground research facility at mol, belgium. EURIDICE report 3, 294.

Bazant, Z. P., Chang, T.-P., 1987. Nonlocal finite element analysis of strain-softening solids. Journal of engineering mechanics 113 (1), 89–105.

Besuelle, P., Chambon, R., Collin, F., 2006. Switching deformation modes in post-localization solutions with a quasibrittle material. Journal of Mechanics of Materials and Structures 3, 1115–1134.

Blanco, P. J., Sánchez, P. J., de Souza Neto, E. A., Feijóo, R. A., 2014. Variational foundations and generalized unified theory of rve-based multiscale models. Archives of Computational Methods in Engineering, 1–63.

Burgess, D., Giles, M., 1997. Renumbering unstructured grids to improve the performance of codes on hierarchical memory machines. Advances in Engineering Software 28 (3), 189–201.

Chambon, R., Caillerie, D., El Hassan, N., 1998. One-dimensional localisation studied with a second grade model. European Journal of Mechanics-A/Solids 17 (4), 637–656.

Chambon, R., Caillerie, D., Matsuchima, T., 2001. Plastic continuum with microstructure, local second gradient theories for geomaterials: localization studies. International Journal of Solids and Structures 38 (46), 8503–8527.

Chambon, R., Desrues, J., Hammad, W., Charlier, R., 1994. Cloe, a new rate-type constitutive model for geomaterials theoretical basis and implementation. International Journal for Numerical and Analytical Methods in Geomechanics 18 (4), 253–278.

Chen, L., Duveau, G., Poutrel, A., Jia, Y., Shao, J.-F., Xie, N., 2014. Numerical study of the interaction between adjacent galleries in a high-level radioactive waste repository. International Journal of Rock Mechanics and Mining Sciences 71, 405–417.

Chow, E., Falgout, R. D., Hu, J. J., Tuminaro, R. S., Yang, U. M., 2006. A survey of parallelization techniques for multigrid solvers. Parallel processing for scientific computing 20, 179–201.

Collin, F., Chambon, R., Charlier, R., 2006. A finite element method for poro mechanical modelling of geotechnical problems using local second gradient models. International journal for numerical methods in engineering 65 (11), 1749–1772.

Crisfield, M., Wills, J., 1988. Solution strategies and softening materials. Computer methods in applied mechanics and engineering 66 (3), 267–289.

Dao, L.-Q., Cui, Y.-J., Tang, A.-M., Pereira, J.-M., Li, X.-L., Sillen, X., 2015. Impact of excavation damage on the thermo-hydro-mechanical properties of natural boom clay. Engineering Geology 195, 196–205.

De, R. P. R., De Vree, J., 1996. Gradient enhanced damage for quasi-brittle materials. International Journal for numerical methods in engineering 39, 3391–3403.

De Borst, R., 1987. Computation of post-bifurcation and post-failure behavior of strain-softening solids. Computers & Structures 25 (2), 211–224.

De Borst, R., Mühlhaus, H.-B., 1992. Gradient-dependent plasticity: formulation and algorithmic aspects. International Journal for Numerical Methods in Engineering 35, 521-539.(1992).

de Montleau, P., Cela, J. M., Mpong, S. M., Godinass, A., 2002. A parallel computing model for the acceleration of a finite element software. In: International Symposium on High Performance Computing. Springer, pp. 449–456.

de Souza Neto, E., Blanco, P., Sánchez, P., Feijóo, R., 2015. An rve-based multiscale theory of solids with micro-scale inertia and body force effects. Mechanics of Materials 80, 136–144.

Desrues, J., Nguyen, T., Combe, G., Caillerie, D., 2015. Femxdem multi-scale analysis of boundary value problems involving strain localization. In: Chau, K.-T., Zhao, J. (Eds.), Bifurcation and Degradation of Geomaterials in the New Millennium. Springer Series in Geomechanics and Geoengineering. Springer International Publishing, pp. 259–265.

Desrues, J., Viggiani, G., 2004. Strain localization in sand: an overview of the experimental results obtained in grenoble using stereophotogrammetry. International Journal for Numerical and Analytical Methods in Geomechanics 28 (4), 279–321.

Dobruschin, P., 1968. The description of a random field by means of conditional probabilities and conditions of its regularity. Theory of Probability & Its Applications 13 (2), 197–224.

Drucker, D. C., Prager, W., 2013. Soil mechanics and plastic analysis or limit design. Quarterly of applied mathematics 10.

Duchêne, L., 2003. Fem study of metal sheets with a texture based, local description of the yield locus. Ph.D. thesis, Université de Liège, Liège, Belgique.

Erdogan, F., 2000. Fracture mechanics. International Journal of Solids and Structures 37 (1–2), 171–183.

Eringen, A. C., 1972. Nonlocal polar elastic continua. International journal of engineering science 10 (1), 1–16.

Farhat, C., Crivelli, L., 1989. A general approach to nonlinear fe computations on shared-memory multiprocessors. Computer Methods in Applied Mechanics and Engineering 72 (2), 153–171.

Flatscher, T., Pettermann, H., 2011. A constitutive model for fiber-reinforced polymer plies accounting for plasticity and brittle damage including softening–implementation for implicit fem. Composite Structures 93 (9), 2241–2249.

Gastebled, O., May, I., 2000. Bifurcation in the numerical simulation of softening mechanisms. Computers & Structures 78 (6), 745–755.

Geers, M. G., Kouznetsova, V. G., Brekelmans, W., 2010. Multi-scale computational homogenization: Trends and challenges. Journal of computational and applied mathematics 234 (7), 2175–2182.

Germain, P., 1973. La méthode des puissances virtuelles en mécanique des milieux continus. J. Mécanique 12, 236–274.

Golub, G. H., Van Loan, C. F., 2012. Matrix computations. Vol. 3. JHU Press.

Govender, N., Rajamani, R. K., Kok, S., Wilke, D. N., 2015. Discrete element simulation of mill charge in 3d using the blaze-dem gpu framework. Minerals Engineering 79, 152–168.

Guayacán-Carrillo, L.-M., Sulem, J., Seyedi, D. M., Ghabezloo, S., Noiret, A., Armand, G., 2016. Analysis of long-term anisotropic convergence in drifts excavated in callovo-oxfordian claystone. Rock Mechanics and Rock Engineering 49 (1), 97–114.

Guo, N., Zhao, J., 2013. A hierarchical model for cross-scale simulation of granular media. In: AIP Conf Proc. Vol. 1542. pp. 1222–1225.

Guo, N., Zhao, J., 2014. A coupled fem/dem approach for hierarchical multiscale modelling of granular media. International Journal for Numerical Methods in Engineering.

Guo, N., Zhao, J., 2015. Multiscale insights into classical geomechanics problems. International Journal for Numerical and Analytical Methods in Geomechanics.

Guo, N., Zhao, J., 2016a. 3d multiscale modeling of strain localization in granular media. Computers and Geotechnics.

Guo, N., Zhao, J., 2016b. Parallel hierarchical multiscale modelling of hydro-mechanical problems for saturated granular soils. Computer Methods in Applied Mechanics and Engineering 305, 37–61.

Guo, X., Lange, M., Gorman, G., Mitchell, L., Weiland, M., 2014. Developing a scalable hybrid mpi/openmp unstructured finite element model. Computers & Fluids.

Habata, S., Yokokawa, M., Kitawaki, S., 2003. The earth simulator system. NEC Research and Development 44 (1), 21–26.

Hautefeuille, M., Colliat, J.-B., Ibrahimbegovic, A., Matthies, H., Villon, P., 2012. A multi-scale approach to model localized failure with softening. Computers & Structures 94, 83–95.

Hill, R., 1962. Acceleration waves in solids. Journal of the Mechanics and Physics of Solids 10 (1), 1–16.

Jouan, G., Kotronis, P., Collin, F., 2014. Using a second gradient model to simulate the behaviour of concrete structural elements. Finite Elements in Analysis and Design 90, 50–60.

Kaneko, K., Terada, K., Kyoya, T., Kishino, Y., 2003. Global–local analysis of granular media in quasi-static equilibrium. International Journal of Solids and Structures 40 (15), 4043–4069.

Kanfar, M. F., Chen, Z., Rahman, S., 2015. Effect of material anisotropy on time-dependent wellbore stability. International Journal of Rock Mechanics and Mining Sciences 78, 36–45.

Kouznetsova, V., Brekelmans, W., Baaijens, F., 2001. An approach to micro-macro modeling of heterogeneous materials. Computational Mechanics 27 (1), 37–48.

Kouznetsova, V., Geers, M., Brekelmans, W., 2004. Multi-scale second-order computational homogenization of multi-phase materials: a nested finite element solution strategy. Computer Methods in Applied Mechanics and Engineering 193 (48), 5525–5550.

Kruyt, N., Rothenburg, L., 1998. Statistical theories for the elastic moduli of two-dimensional assemblies of granular materials. International journal of engineering science 36 (10), 1127–1142.

Lisjak, A., Garitte, B., Grasselli, G., Müller, H., Vietor, T., 2015. The excavation of a circular tunnel in a bedded argillaceous rock (opalinus clay): short-term rock mass response and fdem numerical analysis. Tunnelling and Underground Space Technology 45, 227–248.

Lisjak, A., Grasselli, G., Vietor, T., 2014. Continuum–discontinuum analysis of failure mechanisms around unsupported circular excavations in anisotropic clay shales. International Journal of Rock Mechanics and Mining Sciences 65, 96–115.

Liu, Y., Sun, W., Yuan, Z., Fish, J., 2015. A nonlocal multiscale discrete-continuum model for predicting mechanical behavior of granular materials. International Journal for Numerical Methods in Engineering.

Loret, B., Prevost, J. H., 1990. Dynamic strain localization in elasto-(visco-) plastic solids, part 1. general formulation and one-dimensional examples. Computer Methods in Applied Mechanics and Engineering 83 (3), 247–273.

Love, A. E. H., 2013. A treatise on the mathematical theory of elasticity. Vol. 1. Cambridge University Press.

Marinelli, F., 2013. Comportement couplé des géomatériaux: deus approches de módelisation numérique. Ph.D. thesis.

Marinelli, F., Sieffert, Y., Chambon, R., 2015. Hydromechanical modeling of an initial boundary value problem: Studies of non-uniqueness with a second gradient continuum. International Journal of Solids and Structures 54, 238–257.

Matsushima, T., Chambon, R., Caillerie, D., 2000. Second gradient models as a particular case of microstructured models: a large strain finite elements analysis. Comptes Rendus de l'Académie des Sciences-Series IIB-Mechanics-Physics-Astronomy 328 (2), 179–186.

Matsushima, T., Chambon, R., Caillerie, D., 2002. Large strain finite element analysis of a local second gradient model: application to localization. International journal for numerical methods in engineering 54 (4), 499–521.

Matthies, H. G., Brenner, C. E., Bucher, C. G., Soares, C. G., 1997. Uncertainties in probabilistic numerical analysis of structures and solids-stochastic finite elements. Structural safety 19 (3), 283–336.

Meier, H., Steinmann, P., Kuhl, E., 2008. Towards multiscale computation of confined granular media,. Technische Mechanik 28 (1), 32–42.

Menard, L., 1965. Règles pour le calcul de la force portante et du tassement des fondations en fonction des résultats pressiométriques. In: Proceedings of the Sixth International Conference on Soil Mechanics and Foundation Engineering. Vol. 2. pp. 295–299.

Miehe, C., Dettmar, J., Zäh, D., 2010a. Homogenization and two-scale simulations of granular materials for different microstructural constraints. International Journal for Numerical Methods in Engineering 83 (8-9), 1206–1236.

Miehe, C., Dettmar, J., Zäh, D., 2010b. Homogenization and two-scale simulations of granular materials for different microstructural constraints. International Journal for Numerical Methods in Engineering 83 (8-9), 1206–1236.

Mindlin, R. D., 1964. Micro-structure in linear elasticity. Archive for Rational Mechanics and Analysis 16 (1), 51–78.

Mindlin, R. D., 1965. Second gradient of strain and surface-tension in linear elasticity. International Journal of Solids and Structures 1 (4), 417–438.

Moore, G. E., 2006. Cramming more components onto integrated circuits, reprinted from electronics, volume 38, number 8, april 19, 1965, pp. 114 ff. IEEE Solid-State Circuits Newsletter 3 (20), 33–35.

Moore, G. E., et al., 1975. Progress in digital integrated electronics. In: Electron Devices Meeting. Vol. 21. pp. 11–13.

Moradabadi, E., Laefer, D. F., Clarke, J. A., Lourenço, P. B., 2015. A semi-random field finite element method to predict the maximum eccentric compressive load for masonry prisms. Construction and Building Materials 77, 489–500.

Moto Mpong, S., de Montleau, P., Godinas, A., Habraken, A., 2002. A parallel computing model for the acceleration of a finite element software. In: Proceedings of the International Conference on Parallel and Distributed Processing Techniques and Applications. CSREA Press, pp. 185–191.

Nakajima, K., 2005. Three-level hybrid vs. flat mpi on the earth simulator: Parallel iterative solvers for finite-element method. Applied Numerical Mathematics 54 (2), 237–255.

Needleman, A., 1988. Material rate dependence and mesh sensitivity in localization problems. Computer methods in applied mechanics and engineering 67 (1), 69–85.

Nguyen, T., 2013. Modélisation numérique à double échelle des matériaux granulaires cohésifs : Approche par éléments finis-éléments discrets. Ph.D. thesis.

Nguyen, T., Combe, G., Caillerie, D., Desrues, J., 2014. Fem× dem modelling of cohesive granular materials: Numerical homogenisation and multi-scale simulations. Acta Geophysica 62 (5), 1109–1126.

Nguyen, T. K., Combe, G., Caillerie, D., Desrues, J., 2013. Modeling of a cohesive granular materials by a multi-scale approach. AIP Conference Proceedings 1542 (1).

Nitka, M., Combe, G., Dascalu, C., Desrues, J., 2011. Two-scale modeling of granular materials: a dem-fem approach. Granular Matter 13 (3), 277–281.

Nova, R., 1994. Controllability of the incremental response of soil specimens subjected to arbitrary loading programmes. Journal of the Mechanical behavior of Materials 5 (2), 193–202.

OpenMP, A. R. B., 2011. Openmp application program interface, version 3.1. available from http://www.openmp.org.

Pamin, J. K., 1994. Gradient-dependent plasticity in numerical simulation of localization phenomena. TU Delft, Delft University of Technology.

Pantalé, O., 2005. Parallelization of an object-oriented fem dynamics code: influence of the strategies on the speedup. Advances in Engineering Software 36 (6), 361–373.

Pasternak, E., Dyskin, A. V., Sevel, G., 2014. Chains of oscillators with negative stiffness elements. Journal of Sound and Vibration.

Paulino, G. H., Liu, Y., 2001. Implicit consistent and continuum tangent operators in elastoplastic boundary element formulations. Computer methods in applied mechanics and engineering 190 (15), 2157–2179.

Pietruszczak, S., Mroz, Z., 1981. Finite element analysis of deformation of strain-softening materials. International Journal for Numerical Methods in Engineering 17 (3), 327–334.

Puła, W., et al., 2016. Calibration of characteristic values of soil properties using the random finite element method. Archives of Civil and Mechanical Engineering 16 (1), 112–124.

Radjai, F., Dubois, F. (Eds.), 2010. Discrete Numerical Modeling of Granular Materials. Wiley.

Rice, J. R., 1976. The localization of plastic deformation. Division of Engineering, Brown University.

Richefeu, V., Combe, G., Viggiani, G., 2012. An experimental assessment of displacement fluctuations in a 2d granular material subjected to shear. arXiv preprint arXiv:1208.0485.

Roux, J., Combe, G., 2010. How granular materials deform in quasistatic conditions. In: 260-270 (Ed.), IUTAM-ISIMM Symposium on Mathematical Modeling and Physical Instances of Granular Flows, AIP Conference Proceedings. Vol. 1227. pp. 260–270.

Roux, J.-N., Combe, G., 2002. Quasistatic rheology and the origins of strain. Comptes Rendus Physique 3 (2), 131–140.

Saad, Y., Van Der Vorst, H. A., 2000. Iterative solution of linear systems in the 20th century. Journal of Computational and Applied Mathematics 123 (1), 1–33.

Saint-Cyr, B., Krzysztof, S., Voivret, C., Azéma, E., Richefeu, V., Delenne, J.-Y., Combe, G., Cécile, N.-L., Pascal, V., Philippe, S., Marie, C., Radjai, F., 2012. Particle shape dependence in 2D granular media. Europhysics letters - EPL 98 (4), 44008.

Salehnia, F., Collin, F., Li, X. L., Dizier, A., Sillen, X., Charlier, R., 2015. Coupled modeling of excavation damaged zone in boom clay: Strain localization in rock and distribution of contact pressure on the gallery's lining. Computers and Geotechnics 69, 396–410.

Schuėller, G., et al., 1997. A state-of-the-art report on computational stochastic mechanics. Probab. Eng. Mech 12 (4), 197–321.

Shahin, G., Desrues, J., Dal Pont, S., Combe, G., Argilaga, A., 2016. A study of the influence of rev variability in double scale fem× dem analysis. International Journal for Numerical Methods in Engineering.

Shi, J., Crisfield, M., 1992. A simple indicator and branch switching technique for hidden unstable equilibrium paths. Finite elements in analysis and design 12 (3), 303–312.

Shmigelskyi, P., Farmaga, I., Spiewak, P., Ciupinski, L., 2011. Evaluation of computational complexity of finite element analysis using gaussian elimination. Electronics and Informatics (4).

Sieffert, Y., Al Holo, S., Chambon, R., 2009. Loss of uniqueness of numerical solutions of the borehole problem modelled with enhanced media. International Journal of Solids and Structures 46 (17), 3173–3197.

Simo, J. C., Hughes, T. J., 2006. Computational inelasticity. Vol. 7. Springer Science & Business Media.

Sluys, L., De Borst, R., Mühlhaus, H.-B., 1993. Wave propagation, localization and dispersion in a gradient-dependent medium. International Journal of Solids and Structures 30 (9), 1153–1171.

Smit, R., Brekelmans, W., Meijer, H., 1998. Prediction of the mechanical behavior of nonlinear heterogeneous systems by multi-level finite element modeling. Computer Methods in Applied Mechanics and Engineering 155 (1), 181–192.

Sudret, B., Der Kiureghian, A., 2000. Stochastic finite element methods and reliability: a state-of-the-art report. Department of Civil and Environmental Engineering, University of California Berkeley, CA.

Szarf, K., Combe, G., Villard, P., 2009. Influence of the grains shape on the mechanical behavior of granular materials. Powders and grains 357.

Tailhan, J.-L., Dal Pont, S., Rossi, P., 2010. From local to global probabilistic modeling of concrete cracking. Annals of Solid and Structural Mechanics 1 (2), 103–115.

Tokiwa, T., Tsusaka, K., Matsubara, M., Ishikawa, T., Ogawa, D., 2013. Formation mechanism of extension fractures induced by excavation of a gallery in soft sedimentary rock, horonobe area, northern japan. Geoscience Frontiers 4 (1), 105–111.

van den Eijnden, A., Bésuelle, P., Collin, F., Chambon, R., Desrues, J., 2016. Modeling the strain localization around an underground gallery with a hydro-mechanical double scale model; effect of anisotropy. Computers and Geotechnics.

Wang, J., 2014. On area-specific underground research laboratory for geological disposal of high-level radioactive waste in china. Journal of Rock Mechanics and Geotechnical Engineering 6 (2), 99–104.

Wang, K., Sun, W., 2016. A semi-implicit discrete-continuum coupling method for porous media based on the effective stress principle at finite strain. Computer Methods in Applied Mechanics and Engineering 304, 546–583.

Wang, N., Montagner, J.-P., Fichtner, A., Capdeville, Y., 2013. Intrinsic versus extrinsic seismic anisotropy: The radial anisotropy in reference earth models. Geophysical Research Letters 40 (16), 4284–4288.

Yang, Y., Misra, A., 2012. Micromechanics based second gradient continuum theory for shear band modeling in cohesive granular materials following damage elasticity. International Journal of Solids and Structures 49 (18), 2500–2514.

You, S., Ji, H., Labiouse, V., Hall, S. A., Viggiani, G., 2015. Quantitative analysis of deformation in hollow cylinder tests on anisotropic clay formations. International Journal of Mining Science and Technology 25 (2), 299–303.

Résumé substantiel française

L'approche multi-échelle FEMxDEM est une nouvelle méthode numérique appliquée aux problèmes géotechniques. En utilisant à la fois la méthode des éléments finis (FEM) à la macro-échelle et de la méthode des éléments discrets (DEM) à l'échelle de la microstructure du matériau. L'avantage de cette approche est qu'elle évite l'utilisation des relations constitutives phénoménologiques, celles qui ont besoin de la calibration des paramètres qui n'ont pas un sens physique claire. Au lieu de cela, la relation constitutive provient du modèle microscopique qui est régi par des paramètres ayant un sens plus physique. Le lien entre les échelles se fait via une homogénéisation numérique. De cette façon, la loi de comportement numérique des milieux continus et la matrice tangente correspondante sont obtenues directement à partir de la réponse discrète de la microstructure.

L'approche, dans la façon dont il a été construit dans le présent travail, présente quelques inconvénients; la vitesse de convergence et la robustesse de la méthode de Newton sont pires que celles observées dans les modèles FEM classiques, en outre, la charge computationnelle de l'intégration de la micro-échelle rend le modèle multi-échelle FEMxDEM pas pratique à utiliser. Enfin, pas particulièrement de cette méthode, mais une question générale des modèles mécaniques FEM avec de l'adoucissement est qu'il souffre de dépendance du maillage.

On considère l'évolution quasi-statique d'un milieu continu en grandes déformations. L'équation constitutive anélastique qui est délivré à partir d'une simulation DEM, partage des caractéristiques, au moins d'un point de vue numérique, avec d'autres équations constitutives de la géomécanique, par exemple élastoplasticité et hypoplasticité. La simulation numérique, réalisée dans le cadre d'éléments finis (Lagamine, ULg), est basée sur une méthode pas à pas. Complétée par des conditions aux limites, le problème aux limites, non linéaire en général, est résolu en utilisant la méthode de Newton. A chaque itération, les équations sont développées au premier ordre par rapport aux inconnues. Ensuite, le problème linéaire correspondant est résolu, les inconnues sont mises à jour, prêt pour l'itération suivante. La stricte application de la méthode de Newton doit différencier la relation constitutive, le gradient de celui-ci est souvent appelé le "opérateur consistent", il est défini par C: Avec l'exception de certains cas simples pour lesquels une forme fermée de l'expression du tenseur C peut être trouvé, la détermination de C est réalisée numériquement en utilisant une méthode de perturbation.

Dans le cas présent, la détermination de σ^f en terme de F^f est particulier dans le

sens qu'il n'est pas fourni par l'intégration d'une équation constitutive incrémentale ou partiellement incrémentielle sur un pas de temps comme dans le cas de hypoplasticité ou élastoplasticité, mais par le calcul DEM du champ de déplacement d'un ensemble des grains spatialement périodique. La condition de périodicité signifie que, à chaque étape de son évolution, la géométrie de l'assemblage est périodique. Cela revient à dire que les positions des grains sont donnés à celles des grains d'un sous-ensemble, appelé cellule de base. Pour déterminer le mouvement des grains de l'ensemble de l'assemblage, il suffit de déterminer que les gains de la cellule de base en prenant en compte les interactions possibles de ces grains avec celles des cellules adjacentes. Les rotations des grains sont supposés périodiques. Le mouvement des grains de la cellule de base est déterminé par intégration numérique des équations dynamiques de Newton, les grains interagissent par des forces de contact qui sont en partie élastique et qui remplissent les conditions Signorini-Coulomb de friction. Une certaine cohésion peut être prise en compte, mais les couples d'interaction sont ignorées. Les inconnues sont les déplacements et rotations des grains, ainsi que les forces d'interaction. Le calcul DEM est effectué jusqu'à ce que les grains de la cellule de base sont équilibrés (énergie cinétique inférieure à un seuil, plus la création ou la perte de contact, ...) de telle manière que le calcul de la DEM doit être compatible avec la caractéristique quasi-statique de la modélisation macroscopique. Pour accélérer cette dernière partie du calcul un terme d'amortissement peut être ajouté aux forces en interaction.

A la fin du calcul, la DEM fournit les positions des grains de la cellule de base et les forces de contact. Le tenseur des contraintes est déterminé selon la formule de Cauchy-Poisson.

L'approche FEMxDEM est computianellement coûteux en raison de l'intégration nécessaire de la micro-échelle. Ceci est aggrave par des problèmes de convergence avec différentes origines, principalement en raison de l'adoucissement et le comportement bruyant du modèle de DEM.

Les particularités de la méthode FEMxDEM rend l'utilisation du CTO inappropriée dans la méthode de Newton à cause d'un mauvais conditionnement de la matrice du système et de l'instabilité conséquente, principalement à conséquence de la loi bruyante fournie par la DEM et le temps de calcul consacrée à intégrer la loi. L'AEO (moyenne temporal de l'opérateur) est une solution déjà présenté par d'autres auteurs qui permet à la méthode de Newton de fonctionner avec FEMxDEM, notamment dans la région post-pic, d'autres approches comme "Kruyt" qui représente une approche plus pragmatique qui donne une nouvelle amélioration par rapport à AEO, KAO est destiné à fournir une meilleure description du milieu de la DEM que Kruyt, mais en termes de performances, il possède des propriétés similaires. Enfin, deux opérateurs; DEMQO et PSTLO, qui dans le plan théorique donnent les mêmes valeurs, mais du point ou vue numérique sont obtenus en utilisant différentes techniques, donne les meilleurs résultats en termes de vitesse de convergence à la fois dans les régimes de pré et post-pic.

Pour conclure l'étude de l'opérateur Newton: en raison du temps de calcul consacrée à la résolution d'un système linéaire avec un nombre de DOF proportionnelle au nombre de particules de la DEM, le PSTLO nécessite plus de temps de calcul. Le DEMQO reste

le meilleur opérateur en raison de sa stabilité, le taux de convergence et temps de calcul.

L'un des défis pour la méthode de Newton est d'atteindre la précision à l'approche d'une bifurcation. Souvent, lorsque le point de bifurcation est passé, la méthode de Newton augmente son efficacité en réduisant à nouveau le nombre d'itérations. L'homogénéité initiale de l'échantillon semble être à l'origine de la faible vitesse de convergence. Différentes méthodes pour introduire l'hétérogénéité ont été testés, un intérêt particulier est l'utilisation de la génération de de la DEM lui-même pour créer une variabilité aléatoire sans perturber les paramètres du modèle.

L'utilisation d'une description de la mécanique des milieux continus pour résoudre un problème aux limites fournit une description homogène du domaine en raison de la simplification des incertitudes. Cela contredit les observations des matériaux réels qui présentent une hétérogénéité spatiale. Ceci est particulièrement important parce que la rupture des symétries déterminera le dépliage des bifurcations et donc l'évolution du problème. D'accord avec la bibliographie, la rupture des symétries et augmentation conséquente de la complication du modèle permet la méthode FEM×DEM de mieux prédire le comportement mécanique des matériaux réels et suppose aussi une augmentation des performances de calcul.

L'approche FEMxDEM a un avantage par rapport au FEM classique lorsqu'il traite avec l'hétérogénéité spatiale, l'hétérogénéité souhaitée peut être introduite en générant des ensembles DEM différents mais en gardant les mêmes paramètres à la micro-échelle, cela se traduit par des ensembles DEM qui sont représentatifs du même matériau, mais présentant différents comportements dus à la disposition différente des particules dans chaque cellule DEM, d'une manière similaire aux matériaux réels.

Bien qu'étant les cellules de la DEM représentants du même matériau, ces différences peuvent avoir un effet important sur le comportement mécanique de l'ensemble granulaire comme le montrent les simulations DEM pures. Les simulations homogènes FEM×DEM réalisées ont montré un comportement similaire à l'à la micro-échelle respective utilisée, mais avec une réponse beaucoup plus lisse.

Les milieux continus de la mécanique classique ne peuvent pas reproduire correctement l'évolution des matériaux présentant de fortes hétérogénéités dans le champ de déformation, par exemple la localisation des déformations. Modèles sans une représentation à la micro-échelle ne peuvent pas correctement reproduire les mécanismes à la micro-échelle qui déclenchent la localisation de la déformation. Par ailleurs, les modèles de premier gradient ne présentent aucun paramètre de longueur dans la formulation, il en résulte un modèle sans une longueur caractéristique.

Un modèle de premier ordre utilise une relation constitutive de premier ordre entre les contraintes et les déformations. Dans l'approche FEMxDEM, une homogénéisation de calcul DEM à la micro-échelle fournit cette relation (Fig. 4.1).

Par conséquent, les approches numériques utilisant une approximation de premier ordre de la mécanique classique ne peuvent pas prédire correctement le comportement d'un milieu avec des gradients de contrainte élevés. Ces approches souffrent de non-

objectivité en raison de la dépendance du maillage dans de problèmes avec localisation, cela viole aussi le principe de l'action locale et donc la séparation des échelles.

Les causes possibles: les approximations de premier ordre ne donnent aucune information sur la longueur interne du modèle; d'un point de vue théorique, il y a une infinité de solutions dans le régime post-localisation, d'un point de vue numérique l'épaisseur de la bande de localisation aura tendance à se rétrécir à une taille proportionnelle à la taille du maillage. De cette façon, si le maillage est raffiné faisant la taille des éléments tendent à zéro afin d'obtenir une solution exacte, la déformation se concentrera dans une bande de taille nulle posant des problèmes évidents.

Il est nécessaire d'établir une relation entre l'hétérogénéité à la micro-échelle et la longueur caractéristique à la macro-échelle afin d'établir un effet de la taille de la micro-échelle appropriée sur la macro-échelle. Plusieurs approches existent dans la littérature, second gradient est retenu dans le présent projet.

Second gradient est utilisé pour fournir le modèle d'une longueur interne. En rétablissant l'objectivité du modèle, l'approche permet également d'accomplir le principe de l'action locale et donc la séparation d'échelles dans les points matériels.

Second gradient est un modèle local à la microstructure, cela signifie que la relation peut être appliquée en un point matériel de la même façon que une loi de comportement classique (Fig. 4.2). Ceci présente des avantages par rapport à des modèles non locaux qui an une dépendent du voisinage des points matériels pour construire la relation constitutive, cela a besoin d'autres considérations dans les limites du domaine.

La longueur interne introduite par la régularisation second gradient est obtenue de façon phénoménologique, puis les paramètres du second gradient sont calibrés pour obtenir la longueur interne souhaitée. Dans ce cas, l'équation du second gradient dépend d'un seul paramètre. La longueur interne dépend des modules de déchargement du matériau, ce qui est a priori inconnu, à cause de cela, afin de trouver le paramètre second gradient approprié une étude paramétrique est nécessaire. Un modèle avec une loi analytique est utilisé pour calibrer le paramètre second gradient, ceci est fait pour éviter le coût de calcul d'une série d'études paramétriques utilisant FEMxDEM.

Les résultats montrent que la régularisation est capable de rendre la méthode FEMxDEM objective. La régularisation est d'un intérêt particulier dans le modèle FEMxDEM; en raison du comportement bruyant de la loi DEM le problème est très susceptible de perdre son ellipticité conduisant à un problème mal posé. Le second gradient permet d'éviter la perte d'ellipticité non seulement régularisant le problème, mais aussi permet une convergence plus rapide.

L'approche FEMxDEM substitue l'expression analytique de la loi par un modèle numérique DEM incorporé dans les points matériels. La charge de calcul créée par les calculs supplémentaires nécessaires peut augmenter le temps de calcul de manière que la méthode devient peu pratique à utiliser. Les techniques de calcul disponibles, notamment la parallélisation, sont étudiés afin d'atténuer le problème de calcul des coûts.

Le modèle FEMxDEM est analysé afin de caractériser les charges computationnelles des différentes parties du code, l'intérêt est principalement discerner entre le solveur et

l'intégration de la loi. L'équilibre des charges computationnelles de ces deux détermine la stratégie de parallélisation optimale. Le paradigme de la parallélisation utilisée dans ce travail est un paradigme de mémoire partagée (OpenMP). L'alternative à la mémoire partagée est l'interface de passage de messages (MPI), qui permet la mise en œuvre d'une parallélisation massive, et ainsi prendre profit de la computation d'haute performance (HPC). Une parallélisation MPI de LAGAMINE a également été réalisée (J. Desrues, non publié, en préparation), cette seconde technique n'a pas été traitée dans ce document.

Le chemin critique d'un modèle FEM peut être divisé entre l'intégration de la loi au niveau du point de Gauss et la résolution de la matrice de rigidité globale (solveur). Le temps de calcul d'une de ces deux parties contribuera à augmenter le temps computationnel total. Parallélisation peut être utilisé pour diminuer efficacement le temps de calcul total à la fois dans les points de Gauss et le solveur.

L'intégration des points de Gauss dans un domaine FEM est indépendante d'un point de Gauss à l'autre. Ceci rend la parallélisation des points de Gauss une procédure triviale. L'accélération potentielle est proportionnelle au nombre de processeurs / cœurs disponibles.

D'autre part, le solveur doit résoudre un système d'équations linéaires conformées par la matrice de rigidité globale, le vecteur de forces et le vecteur de déplacements. Cette tâche ne peut être divisé en différentes tâches parallèles car elle se compose d'une procédure dépend en arrière.

Pour le projet présent la parallélisation sur la boucle des éléments peut fournir une grande amélioration de la performance, jusqu'à 99 % d'accélération en fonction de la relation éléments-solveur d'un test avec 512 éléments. Pour le moment, il n'y a pas d'intérêt sur la parallélisation du solveur, ce scénario peut changer si à l'avenir, en profitant des architectures parallèles, la taille du problème (nombre de DOF) est sensiblement augmentée.

Les résultats non-déterministes par rapport aux paramètres d'entrée du code parallèle n'invalident pas la mise en œuvre parce que les différences sont expliquées comme étant différentes solutions possibles du même problème. Le déclenchement des différentes solutions est causé par des perturbations numériques introduites par des changements aléatoires de l'ordre de traitement des différents éléments, puisque l'ordre d'assemblage doit être laissé libre dans le but d'optimiser l'efficacité de la parallélisation.

Le même phénomène de non objectivité est observé si une renumérotation des nœuds est utilisée dans la mise en œuvre FÉM.

En fonction de la nature du problème, cela peut aboutir à une solution très différente: un mode de localisation différent, pas de convergence, ou uniquement une différence numérique sans importance pratique. Dans un modèle FEMxDEM le premier est plus probable de se produire en raison de la grande sensibilité de la DEM.

L'accélération computationnelle fournie par la parallélisation permet au code FEMxDEM de rivaliser avec les modèles FEM classiques en termes de temps computationnel. Ensemble avec la régularisation second gradient présenté précédentment, il permet d'envisager des problèmes réels à grande échelle avec des maillages complexes. Ceci est traité dans la suite.

L'importance de la dimension du problème macroscopique est lié à la complexité de la micro-échelle et la séparation des échelles; pour accomplir la séparation des échelles le maillage doit être suffisamment fine pour bien représenter les variations du champ de déformations, cela signifie que les problèmes macroscopiques les plus grands contiennent plus de points de Gauss, chacun de ces points de Gauss exigera un temps de calcul proportionnel à la complexité de la micro-échelle.

Les modèles DEM peuvent efficacement modéliser problèmes aux limites avec quelques centaines ou des milliers de particules. Avec l'accélération GPU, les codes DEM peuvent même traiter des problèmes impliquant des millions de particules. Ces ordres de grandeur peuvent sembler suffisant pour modéliser des problèmes dans un domaine assez grand, mais le fait est que, selon la taille de grain cela peut ne pas être suffisant, par exemple pour traiter un problème de chemins de fer, où les particules constituant le ballast sont des roches avec une taille de plusieurs centimètres, un problème comprenant plusieurs mètres longitudinaux du chemin de fer uniquement contient quelques milliers de particules qui peuvent être facilement traitées. En revanche, si le matériau traité est un sable typique, un centimètre cubique du domaine contiendra environ 15.000 particules, ce qui rend impossible de traiter les problèmes à l'échelle d'ingénierie avec cette taille de particules en utilisant une approche de DEM pure. Il est dans ces conditions lorsque l'approche FEMxDEM peut fournir un outil pour modéliser des problèmes à l'échelle de l'ingénierie avec des matériaux granulaires.

Une série d'études paramétriques ont été réalisées. Ils comprennent les aspects macroscopiques: la géométrie du problème aux limites, le chemin de chargement, second gradient, champ de contrainte anisotropie, et les aspects micro-échelle: la taille de l'ensemble DEM, nombre de coordination DEM cohésion DEM. En outre, l'utilisation de la DEM dans la micro-échelle est exploitée afin de fournir le modèle avec anisotropie intrinsèque du matériau qui peut être utilisé conjointement avec l'anisotropie extrinsèque et un champ de contraintes anisotropie.

Les variations macroscopiques montrent la capacité du modèle FEMxDEM pour traiter problèmes continues aux limites comme se il était une approche classique FEM. D'ailleurs, la régularisation second gradient permet de contrôler le comportement constitutif jusqu'à ce du second ordre des déplacements, ce qui régularise le problème.

Les études paramétriques consistant en variations des paramètres de la micro-échelle montrent les avantages du modèle FEMxDEM en termes de richesse de la micro-échelle, ce qui permet de contrôler le comportement macroscopique. L'ambition du modèle est d'être capable d'extraire les caractéristiques de la micro-échelle du matériau à partir d'expériences et de calibrer la micro-échelle sans nécessité d'un étalonnage macroscopique. La nature multi-échelle du modèle, et en particulier les caractéristiques de la DEM, sont exploitée pour introduire anisotropie intrinsèque du matériau qui ne provient pas d'une relation phénoménologique, mais plutôt de la genèse de la micro-échelle. Cette genèse de la micro-échelle peut émuler la genèse de véritables géomatériaux afin d'obtenir un matériau représentatif sans étalonnages macroscopique.

Une des principales différences entre les résultats numériques et les observations

dans le forage du tunnel sur de matériaux granulaires est que dans le modèle numérique quelques grandes bandes de cisaillement régissent l'évolution de la rupture tandis que dans les observations de nombreuses petites bandes de cisaillement se développent près de la surface d'excavation. Dans une partie précédente, une étude sur la variabilité matérielle a été faite afin de comprendre quels sont les mécanismes impliqués lors de l'apparition de la localisation, dans ce cas, la comparaison entre les résultats numériques et des observations réelles suggèrent que des approches similaires pourraient être d'intérêt pour obtenir un modèle plus précis. Les améliorations susmentionnées rendent l'approche FEMxDEM compétitive avec les modèles FEM classiques en termes de coût de calcul permettant ainsi d'effectuer des simulations multi-échelle FEMxDEM robustes et indépendantes du maillage, depuis l'échelle du laboratoire (par exemple essaie biaxiale test) jusqu'à celle du problème à l'échelle de l'ingénierie (par exemple, excavation d'une galerie).